Universidade de Aveiro Departamento de Engenharia de Materiais e Cerâmica
2016

Anuraag Gaddam

Estrutura e cristalização de vidros de silicato de lítio multicomponentes

Structure and crystallization of multicomponent lithium silicate glasses

Universidade de Aveiro
2016

Departamento de Engenharia de Materiais e Cerâmica

Anuraag Gaddam

Estrutura e cristalização de vidros de silicato de lítio multicomponentes

Structure and crystallization of multicomponent lithium silicate glasses

Tese apresentada à Universidade de Aveiro para cumprimento dos requisitos necessários à obtenção do grau de Doutor em Ciência e Engenharia de Materiais, realizada sob a orientação científica do Doutor José Maria da Fonte Ferreira, Professor Associado com Agregação do Departamento de Engenharia de Materiais e Cerâmica da Universidade de Aveiro

This work was supported by: CICECO Aveiro Institute of Materials, POCI-01-0145-FEDER-007679 (FCT Ref. UID/CTM/50011/2013), and by the FaBiMed project with grant agreement nº 608901, (FP7-FoF.NMP.2013-11).

The support from JECS Trust (Contract No. 201478) is also acknowledged.

To the Loop Family,
(David, Julie and Jocelyn) …

o júri

presidente

Prof. Doutora Anabela Botelho Veloso
professora catedrática do departamento de Economia, Gestão, Eng.ª Industrial e Turismo da Universidade de Aveiro

Prof. Doutor Jorge Ribeiro Frade
professor catedrático do Departamento de Engenharia de Matérias e Cerámica da Universidade de Aveiro

Prof. Doutor Luis Filipe Santos
professor auxiliar do Instituto Superior Técnico, Universidade de Lisboa

Prof. Doutor Alberto Cabral Ferro
professor auxiliar do Departamento de Engenharia Mecânica do Instituto Superior Técnico, Universidade de Lisboa

Prof. Doutor Manuel Joaquim Peixoto Marques Ribeiro
professor adjunto do Instituto Politécnico de Viana do Castelo

Prof. Doutor José Maria da Fonte Ferreira
professor associado com agregação do Departamento de Engenharia de Matérias e Cerámica da Universidade de Aveiro

Acknowledgements

First of all I would like to thank my parents, without their financial and moral support this work could never have been accomplished.

I would like to express my sincere and deep gratitude to my supervisor, Prof. Dr. José Maria Ferreira, who supported and encouraged me during all stages of this project. It had been a great learning experience working under his guidance. He is very hard working, having excellent work ethic and always has been prompt to encourage me during some of the difficult times with great humility. His detailed comments, contributions and insights are greatly appreciated.

My sincere thanks to Dr. Hugo Fernandes who had thought me so much in regards to scientific research in the field of glasses and glass-ceramics since the beginning of this work. He has always been available to me for scientific discussions and guided me through simple to important decisions. It had been a great pleasure working with him.

I would like to thank Prof. Dr. Lionel Montagne for teaching me and training me in NMR spectroscopy. Discussions with him on glass structure had been extremely useful and helped me grow in this area.

I would like to express my gratitude to Dr. Budhendra Kumar Singh and Dr. Ajay Kaushal and for their friendship, encouragement and support. Special thanks also to Dr. Allu Amarnath Reddy for helping and supporting me during the first year of my arrival in Portugal. My heartfelt thanks to all of them for teaching me some important aspects of research life.

I'm very grateful to Dr. Susana Olhero for her support and friendship.

I would like to thank all my laboratory colleagues who provided me an excellent work atmosphere during the course of this project. Their friendship is deeply acknowledged and cherished: Saurabh Kapoor, Catarina Marques, Paula Torres, Avito Rebelo, B C Jamaliah and Sofia Neto.

Thanks to all colleagues and technicians of DEMaC and CICECO for the support to this work.

Finally my heartiest appreciation and gratitude to Prof. Dr. Parag Bhargava who first introduced me to glass science.

palavras-chave vidros, vitro-cerâmicos, silicato de lítio, estrutura do vidro, cristalização.

resumo

A presente tese tem como objetivo adquirir uma compreensão aprofundada acerca do processo de cristalização de vidros à base de silicato de lítio com a adição de pequenas quantidades de outros componentes. Os principais componentes investigados neste estudo são os óxidos de Mn, Al, B e P. Estudaram-se os efeitos de cada um destes componentes na estrutura do vidro, na separação de fases líquido-líquido, nos processos de nucleação e crescimento de cristais, na microestrutura e no conjunto das fases cristalinas formadas. Os vitro-cerâmicos utilizados neste estudo são produzidos a partir de amostras tridimensionais de vidro fundido e vertido em moldes, ou a partir de pós de frita obtida por arrefecimento dos fundidos em água.

A adição de óxidos de Mn aos vidros de silicato de lítio resulta na criação de entidades moleculares individuais de Mn. Por conseguinte, estas entidades moleculares dificultam o todo o processo de cristalização do vidro. Óxidos de Al e B são incorporados na rede de vidro como formadores de rede. Estes componentes, por conseguinte, também diminuem a tendência do vidro para a cristalização. O P_2O_5 também desempenha um papel de formador de rede do vidro. No entanto, ele aumenta a tendência do vidro para a cristalização. Dá-se uma ênfase especial ao estabelecimento de correlações entre a estrutura do vidro e seu comportamento na cristalização. Estes esforços levaram à introdução de um novo modelo matemático baseado na mecânica estatística para descrever a estrutura de vidro. O modelo foi desenvolvido principalmente para silicatos binários e mais tarde estendido para composições de silicatos multicomponentes.

keywords glasses, glass-ceramics, lithium silicate, glass structure, crystallization.

abstract

The present thesis is aimed at gaining an in-depth understanding of the crystallization process in multicomponent lithium silicate based glasses when other components are added in small amounts. The added components investigated in this study are oxides of Mn, Al, B and P. The effects of each of these components on glass structure, liquid-liquid phase separation, crystal nucleation, crystal growth, microstructure and phase assemblage are studied. The glass ceramics used in this study are produced by both bulk glasses obtained by melt quenching as well as by powder methods from glass frits.

Oxides of Mn when added to lithium silicate glasses result in creating individual Mn molecular entities. Consequently, these molecular entities hinder the overall crystallization ability of the glass. Oxides of Al and B are incorporated into glass network as network formers. These components consequently decrease the overall crystallization ability of the glass. P_2O_5 is also incorporated into glass network as network former. However, it increases the overall crystallization ability of the glass. Particular emphasis is given to establishing correlations between glass structure and its corresponding crystallization behaviour. These efforts led to introducing a new mathematical model based on statistical mechanics for describing the glass structure. The model was primarily developed for binary silicates and later on extended to multicomponent silicates.

Contents

List of Figures

List of Tables

List of Symbols

α: Linear Attenuation Coefficient

β: Heating Rate

δ_{iso}: Isotropic Chemical Shift

Δ_o: Ligand Field Strength

ΔG_{mix}: Gibbs's Free Energy of Mixing

ΔH_{mix}: Heat of Mixing

ΔS_{mix}: Entropy of Mixing

η: Asymmetry Parameter

Λ_{cal}: Calculated Optical Basicity

τ_{obs}: Experimental Time Scale

τ_{relax}: Relaxation Time

B: Racah Parameter

B^{IV}: Four Coordinated Boron

B^{III}: Three Coordinated Boron

B_o: Magnetic Field

C_Q: Quadrupolar Coupling Constant

D: Debora Number

E_g : Band Gap Energy

H: Enthalpy

$\mathcal{H}$: Hamiltonian

h: Planck Constant

$\hbar$: Dirac Constant

k_B: Boltzmann Constant

K_H: Hrubÿ Parameter of Glass Stability

LS_2: Lithium Disilicate

LS: Lithium Metasilicate

P: Pressure

PEL: Potential Energy Landscape

R: Gas Constant

RF: Radio Frequency

S: Entropy

T: Temperature

t: Time

T_D: Softening Temperature

T_f: Fictive Temperature

T_F: Flow Point

T_{FS}: First Shrinkage Temperature

T_g: Glass Transition Temperature

T_{gr}: Reduced Glass-Transition Temperature

T_{HB}: Half Ball

T_L: Liquidus Temperature

T_m: Melting Point

T_{MS}: Maximum Shrinkage Temperature

T_P: Peak Crystallization Temperature

V_m: Molar Volumes

W: Number of Ways

Z: Partition Function

List of Abbreviations

BO: Bridging Oxygen

CNT: Classical Nucleation Theory

DTA: Differential Thermal Analysis

FTIR: Fourier Transform Infrared Spectroscopy

GC: Glass-Ceramic

HSM: Hot Stage Microscopy

LLPS: Liquid-Liquid Phase Segregation

MAS: Magic Angle Spinning

NBO: Non-Bridging Oxygen

NMR: Nuclear Magnetic Resonance

SEM: Scanning Electron Microscopy

UV-VIS-NIR: Ultraviolet Visible Near-Infrared

XRD: X-Ray Diffraction

List of Equations

List of Publications

PhD Thesis

1. Role of manganese on the structure, crystallization and sintering of non-stoichiometric lithium disilicate glasses.
   Anuraag Gaddam, Hugo R. Fernandes, Dilshat U. Tulyaganov, María J. Pascual, José M. F. Ferreira.
   RSC Advances, 4 (2014) 13581-13592.
   DOI: 10.1039/c3ra46393a

2. Glass structure and crystallization of Al and B containing glasses belonging to the Li_2O-SiO_2 system.
   Anuraag Gaddam, Hugo R. Fernandes, José M. F. Ferreira.
   RSC Advances, 5 (2015) 41066-41078.
   DOI: 10.1039/C5RA04184H

3. Influence of Al_2O_3 and B_2O_3 on Sintering and Crystallization of Lithium Silicate Glass System.
   Anuraag Gaddam, Hugo R. Fernandes, María J. Pascual, José M. F. Ferreira.
   Journal of the American Ceramic Society, 99 (2016) 833-840.
   DOI: 10.1111/jace.14040

4. Statistics of silicate units in binary glasses.
   Anuraag Gaddam, Lionel Montagne, José M. F. Ferreira.
   The Journal of Chemical Physics, 145 (2016) 124505.
   DOI: 10.1063/1.4963341

5. The roles of P_2O_5 and SiO_2/Li_2O ratio on the network structure and crystallization kinetics of non-stoichiometric lithium disilicate based glasses.
   Anuraag Gaddam, Hugo R. Fernandes, Dilshat U. Tulyaganov, Manuel J. Ribeiro, José M.F. Ferreira.
   Journal of Non-Crystalline Solids, (2016, Submitted).

6. Structure and thermal relaxation of network units and crystallization of lithium silicate based glasses doped with oxides of Al and B.
   Anuraag Gaddam, Hugo R. Fernandes, Bertrand Doumert, Lionel Montagne, José M. F. Ferreira.
   Physical Chemistry Chemical Physics, (2016, Submitted).

Other Publications

7. Lithium Disilicate based Glass-Ceramics for Dental Applications.
   Anuraag Gaddam, Mudit Goyal, Sudhanshu Jain, Parag Bhargava.
   Transactions of the Indian Ceramic Society, 72 (2013) 56-60.
   DOI: 10.1080/0371750X.2013.794027

8. Structure, properties and crystallization of non-stoichiometric lithium disilicate glasses containing CaF_2.
   Hugo R. Fernandes, **Anuraag Gaddam**, Dilshat U. Tulyaganov, José M. F. Ferreira.
   Journal of Non-Crystalline Solids, 406 (2014) 54-61.
   DOI: 10.1016/j.jnoncrysol.2014.09.039.

Chapter 1

Introduction

The works of the LORD are great, sought out of all them that have pleasure therein.

(Psalms 111:2)

1.1 Background

The discovery of glass-ceramics (*GC*s) by S. D. Stookey in 1950s, invoked huge interest in these materials from both academic as well as industrial areas. Today, the usage of these materials covers a wide spectrum of applications.[1] The academic research in this area can be divided into two categories according to the glass systems studied: (1) stoichiometric and binary systems and (2) multicomponent systems. Due to the relative simplicity of the first category of glass systems, deeper fundamental studies were possible, addressing various aspects of glass crystallization. However, there are still several open problems even in this area which needs further light to be shed upon.[2–4] Coming to the second category of glass systems, the compositions studied so far typically came from particular applications. These glass systems usually have more than five components, mostly non-stoichiometric and have nucleating agents present in them. Most of the studies in this area are primarily focused on elucidating the role of a component(s) on,

- The final properties of *GC*s correlating with its microstructure and/or phase content
- Kinetics of the overall crystallization

However, due to the extreme complexity of such multicomponent systems, these studies severely lack in providing any understanding of the mechanism on how these component(s) influence the crystallization process itself. Studies like these mainly benefit optimizing the process parameters or in fine tuning of the chemical compositions in already developed *GC*s but, hardly contribute to the development of new *GC*s. This is similar to the plight of glass research, where advancements in fundamental understanding lag far behind that of technological advancements.[5] As a result, there exists a lack of knowledge in this area and due to this, a study done by Montazerian *et al.*[6], on the commercialization of *GC* research, clearly showed a decline in the number of patents in last decade. This is a concern and thus, industry also urges for a renewed focus on fundamental physics and chemistry governing *GC*s.[7]

Therefore the goal of this doctoral work is to enhance our understanding of glass crystallization in multicomponent systems. For this, lithium silicate system has been chosen and role of the components Mn, P, Al and B which have practical interest was

investigated. Particular attention was given to the understanding the structure and thermodynamics of the liquid phase.

1.2 Objectives

The main objective of this research work is to gain fundamental understanding of nucleation and crystallization processes occurring in complex glass compositions based on lithium disilicate. The base glass composition used for this study belonged to $x\mathrm{Li_2O} - (100–x)\mathrm{SiO_2}$ glass system for x = 24–28 (mol %), which are non-stoichiometric LS_2 based glass composition with excess silica present in them. For this glass system, the effect of a particular dopant both in the presence and in the absence of nucleating agents was evaluated on four aspects of glass crystallization; which are: (1) liquid-liquid phase segregation, (2) crystal nucleation, (3) crystal growth and (4) phase transformation at higher temperature. The dopants which are relevant for many applications among others are the oxides of Mn, P, Al and B, used extensively to achieve specific properties to the final glass-ceramics. When present even in small concentrations, these dopants might have a huge impact on the whole nucleation and crystallization process. In this current work these four dopants were used to carry out studies about their influence on the overall process of crystallization of LS_2 based glasses. The objectives of this thesis are twofold:

1. To study the effects of a dopant on glass structure and overall crystallization. The applications of this kind of study are enormous and important.
2. To establish glass structure-nucleation correlations.

1.3 Structure of the Report

This report consists of five chapters. This first chapter gives a brief introduction on the background and objectives of the current work. The second chapter provides a succinct literature review covering various fields within glass science highlighting our current understanding in these fields. The third chapter is divided into seven sub-chapters containing all the scientific work done within the frame work of the objective mentioned (Section 1.2). This chapter also contains literature review whenever it is required. The fourth chapter contains the entire conclusions from this current study. Finally, the fifth chapter presents suggestions for the future work.

Chapter 2

Literature Review

For the invisible things of him from the creation of the world are clearly seen, being understood by the things that are made, even his eternal power and Godhead; so that they are without excuse…

(Romans 1:20)

2.1 Glass

Glasses belong to an important class of materials available to scientists and engineers. Throughout history, mankind has been using these materials in both art and architecture. In modern times, glasses gained huge technological value with wide range of applications. Moreover, glasses also occur in nature through different natural processes examples include: (a) rapidly cooled magma from volcanos produces volcanic glass; (b) lightning strikes produce Fulgurite and etc. Further, these materials are also found on the lunar soil, which makes us believe that these materials are found everywhere in the universe. As a result, glass research has not only been of interest to the field of materials engineering, but also to other fields of science such as geology, minerology, and petrology etc. In all the cases, glasses formed in nature are prepared by sudden quenching of the molten rock. Traditionally, this same method has been employed by mankind to produce glasses; this method is termed as *melt quenching technique*. However, currently there are many other methods available to produce glasses. Further, as natural glasses which are mainly made of silicates, traditional glasses were prepared from silicates. However, today with advancement of technology, we have glasses prepared from many other materials.

A glass is defined as: *An amorphous solid completely lacking in long range, periodic atomic structure, and exhibiting a region of glass transformation behaviour*.[8] This definition describes two fundamental properties of glass: (1) glass structure (or the lack of it!) and (2) glass transition. In the next two sections, these two properties of glasses will be expounded.

2.2 Glass Structure

One of the earliest consideration of the glass structure was proposed by Zachariasen in his classic paper.[9] Today, his ideas remain central to the field of glass research and they are called as *random network theory*. According to Zachariasen, the atoms in a crystal and a glass are linked together by the same interactions and vibrate about their equilibrium positions. Howbeit, the main structural distinction between both is that, a glass lacks periodicity and symmetry in the structure contrary to a crystal. Due to lack of symmetry, the properties of glasses are isotropic (unless prepared in an

external field). Another essential consequence of the lack of symmetry is that the unit cell of the glass is of infinite size. Next in his paper, Zachariasen goes into considerable detail on the glass structure by taking examples of oxide glasses; which is also the interest of the current thesis. In analysing the structure of vitreous silica, Zachariasen noticed that the glass network is built up of oxygen tetrahedra surrounding silicon atoms. The tetrahedra are connected to each other by corner sharing such that each oxygen atom is linked to two silicon atoms. A two dimensional representation of this structure is presented in **Figure 2.2.1a–b** with tetrahedra represented as triangles. Zachariasen concluded that a vitreous network can only be built by oxygen tetrahedra or oxygen triangles, because oxygen octahedra or oxygen cubes would lead to periodic structures.

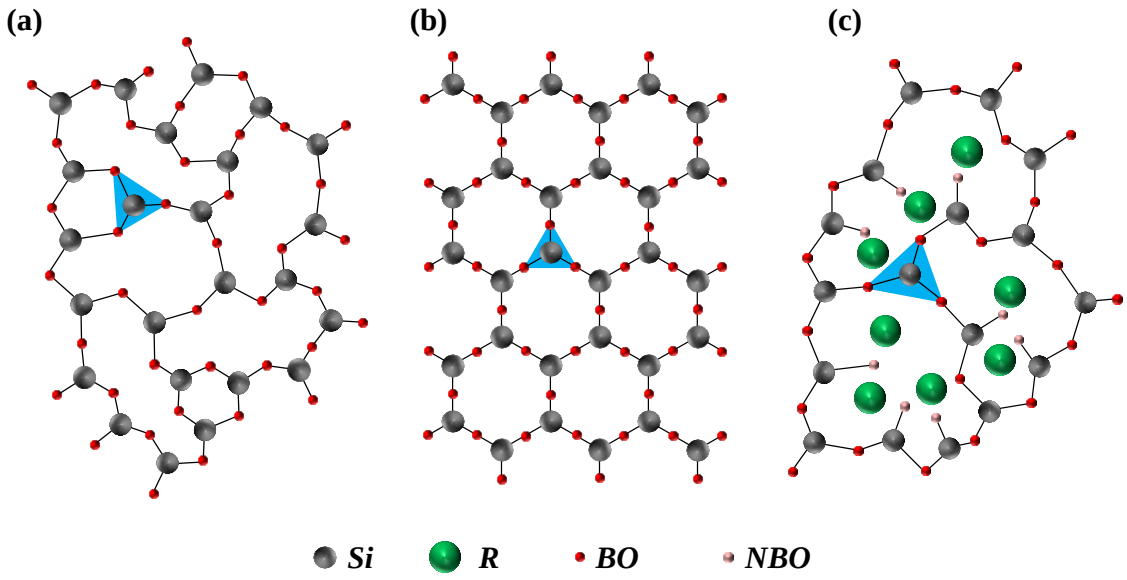

Figure 2.2.1 Two dimensional representation of network structure of (a) vitreous and (b) crystalline silica; (c) vitreous silicate.

Zachariasen noticed that the following general rules hold for vitreous oxides.

1. Each oxygen atom is linked to no more than two cations.
2. The oxygen coordination number of the network cation is small.
3. Oxygen tetrahedra or triangles share only corners and not edges or faces.
4. At least 3 corners of each oxygen polyhedron must be shared in order to form a 3–dimensional network.
5. Sample contains a high percentage of cations which are surrounded by oxygen tetrahedra or by oxygen triangles.

These general rules have become rules for the glass formation. However, they do not explain the formation of glasses in non-oxide systems and some of the rules are not valid even for the oxide systems: for example the existence of oxygen triclusters.[10] Therefore, today glass researchers do not take these rules dogmatically; but they gave a starting point to the structural analysis of glasses.

By introducing some components such as alkali and alkaline earth oxides into the vitreous oxide networks, the extra oxygens do not form bridges but form free ends as shown in **Figure 2.2.1c**; having a different structural functionality. Therefore, depending upon the type of structural function the components in oxide glasses are divided into three groups:

1. *Network formers:* This type of components build the glass network by forming oxygen tetrahedra and oxygen triangles which are also called *network units* or *structural units*. These units are connected to each other by corner sharing creating oxygen bridges, which are called *bridging oxygens* (*BO*) as described by *random network theory* (shown in **Figure 2.2.1a**). The common examples are: SiO_2, B_2O_3 and P_2O_5.
2. *Network modifiers:* This type of components break down the glass network by creating terminal oxygens also called *non-bridging oxygens* (*NBO*) as shown in the **Figure 2.2.1c**. The common examples are alkali and alkaline earth oxides.
3. *Intermediate oxides:* This type of components assumes either the role of network formers or network modifiers. One of most common examples (also of interest in this thesis) is Al_2O_3.

In silicate glasses, depending upon the number of *BO*s and *NBO*s present on a particular silicate tetrahedron, the unit is called Q_n unit; where, n is the number of *BO*s and $n \in \{0, 1, 2, 3 \text{ and } 4\}$.

2.2.1 Structure of binary glasses

The distribution of Q_n units, also called *network speciation*, in a glass composition is of central importance for understanding the structure of the glass.[11–17] Therefore, theoretical models were proposed for binary silicate systems in order to predict the Q_n distribution.[11,15,18] Two prominent models are: (1) binary model and (2) statistical model which take the composition of the glass to be: x (R_2O or RO) – (1–x) SiO_2; where R

corresponds to alkali or alkaline earth element and $x \in [0, 2/3]$. In the binary model, only two types of adjacent Q_n units are possible at each composition as described in the Eq. (2.2-1) and the distribution plotted in **Figure 2.2.2a**. Thus, this model is only applicable to crystalline silicates, which exhibit an ordered distribution.

$$Q_n^{bin}(\%) = \begin{cases} \dfrac{n(1-x)+5x-3}{1-x} & x \in \left[\dfrac{3-n}{5-n}, \dfrac{4-n}{6-n}\right] \\ \dfrac{n(x-1)-7x+5}{1-x} & x \in \left(\dfrac{4-n}{6-n}, \dfrac{5-n}{7-n}\right] \\ 0 & x \in \left[0, \dfrac{2}{3}\right] \cap \left(\dfrac{3-n}{5-n}, \dfrac{5-n}{7-n}\right) \end{cases} \qquad \text{Eq. (2.2-1)}$$

The statistical model on the other hand assumes a completely random distribution of Q_n units. To calculate the amount of each Q_n unit, it uses binomial probability mass distribution function where, the probability for n successes associated with choosing *BO*(s) out of 4 trials is calculated. The equation describing this distribution is given in the Eq. (2.2-2) and plotted in **Figure 2.2.2b**.

$$Q_n^{stat}(\%) = \binom{4}{n} \frac{(x)^n (2-3x)^{4-n}}{2(1-x)} \qquad \text{Eq. (2.2-2)}$$

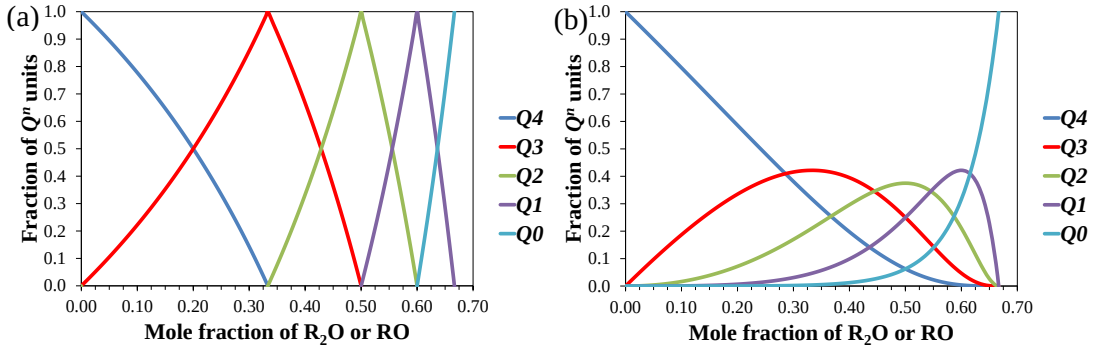

Figure 2.2.2 (a) Binary and (b) statistical models for Q_n distribution in silicate glasses.

In practice, glass compositions are not in agreement with either of the models discussed above. Most of the experimental glasses however show distributions that lie in between the distributions of binary and statistical models.[19,20] Further, they also show

a temperature dependence of the distribution. Therefore in Chapter 3.6, a new model is proposed that has capability to predict the actual Q_n distribution.

2.2.2 Structure of multicomponent glasses

Other network formers such as B_2O_3 and P_2O_5 also undergo network speciation when added into silicate glasses. Similar to SiO_2, P_2O_5 also exists as a tetrahedral unit having one doubly bonded oxygen on one corner, which acts as terminal oxygen similar to *NBO*. On other three corners, the oxygens can be either *BO* or *NBO*. Therefore, depending upon the number of *BO*s and *NBO*s present on a particular phosphate tetrahedron, the unit is called $Q_{n(P)}$ unit; where, n is the number of *BO*s and $n \in \{0, 1, 2 \text{ and } 3\}$. And B_2O_3 in borate and borosilicate glasses, undergoes a different kind of network speciation where, it speciates into three coordinated trigonal unit (B^{III}) and four coordinated tetrahedral unit (B^{IV}). The B^{IV} has a net one unit of negative charge on it; therefore in order to balance the charge it requires a cation called *charge compensator*. This is fulfilled by network modifiers that also act as charge compensators. The individual boron units, just as silicate units, could further speciate in terms of number of *BO*s and *NBO*s on each unit forming different extended structures.[21] The B-speciation in borosilicate glasses is described by empirical models proposed based on the experimental data.[22–25] In Chapter 3.7 however, an extended model for multicomponent systems is proposed.

2.3 Glass transition

2.3.1 Classical approach

Traditionally, the glass transition behaviour is understood based on the volume vs temperature (*V–T*) or enthalpy vs temperature (*H–T*) diagrams as shown in **Figure 2.3.1**. The point '***a***' represents the state of the liquid at a temperature above melting point (T_m). As the liquid is cooled, the volume (or enthalpy) decreases with the structure of the liquid rearranging to an equilibrium structure. Now, as it passes through T_m, avoiding crystallization, it reaches a regime called *supercooled liquid*; represented by a point '***b***'. At lower temperatures, rearrangement of the atomic units in the liquid slow down. Therefore, at some temperature, liquid starts falling out of the equilibrium entering into a region called *glass transition region* represented by point '***c***'. Further decrease of the temperature would lead to extremely slow transformations such that the

structure becomes rigid which is called *glass*; represented by the point '***d***'. The glass transition is a kinetic phenomenon that depends on both the relaxation time (τ_{relax}) and the experimental time scale (τ_{obs}). The time τ_{relax} is a temperature dependent function, corresponding to the time needed for the glass to relax to its equilibrium state; it is an intrinsic property of a particular glass system. While the time τ_{obs} corresponds to the observational time used in a particular experiment. The ratio between both times is called *Debora number* (D) given by,[26]

$$D = \frac{\tau_{relax}}{\tau_{obs}} \qquad \text{Eq. (2.3-1)}$$

In the supercooled region: $D < 1$; in the glass transition region: $D = 1$; in glassy state region: $D > 1$. Therefore, by controlling the cooling (or heating) rates different τ_{obs} values can be chosen, correspondingly different glass transition ranges. **Figure 2.3.1** shows two glass transition ranges for fast and slow cooling.

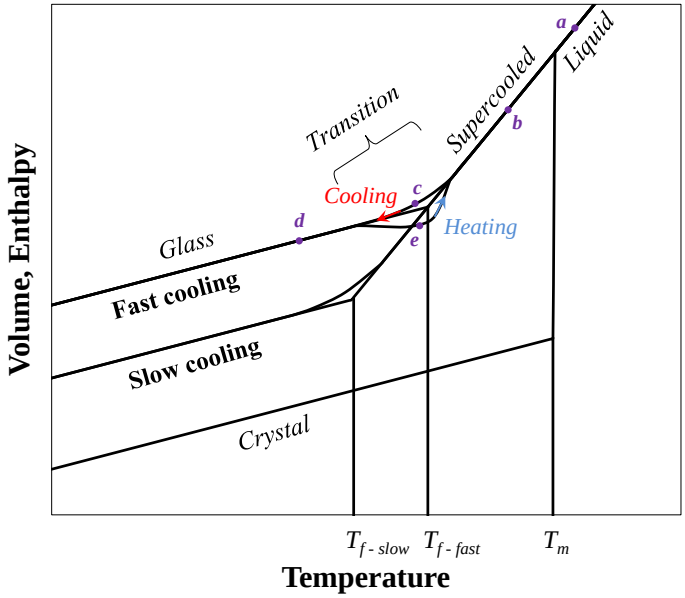

Figure 2.3.1 Temperature dependence on the properties of the liquid leading to glass transition (Adapted from [27]).

The glass transition region is a smooth continuous function and does not occur at a single point. However, glass scientists like to define a point called *glass transition temperature* (T_g) which is point that lies in the glass transition region. Depending upon the type of experimental technique employed to measure T_g, several conventions have been adopted to determine its value. Typical experimental heating and cooling rates involved when measuring T_g, range between two orders of magnitude ($10^{0 \text{ to } 2}$) in K min^{-}

[1]. At these time scales, the glass transition occurs at temperatures where viscosity is between 10^{12} to 10^{13} Pa·s. Therefore, T_g has been conventionally defined as the temperature at which the liquid has viscosity of 10^{12} Pa·s;[28] sometimes this temperature is also called as T_{12}. There is another quantity called *fictive temperature* (T_f) defined by the intersection of extrapolated glass and liquid lines. The physical meaning of T_f is understood as the temperature at which the equilibrium liquid structure resembles that of glass structure.[29] However, since the beginning, this concept has been controvertial;[30] which will be discussed later in this section. When different heating and cooling rates are employed, the glass transition region shows a profile similar to a hysteresis loop: where, the cooling and the heating paths are different. Usual cooling rates involved in the glass preparation by air cooling are between 10^3 to 10^4 K min^{-1}; which are higher than the heating rates used in measuring the glass transition. As a result while cooling, the system goes through ***bcd*** and while heating, it goes through ***deb***.

2.3.2 Energy landscape approach

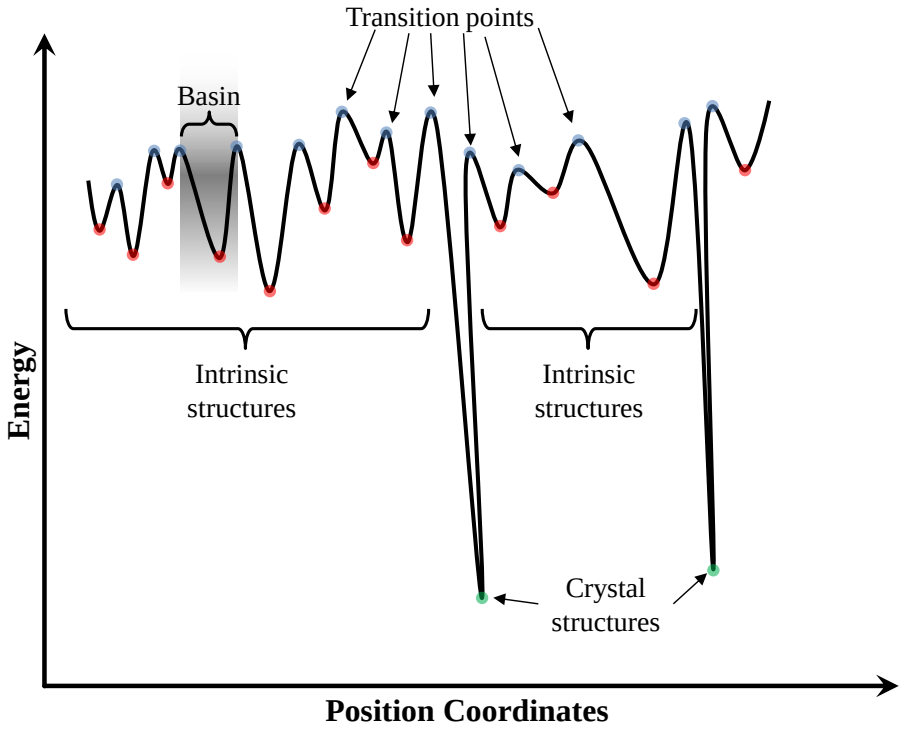

Figure 2.3.2 Schematic of *PEL* hypersurface (Adapted from [31]).

So far in the above discussion, the glass transition behaviour was understood by considering some macroscopic property of the system. The microscopic physics of the glass transition behaviour is understood using the concept of *potential energy landscape*

(*PEL*) approach.[31–34] In *PEL* approach, a system of *N* particles with appropriate potentials is considered and the classical Hamiltonian ($\boldsymbol{\mathcal{H}}$) is written for this system given by,

$$\mathcal{H}(\boldsymbol{r_1}, \boldsymbol{r_2}, \boldsymbol{r_3} \ldots \boldsymbol{r_N}) = \mathcal{H}(q_1, q_2 \ldots q_{3N}) \qquad \text{Eq. (2.3-2)}$$

Where, $\boldsymbol{r_1}$, $\boldsymbol{r_2}$, $\boldsymbol{r_3}$ … $\boldsymbol{r_N}$ are the position vectors of *N* particles. This expression does not include canonical momenta since we are dealing with condensed matter. Therefore, the phase space is 3*N* dimensional space and function $\boldsymbol{\mathcal{H}}$ is a hypersurface in 3*N* + 1 dimensional space; a 2-dimensional analogue is presented in **Figure 2.3.2**. This surface contains a lot of local minima, each of which is called *intrinsic structure*. Any two local minima are connected by a saddle point also called as *transition point*. The volume of space containing the steep descent from transition point to the intrinsic structure is called a '*basin*'. For a particular system, if there are Ω number of intrinsic structures, we can construct a Ω × Ω energy matrix,[35]

$$\boldsymbol{\mathcal{H}} = \begin{pmatrix} \mathcal{H}_{11} & \mathcal{H}_{12} & \mathcal{H}_{13} & . & . & \mathcal{H}_{1\Omega} \\ \mathcal{H}_{21} & \mathcal{H}_{22} & \mathcal{H}_{23} & . & . & \mathcal{H}_{2\Omega} \\ \mathcal{H}_{31} & \mathcal{H}_{32} & \mathcal{H}_{33} & . & . & \mathcal{H}_{3\Omega} \\ . & . & . & . & . & . \\ . & . & . & . & . & . \\ \mathcal{H}_{\Omega 1} & \mathcal{H}_{\Omega 2} & \mathcal{H}_{\Omega 3} & . & . & \mathcal{H}_{\Omega\Omega} \end{pmatrix} \qquad \text{Eq. (2.3-3)}$$

The diagonal elements denoted by $\boldsymbol{\mathcal{H}}_{ii}$ are the energies of i^{th} intrinsic structure whereas the non-diagonal elements are denoted by $\boldsymbol{\mathcal{H}}_{ij}$ are the energies of transition points connecting i^{th} and j^{th} intrinsic structures. Moreover, the matrix $\boldsymbol{\mathcal{H}}$ is a symmetric matrix; *i.e.* $\boldsymbol{\mathcal{H}} = \boldsymbol{\mathcal{H}}^{\text{T}}$. The initial (time $t = 0$) equilibrium probability distribution of the system among various intrinsic structures some temperature $T(0)$ is given by,

$$f_i(0) = \frac{1}{Q} \exp\left(\frac{\mathcal{H}_{ii}}{k_B T(0)}\right) \qquad \text{Eq. (2.3-4)}$$

Where, Q is canonical partition function and k_B is the Boltzmann constant. By cooling the system through some temperature path $T(t)$, the probability distribution $f(t)$ changes. This change is governed by Ω number of coupled master equations given by,

$$\frac{df_i(t)}{dt} = \sum_{j\neq i}^{\Omega} W_{ji}\big(T(t)\big)f_j(t) - \sum_{j\neq i}^{\Omega} W_{ij}\big(T(t)\big)f_i(t) \qquad \text{Eq. (2.3-5)}$$

Where, W_{ij} and W_{ji} are the rate parameters given according to transition state theory,

$$W_{ij}\big(T(t)\big) = \nu_{ij} \exp\left[-\frac{\mathcal{H}_{ij} - \mathcal{H}_{ii}}{k_B T(t)}\right] \qquad \text{Eq. (2.3-6)}$$

Where, ν_{ij} is the attempt frequency. All the rate parameters can also be expressed in the form of matrix,

$$\boldsymbol{W} = \begin{pmatrix} 0 & W_{12} & W_{13} & . & . & W_{1\Omega} \\ W_{21} & 0 & W_{23} & . & . & W_{2\Omega} \\ W_{31} & W_{32} & 0 & . & . & W_{3\Omega} \\ . & . & . & . & . & . \\ . & . & . & . & . & . \\ W_{\Omega 1} & W_{\Omega 2} & W_{\Omega 3} & . & . & 0 \end{pmatrix} \qquad \text{Eq. (2.3-7)}$$

In this case, the $\boldsymbol{W}$ is not a symmetric matrix *i.e.* $\boldsymbol{W} \neq \boldsymbol{W}^{\mathrm{T}}$. As the system evolves along a certain temperature path $T(t)$, the evolution of probability distribution $f(t)$ can be studied. Any property of the system such as volume, entropy etc. given by the parameter $A(t)$ is obtained by taking the ensemble average,

$$A(t) = \sum_{i=1}^{\Omega} A_i f_i(t) \qquad \text{Eq. (2.3-8)}$$

Where, A_i corresponds to the property for the i^{th} intrinsic structure. This way, the temperature dependence of property along a temperature path $T(t)$ can be determined. The main step involves, solving the set of master equations Eq. (2.3-5). This could be computationally expensive process; however, there are several efficient algorithms are used to simplify the process.[36] In the supercooled state, the system can explore all the intrinsic structures where, the transition points act as connectors, connecting all the intrinsic structures together; a Schematic representation is presented in **Figure 2.3.3** as a disconnectivity diagram.[36] In the supercooled state, the system is considered to be *ergodic*. As the temperature decreases, the transition points that have higher energy

become unreachable, disconnecting some of the intrinsic structures; loosing ergodicity. However, the intrinsic structures that are still connected would have internal ergodicity. Thus, in this state the system is considered to have *broken-ergodic*.[37] However, in the real systems the breaking down of ergodicity is a continuous process and are therefore modelled using concept of *continuously broken-ergodic*.[38] It is in this region the glass transition takes place and the system fall out of equilibrium. Further decrease of the temperature results in a complete loss of ergodicity and the system is frozen achieving a glassy state.

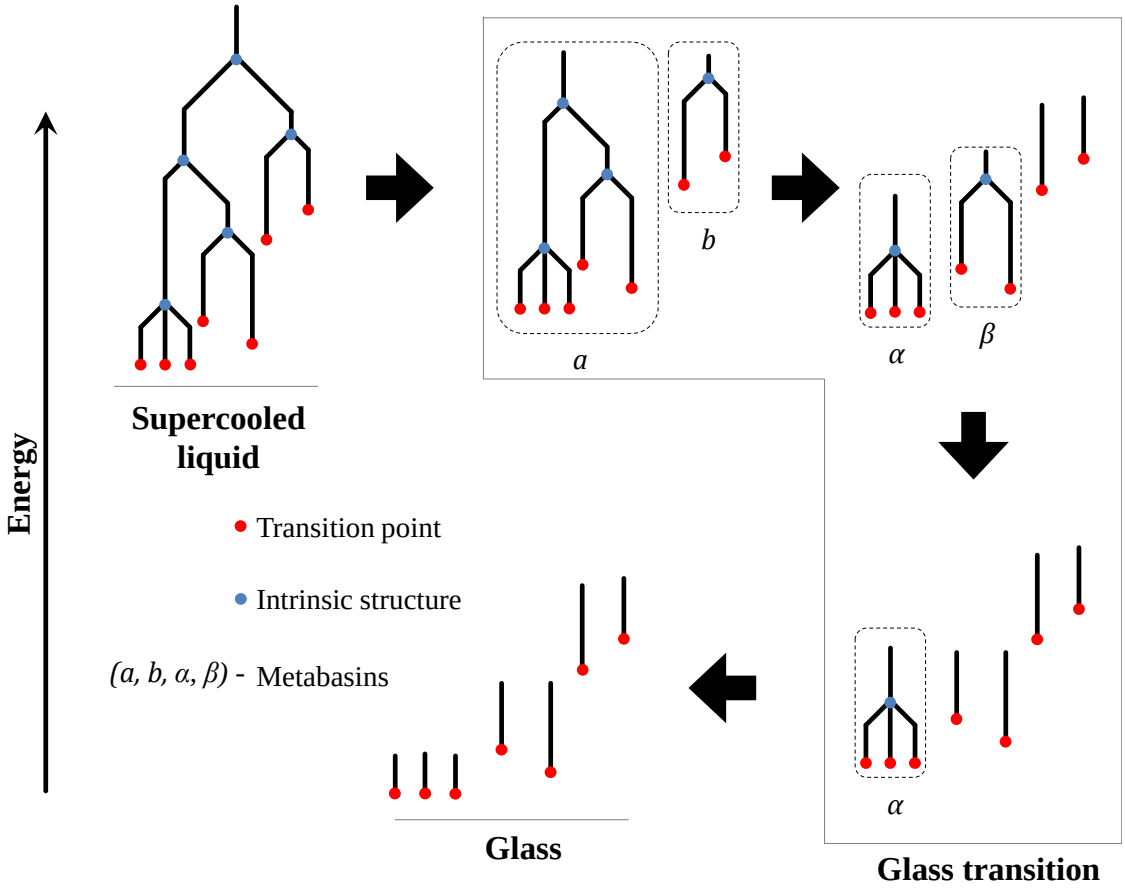

Figure 2.3.3 View of glass transition from the *PEL* perspective (Adapted from [39]).

2.4 Liquid-liquid phase segregation

Liquid-liquid phase segregation (*LLPS*) or liquid-liquid immiscibility is a very common phenomenon in many glass compositions.[8] Binary silicate glasses exhibit *LLPS* with nearly all oxides in the periodic table.[40] It occurs whenever the glass composition departs from the stoichiometry. In glasses, the occurrence of *LLPS* affects the translucency of the glass, due to the scattering of the light. Therefore, controlling the

LLPS is of central importance in glass manufacturing. However, glass-ceramists are usually not worried about the translucency of the *GC*. Nonetheless, glass-ceramists are interested in how *LLPS* affects the crystal nucleation rates; and thus to use *LLPS* for their own advantage. Therefore, from this perspective understanding *LLPS* is of key significance also to the field of *GC*s.

2.4.1 Mechanism of *LLPS*

The *LLPS* involves two relevant aspects: (1) thermodynamics and (2) kinetics. The thermodynamic aspect of *LLPS* can be understood using a simple *Gibbs's free energy of mixing* (ΔG_{mix}) model for binary system, given by the following equation,[41]

$$\Delta G_{mix} = \Delta H_{mix} - T\Delta S_{mix}$$

$$\Delta G_{mix} = \alpha x(1-x) + RT[x \ln x + (1-x)\ln(1-x)] \qquad \text{Eq. (2.4-1)}$$

Where, ΔH_{mix} and ΔS_{mix} are the *heat of mixing* and *entropy of mixing*. Using the regular solution model[42] the equation is expanded in terms of mole fractions of one of the components, *x*. The term α, which depends on the bond energies between atoms, controls the *LLPS*. When it is negative, there will be complete mixing of the liquid without *LLPS*; and when it is positive, the system starts to undergo *LLPS*. The Eq. (2.4-1) is plotted in **Figure 2.4.1a**, for some positive value of α at three different temperatures. In this phase diagram, compositions between the points *a* and *b* would undergo *LLPS*. The points *a* and *b* are the points of tangency for the common tangent drawn as shown in the **Figure 2.4.1a**, and the points *c* and *d* are the inflection points where the condition $\frac{\partial^2 \Delta G_{mix}}{\partial x^2}\Big|_{x_c, x_d} = 0$ is satisfied. Different regions of *LLPS* in a phase diagram are generated by the loci of the points *a*, *b*, *c*, and *d* for all the temperatures as shown in **Figure 2.4.1b**. The boundaries corresponding to the loci of *a* and *b* are called *immiscibility boundaries* whereas, the boundaries corresponding to the loci of *c* and *d* are called *spinodal boundaries*. The immiscibility boundaries produce a region called *immiscibility dome*. The immiscibility dome is divided into three regions (I, II and III) by the spinodal boundaries are shown in the **Figure 2.4.1b**. In the regions I and III the system undergoes droplet like *LLPS* for which, the kinetics of *LLPS* has the same underlying theory as kinetics of crystal nucleation.[41] Here, the two segregated

regions have a large compositional difference. In the region II, the system undergoes spinodal decomposition where, the two segregated regions have a small compositional difference. The detailed kinetic models for the *LLPS* are proposed by Cahn *et al.*[43–45]

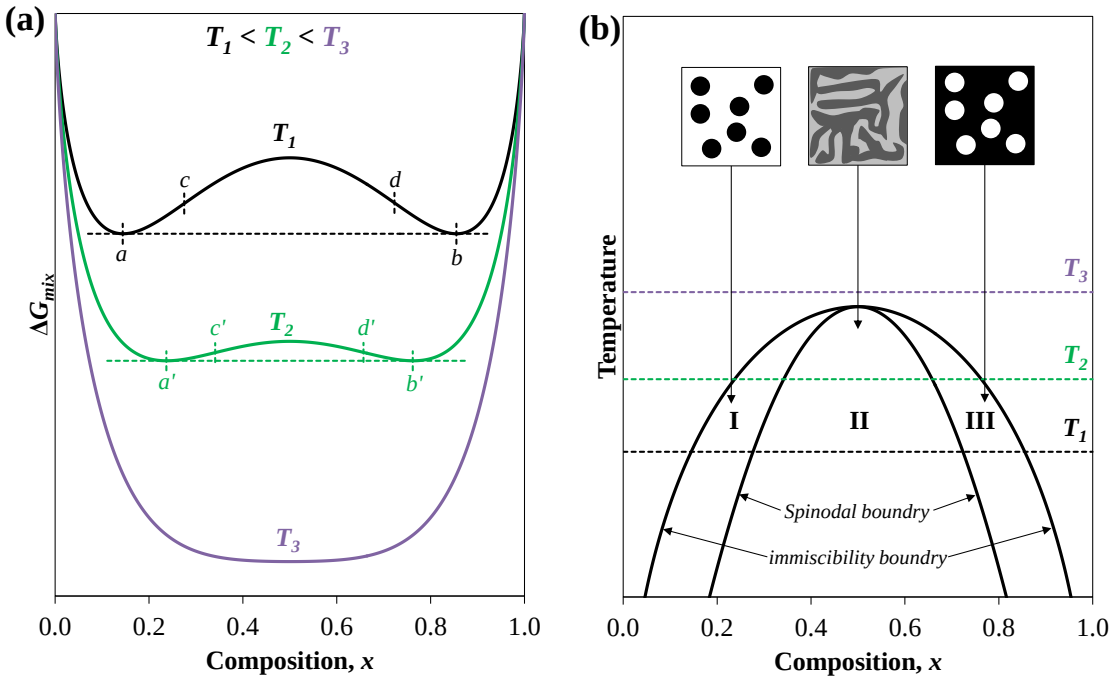

Figure 2.4.1 (a) Schematic of Gibb's free energy of mixing diagram and (b) the corresponding phase diagram with different regions of *LLPS*.

The model presented shows symmetric plots for the free energy diagram as well as phase diagram. However, glass forming compositions show very non-symmetric curves and the variations in the free energy curves are hardly visible.[46–48] The actual free energy curve for the Li_2O–SiO_2 system is plotted in **Figure 3.4.5** and **Figure** 3.4.12 illustrates this point. Nevertheless, this simple model gives a general understanding of the *LLPS*. Further, the mechanism of *LLPS* in multicomponent systems would be an extension of this simple model.[49] The current thesis is mainly concerned with *LLPS* in binary systems.

2.4.2 Stable and metastable immiscibility

Binary silicate melts belonging to the systems: MgO-SiO_2, CaO-SiO_2 and SrO-SiO_2, undergo what is known as *stable immiscibility*.[50] An example of the phase diagram exhibiting this kind of *LLPS* is shown in **Figure 2.4.2a** having a immiscibility dome existing above the *liquidus temperature* (T_L).[51] Inside the immiscibility dome, the liquid phase readily separates into two phases. When the melt is quenched for glass

preparation, one or two glass phases could be obtained.[40,52] The SiO_2-rich phase expectedly forms glass while, the other phase could be crystallized. If the crystallization is avoided, the system continues to undergo *LLPS* to its equilibrium state below T_L; this type of *LLPS* known as *metastable immiscibility* (**Figure 2.4.2a**).

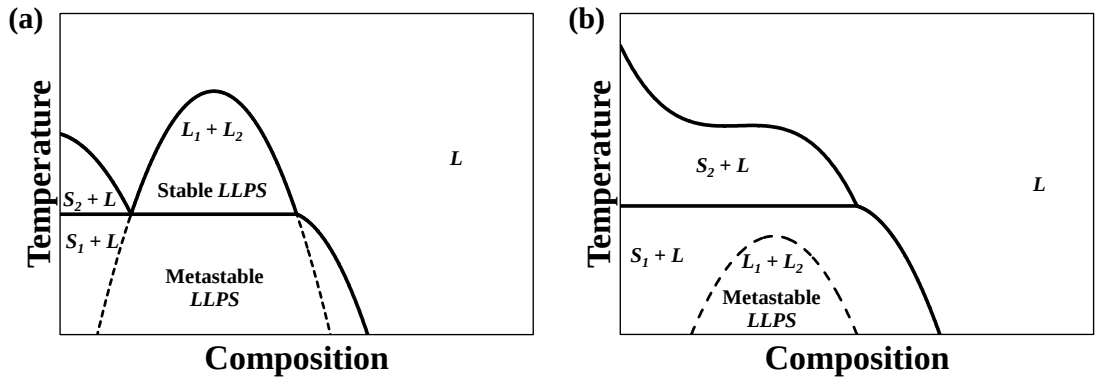

Figure 2.4.2 Schematic of phase diagrams showing (a) stable and (a) – (b) metastable immiscibility.

Binary silicate compositions belonging to the systems: Li_2O-SiO_2, Na_2O-SiO_2 and Ba_2O-SiO_2, have immiscibility dome below the T_L, therefore these compositions always undergo metastable immiscibility (**Figure 2.4.2b**).[53] Therefore, the *LLPS* in these systems is observed only by avoiding devitrification of the supercooled liquid. However, the existence of the immiscibility dome can be inferred from the '*S*' shaped (or its mirror image in the case of reversed compositional axis) liquidus curve as seen in **Figure 2.4.2b**.

2.4.3 Atomistic approach to *LLPS*

Previous sections on *LLPS* dealt with understanding the mechanism of *LLPS* from thermodynamics perspective, which is a macroscopic approach. However, it is also important to understand the *LLPS* from an atomistic approach. In binary alkali and alkaline earth silicate glasses, the tendency for *LLPS* increases in the following order Cs < Rb < K < Na < Li <Ba < Sr < Ca < Mg.[51] Several studies[53–58] have shown that there is strong correlation between *LLPS* and ionic field strengths (Z/r^2, Z is valance and r is radius) or ionic potentials (Z/r) of the modifiers ions in these binary systems. A thorough investigation[59] on 41 different binary silicate systems revealed that higher the ionic potential, the larger is the immiscibility gap. Therefore, it was suggested that the *LLPS* occurs due to coulombic repulsions between poorly screened cations bounded by

*BO*s strongly polarized towards the silicon, and by non-bridging oxygens. There is another school of thought, which suggests that the silicate liquids are made of long range structures containing 3D frameworks, sheets, chains, dimers and monomers. And, the immiscibility is caused by the un-mixing of these polymeric species.[41] Nevertheless, this field of research is still green, and so much work needs to be done in order to understand what causes the *LLPS* at an atomic level.

2.5 Glass-Ceramics

Unlike glasses which are defined based on their properties, *GC*s are defined based on their processing. Therefore, *GCs are defined as the materials produced by controlled crystallization of the glass*.[1] Three parameters are usually controlled when producing *GC*s: (1) chemical composition of the glass, (2) heat treatment temperatures and (3) the durations of the heat treatments. These parameters are controlled in such a way to obtain *GC*s with preferred phase assemblage and microstructure ultimately leading to a material with required properties.

Hence, for the production of *GC*s, it is essential to understand the overall thermodynamics and kinetics of crystallization of the base glass, which includes two steps:

a) Crystal nucleation
b) Crystal growth

Figure 2.5.1 presents an example of temperature dependence of steady-state crystal nucleation and crystal growth rates. Curves like these, giving the kinetic information about crystal nucleation and growth for a particular composition, are essential for designing processing routes for the production of *GC*s. Such curves are conventionally generated by experimentally measuring the rates at each temperature by microscopy.[60] Such experiments are very laborious and time consuming. Therefore, there has been a need for theoretical models which can predict these rates without actually measuring. The crystal nucleation rates in glasses have been attempted to be described by *classical nucleation theory* (*CNT*),[2] which is given by the following equation,

$$I\,(T) = I_o \exp\left(-\frac{W^* + \Delta G_D}{RT}\right) \qquad \text{Eq. (2.5-1)}$$

Where, I is the steady-state nucleation rate, I_o is a constant (or a function with a weak temperature dependence), W^* is the thermodynamic barrier for nucleation ΔG_D is the kinetic barrier for nucleation, R is the gas constant and T is the temperature. The detailed derivation of this equation and its implication to glass science will be in the subsequent sections. The crystal growth rates (U) in oxide glasses are given by two models.[61] The first one is called normal or continuous growth model[62] given by,

$$U\,(T) = \frac{D_u}{\lambda}\left[1 - \exp\left(-\frac{\Delta G}{RT}\right)\right] \qquad \text{Eq. (2.5-2)}$$

Where, $U(T)$ is the temperature steady-state growth rate, λ is the jump distance, ΔG is the thermodynamic driving force, which is the difference between free energies of liquid and sold phase and D_u is the diffusion coefficient for the transport of molecular units to the solid-liquid interface. This model can describe growth rates in SiO_2 and GeO_2 systems. However, growth rates in alkali silicate systems are described well using screw dislocation model[63] given by the following equation,

$$U\,(T) = f\frac{D_u}{\lambda}\left[1 - exp\left(-\frac{\Delta G}{RT}\right)\right] \qquad \text{Eq. (2.5-3)}$$

Where,

$$f = \frac{\lambda \Delta G}{4\pi\sigma V_m} \qquad \text{Eq. (2.5-4)}$$

Here, f is the called site factor which is a fraction representing the amount of available sites at solid-liquid interface where the incoming molecular units can be added.

Combining both the nucleation and growth rates can describe the complete transformation kinetics of a particular system. This theory was developed within the period from 1937 to 1941 by Kolmogorov[64], Johnson and Mehl[65] and Avrami.[66–68] All the proposed models are combined in the JMAK theory.[69] However, there are other less fundamental models that also give useful kinetic information, which are used in sections 3.4.3.1 and 3.5.3.2.

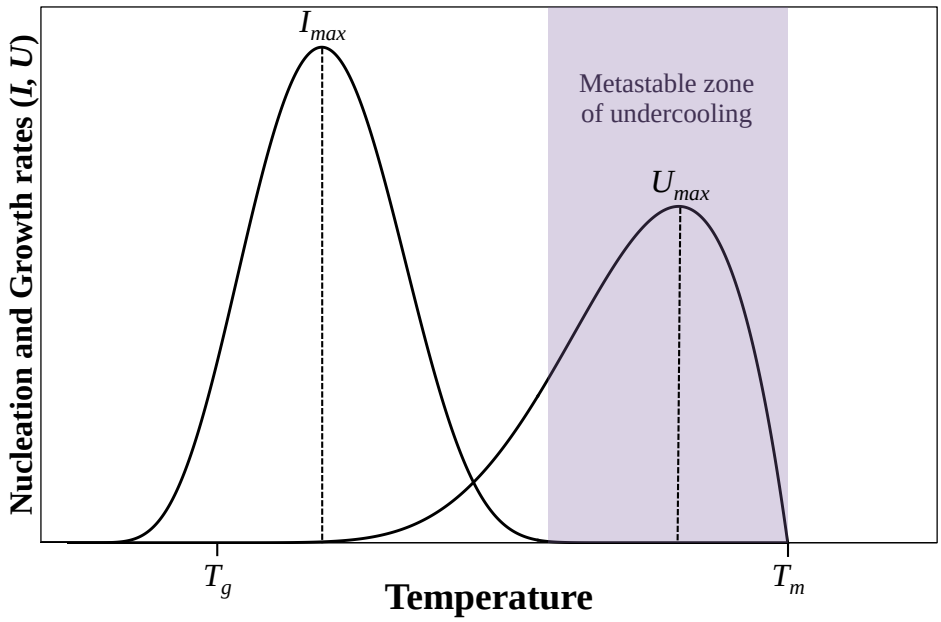

Figure 2.5.1 Schematics of temperature dependence of study-state crystal nucleation and growth rates (Adapted from [8]).

2.5.1 Thermodynamics of Nucleation

In order to derive the nucleation rate, the *CNT* model starts with a thermodynamic argument. A quantity denoted by *W(i)* is defined as shown in Eq. (2.5-5). This function is called as *work function* or *free energy barrier* for nucleation. Here, *i* is the number of atomic units in the nucleating cluster representing the size of the cluster, μ_L and μ_S are the chemical potentials associated liquid and solid phases, *S(i)* is the surface energy of the cluster, which is dependent on the size of the, α depends on geometrical shape of the nucleus and σ is the interfacial surface energy between two droplets.

$$W(i) = -i(\mu_L - \mu_S) + S(i)\sigma$$

$$W(i) = -i\Delta\mu + S(i)\sigma \qquad \text{Eq. (2.5-5)}$$

$$S(i) = \alpha\, i^{2/3}$$

The chemical potential difference between liquid and solid phases denoted by $\Delta\mu$ is the thermodynamic driving force for nucleation. The work function plotted in Figure 2.5.2 shows that the surface energy ($S(i)\sigma$) has a monotonically increasing component whereas volume energy ($-i\Delta\mu$) has a monotonically decreasing component. The net

result of both functions make *W(i)* go through a maximum. The size of the nucleus where this maximum occurs *i.e.* $i = c$ and the corresponding value of *W(i)* are called the critical size and activation energy respectively given by,

$$c = \frac{8}{27}\left(\frac{\alpha\sigma}{\Delta\mu}\right)^3 ; W(c) = \frac{4}{27}\frac{(\alpha\sigma)^3}{\Delta\mu^2} \qquad \text{Eq. (2.5-6)}$$

Any nucleus with size greater than *c* continues to grow to a larger crystal. Otherwise it could dissolve back to the liquid. This thermodynamic argument applies for describing the nucleation occurring in the bulk of the system and it is called as homogenous nucleation. Nucleation that happens by the assistance of external surfaces or on the particles within the system is called heterogeneous nucleation. The next presents the kinetic argument for the crystal nucleation.

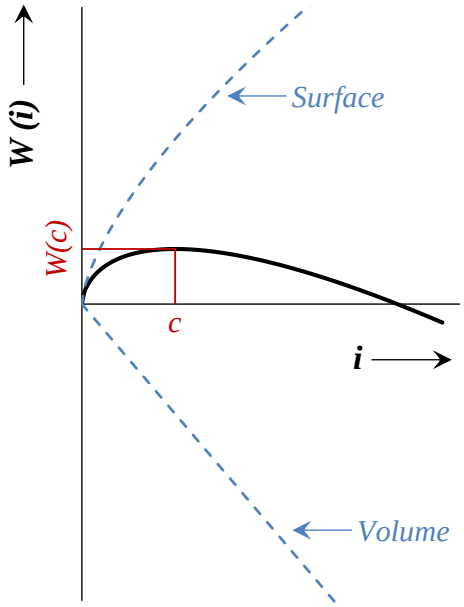

Figure 2.5.2 Variation of work function *W* with the size of the nucleus.

2.5.2 Kinetics of Nucleation: Classical Nucleation Theory

The kinetic description of nucleation is given by *CNT*. The *CNT* model was developed by a series of works by Kaischew and Stranski[70], Volmer and Weber[71] and Becker and Döring[72] based on the following assumptions[61]:

1. It considers a spatially homogenous distribution of components (atoms or molecules) that makeup the system.

2. If C_i stands for the cluster containing i number of components ($i \in \mathbb{N}$), then the cluster can grow or decay by addition of only a single component at a time, given by,

$$C_1 + C_{i-1} \underset{k_i^-}{\overset{k_{i-1}^+}{\rightleftharpoons}} C_i \qquad \text{Eq. (2.5-7)}$$

$$C_1 + C_i \underset{k_{i+1}^-}{\overset{k_i^+}{\rightleftharpoons}} C_{i+1} \qquad \text{Eq. (2.5-8)}$$

Where, k_i^+ and k_i^- are the reaction rate constants associated to attachment and detachment a single component to C_i.

3. By supposing the reactions Eq. (2.5-7) and Eq. **(2.5-8)** are of first order, the net forward flux for both reactions is given by,

$$I_i(t) = k_{i-1}^+ N_{i-1}(t) - k_i^- N_i(t)$$
$$I_{i+1}(t) = k_i^+ N_i(t) - k_{i+1}^- N_{i+1}(t) \qquad \text{Eq. (2.5-9)}$$

Where, N_i is the number of clusters of size i. Therefore the rate of change of N_i is given by,

$$\frac{dN_i(t)}{dt} = I_i(t) - I_{i+1}(t) \qquad \text{Eq. (2.5-10)}$$

4. The clusters are assumed to take an equilibrium shape as they form.
5. The state of the system (*i.e.* T and P) is not changed during the course of nucleation.
6. Once the size of a cluster reaches an upper limit c, called *critical size*, it is removed from the system therefore,

$$N_i(t) = 0;\ \forall\ i \geq c \qquad \text{Eq. (2.5-11)}$$

After the removal of the cluster, c numbers of components are added back into the system. Thus, the number of components is always conserved in the system, given by,

$$N_1(t) + \sum_{i=2}^{c-1} iN_i(t) = Constant \qquad \text{Eq. (2.5-12)}$$

7. During the above mentioned process, after a short amount of time τ, the number of clusters of size *i* approaches an equilibrium value N_i^e; given by,

$$\lim_{t \to \tau} N_i(t) = N_i^e \qquad \text{Eq. (2.5-13)}$$

This is called *steady-state approximation*. As a result, *CNT* only determines *steady-state* nucleation rate; the non-steady state nucleation rate will be discussed in the subsequent section.

8. This steady-state distribution of clusters is modelled as a statistical distribution corresponding to a canonical ensemble of clusters of different sizes, given by equilibrium,

$$N_i^e = Ne^{-\frac{W_i}{k_B T}} \qquad \text{Eq. (2.5-14)}$$

Where, *N* is the total number of components. As a result of this assumption, Eq. (2.5-9) is zero thus, $I_i(t) = I_{i+1}(t)$. Therefore the following relations hold,

$$I = k_1^+ N_1(t) - k_2^- N_2(t)$$

$$I = k_2^+ N_2(t) - k_3^- N_3(t)$$

$$I = k_3^+ N_3(t) - k_4^- N_4(t)$$

…

$$I = k_{i-1}^+ N_{i-1}(t) - k_i^- N_i(t) \qquad \text{Eq. (2.5-15)}$$

$$I = k_i^+ N_i(t) - k_{i+1}^- N_{i+1}(t)$$

…

$$I = k_{c-2}^+ N_{c-2}(t) - k_{c-1}^- N_{c-1}(t)$$

$$I = k_{c-1}^+ N_{c-1}(t)$$

Multiplying, 2nd equation with (k_2^-/k_2^+), 3rd equation with (k_2^-/k_2^+) (k_3^-/k_3^+), i^{th} equation with (k_2^-/k_2^+) (k_3^-/k_3^+) … (k_i^-/k_i^+) and the last equation with (k_2^-/k_2^+) (k_3^-/k_3^+) … (k_i^-/k_i^+) … (k_{c-1}^-/k_{c-1}^+) and solving we get,

$$I = \frac{k_1^+ N_1(t)}{\left[1 + \sum_{i=2}^{c-1}\left(\prod_{n=2}^{i}\left(\frac{k_n^-}{k_n^+}\right)\right)\right]} \qquad \text{Eq. (2.5-16)}$$

9. Now, the principle of detailed balancing due to the microscopic nature of each reaction in Eq. (2.5-15) is applied, which results in the following equations,

$$k_1^+ N_1^e - k_2^- N_2^e = 0$$

$$k_2^+ N_2^e - k_3^- N_3^e = 0$$

$$k_3^+ N_3^e - k_4^- N_4^e = 0 \qquad \text{Eq. (2.5-17)}$$

…

$$k_{i-1}^+ N_{i-1}^e - k_i^- N_i^e = 0$$

As a result we obtain,

$$\prod_{n=2}^{i} \frac{k_n^+}{k_n^-} = \frac{k_i^+ N_i^e}{k_1^+ N_1^e} \qquad \text{Eq. (2.5-18)}$$

10. Assuming $N_1^e = N_1(t) = N$, and from Eq. (2.5-16) and Eq. (2.5-18) we get,

$$I = \frac{1}{\sum_{i=1}^{c-1}\left(\frac{1}{k_i^+ N_i^e}\right)} \qquad \text{Eq. (2.5-19)}$$

11. Assuming Eq. (2.5-14) to be a continuous function, we get,

$$I = \frac{1}{\int_1^{c-1}\left(\frac{1}{k_i^+ N_i^e}\right) di} \qquad \text{Eq. (2.5-20)}$$

12. Assigning a constant value for the $k_i^+ = k^+$ and taking it out of the integral and using Eq. (2.5-14) would yield,

$$I = \frac{Nk^+}{\int_1^{c-1}\left(e^{\frac{W(i)}{k_BT}}\right)di} \qquad \text{Eq. (2.5-21)}$$

13. Expanding $W(i)$ to third order,

$$W(i) = W(c) + \frac{\partial W(c)}{\partial i}(i-c) + \frac{1}{2}\frac{\partial^2 W(c)}{\partial i^2}(i-c)^2 + \cdots \qquad \text{Eq. (2.5-22)}$$

However, because $W(c)$ is the maximum, the following are true for some positive value of φ.

$$\frac{\partial W(c)}{\partial i} = 0 \ \ and \ \ \frac{\partial^2 W(c)}{\partial i^2} = -\varphi \qquad \text{Eq. (2.5-23)}$$

Therefore,

$$W(i) = W(c) - \frac{1}{2}\varphi(i-c)^2 \qquad \text{Eq. (2.5-24)}$$

Substituting Eq. (2.5-24) into Eq. (2.5-21) would give,

$$I = \frac{Nk^+}{\int_1^{c-1} e^{\frac{W(c)}{k_BT}} e^{-\frac{\varphi(i-c)^2}{2k_BT}} di} \qquad \text{Eq. (2.5-25)}$$

Taking,

$$\Gamma_Z = \frac{1}{\int_1^{c-1} e^{-\frac{\varphi(i-c)^2}{2k_BT}} di} \qquad \text{Eq. (2.5-26)}$$

Where, Γ_Z is called the Zeldovich factor. Substituting Eq. (2.5-26) into Eq. **(2.5-25)** would give the basic equation for classical nucleation theory.

$$I = Nk^+\Gamma_Z e^{-\frac{W(c)}{k_BT}} \qquad \text{Eq. (2.5-27)}$$

Chapter 3

Results and Discussion

The simple believeth every word: but the prudent man looketh well to his going.

(Proverbs 14:15)

3.1 Preface

This section contains all the experimental work and scientific contributions that have been accomplished in the frame of the proposed objectives (Section 1.2). It is divided into seven sub-chapters including this preface and they are arranged in a chronological order. Starting from the next, each sub-chapter corresponds to a manuscript resulted from the current research work that has been published in (or submitted to) a SCI journal.

3.1.1 General Study

The next four sub-chapters (3.2 to 3.5) comprise a general study aimed at particularly addressing the primary objective of this thesis that is, the investigation of the role of dopants on lithium silicate glass structure and its crystallization behaviour. This exhaustive general study not only adds fundamental knowledge to the literature, which is necessary for the advancement of glass and glass-ceramic technology but, also develops key concepts required for establishing correlations between glass structure and its crystallization behaviour. To this end, four types of dopants were used, which are oxides of Mn, Al, B and P. Their effects were studied on both monolithic glasses and glass powered compacts. The glass structure was investigated by wide range of methods including several spectroscopic techniques and thermo-physical properties. The crystallization behaviour was studied by thermal analysis and by controlled crystallization experiments. Since sintering is also a part of *GC*s production when they are produced by powdered route, the sintering behaviour was also investigated.

3.1.2 Limitation of existing models

The second objective of this thesis (Section 1.2) involves establishing the correlations between glass structure and its crystal nucleation behaviour. Based on the understanding gained from the previous general study, it was apparent that there is a need for the theoretical models which can establish these correlations in multicomponent silicate glasses. Therefore, the attention was refocused to understanding the existing models related to this area; so that they can be extended to multicomponent composition. The current theoretical progresses in this area are presented in the literature review (Chapter 2).

When it comes to glass structure (Sections 2.2 and 3.6.1), it was realised that currently there are no models describing the Q_n distribution based on fundamental physics even for simple binary systems. Concerning *LLPS*, apart from the thermodynamic model, to my knowledge currently there are no models which rigorously describe the microscopic origin of *LLPS*. The crystal nucleation in glasses, thus far has been tried to be explained by *CNT* (Sections 2.5.1 and 2.5.2). The test of *CNT* on range of simple stoichiometric compositions revealed huge discrepancies between experiments and theory, where the theory predicts nearly 50 orders of magnitude lower values of crystal nucleation rates.[73–76] Therefore, currently there are no fundamental theories available which could describe either the glass structure or the crystal nucleation even for simple glass composition.

3.1.3 Need for new models

Recognizing the limitations of the current models the need for the new models was quickly realised. Considering that the second objective of this thesis involves establishing correlations between glass structure and crystal nucleation rates, a new idea was put forth. Where, it was considered that the crystal nucleation rates are proportional to the probability of structural units coming together by random process (Eq. (3.1-1)).

$$I\,(T) \propto [P_n(T)]^c \qquad \text{Eq. (3.1-1)}$$

Where, $I\,(T)$ is the temperature dependent steady state nucleation rate, $P_n(T)$ is temperature dependence of probability for the occurrence of a given Q_n unit and c is the size of the critical nucleus. Using this idea, kinetic equation was developed with the arguments similar to that of *CNT*. Based on the experimental Q_n-distribution obtained from NMR experiments of lithium disilicate glass, the equation was tested. The calculated value for crystal nucleation rate was 1×10^9 m^{-3} s^{-1}, which is close to the experimental value. Unlike *CNT* model which gives a discrepancy of 50 orders of magnitude, the model based on this new idea seemed to predict nucleation rates very accurately.

However in order to develop this new idea into a full-fledged theory based on the fundamental physics and supported by huge experimental data is beyond the scope of this current thesis. Therefore, this work is assigned as one of the future works and the

directions are presented in Section 5.1. Moreover, apart from the idea presented in Eq. (3.1-1), the exact equations and derivations used for obtaining the crystal nucleation rate in lithium disilicate glass are not presented here because of their potential importance for the future proposals. Nonetheless, a small part of the problem is addressed in this thesis. Unlike *CNT*, nucleation theory based on this new idea can be readily extended to multicomponent glass systems.

It can be seen that Eq. (3.1-1) requires temperature dependent function of probability distribution ($P_n(T)$) of Q_n units. So far, models describing this probability distribution are non-existent. Therefore, a new model was proposed based on statistical and quantum mechanics in sub-chapter 3.6 for binary compositions describing the Q_n distribution. In sub-chapter 3.7, the model was extended to multicomponent compositions. Both these models answer the second objective of this thesis establishing correlations between the glass structure and the crystal nucleation.

3.2 Role of manganese on the structure, crystallization and sintering of non-stoichiometric lithium disilicate glasses

Anuraag Gaddam [a], Hugo R. Fernandes [a], Dilshat U. Tulyaganov [a, b], Maria J. Pascual [c], José M.F. Ferreira [a]

[a] Department of Materials and Ceramics Engineering, University of Aveiro, CICECO, 3810-193 Aveiro, Portugal.

[b] Turin Polytechnic University in Tashkent, 17, Niyazova str., 100095, Tashkent, Uzbekistan.

[c] Instituto de Cerámica y Vidrio (CSIC), C/Kelsen 5, Campus de Cantoblanco, 28049 Madrid, Spain.

RSC Advances, 4 (2014) 13581–13592
DOI: 10.1039/c3ra46393a

Abstract

The structural role of Mn was investigated in a relatively simple non-stoichiometric LS_2 based glass composition. Glasses were prepared by partially replacing SiO_2 by MnO_2 from the base glass belonging to the system Li_2O–K_2O–Al_2O_3–SiO_2. An overall depolymerisation of the glass network was observed according to magic angle spinning nuclear magnetic resonance (MAS-NMR) and Fourier transform infrared (FTIR) spectroscopic studies, suggesting a network modifier role for Mn. However, thermal analysis, phase segregation and nucleation in the glasses suggested that Mn might also act as network former. Moreover, calculated crystal field parameters from the UV-Visible spectroscopy, showing high ligand field strength (Δ_o) and Racah inter electronic repulsion (B) pointed out to a possible existence of Mn as individual molecular entities in the interstitials of the glass network. The crystallization of bulk glasses and the sintering of glass powder compacts were studied in order to get further inputs about the structural role of Mn in glasses/glass-ceramics.

3.2.1 Introduction

MnO_2 is an important industrial raw material. Approximately 500,000 tonnes of MnO_2 are consumed annually as a component of dry cell batteries (Leclanché cell or zinc–carbon batteries). Other important industrial applications include the use of MnO_2 as an inorganic pigment in ceramics and in glassmaking.[77,78]

The obtaining of suitable mechanical, chemical, thermal or electrical properties for the final materials presides to the design of glass-ceramic compositions for most of the functional applications. In particular, dental restorations require the development of a material that reproduces the aesthetic appearance of natural teeth, including colour, translucency, and fluorescence properties. Translucency can be obtained by controlling the relative refractive indices and volume concentrations of the crystalline and residual glassy phases. Colour and fluorescence can be achieved by the addition of transition metal oxides and rare-earth oxides to the base composition.[79] Transition metal oxides can also contribute to the fluorescence properties of inorganic materials. Manganese is a well-known activator in many crystals and glasses and the Mn^{2+} ion exhibits broadband emission characteristics.[80,81] In a molten glass, the Mn cations distribute into couple states such as Mn^{2+}–Mn^{3+}. According to Schreiber,[82] the change in redox depends on glass composition, melting temperature, atmosphere, concentration of redox couples and the presence of other redox couples. At a given melting condition, the redox couple shifts towards the oxidized state when modifier ions or glass basicity are increased.[83]

Mn in glasses may be expected to be in the form of MnO_4^- and MnO_4^{2-} anions, and in the form of Mn^{2+}, Mn^{3+} and Mn^{4+} cations, or a mixture of these.[84] It has been demonstrated that all Mn oxides when heated to 1000 ºC and higher are transformed into Mn orthomanganate ($Mn_2^{2+}Mn^{4+}O_4$).[85,86] Manganese ions exist in different valence states occupying tetrahedral or octahedral sites in a glass network. For example, Mn^{3+} ions in borate glasses exist only in octahedral coordination, whereas in silicate and germanate glasses are in both tetrahedral and octahedral environments.[87] Tetrahedral and octahedral Mn^{2+} ions exhibit luminescence emission in the green and red regions for various glasses, respectively.[88–90] Therefore, Mn^{2+}, having a coordination number of six in silicate glasses, plays a modifying cation role, but Mn^{4+}, forming coordinate polyhedra $[MnO_4]^{4-}$, may participate in the formation of a glass network together with Si^{4+}.

The content and valence states of Mn in various environments in the glasses are dependent on quantitative properties of modifiers and glass formers, size of the ions in the glass structure, their field strength, mobility of the modifier cation, etc.[91,92]

Several interesting studies are available regarding the use of Mn as a colouring agent for glass matrices (e.g. [93–98]), as well as on the environment of Mn ion in various inorganic glass systems (e.g. [99–108]). However, most of these works report studies in borate, phosphate or other glass systems and few studies have been carried on silicate based glasses. The present study aims towards investigating the role of manganese on the glass structure of a relatively simple non-stoichiometric lithium disilicate based glass composition in the glass forming region of $Li_2O–K_2O–Al_2O_3–SiO_2$ with SiO_2/Li_2O molar ratio of 3.12. Based on the established role of the Mn in the glass structure this paper discusses (1) crystallization in bulk glasses and (2) sintering behaviour and crystallization in glass powder compacts.

3.2.2 Experimental procedure

3.2.2.1 Glass Preparation

Four experimental glass compositions were prepared using a general formula (mol.%): $23Li_2O{-}2.64K_2O{-}2.64Al_2O_3{-}(71.72{-}x)SiO_2{–}xMnO_2$, with x varying from 0 to 2 (**Table 3.2.1**). Accordingly, these glasses were designated as $GMn_{0.0}$ (x = 0.0), $GMn_{0.5}$ (x = 0.5), $GMn_{1.0}$ (x = 1.0) and $GMn_{2.0}$ (x = 2.0). In all compositions, molar concentrations of Li_2O, K_2O and Al_2O_3 were kept constant, while SiO_2 has been partially replaced by MnO_2.

Table 3.2.1 Compositions of the glass in mol. %

	$GMn_{0.0}$	$GMn_{0.5}$	$GMn_{1.0}$	$GMn_{2.0}$
Li_2O	23.00	23.00	23.00	23.00
K_2O	2.64	2.64	2.64	2.64
Al_2O_3	2.64	2.64	2.64	2.64
SiO_2	71.72	71.22	70.72	69.72
MnO_2	0.00	0.50	1.00	2.00
SiO_2/Li_2O	3.12	3.10	3.07	3.03

Powders of technical grade SiO_2 (purity >99%) and reagent grade Li_2CO_3 (purity >99%), K_2CO_3 (purity >99%), Al_2O_3 (purity >99%) and MnO_2 (purity >99%) were used as precursors. To give batch compositions of 100 g, these powders were homogenously

mixed by ball milling, and then calcined at 800 °C for 1 h. Pt crucibles were used to melt the compositions at 1550 °C for 1 h in air. Bulk (monolithic) glasses were prepared by pouring the glass melt on a bronze mould and immediately annealing at 450 °C for 1 h. To prepare glass powder, glass frits were obtained by quenching the glass melts in cold water. The frits were dried and milled in a high speed agate mill in order to obtain a particle sizes between 5−10 μm as determined by the particle size analyser (Coulter LS 230, Fraunhofer optical model, Amherst, MA). Rectangular bars having dimensions 4 mm × 5 mm × 50 mm were prepared by uniaxial pressing of glass powders with a pressure of 80 MPa for 10 seconds.

3.2.2.2 Heat treatment schedule

Bulk glasses from all the four compositions were cut into required size and heat treated at a heating rate of 2 ºC min^{-1} in air up to temperatures in the range of 650−900 °C with intervals of 50 ºC and kept for 1 h at the set temperatures. Using the same heating rate (2 ºC min^{-1}), glass powder compacts were sintered at 800, 850 and 900 °C for 1 h in air.

3.2.2.3 Characterization of the samples

Differential thermal analysis (DTA, Setaram Labsys, Setaram Instrumentation, Caluire, France) was carried out on all glass compositions obtained by crushing the glass frits having particle sizes between 5−10 μm (~6 μm, particle size analyser). DTA experiments were carried out in air from ambient temperature to 1000 °C at a heating rate of 20 ºC min^{-1} using ~30 mg of sample in an Alumina crucible, with α-Alumina powder as reference material. For $GMn_{0.0}$ and $GMn_{2.0}$, a heating rate of 5 ºC min^{-1} was also performed to compare with hot-stage microscopy results.

Optical transmission spectra were obtained for all bulk glasses using polished samples (on both parallel sides) with thickness of ~0.9 mm. The spectra were recorded over a range 200−800 nm wavelength using UV-VIS-NIR spectrophotometer (UV-3100, Shimadzu, Japan). Infrared transmittance spectra of glass powders prepared by crushing the bulk annealed glasses were obtained using Fourier Transform Infrared Spectrometer (FTIR, model Mattson Galaxy S-7000, USA) in the range of 300−1400 cm^{-1}. Samples for FTIR were prepared by mixing 1/150 (by weight) portion of the sample with KBr and hand pressed to obtain pellets. ^{29}Si MAS-NMR spectra was

recorded for glass powders prepared from frit glass on a Bruker ASX 400 spectrometer operating at a Larmor frequency of 79.52 MHz with B_o = 9.4 T using a 7 mm probe rotating at 5 kHz. A 5 μs length radio-frequency excitation pulse equivalent to 90º flip angle with 60 s delay time was used. Tetramethylsilane was used as chemical shift reference. ^{27}Al MAS-NMR spectra were recorded on a Bruker ASX 400 spectrometer operating at a Larmor frequency of 104.28 MHz with B_o = 9.4 T using a 4 mm probe rotating at 15 kHz. A 0.78 μs radio-frequency pulse length equivalent to 10º flip angle with 1 s delay time was used. $Al(NO_3)_3$ was used as the chemical shift reference.

Microstructures of the samples were recorded using reflected light optical microscope (Jenaphot 2000, Zeiss, Germany) and scanning electron microscope (SEM, SU-70, Hitachi, Japan). For microstructural observation, samples were polished and etched using 2 vol.% hydrofluoric acid for 60 s. Crystalline phase content in the samples was determined by X-ray diffraction (XRD, Rigaku Geigerflex D/Mac, C Series, Japan) using Cu K_α radiation with 2θ varying from 10−60° steps of 0.02 s^{-1}.

A side-view hot-stage microscope (HSM, Leitz Wetzlar, Germany) equipped with a Pixera video camera and image analysis system was used to investigate the sintering behaviour of glass powder compacts. The cylindrical shaped samples from glass powder compacts with height and diameter of ~3 mm were prepared by cold-pressing the glass powders. The cylindrical samples were placed on a 10 mm ×15 mm ×1 mm alumina (>99.5 wt. % Al_2O_3) support and the measurements were conducted in air with a heating rate (β) of 5 ºC min^{-1}. The temperature was measured with a chromel–alumel thermocouple contacted under the alumina support. The temperatures corresponding to the characteristic viscosity points (first shrinkage (T_{FS}), maximum shrinkage (T_{MS}), softening (T_D), half ball (T_{HB}) and flow (T_F)) were obtained from the graphs and photomicrographs taken during the hot-stage microscopy experiment.

Apparent densities of the all the samples (bulk glasses, bulk glass-ceramics and sintered glass powder compacts) were measured using Archimedes Principle by immersion in ethylene glycol. 3-point bending strength of the sintered glass powder compacts were performed using universal testing machine (Shimadzu Autograph AG 25 TA).

3.2.3 Results

With increasing the MnO_2 content in the experimental glass compositions, the melts demonstrated severe bubbling at temperatures close to 1550 ºC. However, the bubbles were relatively large and confined to the top surface of the melt. Therefore the cast glasses obtained were transparent and bubble free.

3.2.3.1 Optical Study of bulk glasses

Glasses $GMn_{0.0}$ and $GMn_{0.5}$ were colourless and light pink respectively whilst $GMn_{1.0}$ and $GMn_{2.0}$ showed a very strong colouring to purple. **Figure 3.2.1** shows the UV-Visible transmittance spectra of the experimental glasses. Glass with no Mn addition ($GMn_{0.0}$) did not show any absorption bands in the investigated region, whereas Mn doped glasses showed broad absorptions bands with magnitude proportional to Mn content. There are two absorption bands at ~474 nm and 631 nm in glass $GMn_{0.5}$. Glass $GMn_{1.0}$ featured three absorption bands at 489 nm, 581 nm and 638 nm. In the glass $GMn_{2.0}$, the absorption bands are obtained at 478 nm and 631 nm. The purple colour in the Mn doped glasses is usually attributed to Mn^{3+} ions which exhibit absorption at ~480 nm.[82,109–112] With Mn in 2+ oxidation state the absorption bands usually are centred near ultraviolet regions.[111,112] Therefore, based on the UV-Visible spectra of experimental glasses suggesting the strongest absorption bands at ~470 nm, it is reasonable to conclude that Mn ions mostly exist in 3+ oxidation state. This assumption will be further discussed in the subsequent sections.

From **Figure 3.2.1**, the glass $GMn_{1.0}$ was selected and the absorption bands were identified from their position in the UV-Visible spectra using Tanabe-Sugano diagrams. Additionally, the octahedral ligand field splitting parameter Δ_o and inter-electronic repulsion Racah parameter B values were determined. Based on the ligand field strength consideration and $3d^4$ electronic configuration of Mn^{3+}, the electrons can exist in high spin or low spin states for low and high ligand field strengths, respectively.[113] Subsequently, the ground state configurations are ^5E_g and $^3T_{1g}$ for low and high field ligand field strength, respectively. Based on calculations from the Tanabe-Sugano diagrams, the ground state was identified as $^3T_{1g}$. Also the absorption bands in the regions ~480 nm, ~580 nm and ~630 nm correspond to the transitions $^3T_{1g} \rightarrow {}^5E_g$, $^3T_{1g} \rightarrow {}^1T_{2g}$ and $^3T_{1g} \rightarrow {}^1E_g$, respectively. Further, due to Jahn-Teller distortion, the ground

state further splits.[111] For $GMn_{1.0}$, the ligand field splitting parameter was calculated to be Δ_o = 53494 cm^{-1} and Racah parameter B = 1392 cm^{-1}.

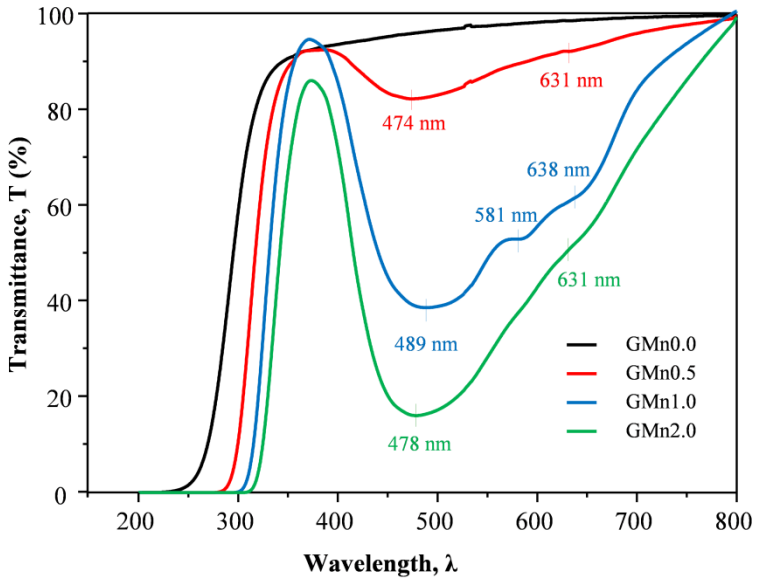

Figure 3.2.1 UV-Visible transmittance spectra of experimental glasses.

From the Beer-Lambert law, the linear attenuation coefficient α can be calculated using an approximate equation given by,

$$\alpha = -\frac{1}{t}\ln T \qquad \text{Eq. (3.2-1)}$$

Where, t is the thickness of the glass sample and T is measured transmittance. From the transmittance spectra, the optical band gap energy can be calculated using Tauc relationship given by the equation,

$$\alpha h\nu = A(h\nu - E_g)^n \qquad \text{Eq. (3.2-2)}$$

where, α is linear attenuation coefficient, h is Planck constant, ν is the frequency of the photon, A is a constant related to the extent of band tailing, E_g is the band gap energy and the exponent n depends on the nature of the material. For direct band gap n = ½, and for indirect band gap n = 2. A Tauc plot is drawn with energy of the photon ($h\nu$) on abscissa and $(\alpha h\nu)^{1/n}$ on ordinate. An extrapolation of the linear portion of the curve onto the abscissa would yield optical band gap energy; because, when $(\alpha h\nu)^{1/n}$ = 0, then $E_g = h\nu$. In the present work, both direct and indirect band gaps were calculated, i.e. for both n = ½ and 2. **Figure 3.2.2a–b** shows the Tauc plots for n = ½ and n = 2,

respectively. In both cases, it can be noticed that there is red shift in the optical band gap (*i.e.* decreasing E_g).

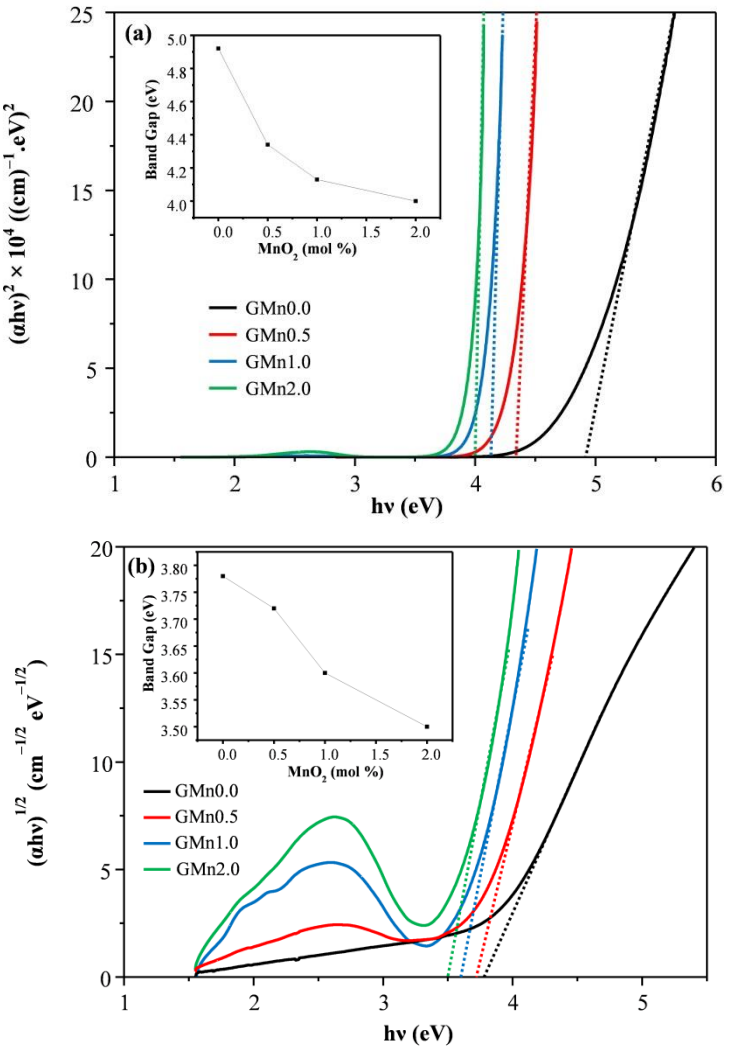

Figure 3.2.2 Tauc plots for (a) direct band gap, n = ½; and (b) indirect band gap, n = 2.

3.2.3.2 FTIR

The FTIR transmittance spectra of the experimental glasses are presented in **Figure 3.2.3**. Due to the amorphous nature of the glasses and wide distribution of Q_n units, there is a lack of sharpness in the absorption bands. All experimental glass compositions showed four absorption bands; of which one broad peak is centred at ~1050 cm^{-1}. Two sharper peaks centred at ~470 cm^{-1} and ~780 cm^{-1}. With Mn content increasing, the peak centred at ~1050 cm^{-1} broadens more. The assignment of these bands is as follows:[114]

1. The low frequency band at ~470 cm^{-1} is attributed to transverse-optical (TO_1) mode *ρ(Si-O-Si)* correspond to rocking motions of oxygen atoms.

2. Band near ~780 cm^{-1} is characteristic of transvers-optical (TO_2) mode v_s(*Si-O-Si*) caused by symmetric stretching of oxygen atoms.

3. The broad band at ~1050 cm^{-1} is due transverse-optical (TO_3) mode v_{as}(*Si-O-Si*) appear as a result of antisymmetric stretching of the oxygen atoms. The shoulder at high frequency side of this band is also a characteristic of this mode.

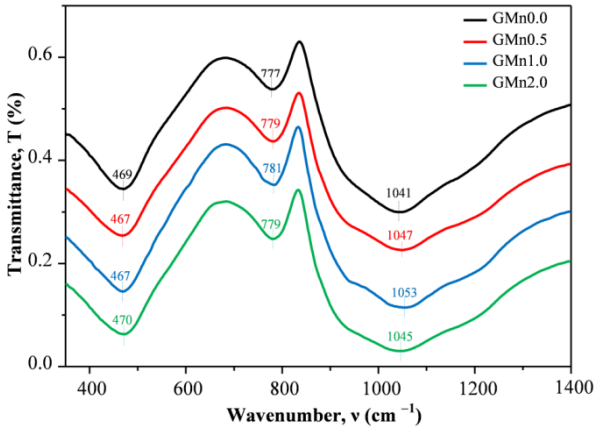

Figure 3.2.3 FTIR of annealed bulk glasses.

3.2.3.3 MAS-NMR

The ^{29}Si MAS-NMR spectra for experimental glasses $GMn_{0.5}$, $GMn_{1.0}$ and $GMn_{2.0}$ are shown in **Figure 3.2.4a**. It is to be noted that due to the amorphous nature of the glasses, they gave a broad peak indicating the wide distribution of Q_n units. The spectra of $GMn_{0.5}$, $GMn_{1.0}$ and $GMn_{2.0}$ glasses show that the broad peak is centred at −95.3 ppm, −93.2 ppm and −92.8 ppm respectively suggesting a depolymerisation trend of the glass network at 0.5 to 2 mol. % MnO_2 additions. At the same time broadening of the main peaks due to extended distribution of the Q_n units can be observed. According to De Jong *et al.*,[115] for various Q_n units the mean chemical shifts were as follows, −107 ppm (Q_4), −92 ppm (Q_3), −82 ppm (Q_2) and −69 ppm (Q_1). Therefore, the centring of the peaks between −92 and −96 ppm in the experimental glasses evidenced that Q_3 is the dominant species. However, the shoulders centred at about −104.5 ppm in glass $GMn_{0.5}$ suggest presence of Q_4 units in the experimental glasses.

^{27}Al MAS-NMR spectra are shown in **Figure 3.2.4b**. It can be noticed that for all the experimental glass compositions the chemical shift peaks are centred at ~52 ppm. This is a characteristic feature for aluminium existing in a glass network with tetrahedral coordination.[116–118]

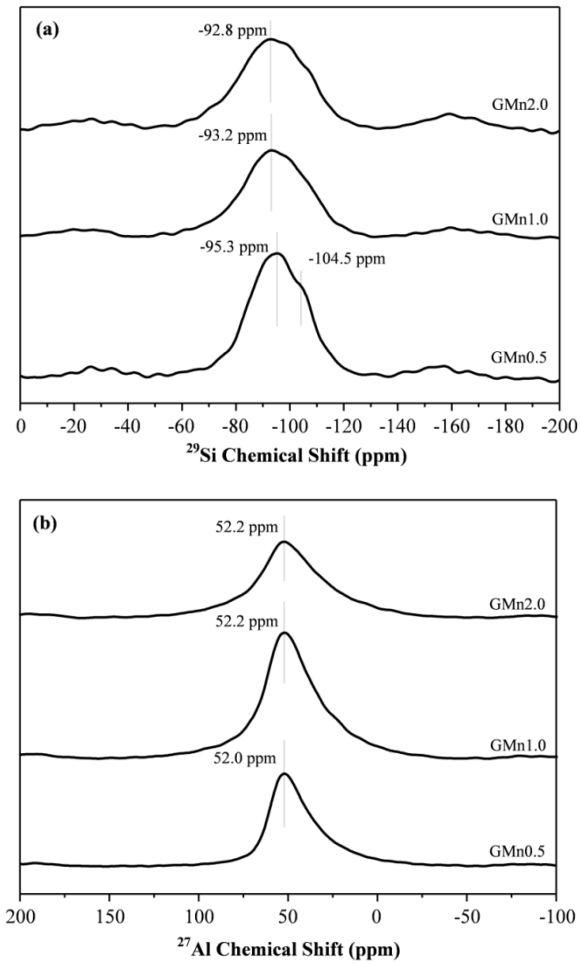

Figure 3.2.4 (a) ^{29}Si MAS-NMR and (b) ^{27}Al MAS-NMR spectra of experimental glasses.

3.2.3.4 Thermal and other properties of bulk glasses

DTA thermographs for the glass powders are shown in **Figure 3.2.5**. The properties of the experimental glasses, including glass transition temperature (T_g), peak crystallization temperature (T_P), molar volumes (V_m), density and optical basicity values of experimental glasses and other thermal parameters are presented in **Table 3.2.2**. The Hrubÿ parameter of glass stability (K_H) was calculated by the equation,[119]

$$K_H = \frac{(T_p - T_g)}{(T_m - T_g)} \qquad \text{Eq. (3.2-3)}$$

The K_H values gradual decrease with Mn addition, while the reduced glass-transition temperature (T_{gr}) given by T_g/T_m shows an apparent opposite trend. The calculation of molar volumes (V_m) given by M/ρ (where, M is molar mass and ρ is density of the glasses) was based on the optical study, assuming that majority of Mn

exists in +3 oxidation state. The optical basicity of glasses was calculated using the general formula:[120]

$$\Lambda_{cal} = X_A \frac{1}{\gamma_A} + X_B \frac{1}{\gamma_B} + \cdots \qquad \text{Eq. (3.2-4)}$$

Where Λ_{cal} is the calculated optical basicity, γ_A and γ_B are basicity moderating parameters, and X_A and X_B are mole fractions of oxides *A* and *B*, respectively.

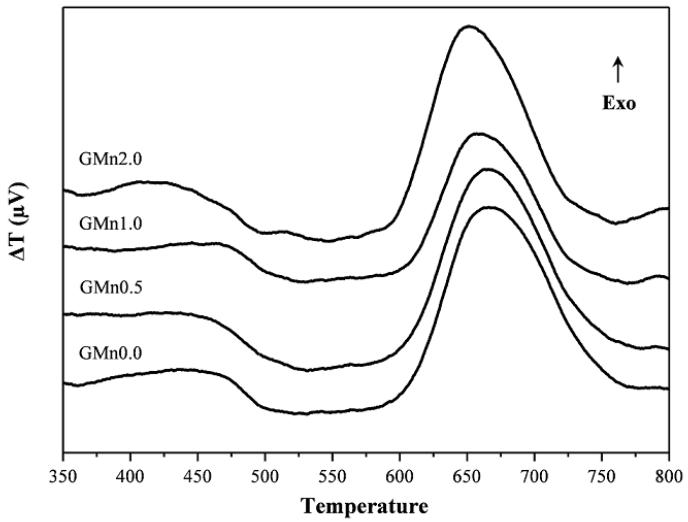

Figure 3.2.5 DTA of experimental glasses at heating rate of 20 K min^{-1}.

Table 3.2.2 Properties of the experimental glasses.

	$GMn_{0.0}$	$GMn_{0.5}$	$GMn_{1.0}$	$GMn_{2.0}$
$T_g \pm 2$ (ºC)	460	458	467	465
$T_p \pm 2$ (ºC)	665	665	657	651
K_H	0.41	0.40	0.40	0.39
T_{gr}	0.58	0.58	0.59	0.59
Density (g cm^{-3})	2.36 ± 0.01	2.38 ± 0.01	2.39 ± 0.01	2.39 ± 0.01
Molar Volume, V_m (cm^3 mol^{-1})	23.37	23.25	23.28	23.46
Calculated optical basicity, Λ_{cal}	0.5279	0.5282	0.5285	0.5291

3.2.3.5 Microstructural and phase analysis of bulk glasses and glass-ceramics

Figure 3.2.6 presents the microstructures of the annealed bulk glasses showing the presence of metastable glass immiscibility regions. With increasing the MnO_2 content two main trends can be inferred from the micrographs: (a) the size of segregated droplets increases; (b) the population density of the droplets decreases. Additionally, in

the composition $GMn_{2.0}$, the microstructure reveals a growth of dendritic type crystals (**Figure 3.2.6, insert**).

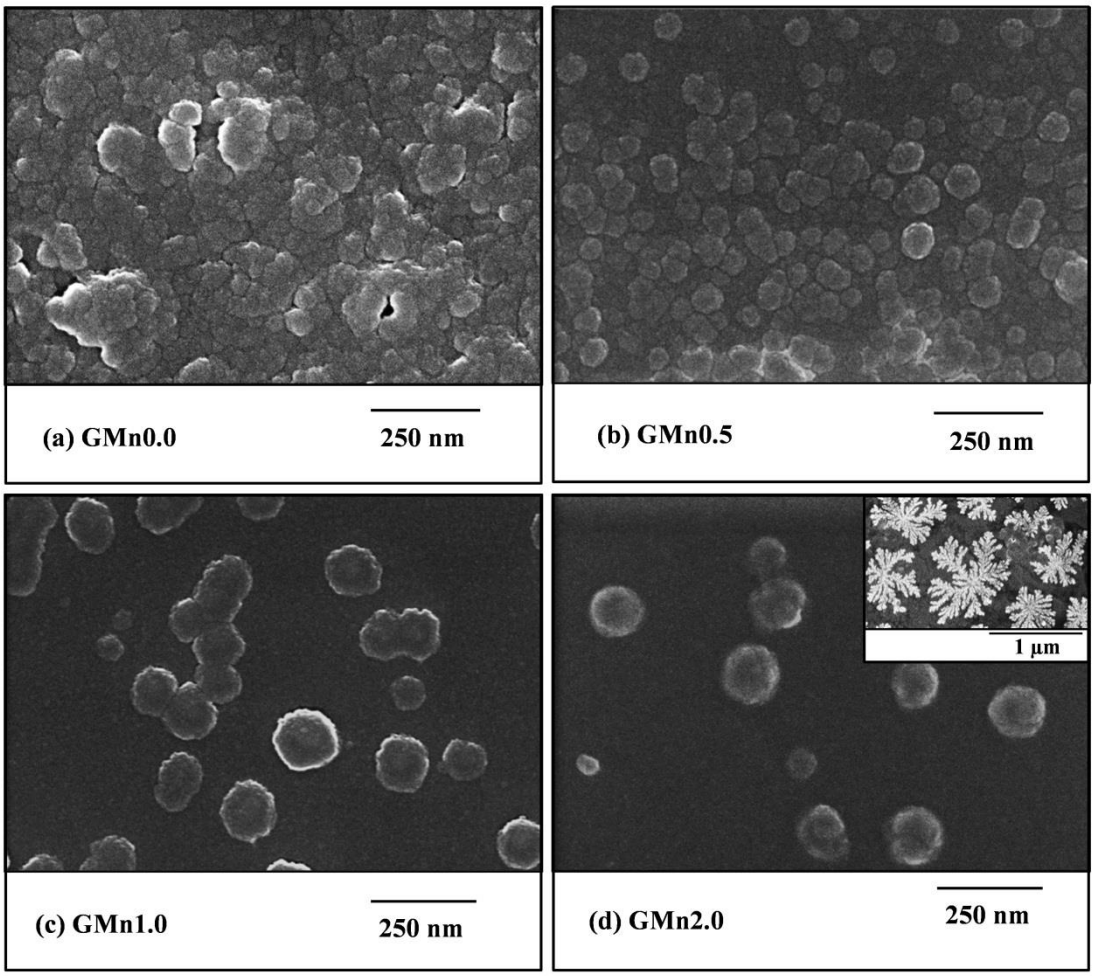

Figure 3.2.6 SEM images of bulk annealed glass revealing phase segregation.

Figure 3.2.7a–d presents optical micrographs of glass samples $GMn_{0.0}$ and $GMn_{0.5}$ heat treated at 700 ºC, (**Figure 3.2.7a–b**) and at 800 ºC (**Figure 3.2.7c–d**). At 700 ºC, the $GMn_{0.0}$ sample reveals the formation of both bulk crystalline clusters and surface dendritic crystallization. The Mn addition ($GMn_{0.5}$) seemingly decreased the population density of bulk crystalline clusters while concomitantly increased the thickness of the surface layer (**Figure 3.2.7b**), variations that can be associated with a favoured tendency towards surface crystallization. With increasing the heat treatment temperature to 800 ºC, the spherulites and dendrides merged resulting in the formation of fully crystallised structures (**Figure 3.2.7c–d**).

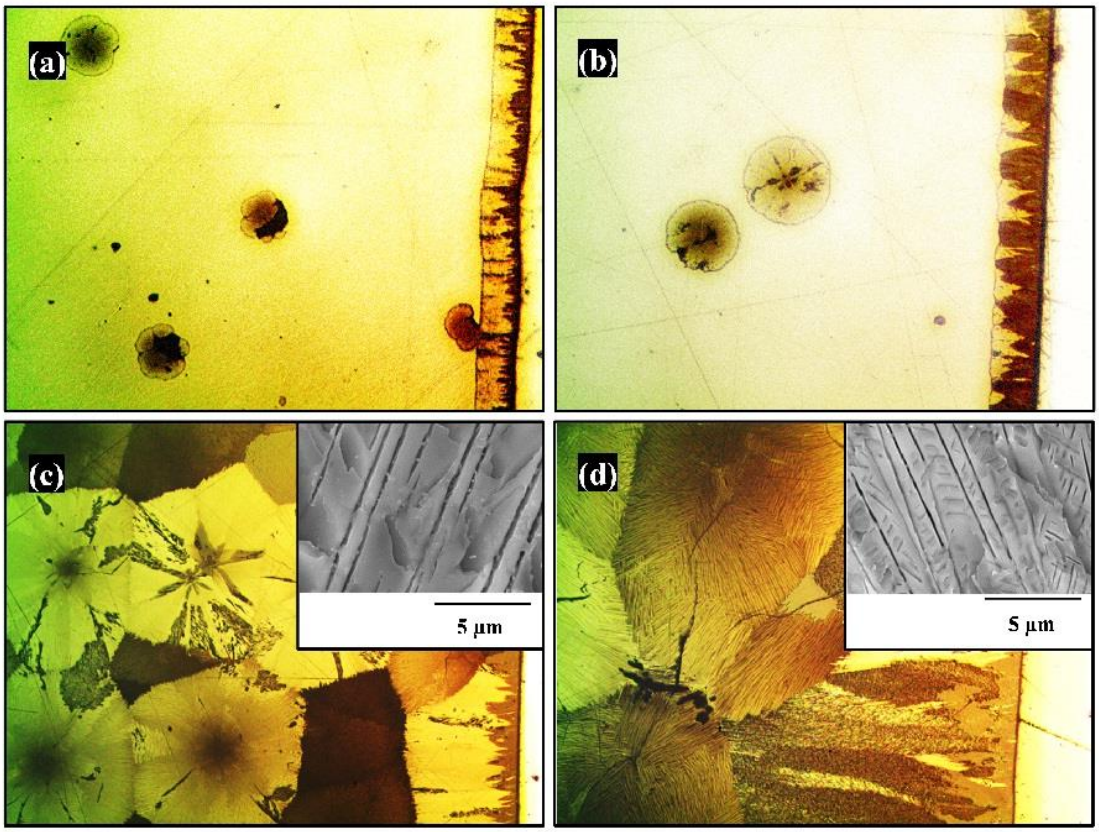

Figure 3.2.7 Microstructures of bulk glass-ceramics of samples (a) $GMn_{0.0}$ and (b) $GMn_{0.5}$ heat treated at 700 ºC for 1 h; and (c) $GMn_{0.0}$ and (d) $GMn_{0.5}$ heat treated at 800 ºC for 1 h; pictures were taken by optical microscope with a magnification of ×50 and the surface layer is on the right side of the image. The inserts in (c) and (d) are the corresponding higher magnification images.

Figure 3.2.8 compares the X-ray diffractograms of experimental bulk glasses heat treated at various temperatures. Key points to be noticed from these diffractograms are as follows:

1. *LS* and LS_2 start to form at 700 ºC in all glass compositions and continue to grow upon further increasing the heat treatment temperature.

2. The formation of minor amounts of quartz took place at 900 ºC for glasses $GMn_{0.0}$ and $GMn_{0.5}$, but at a lower temperature (800 ºC) for glasses $GMn_{1.0}$ and $GMn_{2.0}$.

Non-heat treated annealed bulk glass $GMn_{2.0}$ shows a very low intensity single peak at $2\theta = 31.3^{\circ}$, almost coincident with a peak of *LS*, but which could not be surely assigned to any phase.

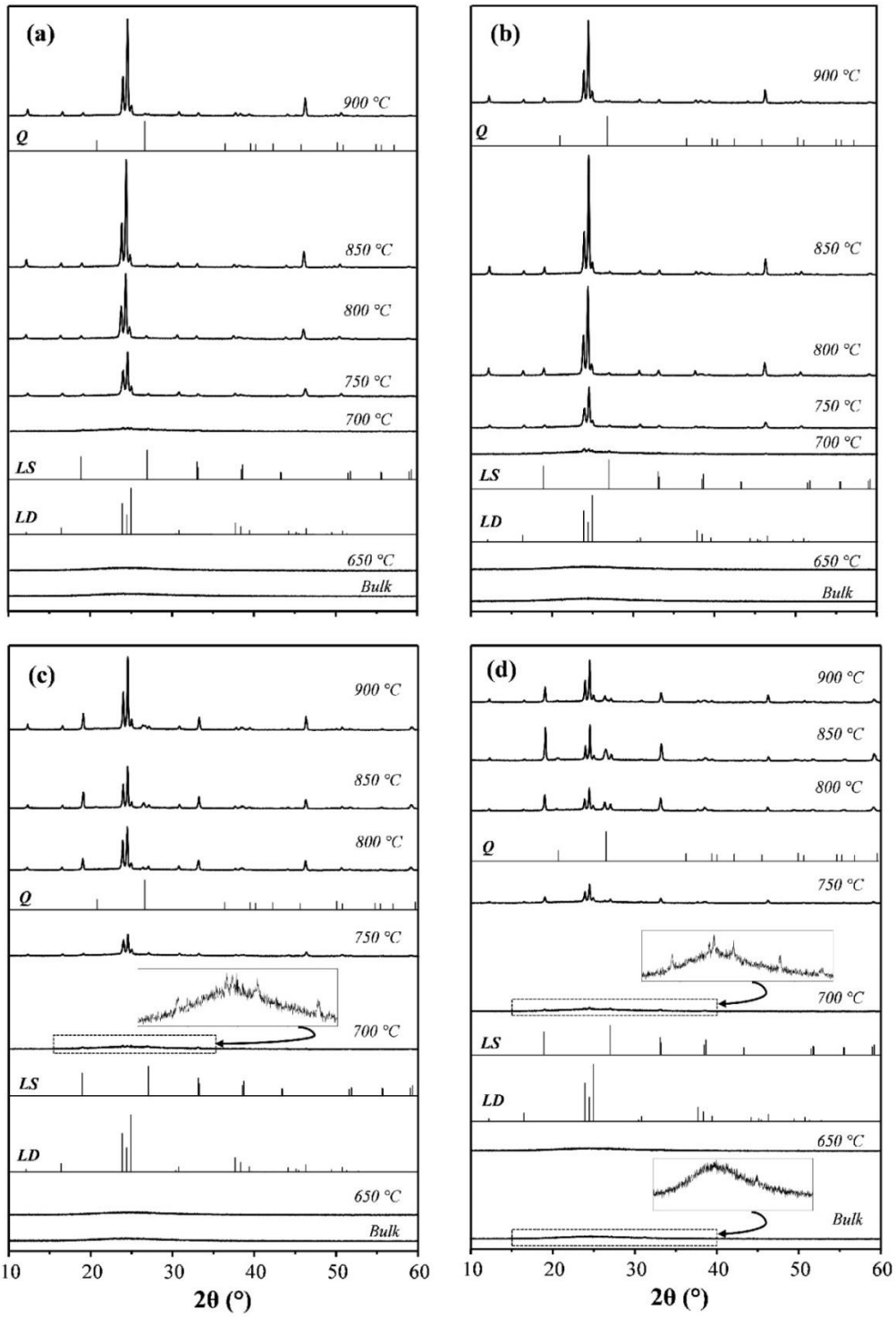

Figure 3.2.8 X-ray diffractograms of bulk glasses (a) $GMn_{0.0}$, (b) $GMn_{0.5}$, (c) $GMn_{1.0}$ and (d) $GMn_{2.0}$ heat treated at various temperatures for 1 h. LS_2: lithium disilicate ($Li_2Si_2O_5$, ICDD card 01-070-4856); *LS*: lithium metasilicate (Li_2SiO_3, ICDD card 01-049-0803); *Q*: quartz (SiO_2, ICDD card 01-077-1060) [scale bar for (a), (b), (c) & (d) is 89000 cps].

3.2.3.6 Microstructural and phase analysis of sintered glass powder compacts

Figure 3.2.9 shows relatively low magnification SEM images of glass-powder compacts made for three compositions (*$GMn_{0.0}$*, *$GMn_{1.0}$*, and *$GMn_{2.0}$ – lines*) sintered at different temperatures (800, 850 and 900 ºC – *columns*), to shed light on the porosity; while **Figure 3.2.10** presents more detailed microstructural features of the same samples sintered at 800 and 900 ºC.

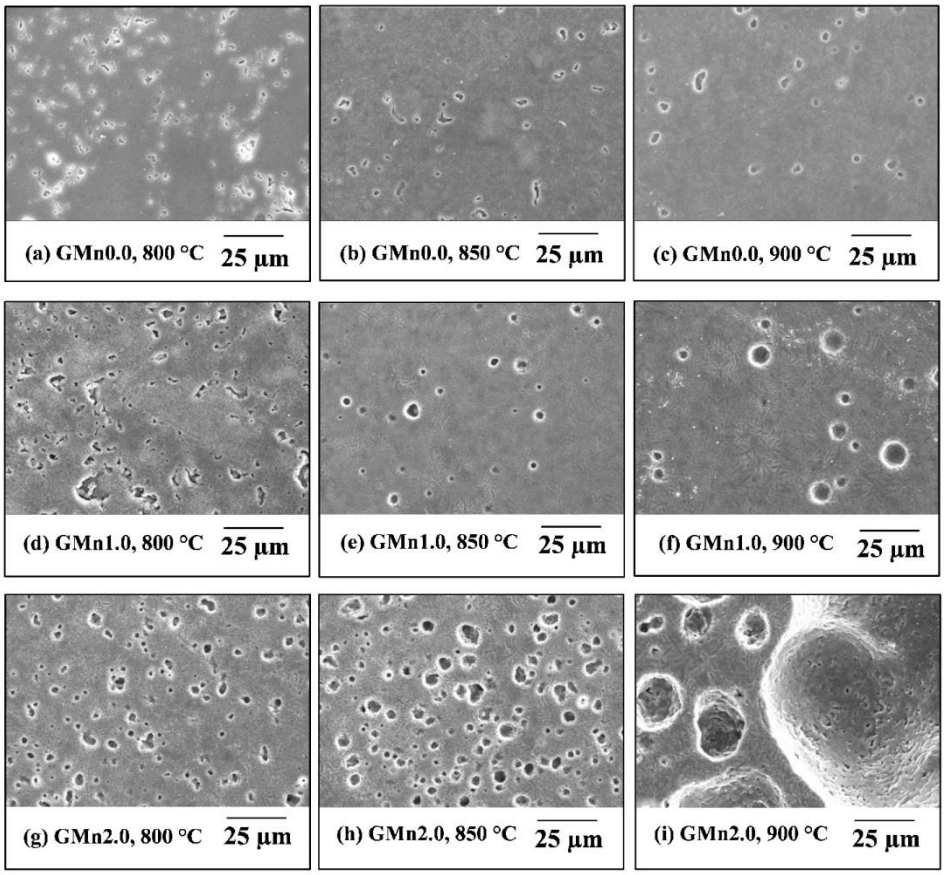

Figure 3.2.9 SEM images showing the effect of sintering temperature and composition on porosity in glass powder compacts heat treated at 800, 850 and 900 ºC for 1 h: (a) to (c) *$GMn_{0.0}$*; (d) to (f) *$GMn_{1.0}$*; and (g) to (i) *$GMn_{2.0}$*.

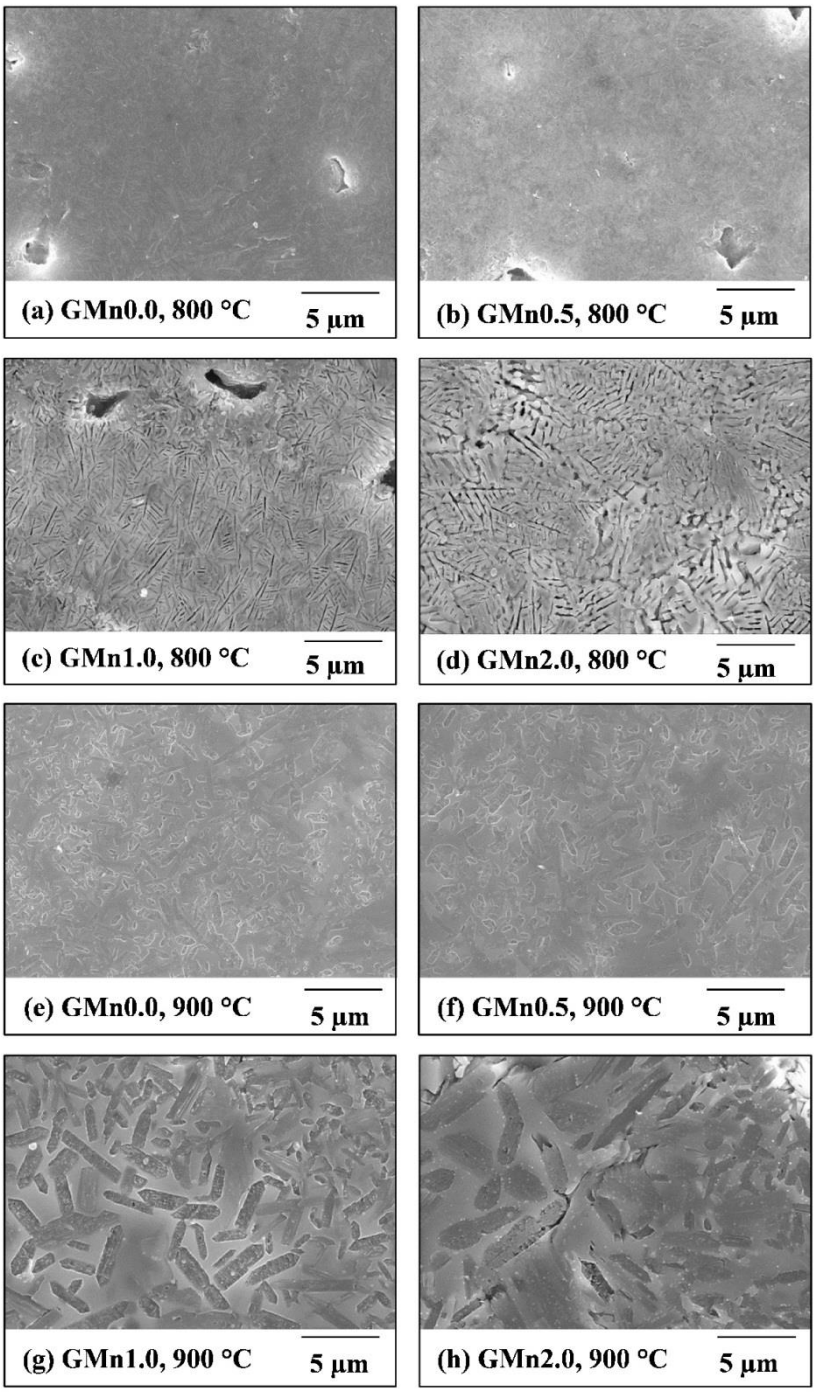

Figure 3.2.10 SEM images showing evolution microstructure of glass powder compacts sintered at: (a) to (d) 800 ºC and (e) to (i) 900 ºC.

X-ray diffractograms of samples sintered in the range from 800–900 ºC are presented in the **Figure 3.2.11**). At 800 ºC, *LS* emerged as major crystalline phase in $GMn_{0.0}$ together with minor amounts of LS_2 and quartz, while LS_2 was already formed at this temperature for all Mn containing samples, becoming even the major phase for the higher added amounts of Mn. Therefore, Mn addition favours the formation of LS_2 over *LS*.

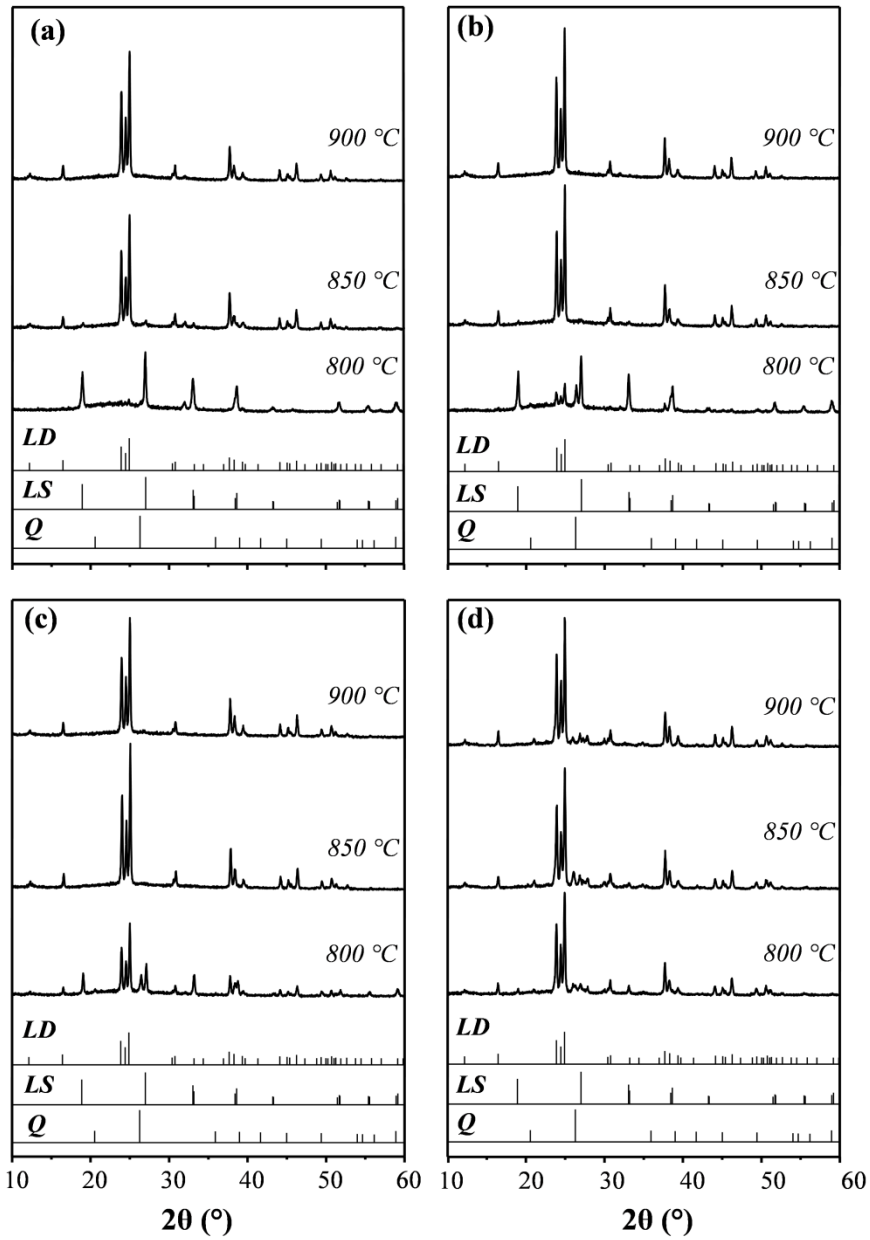

Figure 3.2.11 X-ray diffractograms of sintered glass powder compacts; (a) $GMn_{0.0}$, (b) $GMn_{0.5}$, (c) $GMn_{1.0}$ and (d) $GMn_{2.0}$ sintered at 800, 850 and 900 ºC. LS_2: lithium disilicate ($Li_2Si_2O_5$, ICDD card 01-070-4856); *LS*: lithium metasilicate (Li_2SiO_3, ICDD card 01-070-0330); *Q*: quartz (SiO_2, ICDD card 00-047-1144) [scale bar for (a), (b), (c) & (d) is 22400 cps].

3.2.3.7 Sintering behaviour and mechanical strength of glass powder compacts

Figure 3.2.12 shows the sintering behaviour of the glass powder compacts of $GMn_{0.0}$ and $GMn_{2.0}$ under a constant heating rate of 5 ºC min^{-1} from room temperature to 1000 ºC. DTA curves are also presented along with the HSM results. Characteristic points of sintering and crystallization are presented in **Table 3.2.3**.

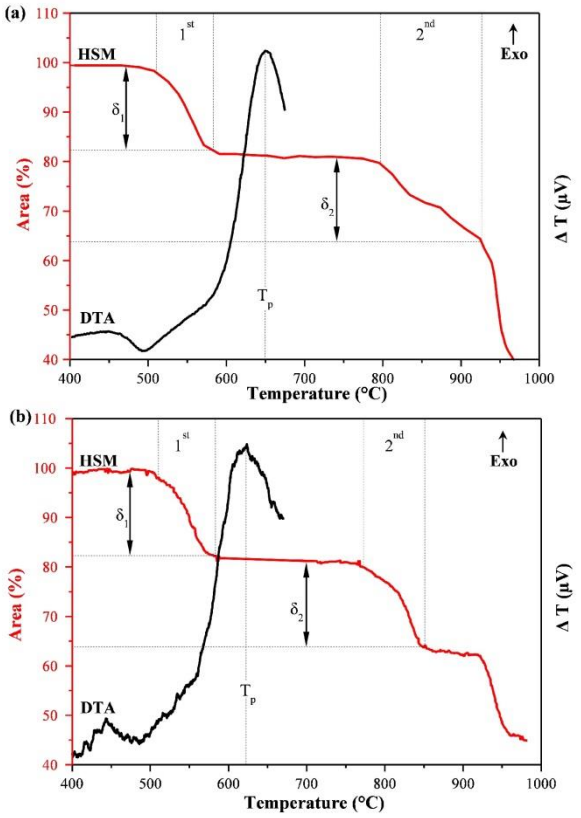

Figure 3.2.12 DTA and HSM curves for glass powder compacts: (a) $GMn_{0.0,}$ (b) $GMn_{2.0}$.

Table 3.2.3 Characteristic points of crystallization and sintering in glasses.

		$GMn_{0.0}$	$GMn_{2.0}$
	$T_g \pm 2$ (ºC)	490	486
DTA	$T_c \pm 2$ (ºC)	571	560
	$T_p \pm 2$ (ºC)	648	624
	$T_{FS1} \pm 5$ (ºC)	510	510
	$T_{MS1} \pm 5$ (ºC)	583	583
	δ_1 (%)	18	18
HSM	$T_{FS2} \pm 5$ (ºC)	794	775
	$T_{MS2} \pm 5$ (ºC)	928	851
	$\delta_2 \pm 5$ (%)	19	19
	$T_{HB} \pm 5$ (ºC)	945	937

The effects of Mn content on density and flexural strengths variations with sintering temperature are presented in **Figure 3.2.13**. Increasing up to maximum values followed decreasing trends are features common to all curves, but they appear shifted to lower temperatures with increasing Mn contents.

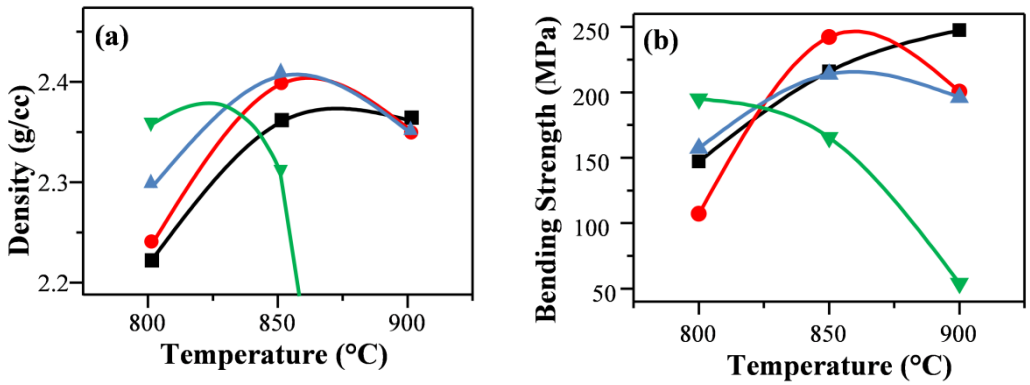

Figure 3.2.13 Some properties of sintered glass powder compacts heat treated at different temperatures; (a) density and (b) bending strength; [■: $GMn_{0.0}$; ●: $GMn_{0.5}$; ▲: $GMn_{1.0}$; ▼: $GMn_{2.0}$].

3.2.4 Discussion

3.2.4.1 Glass Structure

The heat treatment caused a reduction of Mn from Mn^{4+} to lower oxidation states and the release of oxygen, processes that can be described by the following equations:

$$MnO_2 \leftrightarrow Mn_2O_3 + \frac{1}{2}O_2 \qquad \text{Eq. (3.2-5)}$$

$$Mn_2O_3 \leftrightarrow 2MnO + \frac{1}{2}O_2 \qquad \text{Eq. (3.2-6)}$$

The evolution of oxygen during glass preparation was responsible for the observed severe bubbling of the melts with increasing Mn contents. Whenever, added to silicate glass systems, Mn tends to exist either in +3 or +2 oxidation state; higher oxidation states such as +4 and +7 are possible but very unlikely.[111,121] This redox equilibrium is common in glass systems doped with transition elements,[82] and several studies [82,122,123] proved that the redox ratio depends on glass optical basicity (Λ) when other parameters are maintained constant. In the present study, the calculated optical basicity (Λ_{cal}) (**Table 3.2.2**) for the experimental glasses revealed only slight increments with the composition. These results suggest that similar chemical environment and redox ratio exist in all glass compositions, thus reflecting the constancy of melting conditions used. This hypothesis is supported by a near linear variation at $\lambda = 500$ nm of absorbance *versus* concentration according to Beer-Lambert law (not shown). The redox ratio also depends on several other parameters such as melt temperature, oxygen

fugacity (fO_2) etc.[82] Silicate glasses prepared by melting in atmospheric oxygen fugacity tend to have Mn majorly in +3 oxidation state. No evidence of Mn^{2+} was found by Nelson *et al.* [112] in sodium silicate glasses melted in air, since this oxidation state would require reducing conditions during melting.[109,111,112,124] Optical absorption spectra of present glasses with peak maximum at ~500 nm, a characteristic Mn^{3+} absorption band for silicate glass systems, further supports the hypothesis that nearly all Mn in the present experimental glasses exists as Mn^{3+}. In the presence of octahedral ligand field, Mn^{3+} with $3d^4$ electronic configuration experiences Jahn-Teller distortion that causes further splitting of optical absorption bands.[111] This could result in over masking the weaker absorption bands of Mn^{2+} if at all present in the system. However, if Mn^{3+} is present in low spin state, the Jahn-Teller effect would be weak. In the present glass compositions, for $GMn_{1.0}$ with high ligand field splitting parameter (Δ_o) of 53494 cm^{-1}, Mn^{3+} should exist in low spin state and therefore have weak Jahn-Teller effect. Also complex laying on the right side of the vertical line in Tanabe-Sugano diagram of d^4, gives rise to spin forbidden states. Anyway, further experiments like EPR spectroscopy and chemical titrations needs to be done to positively confirm the negligible presence of Mn^{2+} in the system.

Now that we have hypothesized with reasonable assumption that Mn is present in the glass majorly as Mn^{3+}, it is important to understand its role in the glass network. According to Nelson *et al.*,[125] transition metal ions when dissolved in glass systems exist as one of the following species in the glass network structure, (1) as individual molecular entities, (2) as quasi-molecular complexes, (3) as network modifiers and (4) as network formers. When existing as individual molecular entities, they play no role in the network connectivity of the system. As quasi-molecular complexes, these ions are coordinated with non-bridging oxygens and play some role in the network locally. The difference between quasi molecular complex and network modifiers is basically the type of bonding they form, varying from predominantly covalent to ionic, respectively. With this in mind, we will try identifying the role played by Mn in the network of our glasses.

The increase in chemical shifts with the added amounts of Mn observed in the ^{29}Si MAS-NMR spectra (**Figure 3.2.4a**) suggests a network depolymerisation trend and a network modifier role for Mn. But the overall picture should be a bit more complex, considering that MnO_2 was added at the expenses of SiO_2, therefore causing a decrease in the SiO_2/Li_2O molar ratio (**Table 3.2.1**); which, itself, should result in glass network

depolymerisation. From the ^{29}Si MAS-NMR spectra it can be inferred that Q^3 units seem to be the dominant species of $[SiO_4]^{4-}$ polyhedra. Also with increasing manganese content from 0.5 to 2 mol.% the overall paramagnetic broadening of the NMR peaks can be noticed due to small additions of paramagnetic ions.[126] In contrast, no change in the chemical shift can be observed in ^{27}Al MAS-NMR spectra of glasses (**Figure 3.2.4b**), indicating that network connectivity of Al_2O_3 polyhedra was unaffected by Mn addition. The peak centred at ~52 ppm is attributed to aluminium in tetrahedral coordination, therefore, playing the role of network former.

The FTIR absorption broad band centred at ~1050 cm^{-1} attributed to various vibrational and stretching modes of $[SiO_4]^{4-}$ tetrahedra in **Figure 3.2.3** tends to exhibit an increasing shoulder near ~950 cm^{-1} with the addition of MnO_2. According to Innocenzi,[114] this band is associated with the existence of non-bridging oxygens in the glass. This is consistent with NMR results, confirming that MnO_2 addition leads to glass network depolymerisation. On the other hand, the decreasing trend in the band gap energies (**Figure 3.2.2**) accounts for an increased disorder in the system, also consistent with the formation of non-bridging oxygens that are less prone to tightly bound electrons.[127,128] So far, all the evidences point out to a possible (but yet non-conclusive) network modifier role of Mn.

The effects of adding network modifiers on molar volume (V_m) of a glass depend on their ionic radii.[8] For example, smaller radii alkali earth metals (Li, Na) that can fit in interstitial positions of a glass would lead to network shrinkage (smaller V_m values); while the addition of K, Rb and Cs would lead to network expansion of the same glass. Assuming a network modifier role for Mn in the present system, an overall decrease in V_m should be expected as ionic radii of Mn ions (0.58–0.64 Å) are in the same range as Li^{1+} ion (0.59−0.92 Å).[129] But **Table 3.2.2** shows a first decrease of V_m upon adding 0.5 mol.% Mn ($GMn_{0.5}$) and a subsequent increase with further Mn additions, with the value for $GMn_{2.0}$ being greater than that of $GMn_{0.0}$. This increase in V_m suggests that Mn is acting more as a network former, thus contradicting the continuous depolymerization trend inferred from NMR and FTIR results. All these evidences make it difficult assuming either network modifier or network former roles for Mn. It is likely that Mn forms individual molecular entities or quasi-molecular complexes without interacting much with the glass network.

The Δ_o and B crystal field parameters drawn from UV-Visible spectroscopy results of $GMn_{1.0}$ glass can give further hindsight regarding the bonding of this system. If the transition metal acts as network modifier, it is coordinated with non-bridging oxygens by ionic bonds having larger B values due to enhanced electron repulsion among the anions. But being weaker, ionic bonds show smaller Δ_o values. In the case of covalent bonding, overlapping of the atomic orbitals would result in the formation of molecular orbitals with an expansion of the electron cloud, the well-known Nephelauxetic Effect; as a result they show lower B values.[124] Being stronger, covalent bonds show larger Δ_o values. In other words, B and Δ_o values should decrease and increase, respectively, if transition metal ions act as network formers and form covalent bonds. In the present case larger values of both B and Δ_o can be observed. This supports the hypothesis that Mn present in network interstitials is coordinated with oxygen atoms forming almost independent structural units. Mn bonded to oxygen in octahedral coordination might account for the high Δ_o values, while the isolation of the structural units could help explaining the high B values. Upon studying the effects of small additions of Mn into sodium silicate glasses, Mortuza *et al.* [126] arrived to a similar conclusion, suggesting that Mn is not chemically bonded to the glass network.

The replacement of silica by MnO_2 and the consequent decrease of SiO_2/Li_2O ratio are expected to cause depolymerisation of the glass network as seen from MAS-NMR and FTIR spectra. However, the network contraction might be hindered by Mn structural units present in the interstitials that tend to cause network expansion. The relatively constant T_g values (458–467 ºC) (**Table 3.2.2**) also support this interpretation, otherwise a more accentuated reduction in T_g should have been observed.

According to the $Li_2O{-}SiO_2$ phase diagram, for SiO_2/Li_2O ratios less than 5.5 the droplets observed in the micrographs of annealed glasses (**Figure 3.2.6**) are SiO_2-rich dispersed in the Li_2O-rich matrix.[128,130] Moreover, an overall reduction in phase segregation can be noticed from the SEM images. This suggests that the formation of Mn structural units increased the glass viscosity and, as a consequence, reduced its tendency to immiscibility. For a better understanding of these structural units, further experiments, including molecular dynamic simulations, will be required to shed light on its chemical nature and structure.

3.2.4.2 Crystallization in Bulk Glasses

Heat treating the glasses at various temperatures (650–900 ºC) resulted in bulk and surface crystallization, as seen in the optical micrographs of $GMn_{0.0}$ and $GMn_{0.5}$ heat treated at 700 ºC (**Figure 3.2.7a–b**). But the number of crystals in the bulk tends to decrease with incremental additions of Mn due to a less favourable homogenous nucleation in the glass. Using Classical and Adiabatic nucleation theories, Zanotto [3,131] proved that glasses tend to nucleate homogenously when T_{gr} is less than ~0.58−0.60. The T_{gr} values reported in **Table 3.2.2** are within this range. Therefore, adding Mn into the system reduces the overall tendency for homogenous nucleation and enhances surface crystallization. Several studies [3,132,133] proved that liquid-in-liquid phase segregation in glass promotes nucleation. Phase segregated droplets with a composition similar to that of crystals would reduce the kinetic barrier for nucleation. This explains the decreasing number of crystalline clusters in bulk when going from samples $GMn_{0.0}$ to $GMn_{0.5}$ (**Figure 3.2.7**) or even its absence in the case of $GMn_{2.0}$ glass (not shown). The increase in the T_{gr} is attributed to an increase in glass viscosity.

Mn-rich structural units do not appear to have much effect on glass viscosity at higher temperatures as deduced from the decreasing T_P values (**Figure 3.2.5**). This would result in an overall decrease in the activation energy for crystallization with increasing Mn contents. But the concomitant less bulk nucleation extent in glasses resulted in low crystalline content (**Figure 3.2.10**). The overall depolymerisation trend of glass network seems to predominate at higher temperatures causing the crystals to growth. But viscosity measurements and crystallization kinetics studies would be required to better understand these phenomena in the present glasses.

3.2.4.3 Sintered Glass Powder Compacts

From the SEM microstructures of glass powder compacts sintered at various temperatures shown in **Figure 3.2.9**, it can be seen that adding Mn ($GMn_{0.0}$, $GMn_{0.5}$ and $GMn_{1.0}$) enhanced densification at lower temperatures (800–850 ºC). But further increasing the Mn content ($GMn_{2.0}$) and sintering temperature (900 ºC) tended to reduce density. Only the $GMn_{0.0}$ sample shows proper densification at 900 ºC. There was a clear trend for the formation of pores of increasing size with increasing Mn contents and sintering temperatures. This can be explained by the gradual shifting to lower

temperatures of the exothermic DTA peaks (**Figure 3.2.5**) and a concomitant decrease in glass viscosity that favours gas release inside a glassy phase according to Eq. (3.2-5) and Eq. (**3.2-6)**.

The features of crystals formed upon sintering the glass powder compacts at 800 ºC and 900 ºC are shown in the higher magnification SEM images of **Figure 3.2.10**. At both temperatures the size of crystals noticeably increased with increasing Mn contents due to the lowering of glass viscosity and of the activation energy for crystallization. This decrease in activation energy for crystallization is consistent with the reduction in the T_P (**Figure 3.2.5**, **Table 3.2.2**) and with the XRD results displayed in **Figure 3.2.11**, favouring the crystallization process at lower temperatures. Upon sintering at 800 ºC, *LS* was the main crystalline phase obtained from $GMn_{0.0}$, while the formation of LS_2 was favoured from Mn-containing compositions.

The HSM and DTA curves of $GMn_{0.0}$ and $GMn_{2.0}$ glass powders compacts presented in **Figure 3.2.12** and the corresponding results reported in **Table 3.2.3** shed further light on the sequence of thermal events. Until the first shrinkage (T_{FS1}) and maximum shrinkage (T_{MS1}) both $GMn_{0.0}$ and $GMn_{2.0}$ curves followed similar HSM profiles and reached the same T_{FS1} and T_{MS1} values. The formation of necks among the glass particles, especially among the smaller ones starts at T_{FS1} [134] and gradually extends to the coarser ones, making the compact to shrink. But the meanwhile occurrence of devitrification manifested by the exothermic DTA peak tends to hamper further densification. These opposite influences lead to the first maximum shrinkage. The comparison of HSM and DTA curves displayed in **Figure 3.2.12** shows that nucleation/ crystallization processes started at lower temperatures in the $GMn_{2.0}$ sample, likely due to its lower activation energy. Moreover, T_P values are < 700 ºC, the temperature at which the first XRD signs of crystallization appeared for bulk glasses (**Figure 3.2.12**). This suggests that heterogeneous nucleation is taking place at the surface of glass particles.

The balance between densification and crystallization processes leads to the observed shrinkage plateau. With temperature increasing the remaining glassy phase softens and stimulates surface and bulk diffusion and a second shrinkage (T_{FS2}) step starts and continues while the driving forces for densification will predominate over the crystallization and phase transformation. The crystallization process and the second

maximum shrinkage (T_{MS2}) occur earlier for $GMn_{2.0}$ in comparison to $GMn_{0.0}$. Heat treating $GMn_{2.0}$ above T_{MS2} resulted in over firing effects expressed by swelling/foaming due to the release of oxygen inside a partial melted glass. This foaming tendency with increasing Mn contents is clearly illustrated by the increasing porosity (**Figure 3.2.9**). It is also consistent with the evolution of density and bending strength values of sintered glass powder compacts presented in **Figure 3.2.13**, especially by the accentuated decreases observed for $GMn_{2.0}$ at higher temperatures. General increasing trends up to maximum values of these two properties, followed by decreasing tendencies are observed for the other compositions, but the curves appear shifted to lower temperatures as Mn content increases. In the case of $GMn_{0.0}$, there is a continuous increase in the bending strength with sintering temperature. For $GMn_{0.5}$ and $GMn_{1.0}$ the maximum bending strength is reached at 850 ºC and after that, at 900 ºC the bending strength values decline. In the case of $GMn_{2.0}$, there is a continuous decrease in the bending strength values.

3.3 Glass structure and crystallization of Al and B containing glasses belonging to the $Li_2O–SiO_2$ system

Anuraag Gaddam, Hugo R. Fernandes, José M.F. Ferreira

Department of Materials and Ceramics Engineering, University of Aveiro, CICECO, 3810-193 Aveiro, Portugal.

RSC Advances, 5 (2015) 41066–41078
DOI: 10.1039/c5ra04184h

Abstract

The aim of the present work is to investigate the effect of substituting B_2O_3 for Al_2O_3 in a non-stoichiometric *LS_2* glass composition belonging to the system $Li_2O–K_2O–Al_2O_3–SiO_2$. Addition of equimolar amounts of K_2O and Al_2O_3 to binary lithium silicate glass compositions improves chemical resistance, sintering behaviour and mechanical properties of the glass-ceramics produced from sintered glass powder compacts. However, in bulk (monolithic) glasses Al_2O_3 addition hinders bulk nucleation. It also suppresses crystallization of *LS_2* and promotes formation of a meta-stable crystalline phase called *LS*. The results showed that B substitution resulted in the depolymerisation of glass network increasing the percentage of *NBO*s leading to decreasing viscosity, molar volumes, oxygen densities and glass transition temperatures. The simultaneous mixture of Al and B into the glass composition resulted in decreased liquid-liquid phase segregation (*LLPS*) and lower crystal nucleation tendency when compared to Al pure or B pure compositions. Further, Al rich glasses featured lithium metasilicate crystallization at initial stages and then transformed into *LS_2* at higher temperatures, while with B addition glasses crystallize directly into *LS_2*.

3.3.1 Introduction

Glass-ceramics (*GCs*) are used in wide variety of applications ranging from military, biomedical to consumer goods like cooktops.[1] Particularly in restorative dentistry leucite and lithium disilicate (LS_2) based *GCs* are meeting the demand for excellent aesthetic and good mechanical properties with relative ease of processing.[135] These materials' compositions are carefully tailored and given controlled heat treatments to obtain desired nucleation and crystallisation of glasses. By adjusting the crystal size and fraction, required translucency and mechanical properties can be achieved. The key aspect of glass-ceramics in comparison to conventional ceramics is that they are inherently pore free which makes them well suited for high mechanical strength applications.[136] Over last four decades several fundamental studies have been performed on nucleation and crystallization of glasses belonging to various systems addressing various aspects of glass crystallization.[2–4] However, most of these studies were restricted to simple stoichiometric or binary compositions and only few studies were performed on multicomponent systems.[137–145] From an application point of view, in a multicomponent system, the addition of a particular dopant to the glass system changes its structure and chemistry consequently affecting its nucleation and crystallization behaviour; thereby it has a direct effect on final physical and chemical properties of *GCs*. During the initial stages of crystallization the phases that nucleate should directly depend upon local initial glass structure. Therefore, probing the bulk glass structure would offer deeper insights into the initial stages of nucleation.[146] Hence, it is imperative to understand the effect of a specific dopant on glass structure so that its crystallization behaviour can be understood in a new perspective. Therefore the current paper is mainly aimed at evaluating the effect of glass structure on crystal nucleation and overall crystallization of Al and B doped glasses.

Addition of aluminium and boron oxides to silicate glasses is known to improve chemical resistance of both glasses and *GCs*.[147] Apart from enhancing chemical resistance, Al_2O_3 also has a huge influence on the nucleation and crystallization behaviour of the glass. Several detailed studies on effect of Al_2O_3 were carried out by the authors of the present paper. [142,145,148–151] Addition of Al_2O_3 decreases phase segregation in the glass which consequentially results in the reduction of the nucleation rate.[152] Furthermore, Al_2O_3 drops the overall tendency of the glass to devitrify

enhancing its glass stability and also promotes crystallization of *LS* over *LS_2* When it comes to B_2O_3 addition into silicate glasses, apart from promoting chemical resistance like Al_2O_3, B_2O_3 also improves thermal shock resistance and raises electrical resistivity of the glass.[8] Contrary to the role of Al_2O_3, B_2O_3 is known to promote amorphous phase separation.[53]

Most of the commercial *GCs* used in various applications have nucleating agents added into them in order to promote higher nucleation rate and fine grained microstructure. Nonetheless, in a study like the current one, the presence of nucleating agents would make it difficult to ascertain the function of a particular dopant on the glass structure and ultimately the crystallization behaviour. Therefore, in the present study, a relatively simple multicomponent non-stoichiometric glass belonging to the system $Li_2O–K_2O–Al_2O_3–SiO_2$ with no nucleating agents added was chosen. In this system, the effects of substituting Al_2O_3 for B_2O_3 are elucidated. The structure of the glasses is probed employing wide range of characterization techniques. Based on the structural findings the nucleation and crystallization behaviour of these glasses were explored.

3.3.2 Experimental work

3.3.2.1 Preparation of glasses and glass-ceramics

Table 3.3.1 Compositions of the experimental glasses in mol%.

	GB_0	***GB_{25}***	***GB_{50}***	***GB_{75}***	***GB_{100}***
Li_2O	23.00	23.00	23.00	23.00	23.00
K_2O	2.64	2.64	2.64	2.64	2.64
Al_2O_3	2.64	1.98	1.32	0.66	0.00
B_2O_3	0.00	0.66	1.32	1.98	2.64
SiO_2	71.72	71.72	71.72	71.72	71.72
$(B_2O_3) / (B_2O_3+Al_2O_3)$	0.00	0.25	0.50	0.75	1.00

Five experimental glass compositions were prepared including the base glass ($23Li_2O - 2.64K_2O - 2.64Al_2O_3 - 71.72SiO_2$) by partially replacing Al_2O_3 by B_2O_3 in steps of 25%. Accordingly, these glasses were named GB_x for x = 0, 25, 50, 75 and 100% replacement of Al_2O_3. In all the compositions molar concentrations of Li_2O, K_2O and SiO_2 were kept constant with K_2O present in the same equimolar amounts as the

sum of Al_2O_3 and B_2O_3. **Table 3.3.1** presents the compositions of the experimental glasses.

For precursors, powders of technical grade SiO_2 (purity > 99%) and reagent grade Li_2CO_3 (purity > 99%), K_2CO_3 (purity > 99%), Al_2O_3 (purity > 99%) and H_3BO_3 (purity > 99%) were used. These powders were mixed homogenously by ball milling and calcined at 800 ºC in alumina crucibles for 1 h in air. The calcined powders (~100 g batch sizes) were further mixed in mortar-pestle for homogeneity and transferred to Pt-crucibles for melting at temperature of 1550 ºC for 1 h in air. Bulk (monolithic) bar shaped glasses were prepared by pouring the melt on bronze mould. To investigate *LLPS*, samples GB_0, GB_{50}, and GB_{100} were annealed at 520 ºC for a long duration (100 h) in order to bring the samples to thermodynamic equilibrium. Non-annealed bulk glasses were heat treated at temperatures between 650−900 ºC with 50 ºC interval at a rate of 2 K min^{-1} for 1 h in air to investigate the devitrification process.

3.3.2.2 Characterizations of the samples

Optical spectra of the bulk glasses were recorded using UV-VIS-NIR spectrophotometer (UV-3100, Shimadzu) in the range 200–800 nm wavelength with a resolution of 0.2 nm. For this, bulk glass slices of thickness 1.5−2.0 mm were cut from the bars and the both parallel sides were polished to a mirror finish. Fourier transform infrared spectroscopy (FTIR, model Mattson Galaxy S-7000) was carried out in the range of 300−1400 cm^{-1} with a resolution of 4 cm^{-1} on glass powders prepared by crushing the bulk glass. Samples for FTIR were prepared by mixing 1/150 (by weight) portion of the sample with KBr and hand pressed to obtain pellets. Raman spectra (Bruker RFS100 FT-Raman) were recorded for the same glass powders in the range of 300−1800 cm^{-1} with a resolution of 4 cm^{-1}. The samples were excited by an infrared laser of power 350 mW with an excitation wavelength of 1064 nm. ^{29}Si and ^{27}Al magic angle spinning nuclear magnetic resonance spectroscopy (MAS-NMR, Bruker ASX 400) was conducted on selected glass samples prepared by crushing them into fine powder. ^{29}Si MAS-NMR was performed for samples GB_0, GB_{25}, GB_{50} and GB_{100} using tetramethylsilane as a chemical shift reference. The spectrometer was operated at a Larmor frequency of 79.5 MHz with a 9.4 T magnetic field (B_o) using a 7 mm probe rotating at 5 kHz. The samples were excited with a 3.25 μs radiofrequency (*RF*) pulse equivalent to 90º flip angle using a 60 s delay time. ^{27}Al MAS-NMR was carried out on

samples GB_0 and GB_{50} employing $Al(NO_3)_3$ as a chemical shift reference. The spectrometer was operated at a Larmor frequency of 104.3 MHz with a 9.4 T magnetic field (B_o) using a 4 mm probe rotating at 14 kHz. The samples were excited with a 0.7 μs *RF* pulse equivalent to 10º flip angle using a 2 s delay time. ^{11}B MAS-NMR spectra were recorded for the samples GB_{50} and GB_{100} using Hahn-echo technique with 90º and 180º pulses in order to get better resolution of the spectra. The spectrometer was operated at a Larmor frequency of 128.4 MHz with a 9.4 T magnetic field (B_o) using a 4 mm probe rotating at 14 kHz. The samples were excited with a ~6.5 μs *RF* pulse equivalent to 90º flip angle using a 1 s delay time. H_3BO_3 was used as a chemical shift reference. In order to evaluate higher coordinated Al units, ^{27}Al MAS-NMR was performed using higher magnetic field of 16.4 T (Bruker Avance III HD 700) for sample GB_{25}. For this, 4 mm probe was used rotating at 14 kHz with a 10º flip angle and delay time of 1 s. Deconvolutions of all NMR spectra were performed using Dmfit program.

Differential thermal analysis (DTA, Setaram Labsys) was carried out in air from ambient temperature to 1000 ºC with a heating rate of β = 20 ºC min^{-1}. For each DTA experiment, ~30 mg of non-annealed bulk glass crushed to grain sizes in the range of 500−1000 μm (collected by sieving) was used. DTA experiments were carried out using alumina crucibles with α-Al_2O_3 powder as a reference material. Dilatometry (BÄHR Thermo Analyse GmbH 2000, model DIL 801) was performed on all the bulk glass samples from room temperature to 600 ºC at 5 ºC min^{-1} heating rate. Prismatic samples of length ~10 mm and cross section ~3×4 mm^2 were prepared for dilatometry. Densities of all bulk glasses were measured employing Archimedes principle by immersing samples in ethylene glycol solution.

Microstructures of all glasses and *GCs* were recorded using reflected light optical microscope (Jenaphot 2000, Zeiss) and scanning electron microscope (SEM, SU-70, Hitachi). Samples for microstructural observation were polished and etched using 2 vol.% hydrofluoric acid for 60 s. Crystalline phase content in all glasses and glass-ceramic samples was determined by X-ray diffraction (XRD, Rigaku Geigerflex D/Mac, C Series) using Cu K_α radiation with 2θ varying from 10–60º steps of 0.02º s^{-1}.

3.3.3 Results

All the bulk cast glasses obtained after melting at 1550 ºC were transparent and bubble free. X-ray diffraction conducted on the glasses (not shown) revealed no crystalline phases confirming they are all amorphous. Considering the high melting temperature, at which the lighter elements (such as Li and B in the current compositions) are prone to the volatilization, weight losses of the glasses were measured before and after melting. The weight losses were less than 0.2 %; which is a negligible value and it is within the limits of experimental errors.[8] In the case of boron, since it is present at a dopant level concentration, its volatilization would be far more negligible.[153]

3.3.3.1 MAS-NMR Spectroscopy

Figure 3.3.1a–c show the ^{29}Si, ^{27}Al and ^{11}B MAS-NMR spectra of the experimental glasses, respectively. In all three Figures, the spectra show relatively broad peaks which are tell-tale features for glasses, revealing their amorphous nature and wide distributions of bond angles and bond lengths. From ^{29}Si MAS-NMR spectra in **Figure 3.3.1a**, it can be seen that for all glass samples, the spectra presents a peak maximum near ~ −92 ppm and a shoulder in the range of −104 to −106 ppm, corresponding to Q_3 and Q_4 units of $(SiO_4)^{-2}$ tetrahedra respectively.[115,154] By performing boron substitution, the peak corresponding to Q_4 gets more resolved by shifting to lower values of the chemical shifts i.e. from −104.4 to −106.4 ppm for 0 and 100% replacement of boron respectively. However, peak maximum corresponding to Q_3 remains unchanged in all compositions. Also all glasses show a small shoulder approximately near −80 ppm corresponding to Q_2. Between the two major peaks (i.e. −92 and −104.4 ppm), glasses GB_{25} and GB_{50} show two small shoulders; these shoulders are not present in Al pure (GB_0) or B pure (GB_{100}) compositions. Deconvolution of ^{29}Si spectra was performed in order to quantitatively determine the fractions of Si units present. For the deconvolution of ^{29}Si NMR spectra, four Gaussian line shapes were used corresponding to Q_2, Q_3, Q_4 and $Q_4(1X)$ (Q_4 connected to one X (Al or B) atom in second coordination sphere). An example of ^{29}Si deconvolution is presented in **Figure 3.3.2a** and relative amounts of each Q unit as well as the fitting parameters are presented in **Table 3.3.2**. However, due to the complexity of current glass compositions with the formation of additional linkages such as Si−O−Al and Si−O−B leads to the creation of new Q units which

strongly affect the ^{29}Si chemical shift. [154,155] Therefore, the information obtained from the NMR deconvolution were used carefully within the limitations of experimental errors.

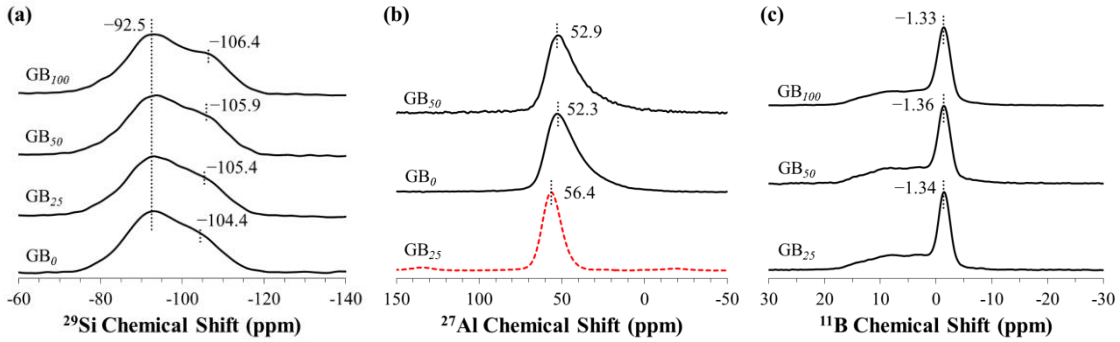

Figure 3.3.1 Multinuclear NMR spectra of (a) ^{29}Si, (b) ^{27}Al and (c) ^{11}B of bulk non-annealed experimental glasses. (——: B_o = 9.4 T and – – –: B_o = 16.4 T)

Table 3.3.2 NMR parameters for ^{29}Si deconvolution.

		GB₀	***GB₂₅***	***GB₅₀***	***GB₁₀₀***
δ$_{iso}$ (ppm)	Q^2	−78.5	〃	〃	〃
	Q^3	−92.6	〃	〃	〃
	Q^4(1X)	−103.4	〃	〃	−104.0
	Q^4	−108.9	〃	〃	〃
FWHM (ppm)	Q^2	5.1	8.5	10.3	9.5
	Q^3	15.7	〃	15.1	14.8
	Q^4(1X)	9.7	10.7	10.9	10.8
	Q^4	10.4	10.3	10.4	10.5
Amount *(%)*	Q^2	1	3	4	4
	Q^3†	74	70	65	64
	Q^4(1X)	15	16	18	17
	Q^4	10	11	13	15

δ$_{iso}$: *Chemical shift*
FWHM: *Full width at half maximum*
X: *Al or B*
†: Corresponds to both Q^3 and Q^4(3Al)

The ^{27}Al MAS-NMR spectra of the samples *GB₀*, *GB₂₅* and *GB₅₀* presented in the **Figure 3.3.1b** show non-symmetrical peaks for *GB₀* and *GB₅₀* and a near symmetrical peak for *GB₂₅* with peak maximums centred at ~52 and 56.4 ppm respectively. ^{27}Al being spin I=5/2 nuclei, experiences quadrupolar interactions with electric field gradient resulting in broadening and shifting of the peaks from the isotropic chemical shift values.[154] However, at higher magnetic fields quadrupolar effects are reduced and therefore *GB₂₅* shows lower quadrupolar effects and confirming the nonexistence of 5− and 6−fold coordinated Al.[118] In order to find out the true chemical shift values for *GB₀*

and GB_{50} the spectral deconvolution was performed using Czejeck distribution model according to Neuville *et al.*[156] by fitting one line shape. The peaks obtained have chemical shifts 58.85 and 58.84 ppm and quadrupolar coupling constants (C_Q) 4.4 and 4.5 MHz for GB_0 and GB_{50} respectively. Therefore, being able to fit with one line shape and with the obtained chemical shift values, it can be concluded that majority of Al exists in 4-fold coordination. [117,118,154,157]

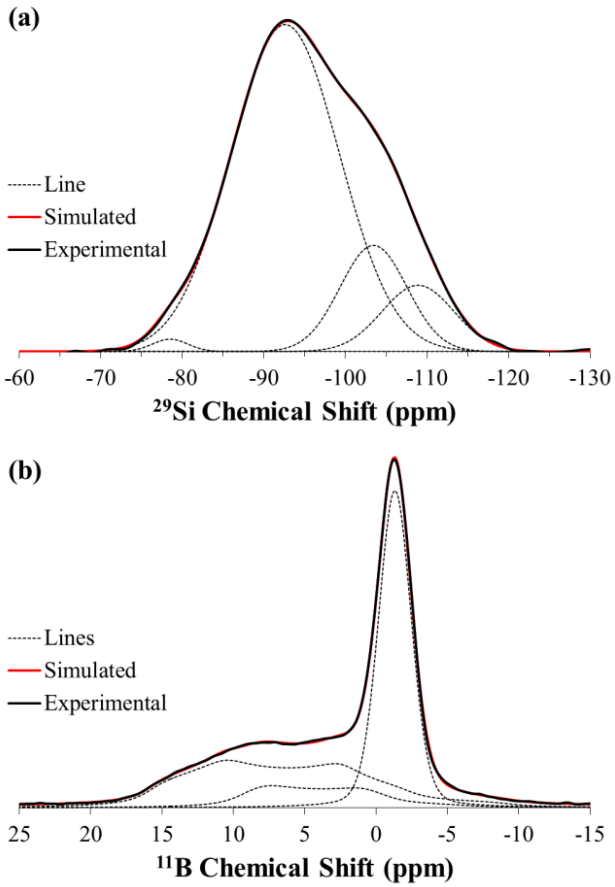

Figure 3.3.2 Deconvolution of (a) ^{29}Si nuclei of GB_0 and (b) ^{11}B nuclei of GB_{100} NMR spectra.

^{11}B MAS-NMR spectra for glasses GB_{25}, GB_{50} and GB_{100} shown in the **Figure 3.3.1c** have one broad peak and another relatively sharper peak centred close to −1.3 ppm, each corresponding to trigonal (BO_3, B^{III}) and tetrahedral (BO_4, B^{IV}) boron species respectively.[154] The peak at −1.3 ppm can be attributed to reedmergnerite like structural units of boron where each of the tetrahedral boron is coordinated with four Si tetrahedrons. [154,158] In order to identify the relative contents of B^{III} and B^{IV} units of boron, the ^{11}B MAS-NMR spectra were deconvoluted and an example is presented in **Figure 3.3.2b**. The line shapes were simulated by using two trigonal peaks with second-order quadrupolar effects each corresponding to symmetric (B^{IIIs}, boron with 0 or 3

bridging oxygens) and asymmetric trigonal (B^{IIIa}, boron with 1 or 2 bridging oxygens) boron units.[159] For tetrahedral boron units a single mixed Gaussian/Lorentzian peak was used. The NMR parameters used for the deconvolution of the spectra, which are isotropic chemical shift (δ_{iso}), quadrupolar coupling constant (C_Q), and quadrupolar asymmetry parameter (η) along with the relative contents of each boron species, are presented in **Table 3.3.3**.

Table 3.3.3 NMR parameters for ^{11}B deconvolution.

Boron Site	δ_{iso} (ppm)	C_Q (MHz)	η	Amount (%)
***GB*$_{25}$**				
B^{IV}	–1.38	---	---	38.25
B^{IIIa}	17.00	2.64	0.42	46.45
B^{IIIs}	11.50	2.14	0.04	15.30
***GB*$_{50}$**				
B^{IV}	–1.36	---	---	43.28
B^{IIIa}	17.07	2.58	0.42	38.27
B^{IIIs}	11.48	2.34	0.04	18.45
***GB*$_{100}$**				
B^{IV}	–1.33	---	---	48.04
B^{IIIa}	17.41	2.63	0.35	38.81
B^{IIIs}	11.16	2.14	0.17	13.15

δ_{iso}: *Chemical shift*
C_Q: *Quadrupolar coupling constant*
η: *asymmetry parameter*

3.3.3.2 Raman Spectroscopy

The Raman spectra of the experimental glasses are presented in **Figure 3.3.3**. All glasses showed a broad peak between 400–600 cm^{-1} with peak maximum at ~550 cm^{-1}. Other peak positions are at wavenumbers 789, ~954 and ~1086 cm^{-1}. The assignments of these peaks are as follows: [155,160,161]

1. The broad peaks between 400−600 cm^{-1} are attributed to mixed stretching and bending modes of Si−O−Si bridging bonds.

2. The peak at 789 cm^{-1} corresponds to inter-tetrahedral deformation mode involving significant cation motion.

3. The peaks near ~954 cm^{-1} correspond to Si−O symmetric stretching in a structural unit with two terminal oxygens (Q^2).

4. The broad peaks ranging from 1000−1200 cm^{-1} could be attributed to both Q^3 and vibration of non-bridging oxygens; however peak maximum at 1086 cm^{-1} indicate that Q^3 is present in bigger amounts.

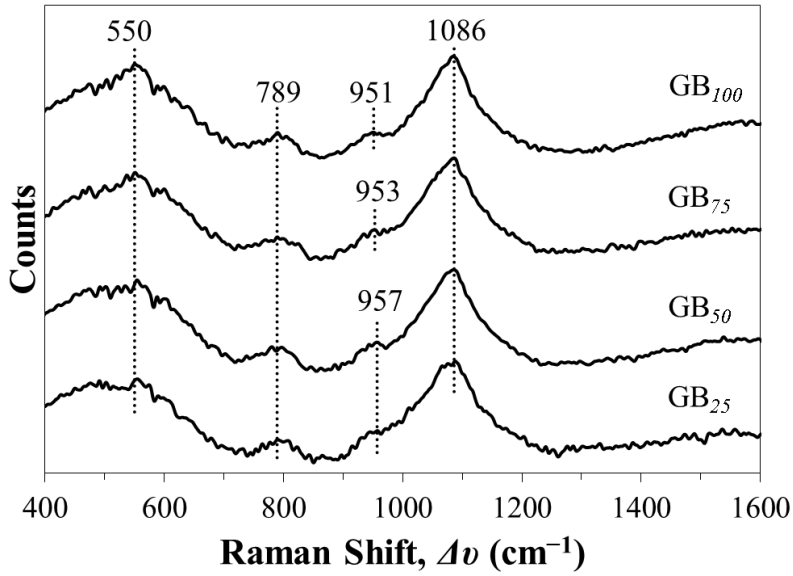

Figure 3.3.3 Raman spectra of experimental glasses.

3.3.3.3 FTIR

The FTIR transmittance spectra of the experimental glasses presented in **Figure 3.2.4** also show broad peaks indicating amorphous nature of the glasses and wide distribution of Q_n units. All experimental glass compositions showed four absorption bands; of which one broad peak is centred at ~1050 cm^{-1}. Two relatively sharper peaks appear centred at ~467 cm^{-1} and 780 cm^{-1}. These peak positions are assigned to various vibrational modes according Innocenzi: [114]

1. The low frequency band at ~470 cm^{-1} is attributed to transverse-optical (TO_1) mode ρ(Si−O−Si) correspond to rocking motions of oxygen atoms. It could also be attributed to the symmetric stretching vibrations of LiO_4 tetrahedra.

2. The band near ~780 cm^{-1} is characteristic of transverse-optical (TO_2) mode υ_s(Si−O−Si) caused by symmetric stretching of oxygen atoms.

3. The broad band at ~1050 cm^{-1} is due transverse-optical (TO_3) mode υ_{as}(Si–O–Si) appear as a result of antisymmetric stretching of the oxygen atoms. The shoulder at high frequency side of this band is also a characteristic of this mode.

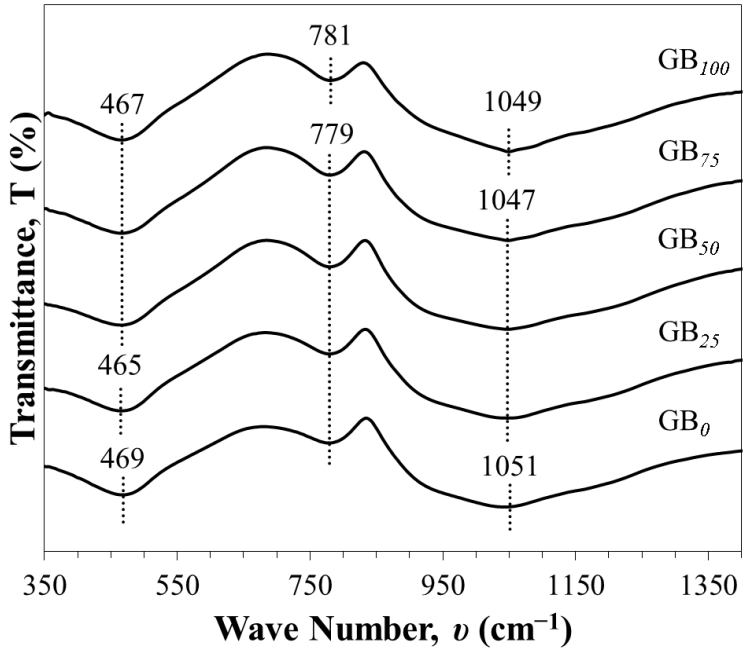

Figure 3.3.4 FTIR spectra of experimental glasses.

3.3.3.4 UV-Visible Spectroscopy

Figure 3.3.5a shows optical transmission spectra of the experimental glasses. Apart from the strong UV absorption edge near ~300 nm in the UV region, glasses did not show any other absorption band in the examined region. The spectral curves for GB_{50}, GB_{75} and GB_{100} show almost same profile and therefore indistinguishable in the **Figure 3.3.5a**. The band gap energy (E_g) for all the glasses was calculated using Tauc relationship given by the,

$$\alpha h\nu = A\left(h\nu - E_g\right)^n \qquad \text{Eq. (3.3-1)}$$

$$Where,\ \ \alpha = -\frac{1}{t} ln\, T \quad (approx.) \qquad \text{Eq. (3.3-2)}$$

Here, α is the linear attenuation coefficient, T is the percent transmittance, t is the thickness of the sample, h is the Planck's constant, ν if the frequency of the photon, A is a constant related to band tailing, E_g is the band gap energy and the value of n depends on type of transition with values ½ and 2 for direct and indirect band gaps respectively. From the Tauc plots with $(\alpha h\nu)^{1/n}$ versus $h\nu$, the linear portion of each plot is extrapolated to intersect abscissa to give optical band gaps. In the present paper indirect band baps were calculated for all experimental glasses by taking n = 2. The results of

the band gaps presented in **Figure 3.3.5b insert** and **Table 3.3.4** increase with increasing B substitution.

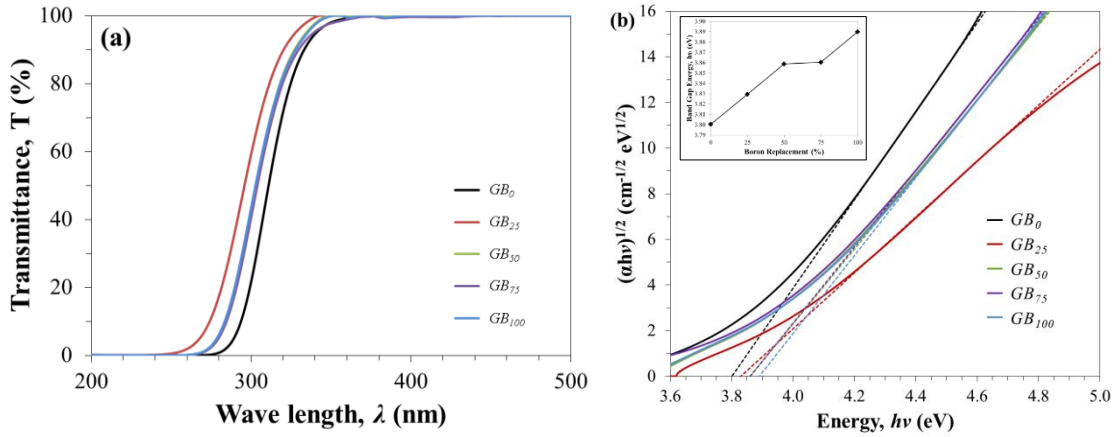

Figure 3.3.5 (a) UV-Visible spectra and (b) optical band gaps of experimental glasses.

3.3.3.5 Physical and thermal properties of glasses

Densities of all monolithic glasses are presented in **Table 3.3.4**. The values of density (ρ), molar volume (V_m) and oxygen density (ρ_O) were calculated using following formulas:

$$V_m = \frac{M}{\rho} \qquad \text{Eq. (3.3-3)}$$

$$\rho_O = \frac{M_O\left(X_{Li_2O} + X_{K_2O} + 3X_{Al_2O_3} + 3X_{B_2O_3} + 2X_{SiO_2}\right)}{V_m} \qquad \text{Eq. (3.3-4)}$$

Where M and ρ are molecular weight and density of the glass, M_O is the molecular weight of oxygen and X is the molar fraction of each oxide component present in each glass. Values of molar volumes and densities are presented in in **Table 3.3.4** and **Figure 3.3.6**. Values for coefficient of thermal expansion (CTE, 200–400 ºC) and glass softening or deformation temperatures (T_d) determined from dilatometry are also presented in **Table 3.3.4** as well as the characteristic points (T_g: glass transition temperature, T_c: crystallization onset temperature, T_p: crystallization peak temperature, T_S: solidus point and T_L: liquidus point) from the DTA curves for all glasses. To identify these characteristic points, the intersection method was employed as shown in the **Figure 3.3.7**; for T_g onset of baseline shift was used. Hrubý parameter (K_H) for glass

stability [119,162] and reduced glass transition temperature [163] (T_{gr}) for the glasses were calculated by the formula:

$$K_H = \frac{T_C - T_g}{T_S - T_c} \qquad \text{Eq. (3.3-5)}$$

$$T_{gr} = \frac{T_g}{T_L} \quad (temp.\,in\,K) \qquad \text{Eq. (3.3-6)}$$

The percentage of non-bridging oxygens (*NBO*s) with respect to total number oxygens present as an indicator of polymerization of glass network for each glass composition was calculated based on the formula:

$$NBO\ (\%) = \frac{2\times([Li_2O]+[K_2O]-[Al_2O_3]-[B^{IV}{}_2O_3])}{[Li_2O]+[K_2O]+3[Al_2O_3]+3[B_2O_3]+2[SiO_2]} \qquad \text{Eq. (3.3-7)}$$

Here all Al is assumed to be in tetrahedral coordination and the amount of B^{IV} units is obtained from ^{11}B NMR deconvolution. The values of *NBO* percentage are presented in **Table 3.3.4** for glass compositions GB_0, GB_{25}, GB_{50} and GB_{100}.

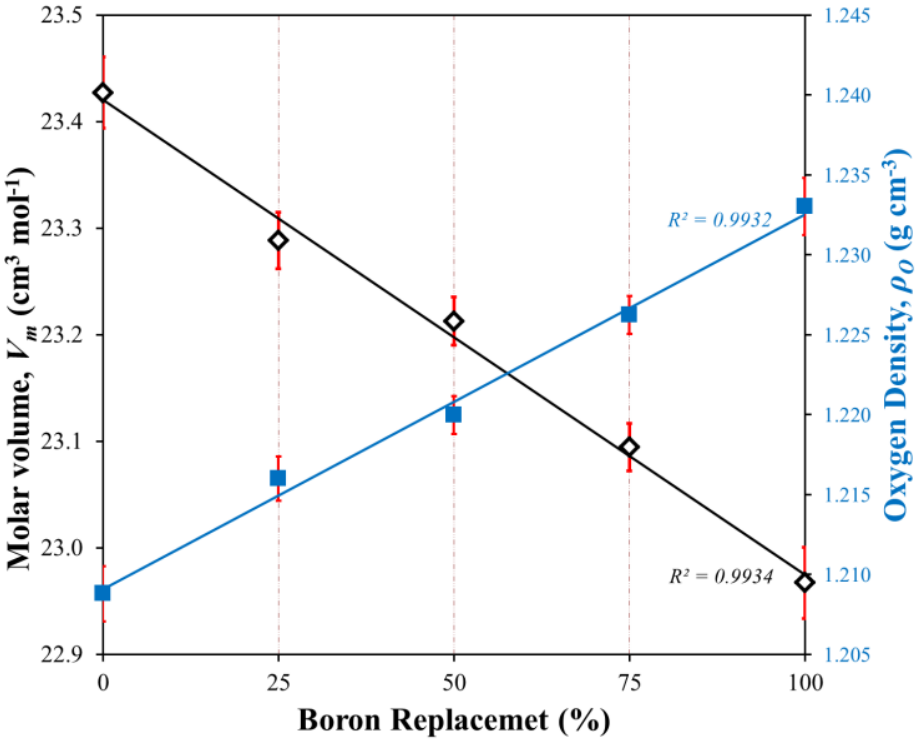

Figure 3.3.6 Molar volumes (V_m, ◇) and oxygen densities (ρ_O, ■) of experimental glasses as a function of boron replacement.

Table 3.3.4 Properties of experimental glasses

		GB_0	GB_{25}	GB_{50}	GB_{75}	GB_{100}
T_g		480	480	480	479	476
T_d		522	507	514	501	497
T_c		707	703	699	688	679
T_p	(°C)	824	812	797	767	768
T_S		951	952	925	918	917
T_L		987	986	981	977	970
$T_c - T_g$		227	223	219	209	203
T_{gr}		0.598	0.598	0.601	0.602	0.602
K_H		0.93	0.89	0.97	0.91	0.85
Density	($g\ cm^{-3}$)	2.35 ± 0.003	2.36 ± 0.003	2.36 ± 0.002	2.36 ± 0.002	2.36 ± 0.003
Oxygen Density	($g\ cm^{-3}$)	1.209 ± 0.002	1.216 ± 0.001	1.220 ± 0.001	1.226 ± 0.001	1.233 ± 0.002
Molar Volume	($cm^3\ mol^{-1}$)	23.43 ± 0.03	23.29 ± 0.03	23.21 ± 0.02	23.09 ± 0.02	22.97 ± 0.03
CTE	$\times 10^{-6}\ K^{-1}$	9.6	9.9	10.1	9.9	10
Band Gap Energy	eV	3.8	3.83	3.86	3.86	3.89
NBO	%	26	26.4	26.8	---	27.5

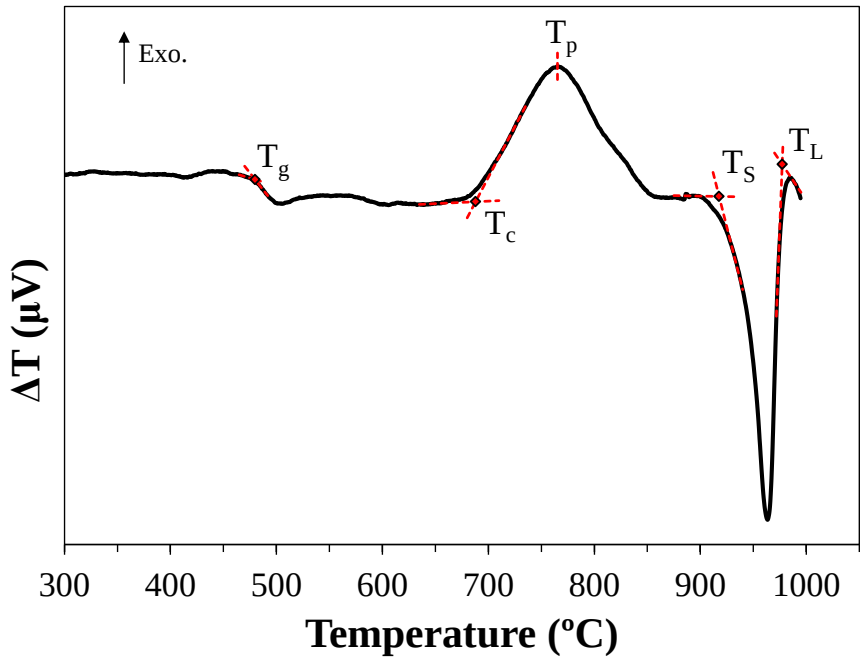

Figure 3.3.7 DTA curve of glass GB_{75} at heating rate of 20 °C min^{-1}.

3.3.3.6 Microstructures and phase analysis

The non-annealed cast glasses showed small signs of liquid-liquid phase segregation (*LLPS*) near the edges where thermal conditions must have been prone for its occurrence. To shed further light on *LLPS*, the glasses were annealed at 520 °C for

100 h. Homogenous droplet-like *LLPS* occurred throughout the samples in the following relative extents $GB_0 > GB_{100} > GB_{50}$, as obtained from SEM images (e.g. **Figure 3.3.8c−d**). The size of the droplets varied from few tens to 200 nm. The *LLPS* was also visible macroscopically as the glasses appeared cloudy. The cloudiness was greater for Al-rich sample GB_0 compared to GB_{50} or GB_{100}. XRD analysis of annealed glass samples (not shown) revealed no crystalline phases.

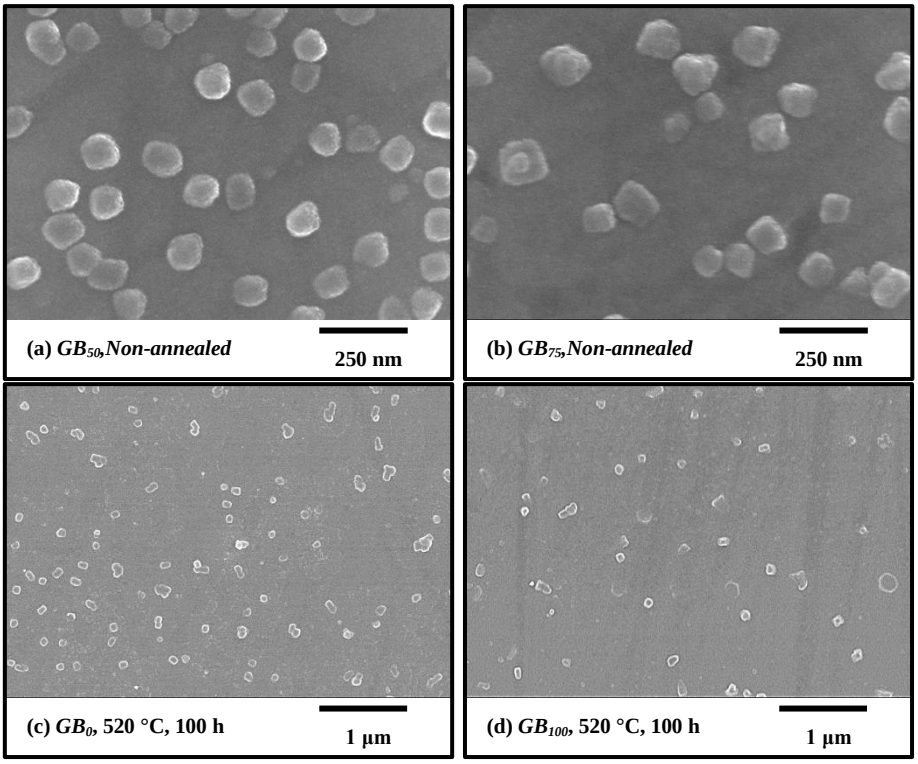

Figure 3.3.8 Metastable liquid-liquid phase segregation of (a) & (b) non-annealed glasses and (c) & (d) annealed at 520 ºC for 100 hours.

The microstructures of glasses heat treated at lower temperatures (650− 700 ºC, **Figure 3.3.9**) reveal a nucleation extent dependence on B substitution. The number of spherulitic crystals in bulk glasses (a qualitative measure of nucleation rate) displays an apparent exponential-type increase with B substitution, excepting GB_{25} that shows the lowest nucleation extent. Extensive crystallization occurred upon heat treating the glass samples at temperatures ≥ 700 ºC as seen in the optical (**Figure 3.3.10a−c**) and SEM (**Figure 3.3.10d**) micrographs, with morphological features depending on B substitution and heat treatment temperature.

The X-ray diffractograms for all samples isothermally treated for 1 h at temperatures between 650–900 ºC are presented in **Figure 3.3.11**. Transient phases are not expected under these close to thermodynamic equilibrium conditions. It can be seen

that LS_2 and LS_2-*ss* (low temperature solid solution phase of LS_2) were the prominent crystalline phases formed at 650 ºC. The crystallization propensity was enhanced with increasing B substitution. Al-rich glasses tend to crystallize minor mounts of *LS* phase and retain it at higher temperatures. Increasing B substitution favoured the formation of various polymorphs of silica at higher temperature.

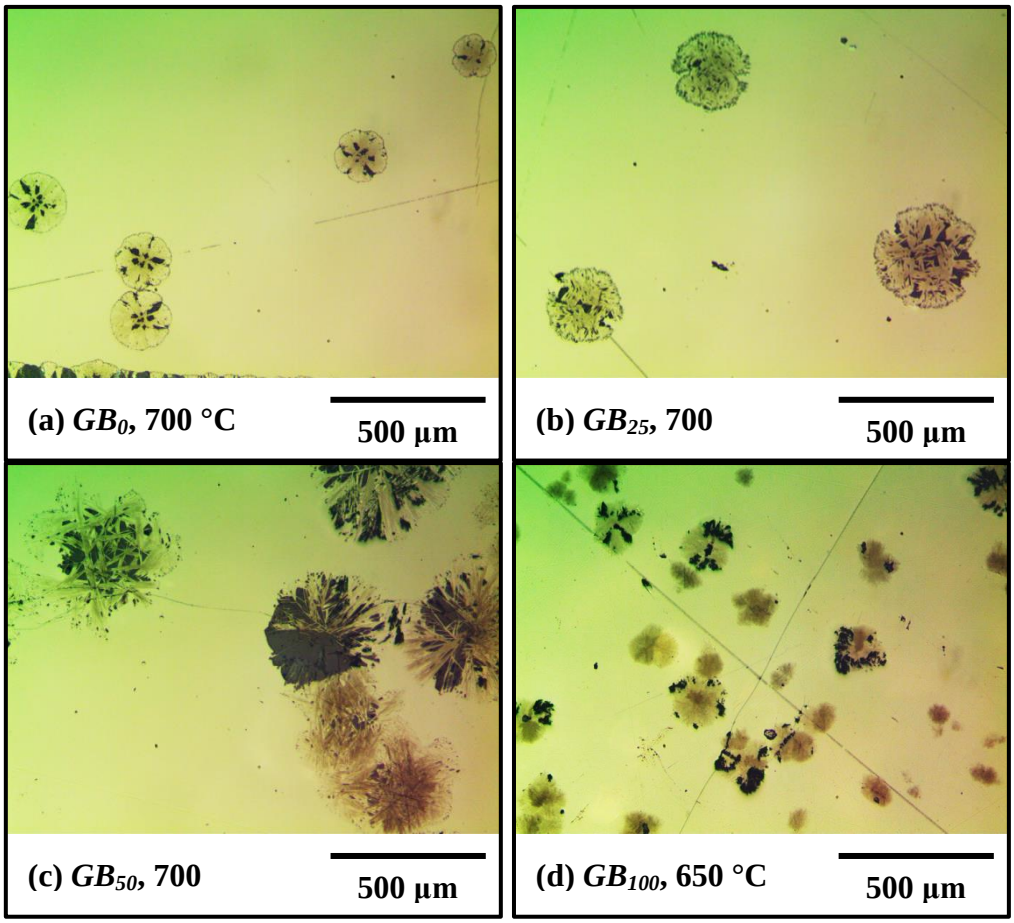

Figure 3.3.9 Optical microscope images showing degree of nucleation with B substitution.

In order to identify any transient phases formed upon heat treating under non-isothermal conditions, the extreme compositions GB_0 and GB_{100} (particle sizes between 500−1000 µm) were subjected to a heat treatment similar to DTA (β = 20 ºC min^{-1}). The samples were quenched from temperatures below melting point in order to preserve any transient crystalline phase formed. The diffractograms of these samples presented in **Figure 3.3.12b** show formation of *LS* and LS_2 in GB_0 and GB_{100} respectively. Thus the crystallization and melting peaks in DTA (**Figure 3.3.7**) should correspond to these transient phases.

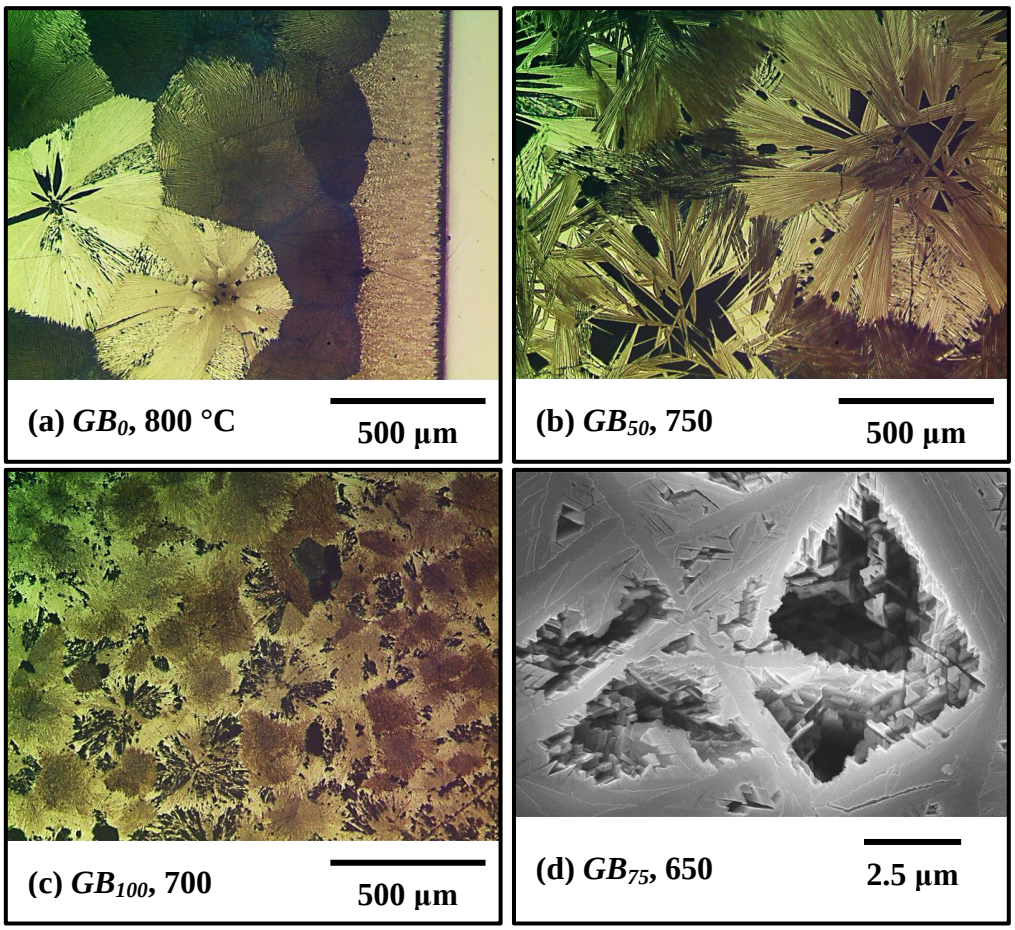

Figure 3.3.10 Micrographs of: (a) – (c) optical microscopy of completely crystallized glasses; (d) SEM morphology of spherulite crystals.

The solidus (T_S) and the liquidus (T_L) points obtained from the DTA curves plotted against the percent boron replacement and the X-ray patterns of resulting GB_0 and GB_{100} samples are displayed in **Figure 3.3.12a–b**. With boron replacement increasing, T_L gradually decreases, while T_S remains constant up to GB_{25}, steeply drops for GB_{50}, being followed by a decreasing trend to constant values. Even not corresponding to equilibrium conditions, the shapes of both these curves together seem physiognomies of a phase diagram.

3.3.4 Discussions

3.3.4.1 Glass structure and properties

The structure of glasses consists essentially of Q^3 and Q^4 network forming units (**Figure 3.3.2a**). According to earlier co-authors' studies [148,149] and other literature reports [115,155], the ^{29}Si NMR spectra of binary lithium silicate glass system ($L_{23}S_{77}$) with similar Li_2O/SiO_2 ratio (3.34) showed two very distinct peaks for Q^3 and Q^4 units with

peak maximums located at approximately −92 and −108 ppm respectively. In the case of GB_0, the presence of equimolar amount of Al_2O_3 and K_2O shifts the −108 ppm peak (seen as a shoulder) to higher values. Since Al is present in this glass system in 4−fold coordination as suggested by ^{27}Al NMR results (**Figure 3.3.1b**), the shift of −108 ppm is due to the deshielding effect on Si nuclei when Al atoms are introduced in the second coordination sphere creating $Q^4(m\text{Al})$-like units.[154,155,164] However, addition of Al had no apparent effect on Q^3 peak suggesting no possible formation of $Q^3(m\text{Al})$-like units. Hence it seems that Al forms tetrahedral units and is preferentially coordinated to Q^4 tetrahedra in the next nearest neighbourhood (NNN). According to the ^{29}Si NMR deconvolution of GB_0 (**Figure 3.3.2a** and **Table 3.3.2**), $Q^4(1\text{X})$ unit positioned at −103.4 ppm with a shift of about 5.5 ppm from Q^4, should be assigned as $Q^4(1\text{Al})$ unit. The result of ^{29}Si NMR deconvolution for GB_0 is in accordance with deconvolution reported earlier[143] for this composition (Q^3: 74.3%, Q^4: 25.7%) where separate peaks for $Q^4(1\text{Al})$ and Q^4 were not considered but a single peak accounting to both m = 0 and 1. Because of this oversimplification, the earlier ^{29}Si NMR deconvolution results were less consistent with the chemical composition. In the present case, the relative amounts of each unit corresponding to Q^2, Q^3, $Q^4(1\text{Al})$ and Q^4 are 1, 74, 15 and 10 % respectively. According to the percentage of $Q^4(1\text{Al})$ units, the amount of Al_2O_3 in the glass composition was calculated to be ~1.32 mol%, i.e., half of total (2.64 mol%) Al_2O_3 incorporated in this glass composition. Also, the percent of Q^3 units is higher than expected for this composition. Since Al−O−Al type linkages are prohibited according to Loewenstein's Rule in aluminosilicate networks,[165–167] the possible explanation for the underestimation of Al would be the involvement of the remaining Al atoms in the formation of other units such as $Q^4(2\text{Al})$ and $Q^4(3\text{Al})$ whose chemical shifts lie at approximately −98 and −92 ppm respectively. Therefore, the upsurge in the amount of Q^3 units is consistent with the creation of $Q^4(3\text{Al})$ units, which have same chemical shift as Q^3 units. The likelihood of the creation of $Q^4(2\text{Al})$ units was also assumed but attempts to quantify these units gave only small values. Considering the broad and overlapping peaks of Q^3 and $Q^4(1\text{Al})$, and that the inclusion of another small peak corresponding to $Q^4(2\text{Al})$ would only make deconvolution less reliable, thus this $Q^4(2\text{Al})$ peak was not taken into account. The deconvolution of GB_0 ^{29}Si NMR spectrum gave a slight (~2 mol %) underestimation of SiO_2 amount, possibly due to the occurrence of some *LLPS* (**Figure 3.3.8)**. The ^{29}Si nuclei present in phase segregated regions richer in SiO_2 would have spin-lattice relaxation times (T_1) extremely large in

comparison to 60 s delay times used in the current NMR experiments.[168] These relaxation times can be reduced by the addition of paramagnetic impurities to glass. But our previous studies[144] showed that even small addition of paramagnetic ions had a huge influence on glass crystallization. The extent of phase separation in the current experimental glasses used for NMR was observed to be very small. **Figure 3.3.8a–b** represent those small phase segregated regions responsible for the underestimation Si content according to ^{29}Si NMR results. To conclude, in sample GB_0, even considering a random mixing of the glass network with a diminutive phase separation, Al atoms would form tetrahedral units that are preferentially coordinated to Q^4 Si units in NNN.

Now considering the composition GB_{100} where entire Al was substituted for B, the shoulder at −104 ppm (**Figure 3.3.2a**) shifted back to a lower value, while a small shoulder appeared near −81 ppm. According to ^{11}B NMR spectral deconvolution of GB_{100} (**Figure 3.3.3b**, **Table 3.3.3**), ~48% B exists as B^{IV} and the rest is present as B^{III} with about a quarter of B^{III} units in symmetric sites. The B^{IV} units can be substituted into the tetrahedral Si sites with an alkali charge compensator similarly to Al, whereas the B^{III} units can form their own network or be coordinated with Si units. Nevertheless, it is well known that in borosilicate melts borate and silicate groups undergo a random mixing with limited formation of individual networks.[169,170] The degree of this random mixing would be in the order $B^{IV} > B^{IIIa} > B^{IIIs}$. The exact information regarding the extent of this mixing can only be determined by other techniques such as ^{17}O NMR spectroscopy where bridges like Si−O−Si, Si−O−B^{IV} and Si−O−B^{III} can be obtained; however this kind of a study is out of the scope of the present paper. Nevertheless, ^{29}Si NMR spectrum is very sensitive to the B^{IV} units if they are present in NNN where Si nuclei experience similar effect of deshielding as $Q^4(m\text{Al})$ units. Nanba *et al.*[147] used the glass optical basicity concept of Duffy and Ingram[171] and hypothesized that the chemical shift of $Q^4(1X)$ would be in the order Al > B^{IV} > B^{III} > Si for each X. Also several studies[155,169,172] used the arguments of Brown and Shannon[173] on bond strengths and showed that B^{III} units in the NNN of Si do not show any deshielding relative to Si. Hence Si units having B^{III} units in the NNN would experience similar deshielding effect as Si NNN units; hence they cannot be easily detected by ^{29}Si NMR spectroscopy. Therefore, $Q^4(1X)$ in ^{29}Si NMR deconvolution of the sample GB_{100} (**Table 3.3.2**) corresponds to $Q^4(1\text{B})$ type unit where B here is only a B^{IV} unit. Due to greater deshielding effect of B^{IV} units compared to Al, the chemical shift of the peak $Q^4(1X)$ for

the sample GB_{100} shows a slightly lower value of −104 ppm compared to GB_0. The relative amounts of Q^2, Q^3, $Q^4(1\text{B})$ and Q^4 peaks were 4, 64, 17 and 15 % respectively. 17 % of $Q^4(1\text{B})$ accounts for the total B^{IV} units obtained from ^{11}B NMR deconvolution, suggesting that, within the limits of experimental errors, no $Q^4(2\text{B})$ or $Q^4(3\text{B})$ units were formed. This means that similarly to Al, B^{IV} units are also preferentially coordinated to Q^4 units of Si in the NNN even in a randomly mixed glass network. However, a small shoulder near −81 ppm should probably correspond to $Q^3(m\text{B})$ type units with m ≥ 2 suggesting a small fraction of B^{IV} units are coordinated to Q^3 units. Specific attempts to quantify this peak give an integrated area of less than 1% which can be neglected in a pragmatic approach. Similarly to the glass GB_0, NMR results of glass GB_{100} also gave underestimation of SiO_2 content possibly for the same reasons (i.e. the presence of *LLPS*). Nonetheless, the deconvolution results for both ^{11}B and ^{29}Si nuclei revealed a reasonable internal consistency with the chemical composition. The increase in FWHM of $Q^4(1X)$ peak is possibly due to the wide distribution of bond lengths and bond angles due to the presence of both B^{III} and B^{IV} units instead of a single Al in GB_0.

In glass compositions with 25−75% boron substitution, the network structure is expected to be a mixture of both endmembers GB_0 and GB_{100}. In these glasses both Al and B^{IV} units contribute to $Q^4(1X)$. Applying structural arguments discussed for the endmembers, when a given amount of Al is removed it is expected that Q^3 and $Q^4(1X)$ contents will decrease, by adding same amount B and since it preferentially create $Q^4(1\text{B})$ units it will increase $Q^4(1X)$ content. The net result would be a gradual decrease in Q^3 and a proportional increase in the rest of the peaks. The qualitative ^{29}Si NMR deconvolution data presented in **Table 3.3.2** show a judicious agreement with this hypothesis. The factors governing the decrement in Q^3 with B substitution are the speciation extents of B into B^{III} and B^{IV} units and of Q^3 into Q^2 and Q^4 units. As quadrupolar nuclei, B requires higher magnetic fields for obtaining well resolved peaks speciation. Therefore, within the limits of these experimental errors, the ^{29}Si and ^{11}B NMR deconvolution results for glasses GB_{25} and GB_{50} were consistent with chemical composition. The FWHM of $Q^4(1X)$ peak goes through a maximum between the two endmembers due to the involvement of all three Al, B^{IV} and B^{III} units as opposed to just one or two in GB_0 and GB_{100}, respectively. The small shoulders in the region between Q^3 and Q^4 should be due to mixtures of $Q^4(1\text{Al})$ and $Q^4(1\text{B})$ units.

The overall effect of replacing Al by B on glass structure is that part of boron in the form of B^{IV} substitutes Al tetrahedra and most of the rest in form of B^{III} bonds to a *NBO*. The net effect is an increase of *NBO*s thus leading to a slight depolymerisation of the glass network as confirmed in **Table 3.3.4**. The percentage of *NBO*s shows an increasing trend from 26 to 27.5% for 0 to 100% boron replacement, respectively.

Whereas ^{29}Si NMR spectra are very sensitive to Al and B^{IV} units when present in NNN, Raman and FTIR spectra, **Figure 3.3.3** and **Figure 3.3.4**, do not show significant variations with Al by B substitution. This can be attributed to the minor changes in network polymerization and the considerably smaller numbers of B−O−M and Al−O−M (M: Al, B, or Si) vibrations in comparison to Si−O−Si. Nevertheless, both Raman and FTIR spectra give a consistent perception of the overall glass structure.

The small variations in band gap energy (**Figure 3.3.5b insert, Table 3.3.4**) are noteworthy considering the small B contents. Interestingly, the band tail slopes of B-containing samples (especially for GB_{25}), are lower in comparison to that of GB_0. Optical absorption edge in glasses is generally caused by excitonic type transitions of valance electrons in *NBO*s to higher levels.[8,174] Therefore, an increase in the number of *NBO*s could lead to a decrease in energy of UV absorption. On the other hand, transitions can also occur between the extra electron of Al in a tetrahedral position and the charge compensating alkali (K) around it. Such K-Al pairing causes a significant reduction in the UV absorption edge and masks the absorption caused by *NBO*s. This effect should also be evident when B is present in 4–fold coordination. When B replaces Al and is present as B^{III} and B^{IV} units, as perceived from the ^{11}B NMR spectra, the sum of K-Al and K-B pairs decreases. Accordingly, the band gap energy increases even when glass network depolymerisation is enhanced.

The ionic radii of network formers in the current glass system are 0.53, 0.25, 0.15 and 0.40 Å for Al^{IV}, B^{IV}, B^{III} and Si^{IV} respectively.[129] Upon replacing Al by B, the total B goes into glass network as B^{IV} and B^{III} units having lower ionic radius than Al resulting in contraction of glass network (**Figure 3.3.6**). The depolymerized glass network further reduces the molar volume. The variations in the molar volume and oxygen density should be strongly linked to B^{IV} to B^{III} ratio which dictates the number *NBO*s, B^{IV} and B^{III}. The near linear variations observed in **Figure 3.3.6** indicate that B^{IV} to B^{III} ratio remains approximately constant in agreement ^{11}B NMR. The CTE (**Table 3.3.4**) is

almost insensitive to B substitution. Glass network depolymerisation causes the interstitials to be filled with modifier ions, tending to enhance the CTE. On the other hand, B−O bonds having higher bond strengths than Al−O bonds should cause a decrease in the CTE values. These two opposing effects cancel out each other, explaining the nearly constant CTE values. The structure of supercooled liquids can be approximated to the glass structure that was discussed so far. Therefore at isokom temperature of glass softening point where viscosity is ~$10^{6.6}$ Pa·s, the structure of a supercooled liquid should be similar to its glassy state. The decrease in the glass softening temperatures with B addition is an indication of decreasing viscosity, therefore clearly supporting the depolymerisation of glass network due to B substitution. However, higher B−O bond strengths do not seem to have great role on viscosity in the supercooled state.

The findings concerning the network structure of supercooled glasses will be useful for understanding the nucleation process that also occurs at deep undercooling as discussed in the following section.

3.3.4.2 Phase segregation and crystal nucleation

Nucleation of non-stoichiometric glasses is greatly influenced by the *LLPS* phenomena. Therefore it is of paramount interest to understand the influence of B substitution on *LLPS*. The role of *LLPS* on crystal nucleation of glasses was thoroughly investigated and clearly established by James *et al.*[132,133,152,175,176] According to their findings, compositional variations brought along the *LLPS* process create ideal zones for the commencement of homogenous nucleation. As shown in **Figure 3.3.8c−d**, the size of droplets in annealed glasses ranging from 20 to 200 nm indicates that nucleation and growth occurred simultaneously at 520 ºC. These droplets should correspond to SiO_2-rich regions embedded in Li_2O-rich matrix. Borosilicate glasses are also likely to show *LLPS* into boron- and silicon-rich regions. But considering the small added amounts of B, the compositions should lie only within the two liquid regions of ternary alkali borosilicate phase diagram[177].

Dopants are likely to affect both kinetics and thermodynamics (Gibbs free energy, the sum of enthalpy and entropy contributions) of *LLPS* in glasses. [178] The main contributions to enthalpy term include: (1) heat of formation of *NBO*s; (2) deformation of the Si tetrahedra in the presence of alkali ions; these reactions are exothermic and

endothermic respectively. Entropy is mainly related to mixing of *NBO* pairs and bridging oxygens (configurational entropy). *LLPS* is mostly enthalpy driven (endothermic deformation of the Si tetrahedral). Topping *et al.*[179] extended this concept to aluminosilicate glasses to explain the reduction of *LLPS* due to Al_2O_3 addition that converts *NBO*s into bridging oxygens with an overall charge of 1− on each AlO_4 tetrahedral unit. Being an exothermic reaction it would reduce the overall driving force for *LLPS*. This enthalpy-based explanation might only be part of the overall picture as it contrasts with the largest extent of *LLPS* observed for the present Al_2O_3-rich GB_0 glass in comparison to B-containing compositions. According to Charles[178], in a binary alkali silicate system the entropy is due to interchanges of *NBO* pairs and bridging oxygens (of Si−O−Si type). However, additional types of bridging oxygens (Si−O−Al, Si−O−B^{III}, Si−O−B^{IV} and B−O−B) should be created upon adding Al_2O_3 and B_2O_3. These units are likely to increase the entropy and with the mixed Al and B glasses should show the large entropy. Hence, it is hypothesised that this increase in entropy might change the free energy curve and reduce thermodynamic driving force and ultimately the extent of *LLPS*, explaining the observed trend $GB_0 > GB_{100} > GB_{50}$. Further work is needed in this direction with more quantitative modelling of entropy on free energy involving ^{17}O NMR in order to evaluate the influence of the various forms of bridging oxygens. Apart thermodynamic driving force, the kinetics of *LLPS* is also dependent on glasses' viscosity, which decreased with increasing B substitution due to the creation of additional *NBO*s. The thermodynamic driving force for *LLPS* changes in the order $GB_0 > GB_{100} > GB_{x'}$ (here x' is 25, 50 or 75) and the kinetic barrier for *LLPS* of glasses change in the order $GB_{100} > GB_{75} > GB_{50} > GB_{25} > GB_0$. Such B content dependence of thermodynamics and kinetics behaviours would have a direct and profound implication on the crystal nucleation rate.

The nucleation rate of crystals depends on the kinetics of *LLPS* where faster kinetics enhances the crystal nucleation rate by shifting the composition of the glass matrix during the process. Considering the glass samples GB_0 and GB_{100}, GB_0 has comparatively larger thermodynamic driving force but higher viscosity. Due to its lowest viscosity, GB_{100} exhibits the fastest kinetics of *LLPS* and the highest crystal nucleation rate in comparison to other glasses. All mixed B and Al containing glasses have lower thermodynamic driving force for *LLPS* in comparison to GB_0 and GB_{100}; however the kinetics barrier for *LLPS* decreases with increasing B substitution, and the

crystal nucleation rates are expected to concomitantly increase. However, because the thermodynamic driving force goes through a minimum between the two end members GB_0 and GB_{100}, at a particular B substitution between the end members, the crystal nucleation rate is expected to be lower than in the rest of the samples. This explains why the glass sample GB_{25} showed lowest crystal nucleation rate among all the experimental glasses (**Figure 3.3.9**).

The crystal nucleation of the glasses is correlated to glass transition temperature by a parameter called reduced glass transition temperature T_{gr}.[131,163] Homogenous nucleation occurs in glasses for $T_{gr} < 0.58-0.60$. The increasing trend of T_{gr} values with B substitution (**Table 3.3.4**) suggests a slowdown in the nucleation rate. Crystallization of metastable LS_2-ss solid solution occurred upon heat treating glasses at 650 ºC (**Figure 3.3.11a**). This phase commonly forms when excess mount of SiO_2 is present in comparison to LS_2 stoichiometry.[180,181] Nonetheless at higher temperatures this phase degrades and transforms into LS_2 and LS_2-ss silica. Increased nucleation rate in non-stoichiometric phase segregated lithium silicate has been ascribed to the nucleation of LS_2-ss phase.[182] Therefore, LS_2-ss can be assumed as the nucleating phase in all glass compositions. Accordingly, a constant T_L value can be assumed for all glass compositions; considering a same nucleating phase, the T_{gr} values tend to follow T_g values which are in accordance with the nucleation rates exhibited by glasses. Therefore, the increasing T_{gr} values with B substitution can be attributed to changing crystallizing phase rather than the nucleating phase.

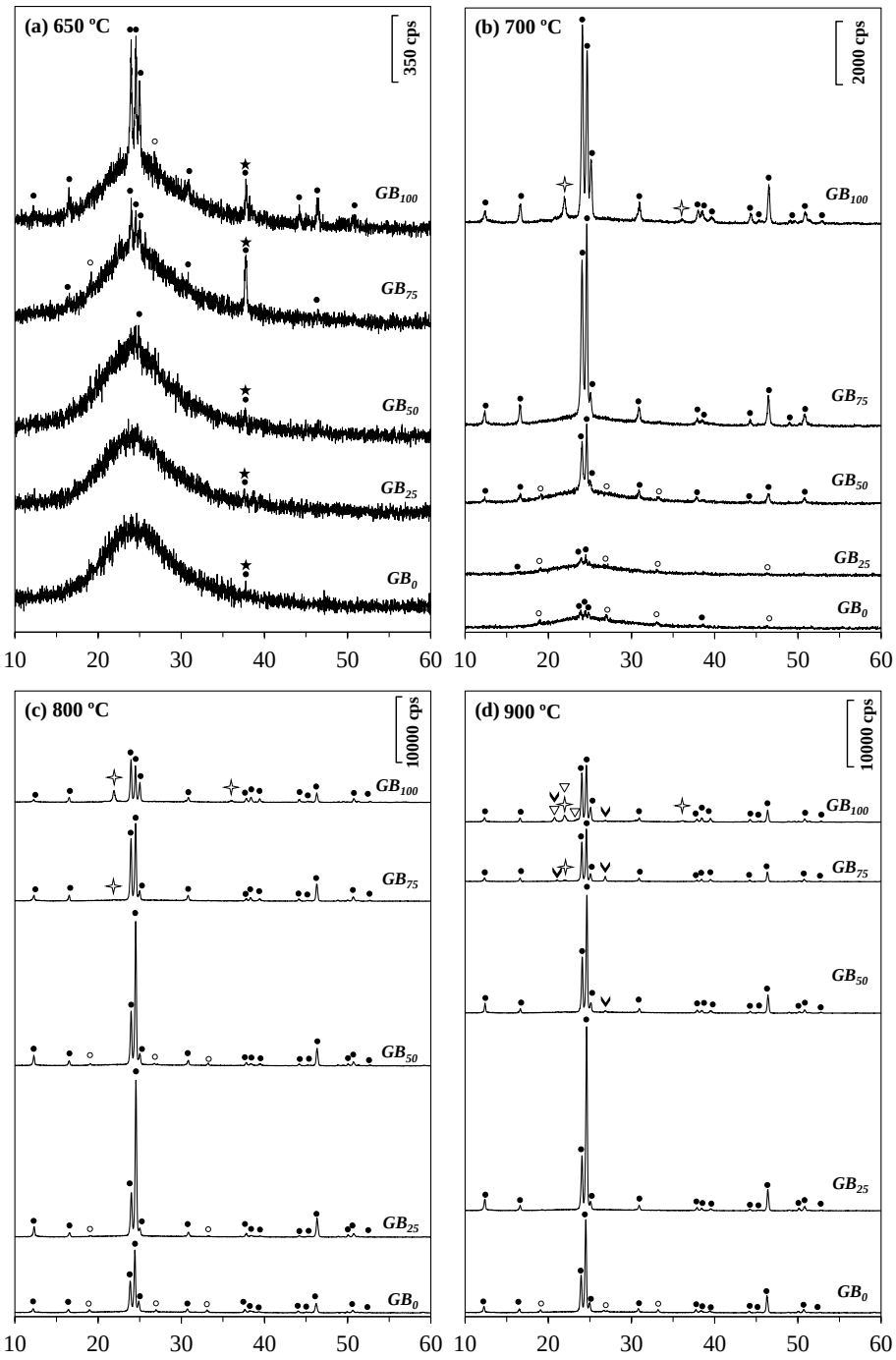

Figure 3.3.11 X-ray diffraction patterns of crystallized glasses at temperatures: (a) 650 ºC, (b) 700 ºC, (c) 800 ºC and (d) 900 ºC (●: Lithium disilicate ($Li_2Si_2O_5$, ICDD 04-009-4359); ○: Lithium metasilicate (Li_2SiO_3, ICDD 00-029-0828); ✧: Cristobalite (SiO_2, ICDD 01-082-0512); ▽: Tridymite (SiO_2, ICDD 01-074-8988); ⮟: Quartz (SiO_2, ICDD 01-082-0512); ★: Lithium disilicate solid solution ($Li_2Si_{2+x}O_{5+2x}$, West et al.[181] and Glasser[180]).

3.3.4.3 Morphology and phase assemblage of crystallised glasses

Al-rich glass compositions exhibited high glass stability as seen from XRD results (**Figure 3.3.11a-b**) and with B substitution the glasses showed an increasing tendency to devitrify under isothermal conditions due to a lowering viscosity. The concomitant crystallization of *LS* and LS_2 reduces the meaningfulness of glass stability parameter K_H (**Table 3.3.4**) derived from non-isothermal (DTA) conditions explaining the apparent lack of consistency observed. The plot of T_S and T_L against B replacement (**Figure 3.3.12a**) resembles a region of Li_2O−SiO_2 phase diagram[183] around LS_2 stoichiometry where a transition from *LS* to LS_2 occurs. **Figure 3.3.12b** shows that pure *LS* and LS_2 are obtained under non-isothermal conditions from the extreme compositions GB_0 and GB_{100}, respectively. Therefore, **Figure 3.3.12a** suggests that *LS* and LS_2 are preferentially formed for B replacement up to 25 % and ≥ 50 %, respectively. Based on the crystallizing phases, the glasses could be divided into two groups (0−25 % and 50−100 % B substitution). In each group the K_H values follow the trend of glass stability as seen by XRD. However, a simple glass stability parameter such T_c−T_g shows better accordance with XRD for all compositions. Complete LS_2 crystallization was achieved for glasses GB_0 and GB_{100} at 800 ºC and 700 ºC, respectively (**Figure 3.3.10**). The early crystallization of *LS* in Al-rich end member suggests that glass becomes Si-depleted for crystallization probably due to increased liquid stability. When present, *LS* is a transient and transforms into LS_2 under suitable heat treatment schedule and might lead to morphological changes (**Figure 3.3.10**).

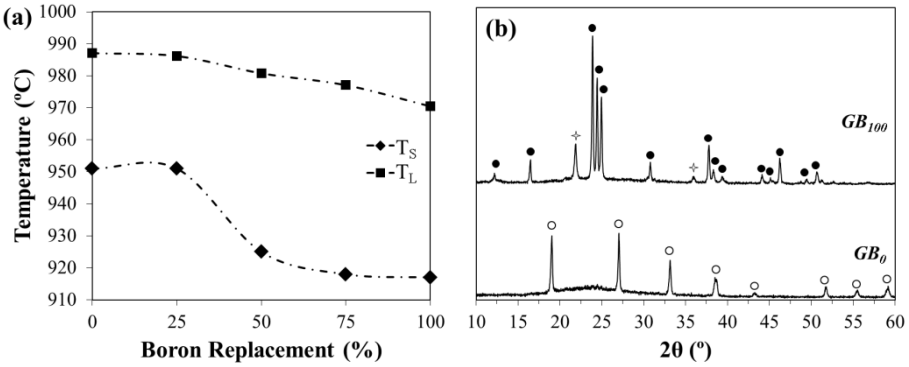

Figure 3.3.12 (a) Variation of solidus and liquidus points as a function of boron replacement. (b) Corresponding XRD patterns for glasses GB_0 and GB_{100} below solidus curve. ●: lithium disilicate ($Li_2Si_2O_5$, ICDD 01-070-4056); ○: lithium metasilicate (Li_2SiO_3, ICDD 01-049-0803); ✧: cristobalite (SiO_2, ICDD 01-089-3607).

3.4 Influence of Al_2O_3 and B_2O_3 on sintering and crystallization of lithium silicate glass system

Anuraag Gaddam [a], Hugo R. Fernandes [a], Maria J. Pascual [b], José M.F. Ferreira [a]

[a] Department of Materials and Ceramics Engineering, University of Aveiro, CICECO, 3810-193 Aveiro, Portugal.

[b] Instituto de Cerámica y Vidrio (CSIC), C/Kelsen 5, Campus de Cantoblanco, 28049 Madrid, Spain.

Journal of American Ceramic Society, 99 (2016) 833–840
DOI: 10.1111/jace.14040

Abstract

This article reports on the effect of Al_2O_3 and B_2O_3 added as dopants on the preparation of glass-ceramics (*GC*s) belonging to the lithium silicate glass system. The *GC*s are prepared by sintering route using glass powders. The reasons for the crystallization of the metastable crystalline phase lithium metasilicate (*LS*) are discussed and the impact of the dopants on the thermodynamics and kinetics of crystallization is investigated. The addition of dopants modifies the thermodynamic equilibrium of the system and this change is mainly entropy driven and also slow down the kinetics of crystallization. Differential thermal analysis and hot-stage microscopy are employed to investigate the glass forming ability, sintering and crystallization behaviour of the studied glasses. The crystalline phase assemblage studied under non-isothermal heating conditions in the temperature range of 800–900 ºC in air. Well sintered and dense glass-ceramics are obtained after sintering of glass powders at 850–900 ºC for 1 h featuring crystalline phase assemblage dominated by lithium disilicate (LS_2).

3.4.1 Introduction

Glass-ceramics (*GC*s) are composite materials of one or more crystalline phases immersed in a residual glassy phase. They generally feature interesting properties such as high strength, low density, chemical stability, low thermal expansion and low dielectric properties, which allow using them in a wide variety of applications.[1,184] *GC*s can be produced by sintering glass particle compacts followed by simultaneous or subsequent crystallization.[1,185,186] The powder technology permits the use of glasses with an extremely wide range of compositions, including compositions that are difficult to adapt to the classical casting-crystallization technologies due to a high viscosity of the melt, or unsuitable crystallization kinetics. In most cases the sintered materials acquire a uniform microcrystalline structure with a high content of a mineral phase. In addition, compared with the classical technology, the physical-chemical properties of the materials obtained can be more stable and reproducible.[187] However, in a glass powder compact system, a competition between crystallization and sintering will begin above the glass transition temperature (T_g) both processes decreasing the free energy of the glass powder.[188] If the crystallization occurs before sintering is complete, further densification will be suppressed by the increased viscosity resulting in glass-ceramic materials with relatively poor mechanical properties due to porosity.[189] Therefore, it is fundamental to understand the densification and crystallization behaviours of the system during the heat treatment of glasses.

Among the diverse glass systems used to produce *GC*s, lithium disilicate (LS_2) based glasses occupy a prominent position due to the intensive activity on this system along the last decades. The interest is motivated by an attractive set of properties exhibited by the resulting *GC*s, making them suitable for different advanced applications (e.g. dental restorations, electrically insulating materials, transparent *GC* armour, etc.).[1,53,136] However, *GC*s derived from binary $Li_2O–SiO_2$ system exhibit some unfavourable characteristics in terms of their mechanical strength and chemical durability which hinder their use in several technological areas.[190] Therefore non-stoichiometric or multicomponent compositions have been developed to overcome this problem. For instance, adding some oxides such as Al_2O_3 and K_2O to the stoichiometric composition have been reported to enhance the chemical durability of $Li_2O–SiO_2$ derived *GC*s.[191,192] In previous works, the effect of Al_2O_3, K_2O, and MnO_2 on the

sintering and crystallization behaviours of non-stoichiometric glasses in the $Li_2O–SiO_2$ system with SiO_2/Li_2O molar ratios greater than 3 has been reported (Section 3.2).[134,142,144,151] Sintering and crystallization studies of glass powder compacts with a binary composition $23Li_2O–77SiO_2$ revealed high fragility, and low flexural strength and density. In contrast, good densification behaviour and improved mechanical strength resulted from adding equimolar amounts (2.63 mol. %) of Al_2O_3 and K_2O to the $Li_2O–SiO_2$ composition.[142] A further insight into the specific effects of adding incremental amounts of K_2O on structure–property relationships and crystallization behaviour of glasses in the $Li_2O–Al_2O_3–K_2O–SiO_2$ revealed that excess K_2O contents within the range of 2.63–12.63 mol. % was found to reduce bulk crystallization in glasses with the predominant formation of lithium metasilicate (*LS*) phase. Only in low-K_2O compositions LS_2 phase was formed, resulting in a *GC* with high mechanical strength (~173–224 MPa), good chemical resistance (~25–50 μg cm^{-2}) and low total conductivity (~2×10^{-18} S cm^{-1}) making the materials suitable for a number of practical applications.[134] In Mn-doped glass powder compacts in the system $23Li_2O–2.64K_2O–2.64Al_2O_3–(71.72–x)SiO_2–xMnO_2$ (x = 0–2 mol. %), sintering and crystallization occurred at lower temperatures than the parent composition conferring higher strength at low sintering temperatures, but the occurrence of foaming in Mn-doped samples at higher temperatures drastically reduced density and mechanical strength.[144]

The present study aims towards investigating the effects of the partial and total substitution of Al_2O_3 by B_2O_3 on the sintering behaviour and crystallization of glass powder compacts of a relatively simple non-stoichiometric lithium disilicate based glass composition in the glass forming region of $Li_2O–K_2O–Al_2O_3–SiO_2$ with SiO_2/Li_2O molar ratio of 3.12. This paper is a continuation of our previous work[193] in which *GC*s of the same compositions were investigated addressing the influence of Al_2O_3 and B_2O_3 on glass network structure, liquid-liquid phase segregation and crystal nucleation in monolithic glasses. In this paper, particular emphasis was given to the crystalline phase evolution and sintering ability of glass powders. The investigation uses several thermodynamic calculations in order to address the crystallization of equilibrium and non-equilibrium crystal phases. The formation kinetics of these phases was also investigated. *GC*s were prepared by sintering green powder compacts and their properties were measured.

3.4.2 Experimental procedure

3.4.2.1 Materials preparation

Five glass compositions were prepared based on the general formula $23.00Li_2O - 2.64K_2O - 2.64(1-z)Al_2O_3 - 2.64(z)B_2O_3 - 71.72SiO_2$ (mol %.) where, z = 0.00, 0.25, 0.50, 0.75 and 1.00. Here Al_2O_3 is replaced by B_2O_3 from 0 to 100 % at steps of 25 %; correspondingly the samples were named GB_0, GB_{25}, GB_{50}, GB_{75} and GB_{100}. **Table 3.4.1** presents details of compositions in mole percentages.

Glasses were synthesized using SiO_2, Li_2CO_3, K_2CO_3, Al_2O_3 and H_3BO_3 precursors in the form of powders (all with purity > 99%). These powders were homogenously mixed in a ball mill and calcined at 800 ºC for 1 h in alumina crucibles. Calcined powders were further mixed for homogeneity using mortar-pestle and transferred to platinum crucibles for melting at the temperature of 1550 ºC for 1 h in air. Melts were quenched into cold water to obtain glass frits. Glass frits were dried and milled in a high speed agate mill for 2 h in order to obtain glass powders of particle mean sizes ranging between 8–12 μm as determined by particle size analyser (Coulter LS 230, Fraunhofer optical model, Amherst, MA).

Table 3.4.1 Compositions of the experimental glasses (in mol %)

	Li_2O	K_2O	Al_2O_3	B_2O_3	SiO_2
GB₀	23.00	2.64	2.64	0.00	71.72
GB₂₅	23.00	2.64	1.98	0.66	71.72
GB₅₀	23.00	2.64	1.32	1.32	71.72
GB₇₅	23.00	2.64	0.66	1.98	71.72
GB₁₀₀	23.00	2.64	0.00	2.64	71.72

*GC*s were prepared by sintering route; rectangular bars of glass powder compacts of dimensions 50 mm × 5 mm × 4 mm were prepared by uniaxial pressing with a pressure of 80 MPa. Glass powder compacts were then sintered at temperatures of 800, 850 and 900 ºC for 1 h in air at a heating rate of 2 ºC min^{-1} to obtain *GC*s.

3.4.2.2 Characterisation

All glass powders were subjected to differential thermal analysis (DTA, Setaram Labsys, Setaram Instrumentation, France) in air from room temperature to 1000 ºC, at

heating rates (β) of 10, 15, 20 and 25 ºC min^{-1}. For DTA, alumina crucibles were used to hold sample powders (~30 mg) with α-Al_2O_3 as reference material. The sintering behaviour of glass powders was studied by side-view hot stage microscope (HSM, Leitz Wetzlar, Germany) equipped with a Pixera video camera and image analysis system. Samples for HSM (GB_0, GB_{50} and GB_{100}) were prepared by pressing glass powders into cylindrical shapes of diameter ~3 mm. Measurements were conducted in air at a heating rate of 5 ºC min^{-1}. Temperatures corresponding to the characteristic points of viscosity (First shrinkage (T_{FS}), maximum shrinkage (T_{MS}), half ball (T_{HB}) and flow (T_F)) were obtained from the graphs and photomicrographs taken during the hot-stage microscopy experiment. In order to compare HSM results with crystallization, DTA with a heating rate of 5 ºC min^{-1} was also employed for samples GB_0, GB_{50} and GB_{100}.

Microstructures of sintered *GC*s were examined by scanning electron microscopy (SEM, SU-70, Hitachi, Japan). Samples for SEM were prepared by grinding, polishing and etching for 60 s using 2 vol. % hydrofluoric acid. Crystalline phases present in the sintered *GC*s were examined by x-ray diffraction (XRD, Rigaku Geigerflex D/Mac, C Series, Japan) using Cu K_α radiation with 2θ varying from 10–60 º steps of 0.02 s^{-1}.

Flexural strengths of sintered *GC*s bars were measured by three-point bending test using universal testing machine (Shimadzu Autograph AG 25 TA). Densities of sintered *GC*s were measured by Archimedes principle by immersing the samples into ethylene glycol. The shrinkages after sintering were calculated by measuring the contraction of lengths.

3.4.3 Results

The glass frits obtained after melting at 1550 ºC were amorphous as examined by XRD (Supplementary information Section 3.4.5.1). In order to estimate the volatilization of the glass melt at high temperatures, weight losses were measured before and after melting.[8] All glass melts showed weight losses of less than 0.2%. This loss is a negligible value which could be attributed mainly to Li and does not significantly affect the overall composition. Some of the experimental results on *GC*s for the sample GB_0 were already reported in our previous article[144], and therefore most of these results are not presented here and the readers are advised to refer to this article.

3.4.3.1 Crystallization

Figure 3.4.1 presents the DTA plots of all the glasses measured at β = 20 ºCmin^{-1}. Samples show 2–3 crystallization peaks (T_{P1}, T_{P2} and T_{P3}) and a melting peak. The phases corresponding to each crystallization peak were identified by XRD (Section 3.4.5.3). In all the glasses, T_{P1} corresponds mainly to the crystallization of *LS* phase and with increasing B_2O_3 substitution, LS_2 also starts to crystallize. T_{P2} corresponds mainly to the crystallization of LS_2 with small amount of cristobalite and quartz; the amounts of these SiO_2 polymorphs increase with B_2O_3 substitution. T_{P3} corresponds to the further crystallization of cristobalite and quartz. The activation energies corresponding to each DTA crystallization event (E_C) were calculated according to Kissinger model[194] given by the Eq. (3.4-1).

$$\ln\frac{\beta}{T_P^2} = -\frac{E_c}{RT_P} + const. \qquad \text{Eq. (3.4-1)}$$

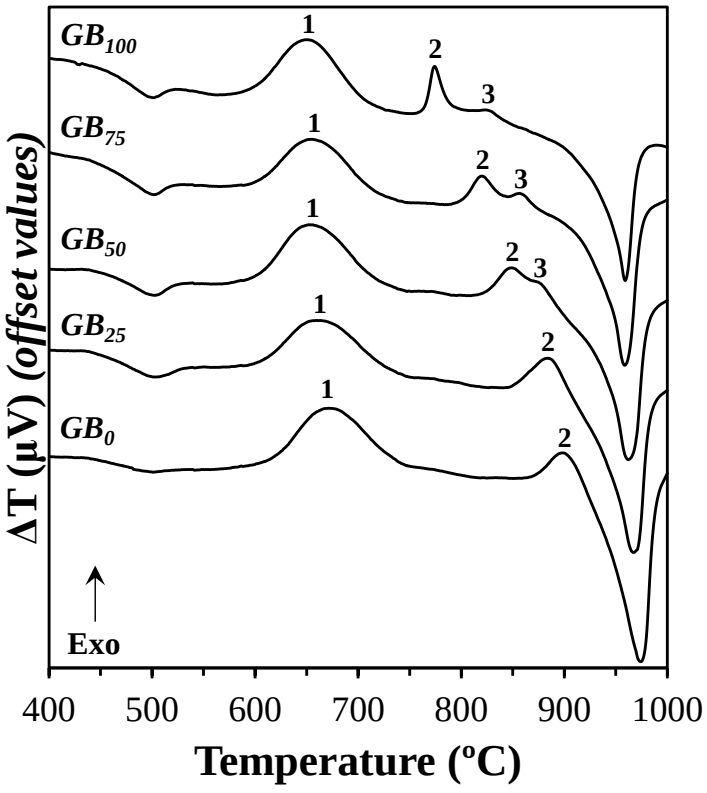

Figure 3.4.1 DTA of glass compositions at β = 20 ºC min^{-1}.

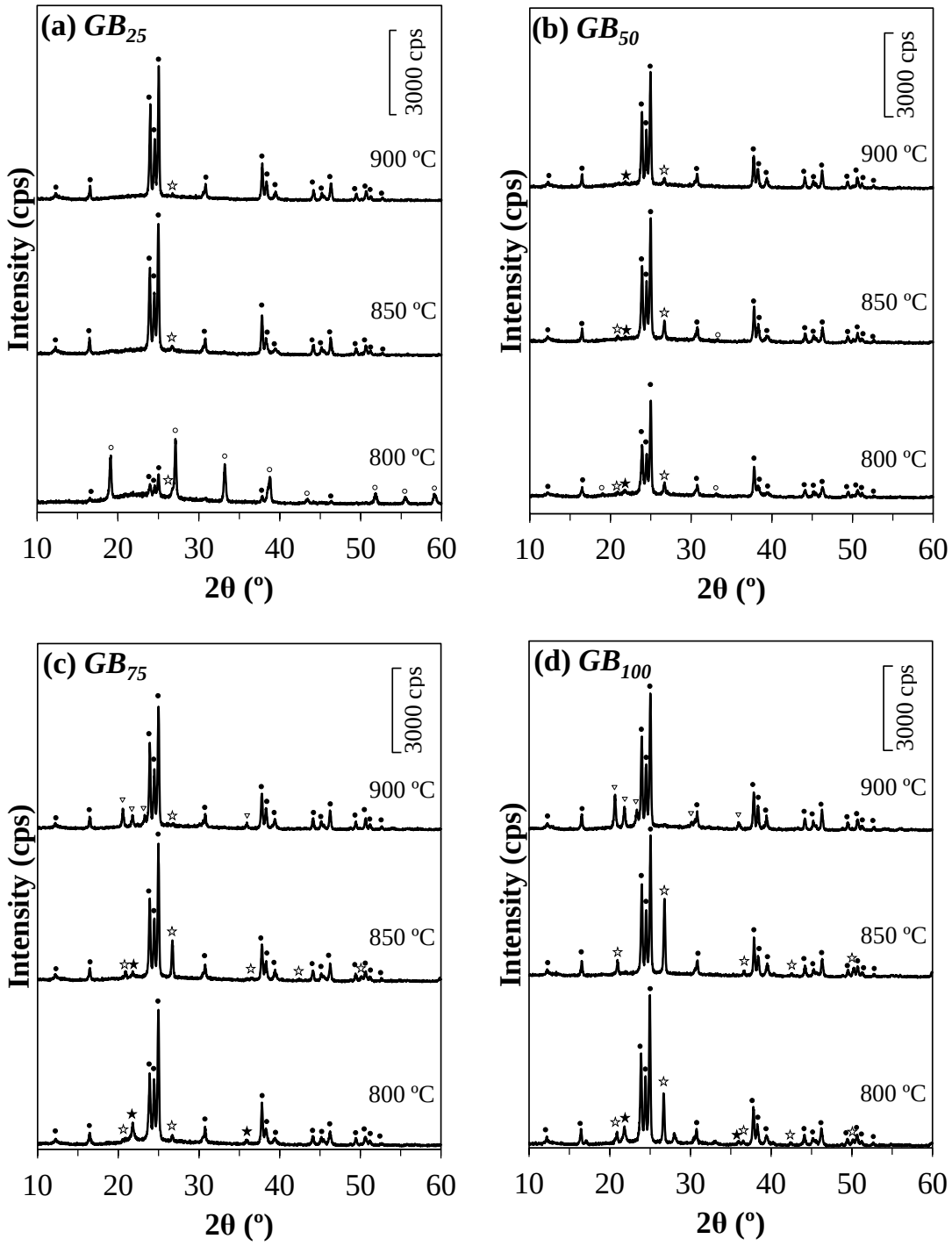

Figure 3.4.2 X-ray diffractograms of sintered *GC*s. [●: Lithium disilicate ($Li_2Si_2O_5$, ICDD 04-009-4359); ○: Lithium metasilicate (Li_2SiO_3, ICDD 00-029-0828); ☆ : Quartz (SiO_2, ICDD 01-075-8321); ▽: Tridymite (SiO_2, ICDD 01-074-8988); ★ : Cristobalite (SiO_2, ICDD 01-082-0512)].

Table 3.4.2 presents the values of E_{C1}, E_{C2} and E_{C3} corresponding to T_{P1}, T_{P2} and T_{P3}, respectively. The curve fitting and fit parameters can be found in the supplementary information (**Figure 3.4.9**). It is interesting to note that the E_C values for the 1st crystallization peak goes through a maximum between end members GB_0 and GB_{100}; while the values of the 2nd crystallization peak continuously decrease. For all the samples the broad endothermic peaks (in the range 900 to 1000 ºC) with a shoulder seems to be a convolution of two endothermic peaks corresponding to *LS* and LS_2 phases. It is difficult to assign the order in which they appear, but this subject will be discussed in the subsequent section. The XRD patterns of sintered *GC*s are presented in **Figure 3.4.2**. Increased B substitution resulted in the decreasing and increasing amounts of *LS* and SiO_2 crystalline phases, respectively. **Figure 3.4.3** presents various microstructural features encountered in the sintered samples. In all the compositions, the predominant phase LS_2 exists as crystals with needle-like morphology and show regional aggregates of large crystals surrounded by smaller crystals (**Figure 3.4.3a**).

Table 3.4.2 Characteristic temperatures and activation energies and fit parameters of each crystallization peak.

		1st peak		*2nd peak*		*3rd peak*		
	T_g ‡	T_{P1} ‡	E_{C1}	T_{P2} ‡	E_{C2}	T_{P3} ‡	E_{C3}	T_L
	ºC	ºC	kJ mol^{-1}	ºC	kJ mol^{-1}	ºC	kJ mol^{-1}	ºC
GB_0	500	671	183	898	628	---	---	972
GB_{25}	504	661	182	884	357	---	---	972
GB_{50}	502	654	193	849	383	873	387	968
GB_{75}	503	655	186	820	318	857	405	963
GB_{100}	499	650	168	774	286	823	312	962

‡*Data for heating rate = 20 °C min^{-1}.*

3.4.3.2 Sintering

Figure 3.4.4 presents HSM curves, micrographs and the corresponding crystallization peak temperatures for the glass samples GB_{50} and GB_{100}. The same plots for the sample with GB_0 labelled as $GMn_{0.0}$ can be found in **Figure 3.2.12** or in the published paper.[144] The crystallization peak temperatures under HSM conditions (5 ºC min^{-1}) were derived by extrapolation from the Kissinger model (Eq. (3.4-1)). This

method was employed because at the low heating rate the DTA gave a noisy curve. The derived peak temperatures are still in good agreement with the experimental results (**Figure 3.4.10**). The corresponding points of sintering (T_P, T_{FS} and T_{MS}) and amounts of shrinkage (δ) after each sintering event according to HSM are presented in **Table 3.4.3**. Sample GB_0 showed two sintering events, while the samples GB_{50} and GB_{100} showed three sintering events. The values of densities, shrinkage and bending strengths of the sintered *GC*s are presented in **Table 3.4.4**.

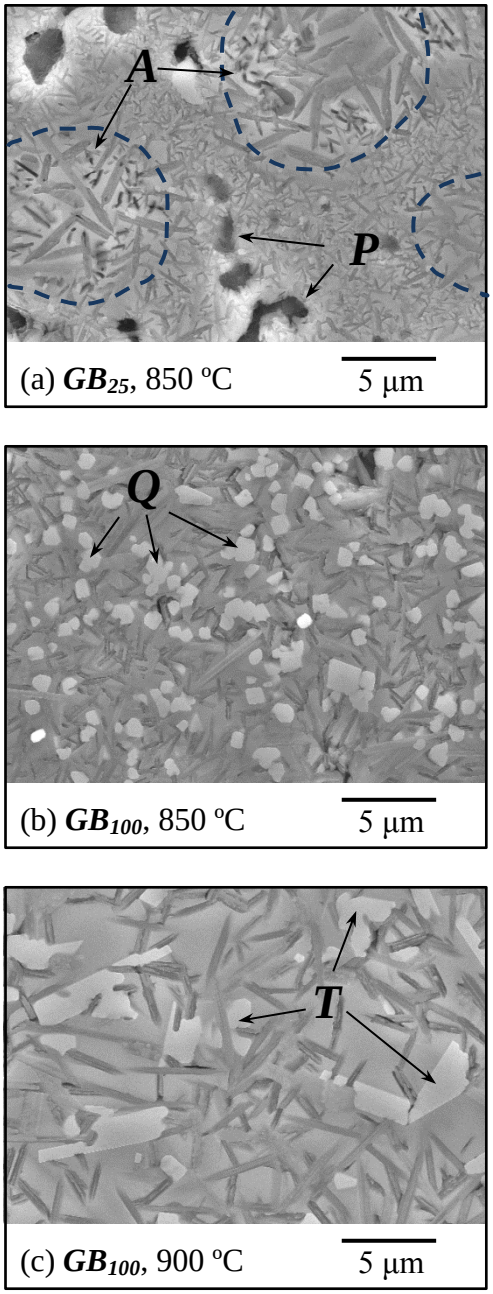

Figure 3.4.3 SEM images of sintered *GC*s. ***A***: aggregates of large crystals inside particles; ***P***: pores; ***Q***: quartz crystals; ***T***: tridymite crystals.

Table 3.4.3 Characteristic points of sintering

		GB_0 †	GB_{50}	GB_{100}
DTA	T_{P1} (ºC)	648	609	599
	T_{P2} (ºC)	875	813	734
	T_{P3} (ºC)	---	836	782
HSM	T_{FS1} (ºC)	510	512	509
	T_{MS1} (ºC)	583	568	557
	δ_1 (%)	18	22	10
	T_{FS2} (ºC)	774	746	711
	T_{MS2} (ºC)	928	796	724
	δ_2 (%)	19	5	3
	T_{FS3} (ºC)	---	880	855
	T_{MS3} (ºC)	---	913	932
	δ_3 (%)	---	10	22
	Total shrinkage	37	37	35

Table 3.4.4 Properties of sintered glass-ceramics

		GB_0	GB_{25}	GB_{50}	GB_{75}	GB_{100}
Density ($g\ cm^{-3}$)	*800 ºC*	2.26 ± 0.008	2.23 ± 0.017	2.27 ± 0.004	2.16 ± 0.005	2.25 ± 0.017
	850 ºC	2.37 ± 0.004	2.27 ± 0.007	2.30 ± 0.050	2.20 ± 0.011	2.36 ± 0.013
	900 ºC	2.37 ± 0.005	2.38 ± 0.004	2.36 ± 0.000	2.32 ± 0.009	2.32 ± 0.004
Shrinkage *(%)*	*800 ºC*	12.60 ± 0.06	13.05 ± 0.13	14.65 ± 0.03	11.75 ± 0.02	14.03 ± 0.03
	850 ºC	15.90 ± 0.17	13.89 ± 0.00	15.49 ± 0.12	13.09 ± 0.05	16.61 ± 0.25
	900 ºC	18.00 ± 0.17	14.76 ± 0.13	15.75 ± 0.09	15.65 ± 0.08	15.47 ± 0.18
Bending Strength *(MPa)*	*800 ºC*	147 ± 14	084 ± 01	236 ± 11	135 ± 11	131 ± 14
	850 ºC	216 ± 03	188 ± 12	174 ± 08	173 ± 19	256 ± 09
	900 ºC	281 ± 05	264 ± 15	245 ± 15	228 ± 10	201 ± 10

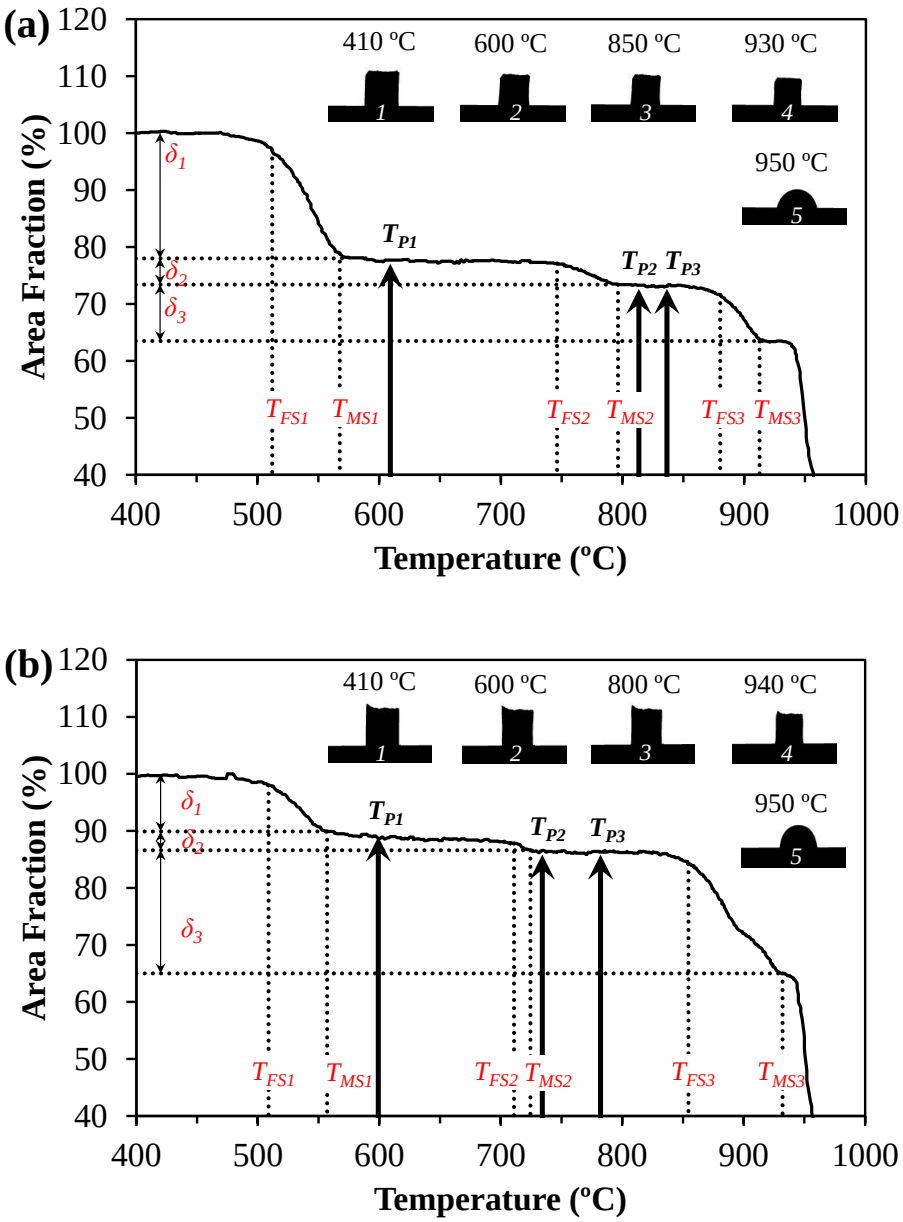

Figure 3.4.4 HSM curves for glass powder compacts (a) GB_{50} and (b) GB_{100}. Insets correspond to HSM micrographs: (1) initial, (2) – (4) after 1st, 2nd and 3rd shrinkages respectively and (5) half ball point.

3.4.3.3 Thermodynamic Analysis

The Gibbs free energy–composition curve for Li_2O–SiO_2 binary liquid was calculated from 0–36 mol. % of Li_2O according to the procedure given by Charles[47] employing extrapolation of Li_2O–SiO_2 phase diagram of Kracek[183] (Section 3.4.5.6). Because the *LS* and LS_2 phases are stoichiometric compounds, they were assumed as points on the free energy–composition diagram (**Figure 3.4.12**). However this is an

approximation because both *LS* and LS_2 are known to exhibit an extended range of solid solutions.[181] Tangents drawn through the points of *LS* and LS_2 to liquid curve, which meet at ≈0.00 mol. % of Li_2O, and are shown along with the liquid curve for temperatures 600 and ~800 ºC in **Figure 3.4.5a and b**.

The Li_2O–SiO_2 phase diagram is redrawn based on the experimental data by Kracek[183] (**Figure 3.4.11**). The crystal–liquid equilibrium lines were extrapolated in order to give the liquidus temperature at non-equilibrium conditions. For a binary Li_2O–SiO_2 system at SiO_2/Li_2O ratio of experimental glasses, this liquidus temperature was obtained to be 997 ºC based on these extrapolations. The thermodynamic liquidus temperatures (T_L) for experimental glass compositions GB_0 and GB_{100} were calculated from DTA according to the procedure suggested by Ferreira *et al.*[195] and are presented in **Table 3.4.2** (**Figure 3.4.13**). These T_L values should correspond to the liquidus points where LS_2 and liquid phases are in equilibrium. Addition of charge compensated oxides of Al and B corresponding in compositions GB_0 and GB_{100} resulted in a 25 and 35 ºC drop of this T_L value, respectively.

The influence of dopants on the binary free energy-composition curve at any composition *x* in the $xLi_2O - (1–x)SiO_2$ system was estimated by deriving an equation. This equation takes the following form,

$$\Delta G^{mix,Multi} \approx (1-c)\left[\Delta G^{mix,binery}(x)\right] + RTg(x,c) \qquad \text{Eq. (3.4-2)}$$

Here, c is total amount of the dopants added to the binary system $\Delta G^{mix,Multi}$, is the final free energy after the addition of dopants as a function of composition, $\Delta G^{mix,binery}$ is the change in the free energy due to the mixing of xLi_2O and $(1–x)SiO_2$ for a binary system and $g(x,c)$ is the associated change due to the addition of dopants. The detailed derivation of Eq. (3.4-2) is presented in supplementary information (Section 3.4.5.8) and we would like to emphasise that this equation is only valid for small concentrations of dopants. The activities of LS_2 (a_{LS_2}) component were calculated in all the compositions based on the drop in the T_L value. The equation was derived based on the freezing point depression and takes the form,

$$ln\left(a_{LS_2}\right) = \frac{1}{R}\left[\left(-\Delta H^{o}_{fus} + P\right) \times \left(\frac{1}{T} - \frac{1}{T_{fus}}\right) + Q\right] \qquad \text{Eq. (3.4-3)}$$

Where,

$$P = AT_{fus} + \frac{B}{2}T_{fus}^2 + \frac{C}{3}T_{fus}^3 + \frac{D}{4}T_{fus}^4 - \frac{E}{T_{fus}} \qquad \text{Eq. (3.4-4)}$$

$$Q = Aln\left(\frac{T_L}{T_{fus}}\right) + \frac{B}{2}(T_L - T_{fus}) + \frac{C}{6}(T_L^2 - T_{fus}^2) + \frac{D}{12}(T_L^3 - T_{fus}^3) + E\left(\frac{1}{T_L^2} - \frac{1}{T_{fus}^2}\right) \qquad \text{Eq. (3.4-5)}$$

Here, R is the gas constant, ΔH_{fus}^o and T_{fus} are the heat and temperature of fusion for pure LS_2 phase respectively and A to E are the constants derived from the difference in specific[196] heats between solid and liquid LS_2. The detailed derivation of Eq. (3.4-3) is presented in the supplementary information (Section 3.4.5.9).

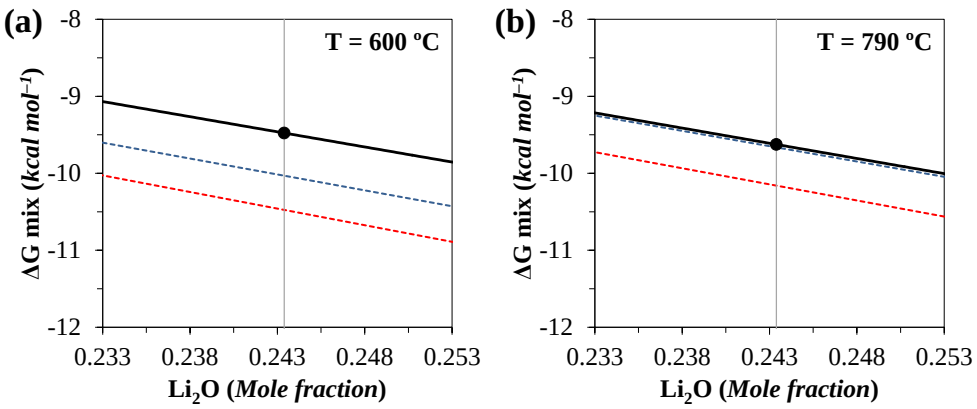

Figure 3.4.5 Free energy–Composition diagrams of binary Li_2O–SiO_2 system. ——— : $\Delta G^{mix,binery}$ of liquidus; - - - - : tangent between liquidus and LS_2; - - - - : tangent between liquidus and LS; ● : Liquidus point of the experimental compositions.

3.4.4 Discussion

3.4.4.1 Occurrence of Lithium Metasilicate Phase

In all *GC*s three crystalline phases were evident, viz. *LS*, LS_2 and polymorphs of SiO_2 (**Figure 3.4.2 & Figure** 3.4.8). Even though all glass compositions had excess SiO_2 compared to stoichiometric LS_2, the crystallization of *LS*, a phase rich in Li occurs at lower temperatures. The reason for the occurrence of this metastable crystalline phase

can be explained from the thermodynamics. According to the free energy–composition diagrams of the binary Li_2O–SiO_2 system (**Figure 3.4.5a and b**), within the range where the experimental compositions lie and for temperatures ≤ 800 ºC there is always a driving force for the crystallization of both *LS* and LS_2. The magnitudes of these driving forces for both *LS* and LS_2 approach a close value as the temperature is decreased. Thermodynamically, at lower temperatures there would be always some equivalent probability for the formation of both *LS* and LS_2 phases in a non-stoichiometric composition. This explains why even in the binary non-stoichiometric system *LS* phase experimentally occurred at lower temperatures (**Figure 3.4.7**). However, this probability would be greatly decreased with increasing temperatures. The formation of this *LS* phase has a technological interest, and is been utilized in the processing LS_2–based machinable dental *GC*s.[197]

3.4.4.2 Influence of Dopants on Crystallization process

Addition of charge compensated dopants as Al and B oxide units would affect the overall free energy of the system. At any composition *x* in the ternary $x Li_2O - (1–x) SiO_2$ system, the change in the overall free energy is described by Eq. (3.4-2). Here, the term $g(x, c)$ which is the contribution from the addition of dopants, is a constant value for a given total amount of dopant *c* since the dependence on *x* is small for a small c. This term $g(x, c)$ would have both enthalpic and entropic influences on it. The entropic contribution would always have a negative effect and thereby decrease the $\Delta G^{mix,Multi}$ value. On the other hand, enthalpic contributions could be either negative or positive and thus affect the $\Delta G^{mix,Multi}$ term by decreasing or increasing it respectively. Thus the net effect of adding dopants is a constant positive or negative value of $g(x, c)$ that would shift the binary curve ($\Delta G^{mix,binery}$) positively or negatively. For a negative shift there would be less driving force for the crystallization; conversely for a positive shift, a greater driving force. Adding Al_2O_3 and B_2O_3 into silicate melts has a negative and a positive contribution to the enthalpy, respectively.[179,198,199] Because of this reason Al_2O_3 when added to silicate glasses is incorporated into the glass network; while B_2O_3, after certain concentration separates into another phase.[177] However, both Al_2O_3 and B_2O_3 have a positive contribution to the entropy to the system; leading to a negative effect on $g(x, c)$. In our previous study[193], we observed experimentally that at small concentration, the enthalpic contributions are small and the state of the system is mainly

driven by entropy. This means the term $g(x,c)$ is always negative for all compositions and in case of mixed Al and B compositions, it is more negative because of much greater entropy. Therefore, the thermodynamic driving force with the B_2O_3 substitution goes through a minimum.

Adding Al and B oxides should lead to the decrease in the overall kinetics of crystallization since a large extent of atomic rearrangements would be needed, requiring higher thermal energies. However, at a very small scale there would be in-homogeneities in the composition due random distribution of Li^{+1} ions in the glass leading to Li-rich and Si-rich regions. Therefore, in these Li-rich regions with depolymerized Si units, kinetically it would be more favourable for the crystallization of *LS* phase to occur. Furthermore, our previous investigation[193] of the current compositions by NMR spectroscopy elucidated that, Al and B tetrahedra preferentially coordinated to highly polymerized Si units. Therefore, this leaves the depolymerized network free from dopants. Thus, it is easier for the liquid to crystallize in (i) depolymerized (Q^2) and dopants free regions rather than in (ii) polymerized (Q^3 or Q^4) dopant containing regions. In regions of (ii) higher thermal energies would be needed for the crystallization to occur.

Therefore simultaneous effect of small driving force for the formation *LS* and the kinetic restriction for the crystallization of LS_2 result in the profound occurrence of *LS* phase whenever dopants are added. This explanation could be generalized to many multi component non-stoichiometric glass systems which report the occurrence of *LS* phase.[200–203]

3.4.4.3 Crystallization and Sintering Sequence

In the current glass compositions, as the temperature is increased above T_g, the system continuously gains thermal energy to undergo a transformation from its liquid state to all the possible crystalline states (*LS*, LS_2 and SiO_2) (**Figure 3.4.1**). However, though there would be a greater driving force for the crystallization of LS_2 and polymorphs of SiO_2, there will be kinetic restriction for the crystallization of these phases because of the reasons discussed in the previous section. Thus, *LS* phase with small driving force crystallizes with the available Q^2 units. The activation energies for the crystallization of the *LS* phase are presented in **Table 3.4.2** for each composition. These values go through a maximum with increasing B_2O_3 substitution. This particular

trend in the kinetic activation energies could be attributed to the thermodynamic driving forces; which also go through a minimum. Since the total concentration of dopants is the same in all the glass compositions, we can expect similar kinetic restrictions in all glasses. But this is not completely true because of their differences in terms of intermolecular interactions. However, these interactions play a minor role as the changes in the system are mainly entropy driven.[193] The presence of both Al and B together provokes larger entropy, consequently leading to stable liquid phase with less free energy, and thus there is less driving force for crystallization. Therefore, the trend in the activation energies is the manifestation of the trend in thermodynamic driving forces; similar correlation was also found by others.[204]

As the temperature is further increased, the driving force for the *LS* crystallization decreases eventually ceasing. This leaves the residual liquid at a composition richer in the concentration of Al or B oxides. With further increments in the temperature to greater than ~800 ºC, the *LS* phase would no longer be stable. At this stage the existing *LS* phase can either transform to LS_2 by taking SiO_2 or rejecting Li_2O (reactions (6) and (7)); or it could dissolve back into the liquid phase as given by reaction (8).

$$Li_2SiO_{3_{(cr)}} + SiO_{2_{(liq)}} \leftrightarrow Li_2Si_2O_{5_{(cr)}} \qquad \Delta H = -12\ kJ\ mol^{-1} \qquad \text{Eq. (3.4-6)}$$

$$Li_2SiO_{3_{(cr)}} \leftrightarrow \frac{1}{2}Li_2Si_2O_{5_{(cr)}} + \frac{1}{2}Li_2O_{(liq)} \qquad \Delta H = +65\ kJ\ mol^{-1} \qquad \text{Eq. (3.4-7)}$$

$$Li_2SiO_{3_{(cr)}} \leftrightarrow Li_2O_{(liq)} + SiO_{2_{(liq)}} \qquad \Delta H = +152\ kJ\ mol^{-1} \qquad \text{Eq. (3.4-8)}$$

The reaction Eq. (3.4-6) is exothermic, whereas the reactions Eq. (3.4-7) and Eq. (3.4-8) are endothermic (obtained from thermochemical tables[196]). Since no peaks were registered in DTA experiments in the range of 800 ºC, it is likely that reactions (6) to (8) require higher thermal energies. Furthermore, XRD results of quenched samples (**Figure 3.4.8**) still showed presence of *LS* phase at same amounts even after the end of second crystallization event (**Figure 3.4.1**). This strongly confirms that *LS* phase did not transform (reaction (6) & (7)) or dissolve back into the liquid (reaction (8)). However, during the isothermal heat treatments for the preparation of *GC*s, the *LS* phase vanishes at higher temperatures (**Figure 3.4.2**), strongly suggesting that the reactions (6), (7) & (8) are kinetically slow and require higher thermal energies.

Further increasing the temperature provides sufficient thermal energies for the crystallization of LS_2 phase. However, at this stage Al and B oxides are no longer dopants in the liquid phase but have significant concentrations in the remaining glassy matrix. As a result there will be significant enthalpic contributions from Al and B oxides to the $g(x,c)$ term (Eq. (3.4-2)). Since B_2O_3 has a positive contribution to the enthalpy, it would increase the overall free energy of the liquid phase. As a result, with B_2O_3 substitution, there would be much greater driving force for crystallization leading to lower thermal activation energies. Therefore, the kinetic activation energies for the crystallization of LS_2 phase (**Table 3.4.2**) show a continuously decreasing trend with B_2O_3 substitution. Additionally, there would be one more contribution to the decreasing E_{C2} values, which is the slight depolymerisation of the glass network because the substituted B units go into the glass network as both 3– and 4–coordinated B units (B^{III} and B^{IV}). This converts the charge compensating oxide into a network modifying oxide, thus decreasing the viscosity. At room temperature the glasses showed equal concentrations of B^{III} and B^{IV} units.[193] However, at higher temperatures the equilibrium could shift more towards B^{III} units,[205,206] creating even more non-bridging oxygens leading to less viscosity. The occurrence of third crystallization peak in GB_{50} to GB_{100} (**Figure 3.4.1**) could also be associated with this decreased viscosity. It is also possible that, due to the increased B_2O_3 concentrations in the liquid phase at the end of the first crystallization, could lead to immiscibility of B_2O_3. This would leave the silicate liquid phase free from dopants with less kinetic restrictions, thus lowering the activation energies. However, this argument is questionable because alkali borosilicate systems do not show any immiscibility at temperatures above 750 ºC.[46,177] Therefore at high temperatures B_2O_3 should still be present in the liquid phase without separating out.

At temperatures greater than 900 ºC all compositions showed melting (**Figure 3.4.1**). This broad endothermic peak could have contributions from both LS and LS_2 phases because each DTA curve shows a small shoulder. Therefore, this suggests that the LS phase might have disassociated according to the reactions Eq. (3.4-7) or Eq. (3.4-8). This argument is supported by the **Figure 3.4.8** where, there is a reduction in the LS content in the beginning of the endothermic peak. The liquidus temperatures measured from the DTA corresponding to the melting of LS_2 decreases from 972 to 962 ºC with B_2O_3 substitution. This depression in the freezing point is associated with different activities of LS_2 phase. With the substitution of B_2O_3 the activities decrease.

The sintering behaviour studied by HSM presented in **Figure 3.4.4** and **Table 3.4.3** shows that all glass composition started to sinter (T_{FS1}) at ~510 ºC; temperature just above T_g which is ~500 ºC for all compositions (**Table 3.4.3**). However, the sintering was interrupted (T_{MS1}) by the first crystallization event (*LS* phase corresponding to T_{P1}). The decreasing values of T_{MS1} with increasing added amounts of B_2O_3 are in accordance with values of T_{P1}. Since activation energies for the crystallization of *LS* go through a maximum with B_2O_3 substitution (**Table 3.4.2**), the amounts of *LS* phase that can crystallize go through minimum. As a consequence, in mixed Al and B compositions there will be less hindrance towards first sintering and the extents of shrinkage (δ_1) follow a trend similar to E_{C1} values. The second sintering event started (T_{FS2}) after the end of first crystallization event and again is interrupted by the second crystallization event (T_{P2}). The values of E_{C2} and T_{P2} decrease with B_2O_3 substitution and accordingly the values of δ_2 and T_{MS2} also decrease. Because of a large E_{C2} value for the sample GB_0, the second crystallization event caused extremely small interruption[144] to the sintering process, subsequently leading to a large δ_2 value (**Table 3.4.3**). Whereas for samples GB_{50} and GB_{100} lower E_{C2} values combined with the third crystallization event (T_{P3}) resulted in a significant interruption to the sintering leading to a plateau region. At the end of all the crystallization events samples GB_{50} and GB_{100} undergone final sintering event (T_{FS3}) until full densification is reached (T_{MS3}).

3.4.4.4 Sintered Glass-Ceramics

Glass-ceramics showed various crystalline phases when sintered isothermally at different temperatures (**Figure 3.4.2**). Samples GB_0[144], GB_{25} and GB_{50} still have the presence of metastable *LS* phase even after sintering for 1 h at 800 ºC. This suggests that in Al_2O_3 rich compositions the conversion of *LS* to LS_2 (for example giving by Eq. (3.4-3)) is kinetically very slow. This transformation becomes faster with B substitution with no presence of *LS* in GB_{75} and GB_{100}. As discussed earlier, the faster kinetics for the formation of LS_2 with B_2O_3 substitution is associated with the slight depolymerisation of the silicate network due to B speciation; apart from a large driving force. In a binary system, at temperatures below 1470 ºC, the stable SiO_2 polymorph is tridymite. But in the current sintered *GC*s the main SiO_2 crystallized polymorph was quartz; also with small amounts of cristobalite. In the samples GB_{75} and GB_{100} prepared at 900 ºC however, the quartz was converted to tridymite.

The sintered *GC*s exhibited various microstructural morphological aspects as presented in **Figure 3.4.3**. The glass powders used for the sintering had average particle sizes ranging between 8–12 μm. **Figure 3.4.3a** captures these particles after sintering which look like aggregates of large crystals; and all glass compositions showed this kind of morphological feature. Inside these particles, the extent of nucleation is limited, leading to concurrent formation of large size crystals. Whereas, at the boundaries of these particles, there is a viscous region during sintering where, increased surface area resulted in increased crystal nucleation, eventually resulting in a large number of small crystals. Also the porosity is associated along the boundaries of these particles. The contrast in all the SEM images was obtained by etching with hydrofluoric acid. Since all the glass compositions are SiO_2 rich, compared to LS_2 stoichiometry, the residual glass after the crystallization of LS_2 became even richer in SiO_2. The degree of etching for each phase would therefore be in the decreasing order for *LS*, LS_2, residual glass (SiO_2 rich) and SiO_2 (crystal), respectively. Therefore, the quartz and tridymite crystals (in **Figure 3.4.3a and b**, respectively) appear protruded from the surface while LS_2 crystals appear caved in. The both SiO_2 phases which are quartz and tridymite showed different crystal morphologies.

Table 3.4.4 presents some physical properties of *GC*s. The densification degree is clearly enhanced with increasing sintering temperature as deduced from the concomitant increases in density and shrinkage. This general trend is not completely followed by the sample GB_{100} that reached maximum density and shrinkage values upon sintering at 850 ºC, followed by decreases with further raising the temperature to 900 ºC. These decreases are associated with the conversion of the dense quartz to less dense tridymite phase. The same effect is not visible for GB_{75} prepared at 900 ºC which also contains tridymite due to its small amounts. The bending strengths of the *GC*s depend both on the densification degree (absence of pores) and crystalline phase content. For *GC*s prepared at 800 ºC, with B_2O_3 substitution the crystalline phase content increases and changes from predominantly *LS* to LS_2. While the densification goes through a maximum because at the low heating rate (2 ºC min^{-1}) the samples got sintered mainly at lower temperatures. Densification is less hindered by crystallization in samples containing mixed Al and B oxides and they sintered better accordingly. It is likely that the low values of bending strengths for B_2O_3 rich compositions are associated with SiO_2 phase transition leading to some micro-cracks.

3.4.5 Supplementary Information

3.4.5.1 Preparation of glasses

X-ray diffractograms of as prepared glass samples are presented in **Figure 3.4.6**; show all the samples are completely amorphous

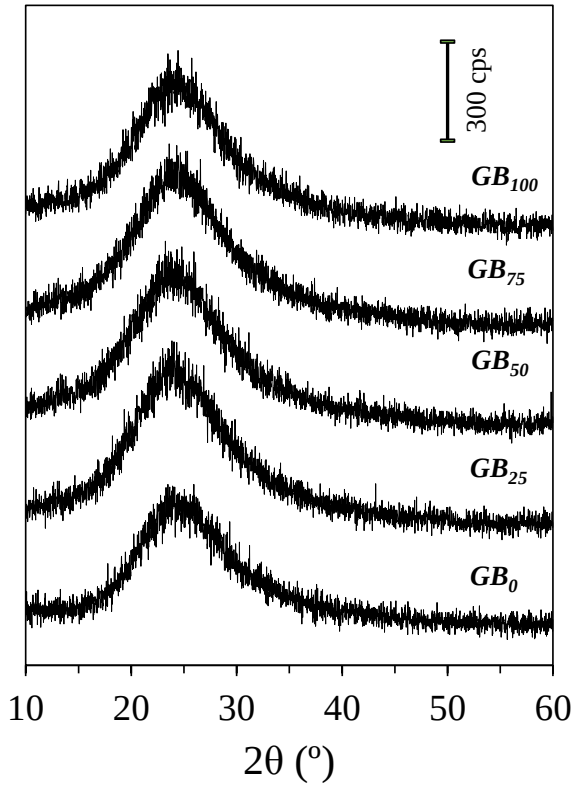

Figure 3.4.6 X-ray diffractograms of glass powders.

3.4.5.2 Occurrence of Li_2SiO_3 phase

Figure 3.4.7 shows the glass powder of non-stoichiometric lithium silicate heat treated at 550 ºC. The chemical composition of this sample named as $L_{23}S_{77}$ is $23Li_2O–77SiO_2$ (mol. %). The X-ray diffractograms clearly shows small occurrence of metastable *LS* phase. There is also another phase showing a peak at $2\theta \approx 22.5º$; probably related to some SiO_2 polymorph.

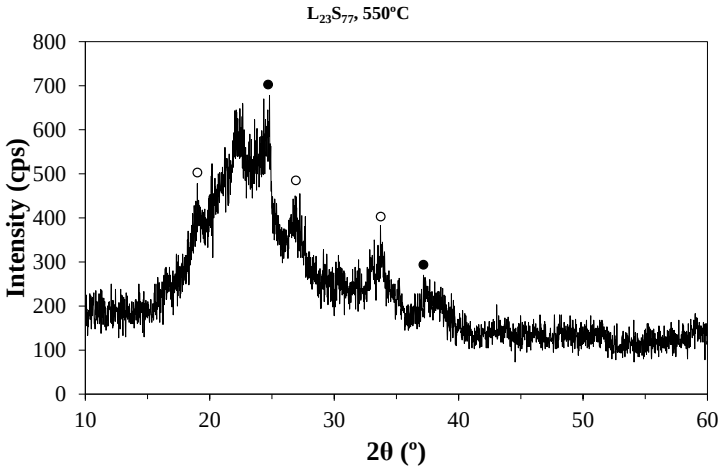

Figure 3.4.7 X-ray diffractograms of $L_{23}S_{77}$ heat-treated at 550 ºC. [●: Lithium disilicate ($Li_2Si_2O_5$, ICDD 04-009-4359); ○: Lithium metasilicate (Li_2SiO_3, ICDD 00-029-0828)].

3.4.5.3 Crystallization events encountered in DTA

The DTA curves in the manuscript (**Figure 3.4.1**) show 2 or 3 crystallization peaks for each sample. The crystalline phases corresponding to each crystallization event in DTA were identified by XRD. The samples were prepared by air quenching them at the end of each crystallization event (T_{P1}, T_{P2} and T_{P3}). **Figure 3.4.8** shows the diffractograms for samples at heating rate of 20 ºC min^{-1}. Same procedure was employed for heating rate of 10 ºC min^{-1} and similar results were obtained.

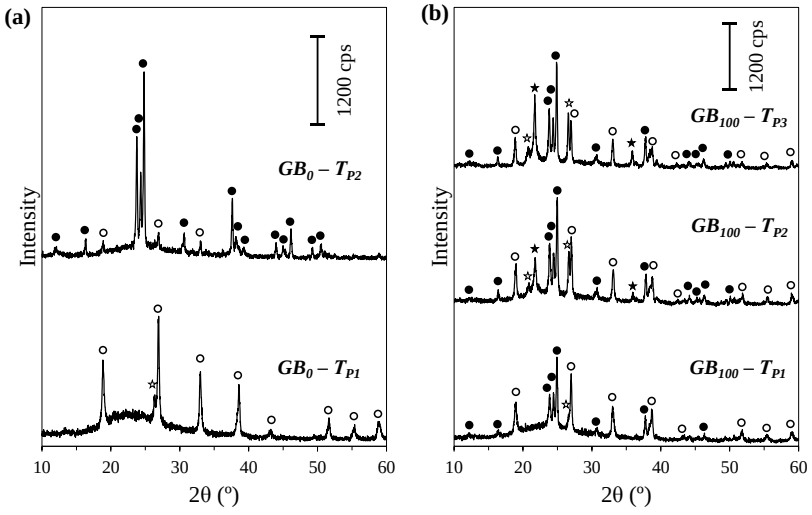

Figure 3.4.8 Crystalline phases corresponding to crystallization peaks in DTA (20 ºC min^{-1}) for (a) GB_0 and (b) GB_{100}. [●: Lithium disilicate ($Li_2Si_2O_5$, ICDD 04-009-4359); ○: Lithium metasilicate (Li_2SiO_3, ICDD 00-029-0828); ☆ : Quartz (SiO2, ICDD 01-075-8321) ; ★ : Cristobalite (SiO_2, ICDD 01-082-0512)].

3.4.5.4 Kissinger plots for crystallization kinetics

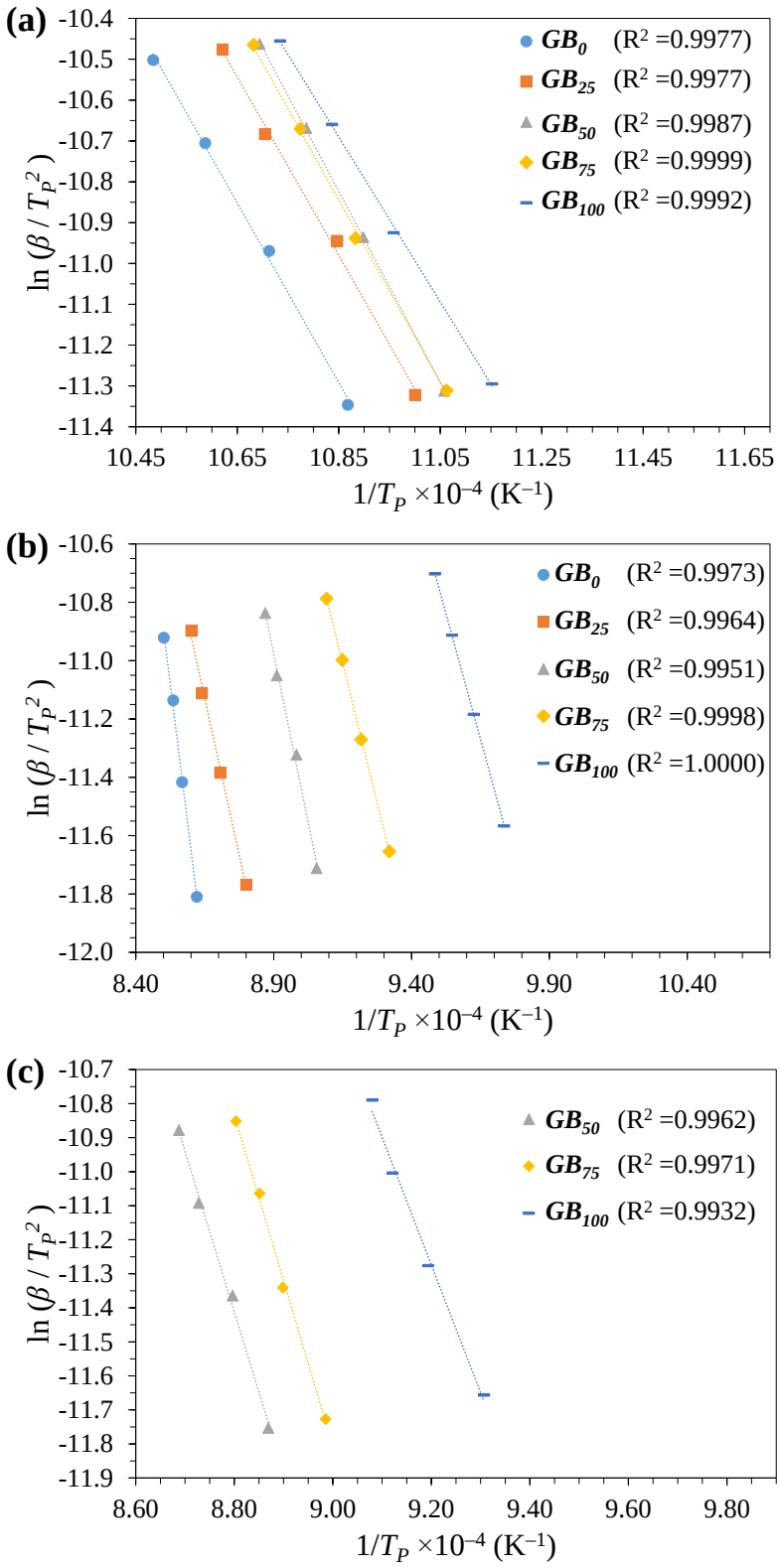

Figure 3.4.9 Plots for the Kissinger model for (a) T_{P1}, (b) T_{P2} and (c) T_{P3}.

3.4.5.5 DTA plots at 5 ºC min–1

Figure 3.4.10 shows DTA plots of the experimental compositions collected from room temperature to 800 ºC; these are used for comparison with HSM data. Peaks obtained from the experimental data shows good agreement with the peaks derived from the Kissinger method. Therefore for peaks at temperatures > 800 ºC, since experimental data is not available, they were derived from the Kissinger method.

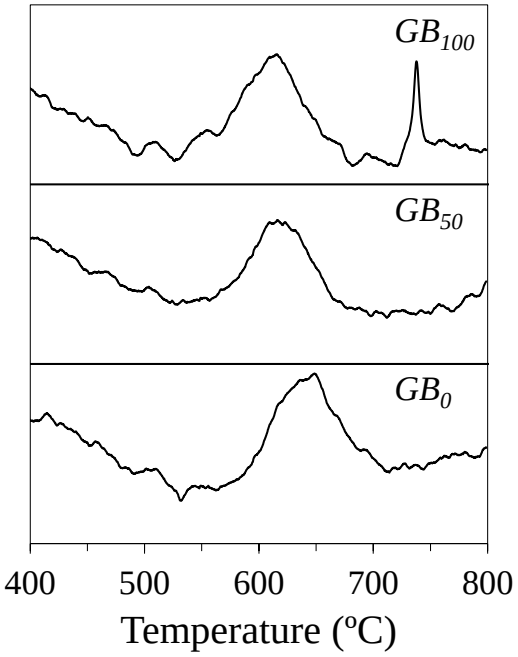

Figure 3.4.10 DTA plots at β = 5 ºC min^{-1}.

3.4.5.6 Calculation free energy vs composition diagrams

In order to calculate the free energy vs composition diagram of binary system, the procedure suggested by Charles[47] was employed. The procedure uses freezing point depression for calculating activities of SiO_2. The Li_2O–SiO_2 phase diagram is constructed based on the data given by Kracek[183] and presented in **Figure 3.4.11**. The equilibrium lines were obtained by fitted data points with polynomial functions represented as $T^c(x)$; x represents the chemical composition in $x\mathrm{Li_2O} - [1-x]\mathrm{SiO_2}$. These polynomial functions are then extrapolated to 500 ºC shown as dotted lines in **Figure 3.4.11**; while the blue line represents the equivalent binary composition of the experimental glasses.

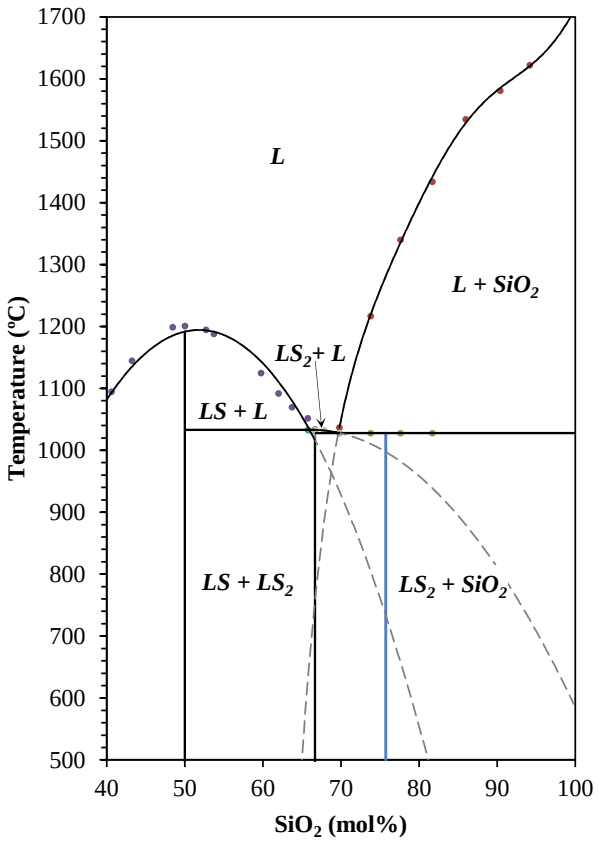

Figure 3.4.11 Li_2O–SiO_2 phase diagram (dots: data from Kracek[183]).

The free energy–composition diagrams were calculated from x = 0.00 to 0.36 are presented in **Figure 3.4.12**. Assuming no formation of solid solutions for LS_2 and LS they were shown by dots.

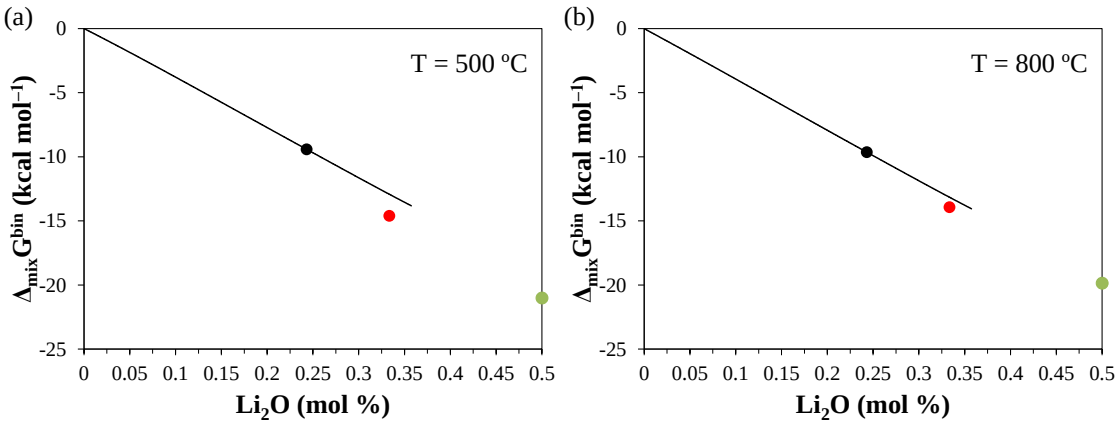

Figure 3.4.12 Free energy–composition diagram of the liquid of the binary Li_2O–SiO_2 system at (a) 500 and (b) 800 ºC. The dots represent molar free energies of, (●) equivalent binary composition of liquid phase, (●) LS_2 and (●) LS.

3.4.5.7 Liquidus temperatures

The liquidus temperatures were determined by the method suggested by Ferreira *et al.*[195] The values for GB_0 and GB_{100} were obtained to be 1245 K (972 ºC) and 1235 K (962 ºC) respectively. **Figure 3.4.13** shows the plots with fitting parameters used for these calculations. The rest of the values are presented in **Table 3.4.2**.

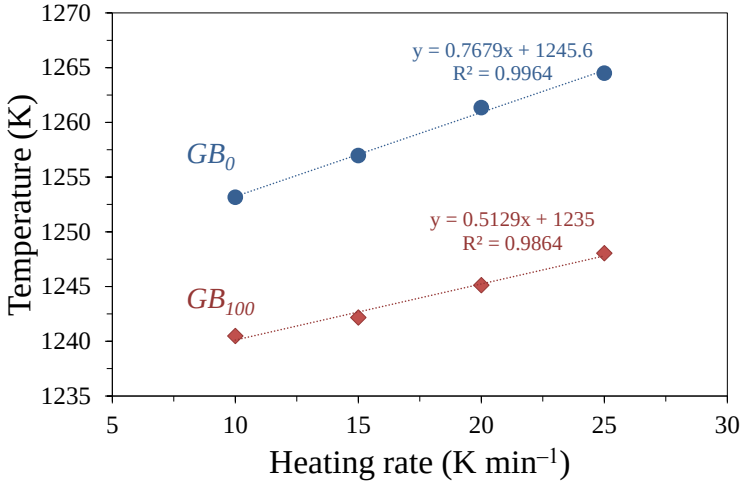

Figure 3.4.13 Determination liquidus temperatures for samples.

3.4.5.8 Influence of dopant

In this we derive the change in free energy due to small addition of dopants. For a binary system the change in free-energy of the system due to mixing of individual components is given as,

$$\Delta G^{mix,binery} = RT\left(x_{Li_2O} \ln a_{Li_2O} + x_{SiO_2} \ln a_{SiO_2}\right) \qquad \text{Eq. (3.4-9)}$$

Where, x_i and a_i are the mole fraction and activities of the i^{th} component. By considering $x = x_{Li_2O}$, and $a_i = \gamma_i x_i$, Eq. (3.4-9) can be represented as,

$$\Delta G^{mix,binery} = RT\left(x \ln \gamma_{Li_2O} + (1-x) \ln \gamma_{SiO_2} + x ln(x) + (1-x) \ln(1-x)\right) \qquad \text{Eq. (3.4-10)}$$

In the case of small addition of N number of dopants to the binary system the change in free energy due to mixing can be represented by,

$$\Delta G^{mix,multi} = RT\left(x'_{Li_2O}\ln a'_{Li_2O} + x'_{SiO_2}\ln a'_{SiO_2} + \sum_{n=1}^{N} x'_n \ln a'_n\right) \quad \text{Eq. (3.4-11)}$$

Again if we write $x = \frac{x'_{Li_2O}}{x'_{Li_2O}+x'_{SiO_2}}$ and $c = \sum_{n=1}^{N} x'_n$; thus,

$$x'_{Li_2O} = x(1-c); x'_{SiO_2} = (1-x)(1-c) \quad \text{Eq. (3.4-12)}$$

All the new parameters in this multicomponent system are represented by a superscript ‘; and the parameters for dopants represented by subscript *n*. From Eq. (3.4-12) and relation $a'_i = \gamma'_i x_i$, Eq. (3.4-11) can be written as,

$$\Delta G^{mix,Multi} = RT\left((1-c)\left[x\ln\gamma'_{Li_2O} + (1-x)\ln\gamma'_{SiO_2} + x\ln x'_{Li_2O} + (1-x)\ln x'_{SiO_2}\right] + \sum_{n=1}^{N} x_n \ln\gamma'_n + \sum_{n=1}^{N} x_n \ln x'_n\right) \quad \text{Eq. (3.4-13)}$$

$$\Delta G^{mix,Multi} = RT\left((1-c)\left[x\ln\gamma'_{Li_2O} + (1-x)\ln\gamma'_{SiO_2} + x\ln x + (1-x)\ln(1-x)\right] + (1-c)\ln(1-c) + \sum_{n=1}^{N} x_n \ln\gamma'_n + \sum_{n=1}^{N} x_n \ln x'_n\right) \quad \text{Eq. (3.4-14)}$$

The activity coefficients are functions of composition and temperature *i.e.* ($\gamma_i(x,c,T)$). However for very small additions of dopants, it can be assumed that the system follows Henry’s law. Therefore the activity coefficients for Li_2O and SiO_2 shouldn’t be affected significantly. Therefore, $\gamma_{Li_2O} \approx \gamma'_{Li_2O}$ and $\gamma_{SiO_2} \approx \gamma'_{SiO_2}$; and the activity coefficients of the dopants would approach a constant value. Thus, from Eq. (3.4-10), Eq. (3.4-14) can be written as,

$$\Delta G^{mix,Multi} \approx (1-c)\left[\Delta G^{mix,binery}\right] + RT[(1-c)\ln(1-c) + \sum_{n=1}^{N} x_n \ln\gamma'_n + \sum_{n=1}^{N} x_n \ln x'_n] \quad \text{Eq. (3.4-15)}$$

The above equation is a general relation for any binary system with *N* different types of dopants added. In the current study it is Li_2O–SiO_2 system and, γ'_n would have a unique value for each dopant. The above equation can also be rewritten as,

$$\Delta G^{mix,Multi} \approx (1-c)\left[\Delta G^{mix,binery}(x)\right] + RTg(x,c) \quad \text{Eq. (3.4-16)}$$

If we assume that the values of γ'_n are independent of x in a small range, then $g(x, c)$ will have a unique value which is either positive or negative depending on the type of dopant. This will shift the entire binary free energy–composition curve by a small value positively or negatively.

3.4.5.9 Activities of LS2 at the liquidus

On the liquid–LS_2 equilibrium line from of the phase diagram (**Figure 3.4.11**), the chemical potentials of pure solid (μ_s^o) and liquid (μ_l) LS_2 are related as,

$$\mu_s^o = \mu_l \qquad \text{Eq. (3.4-17)}$$

$$\mu_s^o = \mu_l^o + RTln\left(a_{LS_2}\right) \qquad \text{Eq. (3.4-18)}$$

$$ln\left(a_{LS_2}\right) = \frac{\mu_l^o - \mu_s^o}{RT} = -\frac{\Delta G_{fus}^o}{RT} \qquad \text{Eq. (3.4-19)}$$

Here, $\mu_l{}^o$ is the chemical potential of pure liquid LS_2; a_{LS_2} is the activity of LS_2 in the solution. Differentiating Eq. (3.4-19) and applying Gibbs–Helmholtz equation gives,

$$\frac{d\left(ln\left(a_{LS_2}\right)\right)}{dT} = \frac{\Delta H_{fus}}{RT^2} \qquad \text{Eq. (3.4-20)}$$

By considering the changes in the specific heats,

$$\Delta H_{fus} = \Delta H_{fus}^o + \int_{T_{fus}}^{T} \Delta C_p dT \qquad \text{Eq. (3.4-21)}$$

Where, ΔC_p is the difference between the specific heats of liquid and solid; for which, values were obtained from the thermochemical tables[207] which takes the form,

$$\Delta C_p = A + BT + CT^2 + DT^3 + ET^{-2} \qquad \text{(S14)}$$

Where,

$A = 72$;

$B = -8.41 \times 10^{-2}$;

$C = 2.3 \times 10^{-5}$;

$D = -1.3 \times 10^{-9}$;

$E = 5.7 \times 10^{6}$;

Now, Eq. (3.4-20) can be written as,

$$\frac{d(\ln a_{LS_2})}{dT} = \frac{\Delta H^o_{fus} + \int_{T_{fus}}^{T} \Delta C_p dT}{RT^2} \qquad \text{Eq. (3.4-22)}$$

Integrating,

$$\int_1^{a_{LS_2}} d\left(ln(a_{LS_2})\right) = \int_{T_{fus}}^{T} \frac{\Delta H^o_{fus} + \int_{T_{fus}}^{T} \Delta C_p dT}{RT^2} dT \qquad \text{Eq. (3.4-23)}$$

Solving the Eq. (3.4-23) gives the following equation,

$$ln(a_{LS_2}) = \frac{1}{R}\left[(-\Delta H^o_{fus} + P) \times \left(\frac{1}{T} - \frac{1}{T_{fus}}\right) + Q\right] \qquad \text{Eq. (3.4-24)}$$

Where,

$$P = AT_{fus} + \frac{B}{2}T_{fus}^2 + \frac{C}{3}T_{fus}^3 + \frac{D}{4}T_{fus}^4 - \frac{E}{T_{fus}} \qquad \text{Eq. (3.4-25)}$$

$$Q = Aln\left(\frac{T}{T_{fus}}\right) + \frac{B}{2}(T - T_{fus}) + \frac{C}{6}(T^2 - T_{fus}^2) + \frac{D}{12}(T^3 - T_{fus}^3) + E\left(\frac{1}{T^2} - \frac{1}{T_{fus}^2}\right) \qquad \text{Eq. (3.4-26)}$$

The activities of LS_2 for each composition can be obtained by substituting $T = T_L$ in Eq. (3.4-25) and Eq. **(3.4-26)**. The values of a_{LS_2} are,

GB_0: 0.78

GB_{25}: 0.78

GB_{50}: 0.77

GB_{75}: 0.75

GB_{100}: 0.75

3.5 The roles of P_2O_5 and SiO_2/Li_2O ratio on the network structure and crystallization kinetics of non-stoichiometric lithium disilicate based glasses

Anuraag Gaddam [a], Hugo R. Fernandes [a], Dilshat U. Tulyaganov [b], Manuel J. Ribeiro [c], José M.F. Ferreira [a]

[a] Department of Materials and Ceramics Engineering, University of Aveiro, CICECO, 3810-193 Aveiro, Portugal.

[b] Turin Polytechnic University in Tashkent, 17, Small ring , 100095, Tashkent, Uzbekistan.

[c] UIDM, ESTG, Polytechnic Institute of Viana do Castelo, 4900 Viana do Castelo, Portugal.

Journal of Non-Crystalline Solids, (Submitted)

Abstract

We report on the effects of SiO_2/Li_2O molar ratio and adding P_2O_5 on the structure and crystallization behaviour of multicomponent lithium disilicate based glasses under non-isothermal conditions. Two non-stoichiometric P_2O_5-free lithium disilicate glasses featuring equimolar contents of K_2O and Al_2O_3 and with SiO_2/Li_2O molar ratios varying between 2.62–2.92 were synthesized in the $Li_2O–SiO_2$ system through the melt-quench technique. The influence of partially replacing (K_2O + Al_2O_3) by P_2O_5 while keeping the same SiO_2/Li_2O molar ratios of P_2O_5-free counterpart glasses was also investigated. Differential thermal analysis was used to study crystallization kinetics of glasses; their structural features were assessed by nuclear magnetic resonance; and the crystalline phase evolution was followed by X-ray diffraction. The results showed that P_2O_5 enhances the formation of fine lithium disilicate crystals. However, an increase in SiO_2/Li_2O molar ratio has an opposite effect, decreasing the overall crystallization rate and preventing the formation of lithium disilicate.

3.5.1 Introduction

Glass-ceramics can be produced by melting glasses and converting the vitreous substances into fine-grained materials through controlled nucleation and growth of crystalline phases via heat treatment.[1,208] In particular, the $Li_2O–SiO_2$ system has attracted great interest since Stookey developed the first glass-ceramic material on the near stoichiometric lithium disilicate composition ($Li_2Si_2O_5$, hereafter named LS_2) [209]. After this, and during the last decades, the nucleation and crystallization in the binary $Li_2O–SiO_2$ system has been widely investigated.[210–213]

However, glass-ceramics derived from the binary system exhibit some unfavourable characteristics in terms of their mechanical and chemical properties which hinder their potential applications in several technological areas. Therefore, nonstoichiometric multicomponent compositions have been developed in order to improve the properties of *LS_2* glass-ceramics. For instance, the addition of Al_2O_3 and K_2O to the stoichiometric composition enhanced the chemical durability of the glasses.[53,191,192,214] Several other constituents such as ZnO, ZrO_2, CaO, V_2O_5, etc., have also been added to improve the properties of the final materials.[1,215,216] P_2O_5 has been introduced as nucleating agent playing an important role in phase formation and crystallization of *LS_2* glass-ceramics.[138,217] In addition, Beall and Echeverria[218,219] suggested that the SiO_2/Li_2O ratio is also a key success factor in the formation of the main crystal phase in a *LS_2* glass ceramic system.

The multicomponent *LS_2* based glass-ceramics exhibit promising thermal, chemical and mechanical properties and have been pointed out as potential candidates for various structural and functional applications (e.g. all-ceramic dental restorations, ceramic composites or ceramic-metal sealing).[1,142,143,202,220–223] But the crystal phase formation from multicomponent glasses is more complex than in the binary $Li_2O–SiO_2$ system. Moreover, the crystalline nature of the glass-ceramic products is largely affected by the type and amount of oxides present in the glass composition, including the nucleating agents such as P_2O_5, ZrO_2 or TiO_2.[1,139,141,151]

During the crystallization process of non-stoichiometric *LS_2* glass compositions, several authors suggested that lithium metasilicate ($LiSi_2O_3$, hereafter named *LS*) precedes *LS_2* formation[141,200,224] in contrast to what was observed in the stoichiometric

composition.[141,211] In particular, the crystallization process of non-stoichiometric *LS_2* glass compositions occurs in two stages: (1) *LS* crystallizes in the glass at lower temperatures (in the range of 650–700 ºC), and (2) *LS* reacts with SiO_2 to form *LS_2* at higher temperatures.[139,200] The mechanism of this behaviour was explained in our previous paper.[225]

The properties of the glass-ceramics depend upon the type of phases precipitated from the glasses, the extent of crystallization, crystal morphology, crystal size and aspect ratio. All these features are, in turn, dependent upon the composition of the parent glass (including the addition of nucleating agents) and thermal treatment.[1,226] Therefore, determining the parameters that control the mechanisms of nucleation and growth processes (e.g. kinetic parameters) is of major importance to obtain materials with the desired properties.[1,226] Although kinetic aspects of crystal growth have been extensively investigated in the simple non-stoichiometric Li_2O–SiO_2 binary system, [150,227] the crystallization kinetics in non-stoichiometric multicomponent *LS_2* glasses still needs to be studied.

The aim of the present work was to investigate the influences of SiO_2/Li_2O molar ratio (2.62 and 2.92) and of the added amount of P_2O_5 (1 mol%) on the structure and crystallization behaviour of non-stoichiometric multicomponent lithium silicate glasses based on the system Li_2O–K_2O–Al_2O_3–SiO_2 under non-isothermal conditions.

3.5.2 Experimental procedure

3.5.2.1 Synthesis

Four experimental compositions (**Table 3.5.1**) belonging to Li_2O–K_2O–Al_2O_3–SiO_2–(P_2O_5) system were prepared. Potassium from K_2O was used for charge compensating when Al_2O_3 partially replaces SiO_2 in the binary Li_2O–SiO_2 system, while P_2O_5 was incorporated as a nucleating agent. Powders of technical grade SiO_2 and reagent grade Li_2CO_3, K_2CO_3, Al_2O_3 and $(NH_4)_2HPO_4$ were used as precursors; all having a of purity > 99%. Batch compositions of 100 g were prepared by homogenously mixing the powdered raw materials in a ball mill, followed by calcination at 1073 K (800 ºC) for 1 h. Pt crucibles were used to melt the compositions at 1823 K (1550 ºC) for 1 h in air. Bulk (monolithic) glasses were prepared by pouring the melt on a bronze mould and allowed to cool at ambient temperature. Glasses were not subjected to

annealing in order to avoid any pre-nucleation and crystallization. The glass-ceramics (*GC*s) were prepared from small pieces of the bulk glasses by heating them first to a temperature of 823 K (550 ºC) for 1 h at 10 K min^{-1} in air (for nucleation) followed by heat treatment to temperatures between 873 K (600 ºC), and 1173 K (900 ºC) for 1 h at intervals of 100 K.

Table 3.5.1 Compositions of the experimental glasses and the compositions calculated from the NMR spectra in parenthesis (in mol %)

	Li_2O	K_2O	Al_2O_3	SiO_2	P_2O_5	SiO_2/Li_2O
G24	24.0 (26.0)	3.0 (2.9)	3.0 (2.9)	70.0 (68.1)	0.0 (0.0)	2.9 (2.6)
G24$_P$	24.0 (23.4)	2.5 (2.5)	2.5 (2.5)	70.0 (70.5)	1.0 (1.0)	2.9 (3.0)
G26	26.0 (28.7)	3.0 (2.9)	3.0 (2.9)	68.0 (65.5)	0.0 (0.0)	2.6 (2.3)
G26$_P$	26.0 (26.8)	2.5 (2.5)	2.5 (2.5)	68.0 (67.3)	1.0 (1.0)	2.6 (2.5)

3.5.2.2 Characterization

The network structure of the glasses was investigation by magic angle spinning nuclear magnetic resonance spectroscopy (MAS-NMR, Bruker ASX 400). All samples were crushed to fine powders and characterized in a 400 MHz (9.4 T) spectrometer working at Larmor frequencies of 79.5, 104.3 and 161.9 MHz and were excited by 90º, 45º and 10º pulses for ^{29}Si, ^{27}Al and ^{31}P nuclei respectively. 4 mm rotors for ^{27}Al and ^{31}P nuclei, and 7 mm rotors for ^{29}Si, were used. The MAS frequencies were 5, 14 and 12 kHz for ^{29}Si, ^{27}Al and ^{31}P nuclei respectively. The obtained spectra were deconvoluted using DMFIT program.[228] Fourier transform infrared spectroscopy (FTIR, model Mattson Galaxy S-7000) was carried out in the range of 300–1400 cm^{-1} with a resolution of 4 cm^{-1} on glass powders prepared by crushing the bulk glass. Samples for FTIR were prepared by mixing 1/150 (by weight) portion of the sample with KBr and hand pressed to obtain pellets.

Differential thermal analysis (DTA, Netzsch STA 409 EP, Germany) was carried out on all glass compositions obtained by crushing the bulk glass to particle sizes between 500−1000 μm (collected by sieving). DTA experiments were carried out in air from ambient temperature to ~1173 K (900 ºC) at heating rates α = 10, 15, 20 and 25 K min^{-1} using ~330 mg of sample in an Alumina crucible, with α-Alumina powder as reference material. The previously DTA-calibration is done using α-alumina pre-calcined at 1600°C in both crucibles and for each used heating rate. The results obtained

are then used to calibrate the DTA apparatus by comparison with an internal standard and to make the correction of the DTA-baseline curves using a polynomial function.

Microstructures of both glass and crystallized samples were recorded using scanning electron microscope (SEM, SU-70, Hitachi, Japan) and Stereo Microscope (Leica EZ4 HD). For which samples were polished and etched using 2 vol. % hydrofluoric acid for 60 s. Crystalline phase in the samples was identified by X-ray diffraction (XRD, Rigaku Geigerflex D/Mac, C Series, Japan) using Cu Kα radiation with 2θ varying from 10−60º at steps of 0.02 s^{-1}.

Densities of all bulk glasses were measured employing Archimedes principle by immersing the samples in ethylene glycol solution.

3.5.3 Results

All glass compositions were suitable for easy casting after melting for 1 h at 1823 K (1550 ºC), resulting in homogeneous and transparent bubble free glasses. The amorphous nature of the as-cast glasses was confirmed by XRD (**Figure 3.5.1**). Considering the high melting temperature, at which the lighter elements are prone to volatilization (such as Li in the current compositions), the determined weight losses upon melting the glasses were less than 0.2%. Such values are negligible, being within the limits of experimental errors.[8]

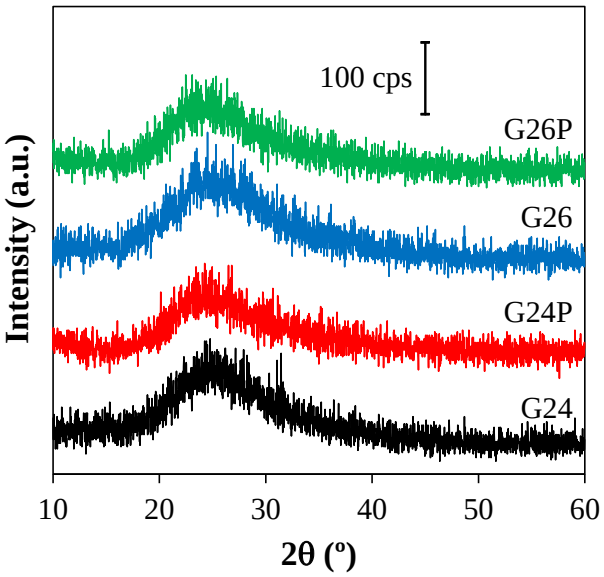

Figure 3.5.1 X-ray diffractograms of non-annealed bulk glasses.

3.5.3.1 MAS-NMR and FTIR spectroscopy

The deconvoluted ^{29}Si NMR spectra into three components of Q_2, Q_3 and Q_4 units are presented in **Figure 3.5.2**. Similarly, the deconvoluted ^{31}P NMR spectra into two components of $Q_{0(P)}$ and $Q_{1(P)}$ are presented in **Figure 3.5.3**. The corresponding NMR parameters of simulations and the relative amounts of each species are presented in **Table 3.5.2**. Due to the large amounts of network modifiers available to charge compensate $(AlO_{4/2})^-$ tetrahedra, the ^{27}Al NMR spectra (**Figure 3.5.4**) for all the glasses exhibit only a single peak at ~58 ppm, which corresponds to Al^{IV} species. The chemical shift was obtained by fitting a single line shape using Czejeck distribution,[156] and the corresponding quadrupolar coupling constant (C_Q) was 4.4 MHz.

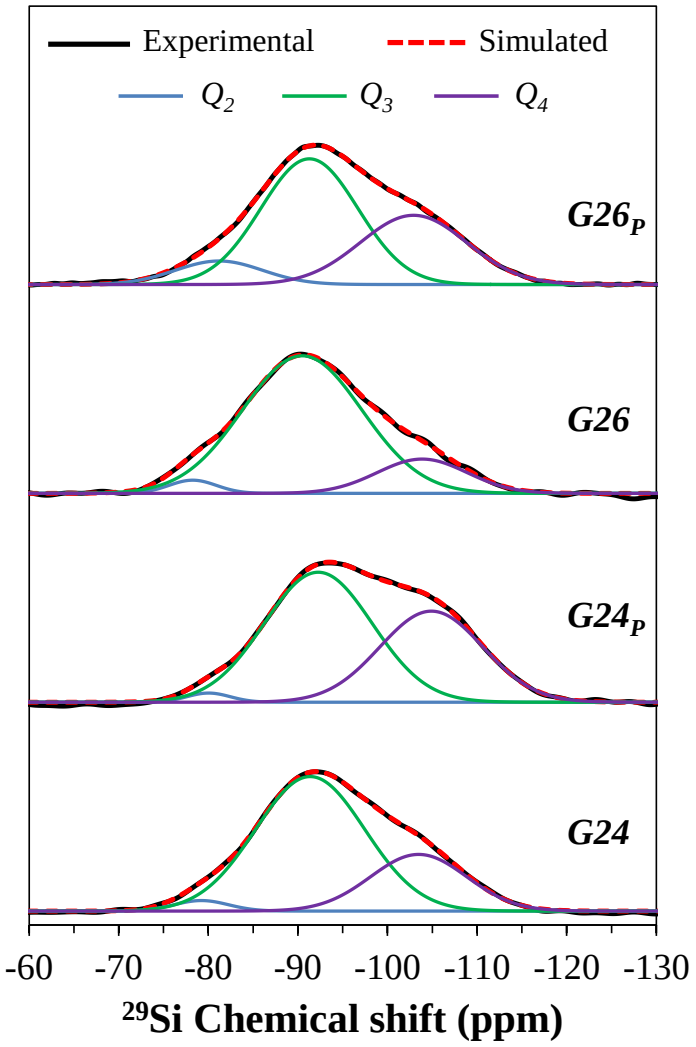

Figure 3.5.2 ^{29}Si NMR spectra and simulated lines of Initial glasses.

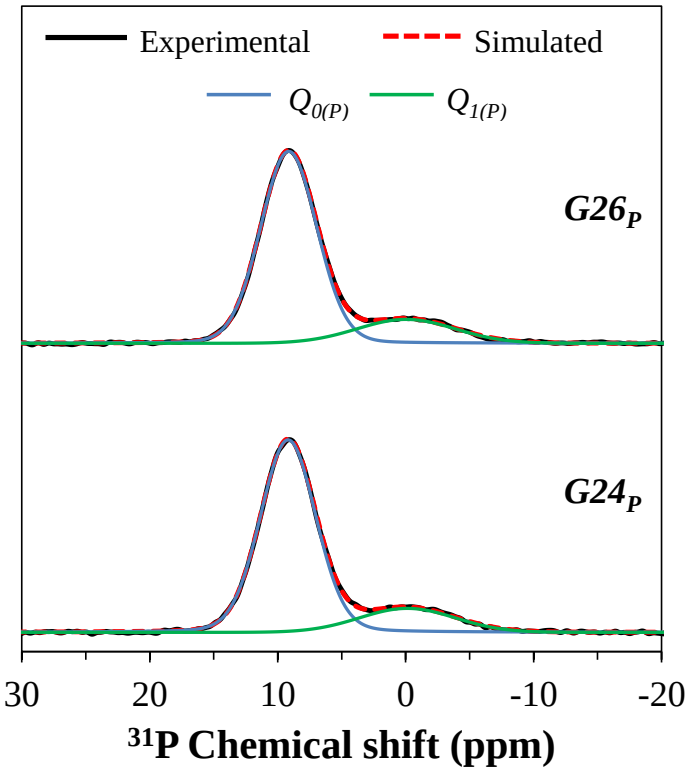

Figure 3.5.3 ^{31}P NMR spectra and simulated lines of initial glasses.

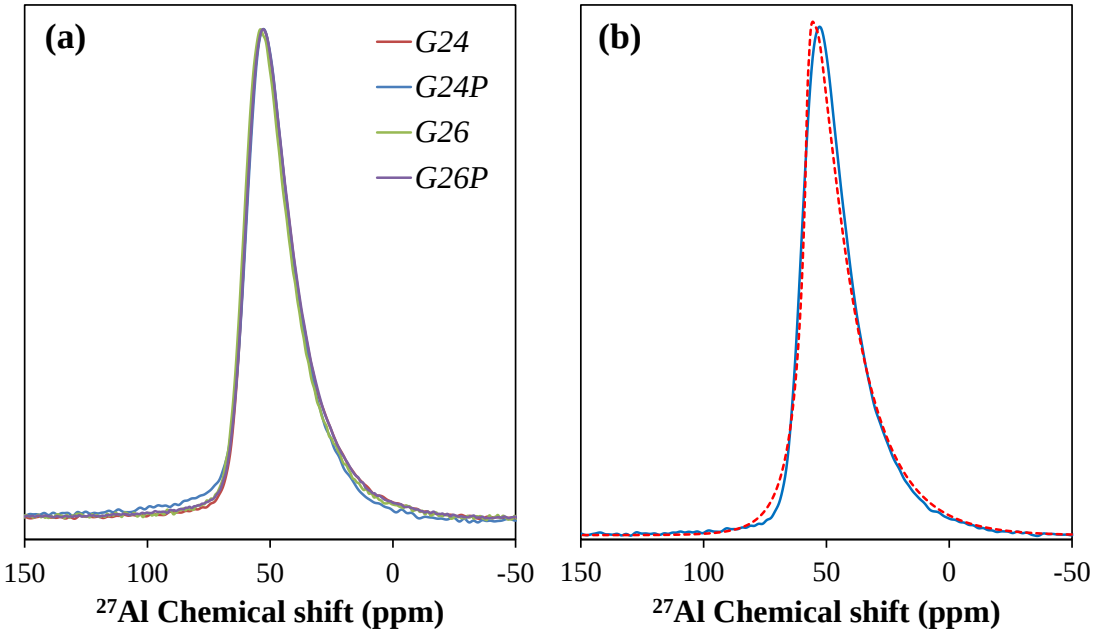

Figure 3.5.4 ^{27}Al NMR spectra initial glasses: (a) normalized spectra, and (b) spectra and simulated line for *G24*.

Table 3.5.2 NMR Parameters from simulation

				G24	***G24$_P$***	***G26***	***G26$_P$***
^{29}Si	***Q$_2$***	δ_{iso}	(ppm)	–79.2	–80.0	–78.3	–81.2
		FWHM		7.1	5.7	6.2	11.4
		Amount	(%)	2.7	1.7	3.1	9.5
	Q$_3$	δ_{iso}	(ppm)	–91.4	–92.3	–90.5	–91.3
		FWHM		14.4	14.2	15.7	12.8
		Amount	(%)	71.0	58.9	81.6	56.4
	Q$_4$	δ_{iso}	(ppm)	–103.5	–104.9	–103.9	–102.9
		FWHM		12.6	13.6	11.8	14.0
		Amount	(%)	26.3	39.4	15.3	34.1
^{31}P	***Q$_{0(P)}$***	δ_{iso}	(ppm)	–	9.2	–	9.1
		FWHM		–	5.1	–	5.2
		Amount	(%)	–	83.1	–	82.7
	Q$_{1(P)}$	δ_{iso}	(ppm)	–	–0.1	–	0.0
		FWHM		–	8.8	–	9.0
		Amount	(%)	–	16.9	–	17.3

***δ_{iso}**: Isotropic Chemical Shift*
***FWHM**: Full width at half maximum*

The FTIR spectra of the experimental glasses (**Figure 3.5.5**) show three absorption peaks at positions ~470, ~775 and ~1050 cm^{-1}, which correspond to the TO_1, TO_2 and TO_3 modes of vibrations, respectively.[114] Due to very small variations in the chemical compositions of the studied glasses, there are no noticeable differences in the spectra.

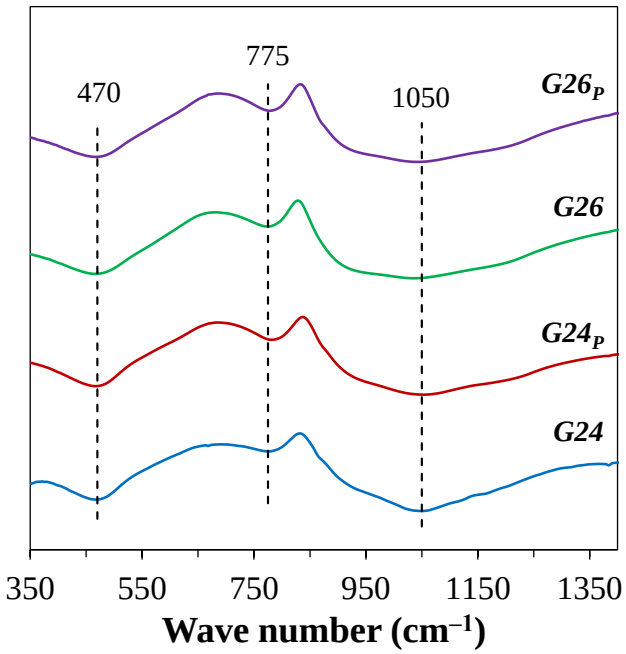

Figure 3.5.5 FTIR spectra of initial glasses.

3.5.3.2 Thermal analysis and crystallization kinetics

Figure 3.5.6 shows the DTA curves of all glasses performed at 20 K min^{-1} in air, while **Table 3.5.3** presents the values of the thermal parameters obtained for these glasses. It can be observed that there are no significant changes in the glass transition region with variation in the composition. However, with increasing Li content (from *G24* to *G26*) the peak crystallization temperature (T_p), which corresponds to *LS* phase shifts to lower values of temperature. The addition of P_2O_5 to both $G24_P$ and $G26_P$ glasses further stimulated the crystallization events (T_p) to occur at lower temperatures, while a second crystallization peak was also observed for these P_2O_5-containing compositions (**Figure 3.5.6**). This second peak can only be partially observed because the DTA experiment was run only up to 900 ºC. Further, this crystallization peak corresponds to LS_2 according to our previous studies.[225] Therefore, in the current study, only the first peak, which corresponds to *LS* phase, was studied for crystallization kinetics for all glasses.

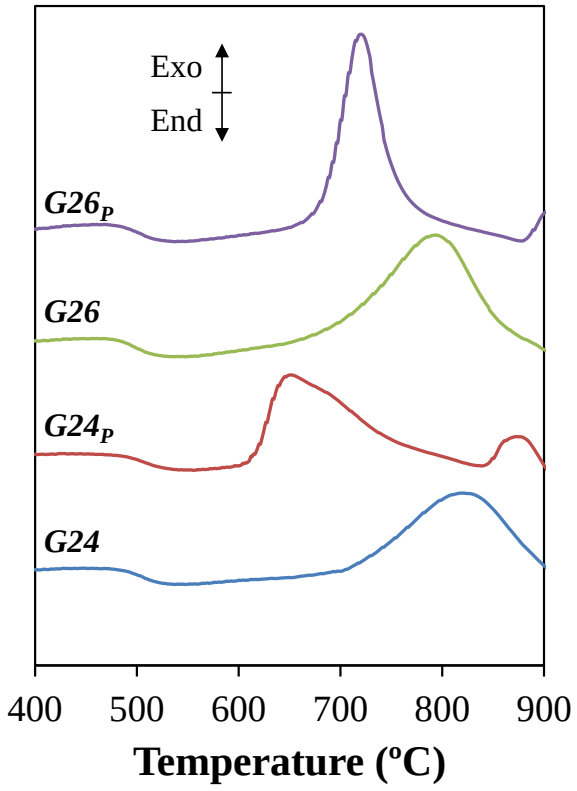

Figure 3.5.6 DTA of glass compositions at β = 20 K min^{-1}.

Table 3.5.3 Properties of the glasses

		G24	***G24$_P$***	***G26***	***G26$_P$***
Density	(g cm^{-3})	2.366	2.347	2.375	2.358
Molar volume	(cm^3 mol^{-1})	24.432	24.810	24.048	24.405
Oxygen density	(g cm^{-3})	1.149	1.151	1.154	1.157
NBO%	(%)	27.3	27.1	29.9	29.7
T_g	(ºC)	481	477	475	482
T_c	(ºC)	712	606	692	684
T_p	(ºC)	820	651	793	720
ΔT	(ºC)	231	129	217	202

In the present study, two kinetic models were used to evaluate kinetic parameters of the glasses: (1) Kissinger's Model [229] and (2) Matusita's Model [230]. The activation energy for crystallization (E_c) can be calculated using the Kissinger's equation given by

$$\ln\frac{\beta}{T_p^2} = -\frac{E_c}{RT_p} + const. \qquad \text{Eq. (3.5-1)}$$

Where β is the heating rate, T_p is the peak crystallization temperature and R is gas constant. Plotting the variation of $ln\ (\beta/T_p^2)$ as a function $1000/RT_p$ allows us to obtain a straight line, with slope equal to the activation energy of crystallization, E_c (in kJ mol^{-1}). The Avrami parameter n can be determined by a method proposed by Augis and Bennett [231] given by the equation

$$n = \frac{2.5}{\Delta T_{FWHM}}\frac{RT_p^2}{E_c} \qquad \text{Eq. (3.5-2)}$$

Where, ΔT_{FWHM} if full width at half maximum of the DTA exothermic peak and E_c is the activation energy as obtained from Eq (1). In Matusita's method, an equation relating crystallized volume fraction (x) with changing temperature (T) at a constant heating rate (β) is used to evaluate activation energy E_c. The equation is given by,

$$\ln[-\ln(1-x)] = -n'\ln\beta - 1.052\,m\,\frac{E_c}{RT} + const. \qquad \text{Eq. (3.5-3)}$$

Here m gives the dimensionality of crystal growth (an equivalent of Avrami's parameter n). And n' is the information of nucleation process: if $n' = m + 1$ no nuclei are present in the glass and if $n' = m$ sufficient number of nuclei are present in the glass.

The crystallized volume fraction was estimated from the DTA curves using the fraction of area under exothermic peak. To calculate this, the exothermic peaks obtained from DTA were integrated and then the integrated data was normalized to unity to give crystallized fraction. **Figure 3.5.7** shows the volume fraction of crystallized phase for the experimental glasses without (a, c), and with added P_2O_5 (b, d), respectively. All curves exhibit a sigmoid type variation with temperature. The crystallized volume fraction slightly increases at the beginning and at the end of the non-isothermal crystallization process (as evidenced by the low slopes in the initial and final branches of the curves in shown **Figure 3.5.7**) suggesting that the reaction proceeds slowly at these stages. On the contrary, the main segment of the curve features a higher slope indicating a faster reaction. Accordingly, the crystallization reaction can be divided into three stages: (1) nucleation starts from the amorphous matrix slowly; (2) the increasing surface of contact between amorphous matrix and crystal nuclei leads to a sharp increase in crystallized fraction, indicating a steady crystallization reaction stage; (3) the interface between crystallized phase and amorphous matrix decreases as a result of nuclei coalesce [232–235].

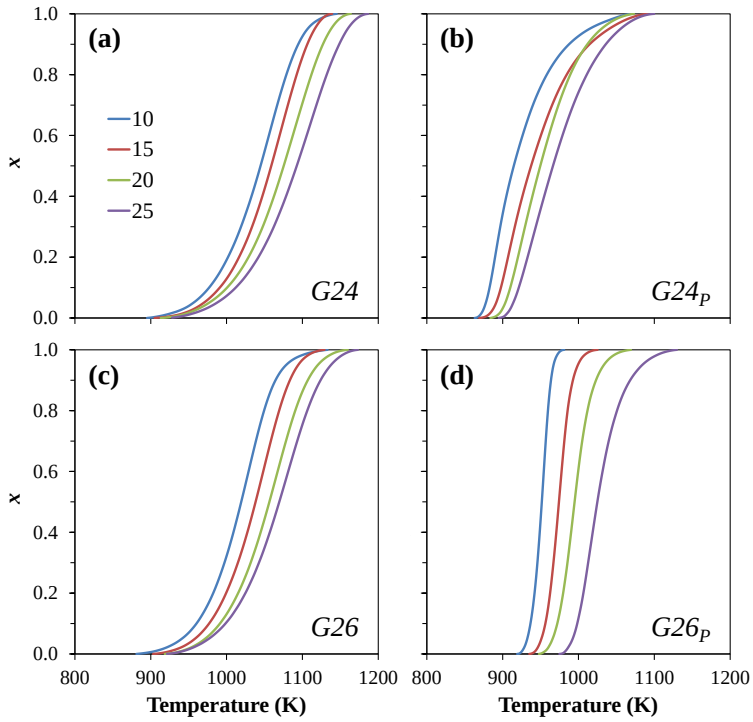

Figure 3.5.7 Evolution of crystallised fraction *x* with temperature for the experimental glasses obtained from DTA and using different heating rates (β = 10, 15, 20 and 25 K min^{-1}): (a) G24, (b) $G24_P$, (c) G26 and (d) $G26_P$.

In the case of Matusita's method, from Eq. (3.5-3), for each composition at a particular temperature, the variation of $ln\ [-ln\ (1-x)]$ *vs.* $-ln\ \beta$ give four points (corresponding to four heat treatments) which were fitted with a straight line whose slope gave *n'*. To calculate *n'* for each composition, at least four temperatures were chosen except for $G26_P$: only three could be chosen due its narrow and distinctly separated peaks. The plots of $[-ln\ (1-x)]$ *vs.* $-1.052\ m/RT$ are straight lines whose slopes enable to extract the values of activation energy E_c. The value $m = n'$ was chosen for all the compositions. In Kissinger's method, the variation of $ln\ (\beta/T_p^2)$ as a function $-1000/RT_p$ gave four points which were fitted with a straight line whose slope gave the activation energy for crystallization. All the kinetic parameters obtained from both methods are summarised in **Table 3.5.4**.

Table 3.5.4 Kinetic parameters from Kissinger's and Matusita's method

	Kissinger Method			**Matusita Method**	
	E_c ($kJ\ mol^{-1}$)	R^2	*n*	E_c ($kJ\ mol^{-1}$)	*m*
G24	155 ± 24	0.93	1.45 ± 0.06	185 ± 09	1.20 ± 0.07
G24$_P$	121 ± 06	0.99	1.84 ± 0.44	085 ± 15	1.35 ± 0.55
G26	141 ± 06	0.99	1.72 ± 0.11	166 ± 08	1.43 ± 0.03
G26$_P$	111 ± 11	0.97	5.32 ± 1.58	125 ± 07	6.44 ± 0.68

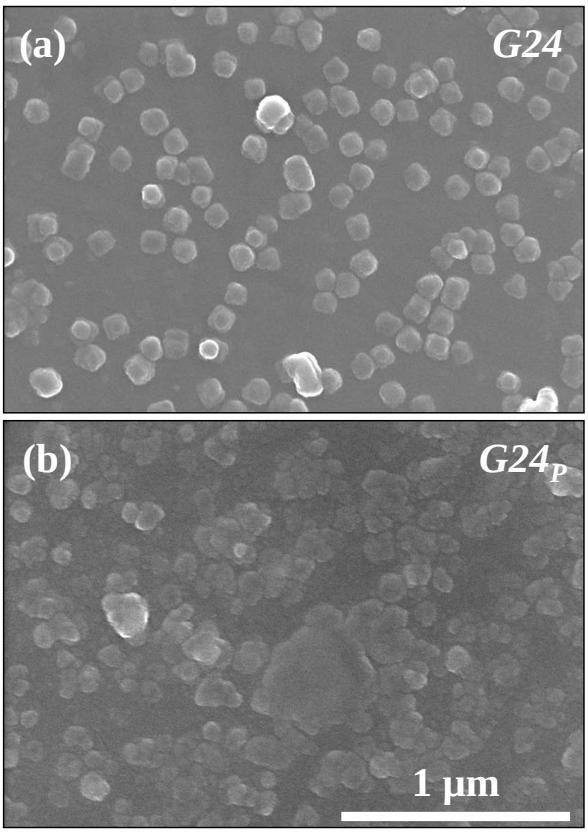

Figure 3.5.8 SEM images of non-annealed bulk glasses *G24* and $G24_P$.

3.5.3.3 Microstructure and phase content

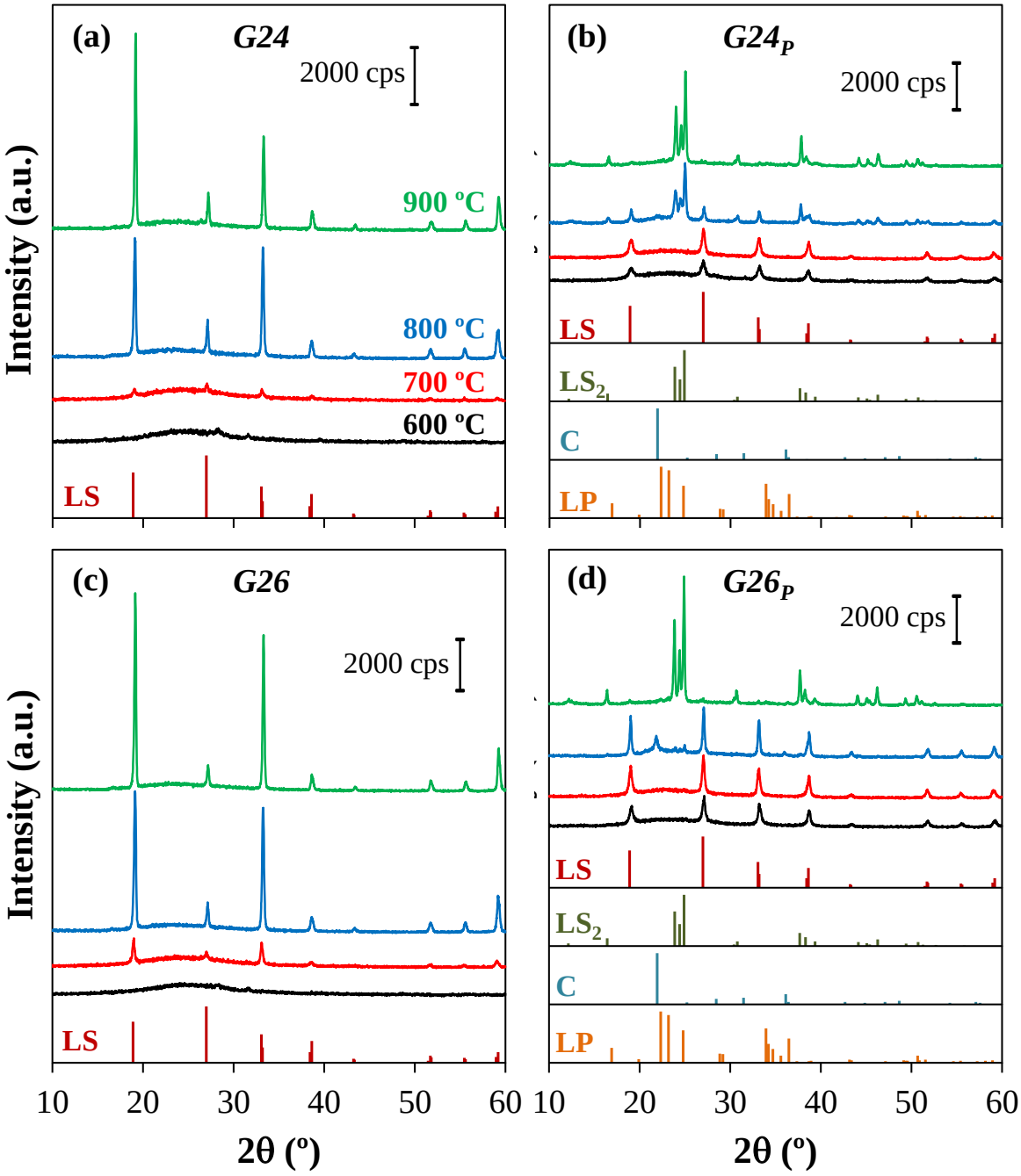

Figure 3.5.9 X-ray diffraction patterns of glasses crystallized at different temperatures as indicated in (a) for: (a) *G24*, (b) $G24_P$, (c) *G26* and (d) $G26_P$. (LS_2: lithium disilicate, $Li_2Si_2O_5$, ICDD 01–070–4856; *LS*: lithium metasilicate. Li_2SiO_3, ICDD 01–070–0330; C: cristobalite, SiO_2, ICDD 00–011–0695). ; LP: lithium orthophosphate, Li_3PO_4, ICCD 00–15–0760).

Figure 3.5.8 shows as an example of microstructure of non-annealed bulk glasses of composition *G24* and $G24_P$. Samples showed drop-let like liquid-liquid phase separation of sizes ranging between few tens to 180 nm. The addition of P_2O_5 increased the extent of phase separation. The crystalline phase evolution in glasses heat treated at various temperatures shows that *LS* (ICDD 01–070–0330) was the first crystalline phase formed in all the glass–ceramics (Error! Reference source not found.). *LS* was lready significantly evident in $G24_P$ and $G26_P$ at 600 ºC (Error! Reference source not found.**b and d**, respectively), while only small peaks could be observed for *G24* and *G26* (Error! Reference source not found.**a and c**, respectively). In the absence of P_2O_5, *S* remained as single phase for glass all compositions heat treated at all temperatures and the peaks are more intense in comparison to those observed for P_2O_5-containing compositions. On the other hand, LS_2 (ICDD 01–070–4856) was formed after heat treating P_2O_5-containing compositions at 800 ºC, but the intensity of LS_2 peaks was much lower for $G26_P$ (only traces) in comparison to that observed for $G24_P$. Moreover, the presence of cristobalite (ICDD 00–011–0695) was also observed in $G26_P$, but this phase was dissolved at 900 ºC. Both $G24_P$ and $G26_P$ featured monomineral LS_2 composition at 900 ºC. ºC. At this temperature, both $G24_P$ and $G26_P$ seemed to feature mono-mineral LS_2 composition, but detailed analysis of the XRD pattern revealed the presence of very small peaks of lithium orthophosphate (LP, Li_3PO_4, ICCD 00–15–0760).

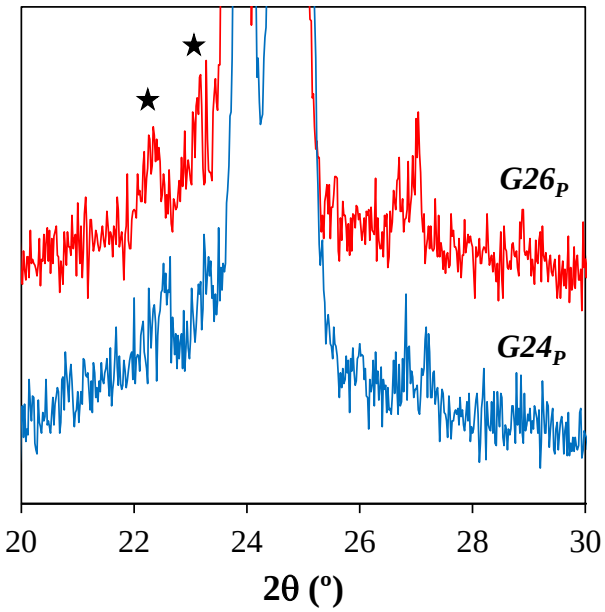

Figure 3.5.10 X-ray patterns of glasses *G24*$_P$ and *G26*$_P$ heat treated for 1 h at 900 ºC (the stars show the main peaks for LP (lithium orthophosphate, Li_3PO_4, ICCD 00–15–0760).

Figure 3.5.11 shows SEM images of glasses heat treated at 700 ºC for 1 h. P_2O_5-free compositions exhibit the presence of spherulites of *LS* phase (**Figure 3.5.11a and c**), the size of which are larger for the lower SiO_2/Li_2O molar ratio in agreement with the intensities of the respective XRD peaks. The insert (**Figure 3.5.11e**) shows a higher magnification detail of the spherulite-like area of sample *G24*, revealing the morphology of *LS* crystals. The addition of P_2O_5 led to a higher degree of crystallization (**Figure 3.5.11b and d**). Glasses *G24*$_P$ and *G26*$_P$ are featured by sub-micrometre *LS* crystals but their sizes tend to increase with decreasing SiO_2/Li_2O molar ratio.

3.5.3.4 Other properties

The density is one of the tools that reveals the degree of structural changes in glass network with composition .[236] The values of density (ρ) for the glasses presented in **Table 3.5.3** are very close, being slightly smaller for P_2O_5-containing compositions. Based on the density data, the molar volume (V_m) and the oxygen density (ρ_O) values of the glasses were calculated by,

$$V_m = \frac{M}{\rho} \qquad \text{Eq. (3.5-4)}$$

And,
$$\rho_O = \frac{M_O\left(X_{Li_2O} + X_{K_2O} + 3X_{Al_2O_3} + 2X_{SiO_2} + 5X_{P_2O_5}\right)}{V_m} \quad \text{Eq. (3.5-5)}$$

Where, M and ρ are molecular weight and density of the glass, M_O is the molecular weight of oxygen and X is the molar fraction of each oxide component present in each glass; these values are also presented in **Table 3.5.3**. In order to evaluate the network polymerization of the glasses, the percentage of non-bridging oxygens (*NBO%*) was calculated from the chemical compositions using the following equation:

$$NBO\% = \frac{2 \times ([Li_2O] + [K_2O] - [Al_2O_3])}{[Li_2O] + [K_2O] + 3[Al_2O_3] + 2[SiO_2] + 3[P_2O_5]} \quad \text{Eq. (3.5-6)}$$

Here, the quantities represented in square brackets are molar concentrations of each oxide. In the above formula, the terminal oxygens which are doubly bonded to phosphorus tetrahedra are not taken into account. The values for *NBO%* are presented in **Table 3.5.4** show a significant variation with changing the content of Li_2O and a small variation with addition of P_2O_5.

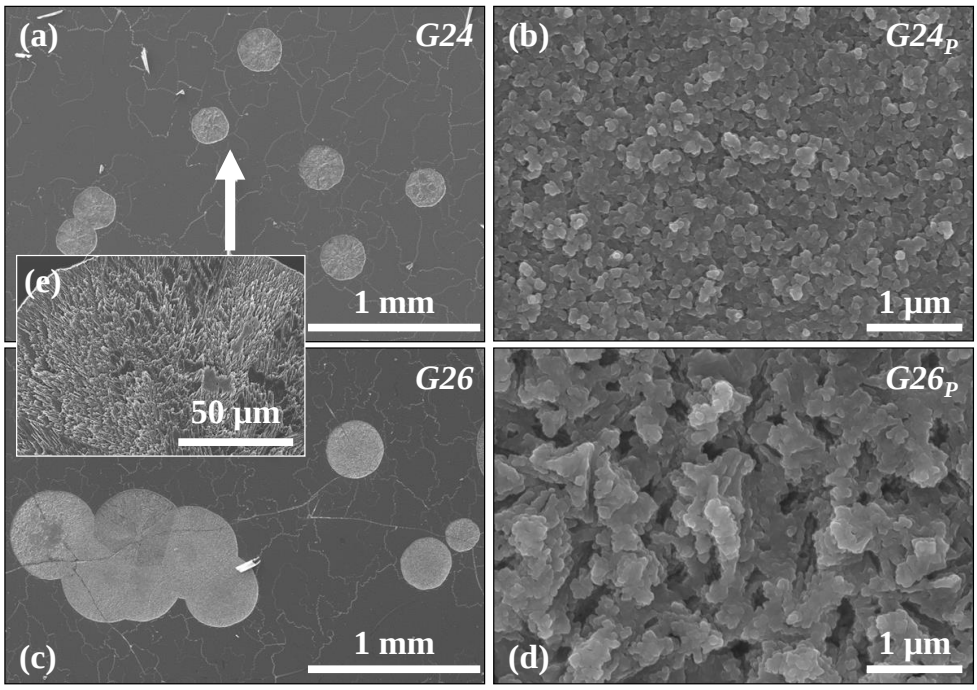

Figure 3.5.11 SEM images of bulk glasses heat treated at 700 ºC for 1 h: (a) *G24*, (b) *G24P*, (c) *G26* and (d) *G26P*. The insert (e) shows a higher magnification detail of the spherulite-like area of sample *G24*.

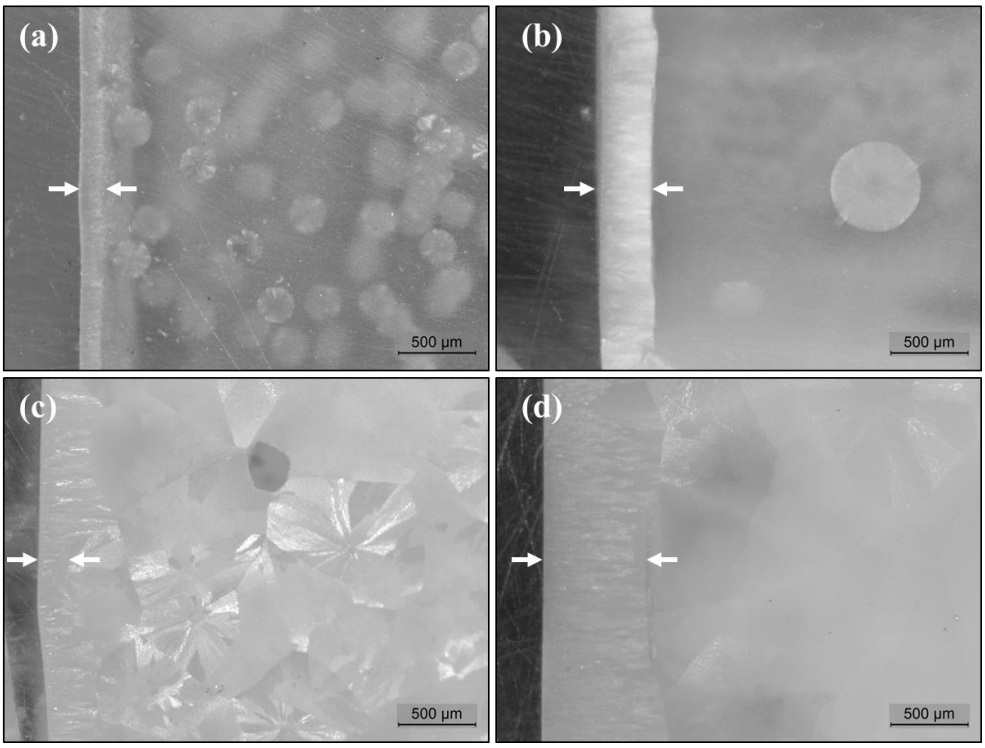

Figure 3.5.12 Optical images of bulk glasses heat treated for 1 h: (a) *G24*–700ºC (b) *G26*–700ºC, (c) *G24*–800ºC and (d) *G26*–800ºC.

3.5.4 Discussion

3.5.4.1 Structure of the glasses

The structure of the glass as interpreted by the NMR and FTIR spectra represent the liquid structure at the fictive temperature. Further, this structure changes by changing the fictive temperature where the glass relaxes to a new equilibrium structure giving rise to a new distribution of Q_n units, through speciation reaction [237]. Although, it must be noted that, in reality the glass structure does not precisely correspond to the liquid structure at any temperature. The concept of fictive temperature gives a simplified view of the glass structure [238]. Based on the ^{29}Si and ^{31}P NMR spectra, the chemical composition of the glasses could be estimated by considering the relative distribution of Q_n and $Q_{n(P)}$ units. By assuming the proportions of SiO_2, Al_2O_3, P_2O_5 and K_2O to be same as the original composition (in **Table 3.5.1**) the amount of Li_2O can be calculated from the Q_n and $Q_{n(P)}$ distributions. This assumption is justified by the fact that majority of the weight losses in the compositions as the current ones (which was negligible) are only associated to the Li_2O evaporation. Accordingly, the chemical compositions obtained from these calculations are presented in **Table 3.5.1**. The results show that for the samples *G24*, *G26* and *G26P* there is an average underestimation of

~1.7 % of SiO_2 whereas, for the sample *G24P* there is an overestimation of 0.5% of SiO_2. While the overestimation of the SiO_2 is expected due the evaporation losses of Li_2O, the underestimation could be a result of either (a) short spin–lattice relaxation times of 60 s employed in the ^{29}Si NMR experiments, which are probably insufficient for complete relaxation of the Q_4 sites or (b) inconsistencies in the deconvolution of ^{29}Si NMR spectra.

According to the ^{27}Al NMR spectra, the Al units are in tetrahedral coordination. Therefore, each Al tetrahedron should be connected to four neighbouring units. However, it is well known that Al–O–Al type linkages are prohibited in aluminosilicate glass networks, this phenomenon is known by Loewenstein's Rule [165–167]; where each Al unit would be coordinated to four Si units forming Al–O–Si type linkages. These Al–O–Si type linkages can be probed by ^{29}Si NMR spectroscopy. When a Q_n unit is coordinated to Al unit forming Q_n (1Al) units, its chemical shift is de-shielded by ~5 ppm [154]. In the current glasses, the chemical shift of Q_4 units is about –104 ppm, which is about 5 ppm higher than the expected value for a Q_4 unit. Moreover, there is no de-shielding effect for Q_2 and Q_3 units. This suggests that Al units are specifically coordinated to Q_4 units. Nevertheless, according to the composition, assuming the existence of only Q_4 (1Al) type units, the number of the expected units from the composition were calculated. Compositions show some differences in the NMR-Q_4 values and calculated-Q_4 (1Al) values which are: –23, 38, –57, 16 (in %) for *G24*, *G24P*, *G26* and *G26P* respectively. Therefore, in the glasses *G24* and *G26,* additional units such as Q_4 (2Al) and Q_4 (3Al) are expected to account for the discrepancy. These units would have chemical shifts values overlapping Q_3 peak. This explains the relatively larger underestimation of SiO_2 in *G24* and *G26* compositions. Therefore, the small differences in the compositions calculated from the NMR spectroscopy could be due to small discrepancies in the deconvolution. Additionally, the short spin–lattice relaxation time of ^{29}Si MAS-NMR experiments could also play a minor role. This analysis is in agreement with our earlier studies [144,193,239].

Further, we want to comment on a former study [151] with similar compositions as the current ones where, a broadening of the ^{27}Al peak was observed when K_2O is removed from the compositions. Though this broadening was explained differently in the original paper, now we have the strong indication that this effect is due to the quadrupolar interaction associated with the increased electric field strength on the ^{27}Al

nucleus when Li^{+1} ion acts as charge compensator [240]. ^{27}Al NMR spectra of the compositions from this past study, were deconvoluted similar to the current compositions, and gave the values of C_Q to be about 4.0 MHz and 5.2 MHz for compositions with and without K_2O respectively. Therefore, the larger C_Q of 5.2 MHz is due to Li^{+1} ion acting as charge compensator. Therefore, in the current compositions, the values of C_Q which were about 4.4 MHz explains that most of the K_2O is associated to Al_2O_3 specifically playing the role of charge compensation.

It could be noticed that the addition of P_2O_5 to the glass compositions *G24* and *G26* results in substitution of one Al tetrahedron with two P tetrahedra. The outcome of this substitution leads to the replacement of 4 bridging oxygens with 6 bridging oxygens. Consequently, the net effect of adding P_2O_5 to the glass compositions *G24* and *G26* resulted in the slight decrease of *NBO content* (**Table 3.5.3**). Moreover, ^{31}P NMR spectra show (**Table 3.5.2**) that about 80% of P_2O_5 exists in the glass network as orthophosphate ($Q_{0(P)}$, PO_4^{-3}) and the rest as pyrophosphate ($Q_{1(P)}$, $P_2O_7^{-4}$) anions. Both these phosphate units are highly depolymerized with two to three *NBO*s associated with them. Consequently, these phosphate units preferably draw Li^+ ions towards them and make the silicate network more polymerized. This phenomenon can be seen in the ^{29}Si NMR spectra where, P_2O_5 addition leads to the increase of the Q_4 peak. Therefore, adding P_2O_5 to the glass compositions not only polymerizes the entire glass network but, preferentially polymerizes the silicate network to a greater extent. Moreover, the substitution of one Al tetrahedron with two P tetrahedra in *G24* and *G26* resulted in the increase of the molar volume (**Table 3.5.3**). This is an expected result because the network tetrahedra build the glass network and P_2O_5 addition leads to increased number of network tetrahedra. Conversely, moving from compositions *G24* to *G26* and $G24_P$ to $G26_P$ resulted in the decrease of the molar volume. This is also an expected result because the network tetrahedra in this case are replaced by network modifiers, which leads to the breaking down of the glass network [8]. Further, from the density values of the glasses, it can be observed that the addition of P_2O_5 led to a decrease in the density of the glass. This behaviour is due to lower molecular weight of P_2O_5 (142 g mol^{-1}) compared to the combined weight of K_2O + Al_2O_3 (196 g mol^{-1}); additionally, the increase in the molar volumes due to the addition of P_2O_5 also contributes to the decrease of the density values (**Table 3.5.3**). The values of the oxygen density however follow a continuous increase from along the line *G24* – $G24_P$ – *G26* – $G26_P$.

Figure 3.5.8 presents the microstructures of non-annealed bulk glasses of compositions *G24* and *G24$_P$*; they reveal homogenous droplet-like liquid–liquid phase segregation (*LLPS*) throughout the whole samples. The *LLPS* occurs in liquid systems when compositions move are away from the stoichiometry and go into the immiscibility dome. In Li_2O–SiO_2 liquid system, this immiscibility is a metastable type phase separation [53,183]. In the current composition droplets varied from a few tens to about 180 nm and the addition of P_2O_5 resulted in the increase of *LLPS*. One of reasons for the increased *LLPS* in P_2O_5 containing composition could be due to Li^+ ions preferably diffuse towards phosphate groups and contribute to an overall increase in degree of polymerization of the silicate network. This shifts the silicate composition to the centre of the immiscibility dome and results in the increased *LLPS*. The fundamental principle leading to increased *LLPS* due to P_2O_5 addition is still not very clear and is a subject of future studies.

3.5.4.2 Crystallization of glasses

The activation energies of crystallization for *G24* and *G26* decreased with decreasing of SiO_2/Li_2O ratio according to both Kissinger's and Matusita's methods (**Table 3.5.4**). From NMR results it can be seen that the K^+ ions are associated to Al tetrahedra playing the role of charge compensators. Therefore, Li^+ ions acting as modifiers, and having greater mobility then the rest of the atomic species, would strongly influence the kinetics. Hence, going from the composition *G24* to *G26* resulted in decreased activation energies of crystallization due to increased amount of Li^+ ions; this increased amount of Li^+ ions could also be inferred from the increased NBO% (**Table 3.5.3**). This argument is in accordance with the XRD results (**Figure 3.5.9**) where *G26* shows stronger diffraction peaks than *G24*, when both *G24* and *G26* were heat treated at 700 ºC for 1 h. This kind of discussion should equally hold valid when going from the composition *G24$_P$* to *G26$_P$* where, one could find an increase NBO% (**Table 3.5.3**) and corresponding increase in the intensity of X-ray diffraction peaks (**Figure 3.5.9**). However, the trends in the activation energies calculated from Kissinger's and Matusita's methods do not agree with each other. Going from the composition *G24$_P$* to *G26$_P$* Kissinger's model shows a decrease in activation energies (in agreement with the earlier discussion), whereas Matusita's model shows an increase in the activation energies. This inconsistency could be a result of the broad crystallization peak of *G24$_P$*, which seems to be probably a convolution of two

crystallization peaks. Therefore, the simpler Kissinger's model which only relies on peak crystallization temperature appears to be more reliable for the current analysis. In the case of glasses doped with P_2O_5, the activation energies were decreased to lower values (**Table 3.5.4**) from *G24* to *G24$_P$* and from *G26* to *G26$_P$*. This decrease is due to the fact that P_2O_5 acts as a nucleating agent (**Figure 3.5.11**) and its addition creates more nucleation sites thus decreasing the activation energy and favouring the crystallization at lower temperature.

Changes of Avrami parameter *n* are also observed with the variation of glass composition (**Table 3.5.4**). Composition *G24* exhibits the lowest value of *n*, suggesting that this glass is more prone to surface crystallisation. However, *n* increased with decreasing SiO_2/Li_2O ratio, suggesting that in *G26* there would be a slight preference to bulk crystallisation mechanism over the surface mechanism. Although the differences in *n* values between *G24* and *G26* are not significant, the surface crystallisation would be still the dominant mechanism; this is confirmed by optical microscopy (**Figure 3.5.12**). Further, the results for *n* values also show that addition of P_2O_5 to glass *G24* did not change significantly the crystallization mechanism since it resulted in only a small variation in *n*. The low value of *n* for *G24$_P$* even in the presence of nucleating agent is probably again due to the broad crystallization peak (**Figure 3.5.6**) that has likely resulted from the convolution of two crystallization peaks. Since the Avrami parameter from both Kissinger's as well as Matusita's methods relies on the broadness and shape of the peak respectively, the exact Avrami parameter could not be determined for this sample. The two overlapping peaks suggests two crystallization mechanisms probably resulting from the more extensive phase segregation in the glass as seen by SEM (**Figure 3.5.8**). This phase segregation would result in P_2O_5-rich and P_2O_5-poor regions averaging the Avrami parameter to less than 2; this hypothesis has to be studied in greater detail. On the contrary, the higher *n* values obtained for *G26$_P$* hint that bulk crystallization is the dominant crystallization mechanism, while DTA shows a strong, sharp and symmetric crystallization peak (**Figure 3.5.6**). The SEM results (**Figure 3.5.11**) show that both *G24$_P$* and *G26$_P$* exhibit higher nucleation rates confirming the role of P_2O_5 as nucleating agent.

The results from both XRD (**Figure 3.5.9**) and crystallization kinetics (**Table 3.5.4**) suggest that the crystallization events are favoured in P_2O_5–containing glasses with the *LS* formed at earlier stages being readily transformed into *LS$_2$* at the higher

temperatures (≥ 800 ºC). The transformation from *LS* to LS_2 in $G24_P$ and $G26_P$ occurs at temperatures above 700 and 800 ºC, respectively. This result is in accordance with the thermodynamic analysis carried out in Section 3.4 where, at temperatures lower than 800 ºC, the examined compositions always showed a preferential crystallization of *LS* phase for two reasons: (1) *LS* being thermodynamically stable at temperatures lower than 800 ºC and (2) Al_2O_3 and B_2O_3 were specifically associated to Q_4 units lowering the kinetics of LS_2 crystallization. These same arguments do hold in the case of current glass compositions. However, since the current compositions are shifted more towards higher Li side, the *LS* phase would be stable at temperatures much higher than 800 ºC. In this case, the *LS* phase was actually stable even at 900 ºC for both *G24* and *G26*. Howbeit, adding P_2O_5 to these compositions shifted the silicate network's composition to SiO_2 rich side where, *LS* would be a stable only at lower temperatures leading to the formation of LS_2 at higher temperatures.

3.5.4.3 Mechanism of P_2O_5 as nucleating agent

The current study clearly shows that P_2O_5 acts as a nucleating agent. However, the exact mechanism behind this role is still not clear and there seems to be some controversy associated with this issue. As the current authors perceive, there are basically two schools of thought explaining the mechanism:

1. During initial stages of crystallization Li_3PO_4 nucleates and acts as epitaxial centres for the heterogeneous nucleation of *LS* and LS_2.

2. P_2O_5 induces phase separation and the crystal nucleation occurs at the interface of phase segregated regions.

The first mechanism is supported by the work of Headley and Loehman[241] who experimentally showed the proof for this mechanism; although *GC*s are not conventionally prepared by the method they have used. The second mechanism is supported by more recent work by Bischoff *et al.*[200] Their experimental results showed that the phosphate species exist in a highly disordered state, even after the crystallization of *LS*. Their findings are clearly in line with experimental results gathered in the current paper, which enable drawing similar conclusions. The XRD (**Figure 3.5.9** & **Figure 3.5.10**) results for $G24_P$ and $G26_P$ confirmed the absence of LP phase below 800 ºC. This shows that the formation of crystalline *LS* in the presence of

P_2O_5 cannot be explained by a heterogeneous nucleation processes through epitaxy from previously precipitated LP phase, but probably a heterogeneous nucleation at the interface of an amorphous LP phase and the glass matrix.

Although the second explanation seems to be in a better accordance with the experimental results, it is in complete contradiction to what we have understood so far about crystal nucleation of glasses in last 3 decades. The role of phase separation on crystal nucleation has been extensively studied in the literature for binary systems, and proved with rigorous experimentation that phase segregated boundaries cannot act as heterogeneous sites for crystal nucleation.[132,152,176] Therefore, the issue of whether or not phase segregated boundaries act as heterogeneous nucleation sites though have been resolved for binary systems, it is still an open problem when dealing with multicomponent systems. One very likely explanation that would not contradict with our previous knowledge could be: the addition of P_2O_5 alters the thermodynamics of liquid phase in such a way that, for example, it enhances the driving force for the crystallization of *LS* or LS_2, causing increased homogenous crystal nucleation rates. Therefore, studying the liquid (or glass) structure in much greater detail would provide deeper insights into the crystal nucleation mechanism. An atomistic approach using statistical mechanics could be an answer to the problems related to crystal nucleation.[242] Therefore, studies as the current one are extremely essential and help us come up better hypotheses.

3.6 Statistics of silicate units in binary glasses

Anuraag Gaddam [a], Lionel Montagne [b], José M.F. Ferreira [a]

[a] Department of Materials and Ceramics Engineering, University of Aveiro, CICECO, 3810-193 Aveiro, Portugal

[b] Univ. Lille, CNRS, Centrale Lille, ENSCL, Univ. Artois, UMR 8181 - UCCS - Unité de Catalyse et Chimie du Solide, F-59000 Lille, France.

Journal of Chemical Physics, 145 (2016) 124505
DOI: 10.1063/1.4963341

Abstract

In this Section a new model is derived to determine the distribution of silicate units in binary glasses (or liquids). The model is based on statistical mechanics and assumes grand canonical ensemble of silicate units which exchange energy and network modifiers from the reservoir. This model complements experimental techniques, which measure short range order in glasses such as *NMR* spectroscopy. The model has potential in calculating the amounts of liquid-liquid phase segregation and crystal nucleation, and it can be easily extended to more complicated compositions. The structural relaxation of the glass as probed by *NMR* spectroscopy is also reported, where the model could find its usefulness.

3.6.1 Introduction

In binary alkali (R^{+1}; R ∈ {Li, Na, K, Rb, Cs}) or alkaline earth ($\acute{R}^{+2}$; Ŕ ∈ {Mg, Ca, Sr, Ba}) silicate glasses (or liquids), silicates form tetrahedral structures that are connected to each other by corner sharing.[9] The oxygens in these glasses exist in three forms, namely: (1) free oxygens (*FO*s, O^{-2}), (2) non-bridging oxygens (*NBO*s, O^{-1}) and (3) bridging oxygens (*BO*s, O^{0}). Though, at lower concentrations of R_2O (or ŔO), the amount of *FO*s in the composition is negligible.[243,244] Providentially, these compositions are of interest to the glass science because of their glass forming ability. The *BO*s and *NBO*s are present on the corners of silicate tetrahedra where, the *BO*s act as connectors between two tetrahedra, while the *NBO*s terminate the connectivity of a given tetrahedron. Therefore, depending upon the number of *NBO*s and *BO*s on a given silicate tetrahedron, the tetrahedron can be classified by Q_n notation where, $n \in \{[0, 4] \cap \mathbb{N}\}$ is the number of *BO*s on a given silicate tetrahedron.

Studies on the distribution of Q_n units are ubiquitous in the field of silicate based glasses. Techniques such as nuclear magnetic resonance (*NMR*) and Raman spectroscopies are routinely employed to assess the distribution of structural units. Also, there are many mathematical models that theoretically address this issue to gain fundamental understanding of this distribution. The binary model presumes only two types of Q_n units at each composition without taking account of the speciation reaction Eq. (3.6-1); therefore, it only describes the distribution that corresponds only to crystalline silicates but not glasses. A pure statistical model based on binomial distribution was suggested, supposing a completely random distribution of *BO*s and *NBO*s.[11] However, this model does not take into account the temperature effects. Further, Brandriss *et al.*[237] suggested a thermodynamic model to take temperature effects into consideration. In this model, equilibrium constants (k_n) are experimentally measured by assuming a speciation reaction (R1) and using the van't Hoff equation ΔH_n is calculated as shown below,

$$2Q_n \leftrightarrow Q_{n-1} + Q_{n+1} \quad \Delta H_n \qquad \text{Eq. (3.6-1)}$$

$$k_n(T) = \frac{[Q_{n+1}][Q_{n-1}]}{[Q_n]^2}\Gamma$$

$$\frac{\partial \ln k_n(T)}{\partial T} = \frac{\Delta H_n}{RT^2}$$

$$\frac{\Delta H_n}{R} = \frac{\ln k_n(T_2) - \ln k_n(T_1)}{\left(\frac{1}{T_1} - \frac{1}{T_2}\right)}$$

Where, $\Gamma \approx 1$ corresponds to a function of activity coefficients. By measuring k_n at any two different temperatures by *NMR* or Raman spectroscopy, ΔH_n is evaluated, and using the value of ΔH_n, k_n at other temperatures could be calculated. Another thermodynamic model of associated solutions was proposed, which employs rigorous thermodynamic theory of affinity.[13–15,245] This model uses Gibbs free energy of formation for all the crystalline compounds formed in a particular glass system. Nevertheless, all these models use either pure statistics or macroscopic thermodynamics and therefore have their own limitations. A statistical mechanical model was proposed by Mauro[238] for the glass systems having a single network modifier and multiple network formers. This model is based on non-central hypergeometric distribution where, the bias is weighted by Boltzmann factors. The model provides a mathematical description for the distribution network modifiers among various network formers; however, it does not address the problem of Q_n distribution.

Therefore, in this paper we introduce a new statistical mechanical model for binary silicate glass systems in order to address the problem of Q_n distribution from a fundamental standpoint. The model assumes presence of no *FO*s. The model has a huge technological importance and has a potential to deal with some of the open problems in the field of glass science such as liquid-liquid phase segregation (*LLPS*), crystal nucleation and structural relaxation.

3.6.2 Formulation of the model

3.6.2.1 Defining silicate units

As described in the introduction, silicate units are defined by the Q_n notation based on the number of *BO*(s) that surround a given Si atom. However, there have been number of suggestions from *NMR* spectroscopy that in glass compositions, silicate units can be further described by considering the next-nearest neighbors.[16,246,247] Based on this new description, the units can be defined as: Q_4^{ijkl} (35), Q_3^{ijk} (20), Q_2^{ij} (10), Q_1^{i} (4)

and Q_0 (1), where $i, j, k, l \in \{[1, 4] \cap \mathbb{N}\}$. For example, a Q_3^{334} unit would have three *BO*s, out of which, two are connected to Q_3 units and one is connected to a Q_4 unit (**Figure 3.6.1**). According to this new definition, there would be 70 different types of silicate units, from all the combinations of the superscripts as listed in **Table 3.6.1**. Howbeit, in this paper we introduce a new S_n^m notation that is more suitable for the derivation of the model; where, $n \in \{[0, 4] \cap \mathbb{N}\}$ while $m \in \{[1, m\,(n)] \cap \mathbb{N}\}$. Here n has same meaning as in Q notation, corresponding to the internal structure of the unit, *i.e.* the amount of alkali or alkaline metal ions present in it. While m corresponds to the external structure, *i.e.* the types of units a given silicate unit is connected to, and m maps a particular combination of $ijkl$ of a Q notation. A comparison between Q notation and S notation is shown in **Table 3.6.1**. In this paper, both notations are used interchangeably according to the convenience (**Figure 3.6.1**). We also define different types of *BO*s in the glass by O_{ij} notation, where O_{ij} is a *BO* connecting Q_i and Q_j ($i, j \in \{[1, 4] \cap \mathbb{N}\}$) units together.

Table 3.6.1 Comparison between Q and S notation and constants associated to network connectivity

No.	S_n^m	$Q_n^{ij...}$	$(4, 3)_n^m$	$(4, 2)_n^m$	$(4, 1)_n^m$	$(3, 2)_n^m$	$(3, 1)_n^m$	$(2, 1)_n^m$
					Units of Q_4^{ijkl}			
1	S_4^1	Q_4^{4444}	0	0	0	0	0	0
2	S_4^2	Q_4^{3444}	1	0	0	0	0	0
3	S_4^3	Q_4^{3344}	2	0	0	0	0	0
4	S_4^4	Q_4^{3334}	3	0	0	0	0	0
5	S_4^5	Q_4^{3333}	4	0	0	0	0	0
6	S_4^6	Q_4^{2444}	0	1	0	0	0	0
7	S_4^7	Q_4^{2344}	1	1	0	0	0	0
8	S_4^8	Q_4^{2334}	2	1	0	0	0	0
9	S_4^9	Q_4^{2333}	3	1	0	0	0	0
10	S_4^{10}	Q_4^{2244}	0	2	0	0	0	0
11	S_4^{11}	Q_4^{2234}	1	2	0	0	0	0
12	S_4^{12}	Q_4^{2233}	2	2	0	0	0	0
13	S_4^{13}	Q_4^{2224}	0	3	0	0	0	0
14	S_4^{14}	Q_4^{2223}	1	3	0	0	0	0
15	S_4^{15}	Q_4^{2222}	0	4	1	0	0	0
16	S_4^{16}	Q_4^{1444}	0	0	1	0	0	0

17	S_4^{17}	Q_4^{1344}	1	0	1	0	0	0
18	S_4^{18}	Q_4^{1334}	2	0	1	0	0	0
19	S_4^{19}	Q_4^{1333}	3	0	1	0	0	0
20	S_4^{20}	Q_4^{1244}	0	1	1	0	0	0
21	S_4^{21}	Q_4^{1234}	1	1	1	0	0	0
22	S_4^{22}	Q_4^{1233}	2	1	1	0	0	0
23	S_4^{23}	Q_4^{1224}	0	2	1	0	0	0
24	S_4^{24}	Q_4^{1223}	1	2	1	0	0	0
25	S_4^{25}	Q_4^{1222}	0	3	1	0	0	0
26	S_4^{26}	Q_4^{1144}	0	0	2	0	0	0
27	S_4^{27}	Q_4^{1134}	1	0	2	0	0	0
28	S_4^{28}	Q_4^{1133}	2	0	2	0	0	0
29	S_4^{29}	Q_4^{1124}	0	1	2	0	0	0
30	S_4^{30}	Q_4^{1123}	1	1	2	0	0	0
31	S_4^{31}	Q_4^{1122}	0	2	2	0	0	0
32	S_4^{32}	Q_4^{1114}	0	0	3	0	0	0
33	S_4^{33}	Q_4^{1113}	1	0	3	0	0	0
34	S_4^{34}	Q_4^{1112}	0	1	3	0	0	0
35	S_4^{35}	Q_4^{1111}	0	0	4	0	0	0
				Units of Q_3^{ijk}				
36	S_3^{1}	Q_3^{444}	-3	0	0	0	0	0
37	S_3^{2}	Q_3^{344}	-2	0	0	0	0	0
38	S_3^{3}	Q_3^{334}	-1	0	0	0	0	0
39	S_3^{4}	Q_3^{333}	0	0	0	0	0	0
40	S_3^{5}	Q_3^{244}	-2	0	0	1	0	0
41	S_3^{6}	Q_3^{234}	-1	0	0	1	0	0
42	S_3^{7}	Q_3^{233}	0	0	0	1	0	0
43	S_3^{8}	Q_3^{224}	-1	0	0	2	0	0
44	S_3^{9}	Q_3^{223}	0	0	0	2	0	0
45	S_3^{10}	Q_3^{222}	0	0	0	3	0	0
46	S_3^{11}	Q_3^{144}	-2	0	0	0	1	0
47	S_3^{12}	Q_3^{134}	-1	0	0	0	1	0
48	S_3^{13}	Q_3^{133}	0	0	0	0	1	0
49	S_3^{14}	Q_3^{124}	-1	0	0	1	1	0
50	S_3^{15}	Q_3^{123}	0	0	0	1	1	0

51	S_3^{16}	Q_3^{122}	0	0	0	2	1	0
52	S_3^{17}	Q_3^{114}	-1	0	0	0	2	0
53	S_3^{18}	Q_3^{113}	0	0	0	0	2	0
54	S_3^{19}	Q_3^{112}	0	0	0	1	2	0
55	S_3^{20}	Q_3^{111}	0	0	0	0	3	0
				Units of Q_2^{ij}				
56	S_2^{1}	Q_2^{44}	0	-2	0	0	0	0
57	S_2^{2}	Q_2^{34}	0	-1	0	-1	0	0
58	S_2^{3}	Q_2^{33}	0	0	0	-2	0	0
59	S_2^{4}	Q_2^{24}	0	-1	0	0	0	0
60	S_2^{5}	Q_2^{23}	0	0	0	-1	0	0
61	S_2^{6}	Q_2^{22}	0	0	0	0	0	0
62	S_2^{7}	Q_2^{14}	0	-1	0	0	0	1
63	S_2^{8}	Q_2^{13}	0	0	0	-1	0	1
64	S_2^{9}	Q_2^{12}	0	0	0	0	0	1
65	S_2^{10}	Q_2^{11}	0	0	0	0	0	2
				Units of Q_1^{i}				
66	S_1^{1}	Q_1^{4}	0	0	-1	0	0	0
67	S_1^{2}	Q_1^{3}	0	0	0	0	-1	0
68	S_1^{3}	Q_1^{2}	0	0	0	0	0	1
69	S_1^{4}	Q_1^{1}	0	0	0	0	0	0
				Units of Q_0				
70	S_0^{1}	Q_0	0	0	0	0	0	0

3.6.2.2 Statistical treatment

Consider a liquid of either alkali (R^{+1}) or alkaline earth ($\acute{R}^{+2}$) silicate composition given by,

$$R_2O \text{ or } \acute{R}O: \quad x$$

$$SiO_2: \quad 1$$

Here, the amount of SiO_2 is scaled to unity and the addition of the network modifiers is given by the variable x; where $x \in [0, 2]$, which corresponds to $R_2O\% \in [0, 2/3]$. If, P_n^m is probability (or fraction) of occurrence of a S_n^m microstate, then the

constraints Eq. (3.6-2) to Eq. (3.6-4) must hold; which are constraints corresponding to the amounts of SiO_2, energy and R_2O or ŔO respectively.

$$\sum_{n,m} P_n^m = 1 \qquad \text{Eq. (3.6-2)}$$

$$\sum_{n,m} E_n^m P_n^m = \langle E \rangle \qquad \text{Eq. (3.6-3)}$$

$$\sum_{n,m} n P_n^m = 2[2 - \langle x \rangle] = \langle N_{BO} \rangle \qquad \text{Eq. (3.6-4)}$$

Where, E_n^m is the energy of a given S_n^m microstate while $\langle E \rangle$, $\langle x \rangle$ and $\langle N_{BO} \rangle \in [0, 4]$ are the expected values of energy, composition and the amount of *BO*s for a given ensemble. Additionally, because S_n^m notation takes into consideration the network linkages with its neighbors, there would be 10 more additional internal constraints connecting the probabilities of different S_n^m microstates corresponding to the 10 different types of *BO*s (O_{ij}). The equations are presented in the appendix (Section 3.6.4.1) and they take the form given by the Eq. (3.6-5).

$$\sum_{n,m} (i,j)_n^m P_n^m = 0 \qquad \text{Eq. (3.6-5)}$$

The coefficients $(i, j)_n^m$ represent the number of network connections between Q_i and Q_j silicate units originating from a given S_n^m unit. The following examples illustrate the physical meaning of these coefficients,

- The value of $(3, 2)_3^8$, which corresponds to the microstate S_3^8 (or Q_3^{224}) would be 2 because there are two 3→2 connections.
- The value of $(4, 3)_3^1$, which corresponds to the microstate S_3^1 (or Q_3^{444}) would be -3 because there are three 3→4 connections; and the negative sign implies the reversal of the originating direction.
- The value of $(4, 3)_3^{20}$, which corresponds to the microstate S_3^{20} (or Q_3^{111}) would be 0 because of the non-existence of any 4→3 connections.

All the values of the coefficients $(i, j)_n^m$ are presented in the **Table 3.6.1**. Basically, Eq. (3.6-4) and Eq. (3.6-5) represent constraints corresponding to chemical

composition and network connectivity, respectively. The entropy generated by a given distribution of S_n^m microstates is given by,

$$S = -k_B \sum_{n,m} [P_n^m \ln P_n^m] \qquad \text{Eq. (3.6-6)}$$

Where, k_B is the Boltzmann constant. Maximizing Eq. (3.6-6) by subjecting to the constraints Eq. (3.6-2) to Eq. (3.6-5) using the method of Lagrange multipliers would yield (Section 3.6.4.2),

$$P_n^m = \frac{1}{Z_{gr}} e^{\frac{\sum_{i \geq j(i,j)_n^m} \mu_{ij} + n\,\mu - E_n^m}{k_B T}} \qquad \text{Eq. (3.6-7)}$$

Where, μ and μ_{ij} are the chemical potentials associated to the exchange of network modifiers (R^+ or $\acute{R}^{2+}$) and network connections respectively, T is the temperature and Z_{gr} is the grand canonical partition function given by,

$$Z_{gr} = \sum_{n,m} e^{\frac{\sum_{i \geq j(i,j)_n^m} \mu_{ij} + n\,\mu - E_n^m}{k_B T}} \qquad \text{Eq. (3.6-8)}$$

3.6.2.3 Energy consideration and quantization

The energy associated with a given S_n^m microstate would be vibrational energy.[248] The frequencies of the vibrational normal modes associated to a particular S_n^m microstate could be obtained by appropriately choosing the interatomic potentials derived from quantum mechanical calculations and then solving the *characteristic equation*. If each S_n^m microstate has N_n^m number of normal modes associated to it, labelled by $\nu \in \{[1, N_n^m] \cap \mathbb{N}\}$, then a given S_n^m unit can be considered to be an N_n^m dimensional quantum harmonic oscillator. Consequently, we can represent the vibrational state of the S_n^m unit existing in some stationary state by a state vector $|S_n^m(\boldsymbol{k_n^m})\rangle$ where, $\boldsymbol{k_n^m}$ is vector $\in \mathbb{Z}^{N_n^m}$ in positive orthant subspace; the meaning of which would be apparent subsequently. When the Hamiltonian ($\widehat{H}$) acts on the state vector $|S_n^m(\boldsymbol{k_n^m})\rangle$, it would yield,

$$\widehat{H}\,|S_n^m(\boldsymbol{k})\rangle = \left[\sum_{\nu=1}^{N_n^m} \left(\frac{1}{2} + k_n^m(\nu)\right) \hbar \omega_n^m(\nu)\right] |S_n^m(\boldsymbol{k_n^m})\rangle \qquad \text{Eq. (3.6-9)}$$

Where, $\hbar$ is the Dirac constant, ${k_n}^m(v) \in \mathbb{N}$ and ${\omega_n}^m(v)$ are quantum numbers and the angular frequency associated to the v^{th} mode of the quantum harmonic oscillator. Here, the vector $\boldsymbol{k_n}^{\boldsymbol{m}}$ corresponds to a set of quantum numbers associated to all the normal modes ($k(1)$, $k(2)$, … $k({N_n}^m)$). In the quantum mechanical framework, the statistical probability is given by the density operator ($\hat{\rho}$), which is based on Eq. (3.6-7) and would take the form,

$$\hat{\rho} = \frac{1}{Z_{gr}} e^{\frac{\sum_{I \geq J} \hat{IJ}\,\mu_{ij} + \hat{n}\,\mu - \hat{H}}{k_B T}} \qquad \text{Eq. (3.6-10)}$$

Here, two new operators $\hat{IJ}$ and $\hat{n}$ are introduced; they act on the state vector $|S_n^m\rangle$ and give Eigen values $(i, j)_n^m$ and n respectively. Both, $\hat{IJ}$ and $\hat{n}$ operators commutate with the Hamiltonian. Further, the partition function Z_{gr} is given by,

$$Z_{gr} = Tr\left(e^{\frac{\sum_{I \geq J} \hat{IJ}\,\mu_{ij} + \hat{n}\,\mu - \hat{H}}{k_B T}} \right) \qquad \text{Eq. (3.6-11)}$$

Where Tr is the trace class. When $\hat{\rho}$ acts on the state vector $|S_n^m\rangle$, gives the probability ${P_n}^m$.

$$\hat{\rho}\,|S_n^m(\boldsymbol{k})\rangle = \frac{1}{Z_{gr}} e^{\frac{\sum_{I \geq J} \hat{IJ}\,\mu_{ij} + \hat{n}\,\mu - \hat{H}}{k_B T}}\; |S_n^m(\boldsymbol{k_n^m})\rangle$$

$$= \frac{1}{Z_{gr}} e^{\frac{\sum_{i \geq j}^{(i,j)_n^m} \mu_{ij} + n\,\mu - \sum_{\nu=1}^{N_n^m} \left(\frac{1}{2} + k_n^m(\nu)\right)\hbar\omega_n^m(\nu)}{k_B T}}\; |S_n^m(\boldsymbol{k_n^m})\rangle \qquad \text{Eq. (3.6-12)}$$

The partition function can be evaluated as,

$$Z_{gr} = \sum_{n,m} \sum_{\boldsymbol{k_n^m}} e^{\frac{\sum_{i \geq j}^{(i,j)_n^m} \mu_{ij} + n\,\mu - \sum_{\nu=1}^{N_n^m} \left(\frac{1}{2} + k_n^m(\nu)\right)\hbar\omega_n^m(\nu)}{k_B T}} \qquad \text{Eq. (3.6-13)}$$

$$= \sum_{n,m} \sum_{\boldsymbol{k_n^m}} e^{\frac{\sum_{i \geq j}^{(i,j)_n^m} \mu_{ij} + n\,\mu}{k_B T}}\; e^{\frac{-\sum_{\nu=1}^{N_n^m} \left(\frac{1}{2} + k_n^m(\nu)\right)\hbar\omega_n^m(\nu)}{k_B T}}$$

$$= \sum_{n,m} e^{\frac{\sum_{i\geq j}{}^{(i,j)_n^m}\mu_{ij}+n\,\mu}{k_B T}} \prod_{\nu=1}^{N_n^m}\left(\frac{1}{2\sinh\left(\frac{\hbar\omega_n^m(\nu)}{2k_B T}\right)}\right)$$

$$= \sum_{n,m} e^{\frac{\sum_{i\geq j}{}^{(i,j)_n^m}\mu_{ij}+n\,\mu}{k_B T}} Z_n^m$$

Where, $Z_n{}^m$ is the canonical partition function associated to a given $S_n{}^m$ microstate. It can also be written in terms Helmholtz free energy ($F_n{}^m$) of the quantum harmonic oscillator as,

$$Z_n^m = e^{-\frac{F_n^m}{k_B T}} \qquad \text{Eq. (3.6-14)}$$

Therefore, the probability distribution of $S_n{}^m$ microstates is given by,

$$P_n^m = \frac{1}{Z_{gr}} e^{\frac{\sum_{i\geq j}{}^{(i,j)_n^m}\mu_{ij}+n\,\mu-F_n^m}{k_B T}} \qquad \text{Eq. (3.6-15)}$$

Comparing Eq. (3.6-15) and Eq. (3.6-7), it can be noticed that, by using the semi quantum mechanical approach, $E_n{}^m$ is changed to $F_n{}^m$.

3.6.2.4 Ensemble averages

The ensemble averages for energy ($\langle E\rangle$), entropy (S) and composition ($\langle N_{BO}\rangle$) are related to the grand partition function by,

$$\langle E\rangle = -k_B T \ln Z_{gr} + TS + \langle N\rangle\mu \qquad \text{Eq. (3.6-16)}$$

The entropy of the liquid is split into configurational and vibrational contributions given,

$$S = -k_B \sum_{n,m} P_n^m \, ln\, P_n^m + \sum_{n,m} P_n^m S_n^m = S_{conf} + S_{vib} \qquad \text{Eq. (3.6-17)}$$

The derivations for Eq. (3.6-16) and Eq. (3.6-17) are presented in section 3.6.4.3. The vibrational energy and entropy of a $S_n{}^m$ microstate is given by,[249]

$$E_n^m = \sum_{\nu=1}^{N_n^m} \hbar\omega_n^m(\nu)\left[\frac{1}{2} + \frac{1}{e^{\frac{\hbar\omega_n^m(\nu)}{k_B T}} - 1}\right]$$

$$S_n^m = \frac{E_n^m - F_n^m}{T} \qquad \text{Eq. (3.6-18)}$$

And, the chemical composition of the glass (from Eq. (3.6-4)) is given by,

$$R_2O \text{ or } RO\ (\%) = \frac{\langle x\rangle}{1+\langle x\rangle} = \frac{4 - \langle N_{BO}\rangle}{6 - \langle N_{BO}\rangle}$$

$$SiO_2(\%) = \frac{1}{1+\langle x\rangle} = \frac{2}{6 - \langle N_{BO}\rangle} \qquad \text{Eq. (3.6-19)}$$

3.6.3 Discussion

3.6.3.1 Generalization of the model

The current model describes probability distribution of silicate units in a binary alkali or alkaline earth silicate glasses where, each microstate assumes a single structural configuration. However, the model can be further extended to take into account all structural configurations by labeling a microstate as S_n^m ($\boldsymbol{\Phi}$, $\boldsymbol{\Omega}$). Where, $\boldsymbol{\Phi}$ accounts for the complete internal structure of the silicate unit, encompassing all the vectors from $\boldsymbol{\varphi_1}$ to $\boldsymbol{\varphi_4} \in \mathbb{R}^3$ as shown in **Figure 3.6.1**. While $\boldsymbol{\Omega}$ takes into account how the neighboring units are connected to a given unit, encompassing all the vectors from $\boldsymbol{\omega_1}$ to $\boldsymbol{\omega_4} \in \mathbb{R}^3$ (**Figure 3.6.1**). Together, $\boldsymbol{\Phi}$ and $\boldsymbol{\Omega}$ consider all variations in the bond lengths and bond angles that are associated to a given silicate unit, acknowledging all possible structural configurations. Though, *n* and *m* have a discrete probability distribution, $\boldsymbol{\Phi}$ and $\boldsymbol{\Omega}$ could assume a continuous probability distribution. In this case, Eq. (3.6-2) to Eq. **(3.6-4)** change to,

$$\iint_{\boldsymbol{\Phi},\boldsymbol{\Omega}} \sum_{n,m} P_n^m(\boldsymbol{\Phi},\boldsymbol{\Omega})\, d\boldsymbol{\Phi} d\,\boldsymbol{\Omega} = 1 \qquad \text{Eq.(3.6-20)}$$

$$\iint_{\boldsymbol{\Phi},\boldsymbol{\Omega}} \sum_{n,m} E_n^m(\boldsymbol{\Phi},\boldsymbol{\Omega}) P_n^m(\boldsymbol{\Phi},\boldsymbol{\Omega})\, d\boldsymbol{\Phi} d\,\boldsymbol{\Omega} = \langle E\rangle \qquad \text{Eq. (3.6-21)}$$

$$\iint_{\boldsymbol{\Phi},\boldsymbol{\Omega}} \sum_{n,m} n P_n^m(\boldsymbol{\Phi},\boldsymbol{\Omega})\, d\boldsymbol{\Phi} d\,\boldsymbol{\Omega} = \langle N_{BO} \rangle \qquad \text{Eq. (3.6-22)}$$

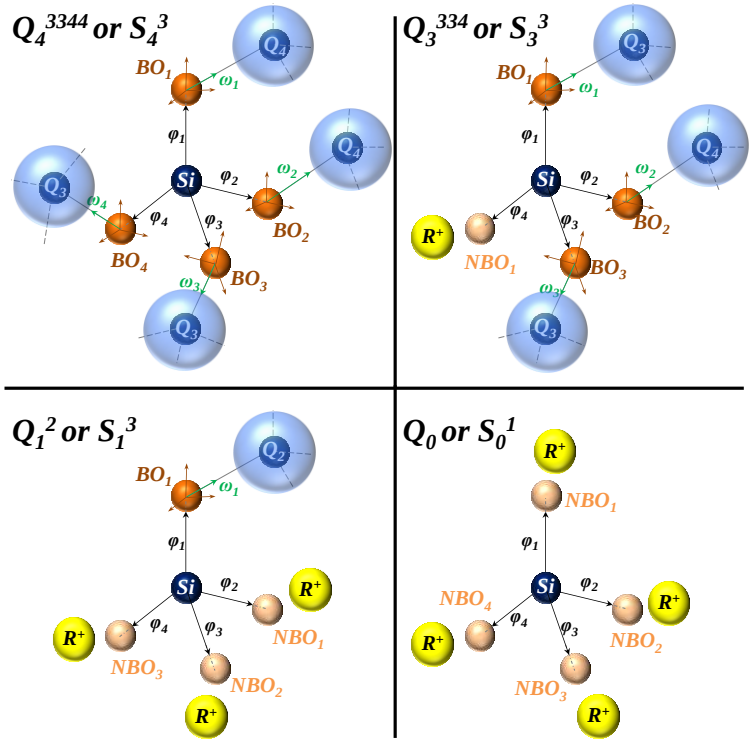

Figure 3.6.1 Examples of silicate units and basis vectors corresponding to $\boldsymbol{\Phi}$ and $\boldsymbol{\Omega}$.

In the model derived in Section 3.6.2, $\boldsymbol{\Phi} = \boldsymbol{\Phi_T}$ where, $\boldsymbol{\Phi_T}$ is the associated vector to a silicate tetrahedron; and $\boldsymbol{\Omega}$ would assume some expected value with some variance. Then, integrating P_n^m ($\boldsymbol{\Phi_T}$, $\boldsymbol{\Omega}$) over the entire space of $\boldsymbol{\Omega}$ would yield the value for P_n^m as shown in Eq. (3.6-23).

$$P_n = \sum_m P_n^m = \sum_m \iint_{\boldsymbol{\Phi},\boldsymbol{\Omega}} P_n^m(\boldsymbol{\Phi_T},\boldsymbol{\Omega}) d\boldsymbol{\Phi} d\,\boldsymbol{\Omega} \qquad \text{Eq. (3.6-23)}$$

It is also possible that $\boldsymbol{\Phi}$ and $\boldsymbol{\Omega}$ take discrete values in the case when structural units are confined to local minima. Consequently, the integrals over $\boldsymbol{\Phi}$ and $\boldsymbol{\Omega}$ (Eq.(3.6-20) to Eq. (3.6-22)) would be replaced with summation over all the states of local minima. When multi-component silicate liquid compositions are used, if the added components are network formers (e.g. Al_2O_3 or B_2O_3 added to silicates), then they could be modelled as additional network units. If units are considered to be atoms of different kind, then one can ignore the internal structure of the unit by dropping off n and $\boldsymbol{\Phi}$. In this case the model could be applicable to metallic glasses. For other oxide glasses such

as borate and phosphate systems, similarly, appropriate internal structures and external correlations should be chosen.

3.6.3.2 LLPS and crystallization

The introduction of S_n^m (or $Q_n^{ij\cdots}$) notation as opposed to previous Q_n notation is essential for answering questions concerning *LLPS* and crystallization. Because of this new notation, which takes into consideration the type of units that surround a given unit, the mixing of different units is automatically considered. Consequently, by obtaining probability distribution of S_n^m units in a given composition by the current model, the amount of *LLPS* could be calculated. This idea has been experimentally tested using the double quantum (*DQ*) *NMR* spectroscopy technique where, the probability distribution of $Q_n^{ij\cdots}$ units was measured and the amount of *LLPS* was estimated.[168,246]

Concerning crystallization, if a particular set of units, which correspond to a set of points in the *nm*–plane (**Figure 3.6.4a**), undergo crystallization, then the probability distribution P_n^m (Φ, Ω), for each S_n^m (Φ, Ω) microstate in $\Phi\Omega$–space, will be sharply peaked, and given by Dirac delta function as,

$$P_n^m(\Phi,\Omega) = \delta(\Phi - \Phi')\ \delta(\Omega - \Omega') \qquad \text{Eq. (3.6-24)}$$

Where, Φ' and Ω' are constants corresponding to a particular crystal structure. Therefore, crystallization (or crystal nucleation) of a particular set of S_n^m units in a supercooled liquid corresponds to: a collection of S_n^m units and sharpening of the P_n^m (Φ, Ω) peak in $\Phi\Omega$–space.

In the glass forming liquids, the time scales required to access the crystalline states are large. Therefore, these states can be eliminated by assuming some broad distribution of probabilities in $\Phi\Omega$–space for a given S_n^m unit. This subject of *LLPS* and crystallization within the framework of the current model will be expounded in a subsequent paper.

3.6.3.3 Structural relaxation

In last two decades, huge advances have been made in the understanding of the nature of glass and structural relaxation using the potential energy landscape (*PEL*) approach.[31,39,250,251] *PEL* approach uses a canonical ensemble of various structural configurations of large number of atoms. Our present model is fundamentally different;

where it employs a grand canonical ensemble of structural units that build the glass network and exchange network modifiers and energy from the reservoir. However, the problem of relaxation can be addressed in a similar way as in *PEL* approach using the concept of *continuously broken ergodicity* (*CBE*) as proposed by Mauro *et al*.[38] Here, we consider conditional probabilities $f_{I,J}(t)$, which correspond to a system occupying a microstate *J* after starting in a known state *I* with subsequent evolution of time *t*; accounting for the actual transition rates between different states. The conditional probabilities would satisfy:

$$\sum_{J} f_{I,J}(t) = 1 \qquad \text{Eq. (3.6-25)}$$

Where *I* and *J* are different S_n^m (Φ, Ω) microstates. In the limit of zero and infinite time evolution, the conditional probabilities reduce to Kronecker delta function ($\delta_{I,J}$) and equilibrium probabilities respectively, given by,

$$\lim_{t\to 0} f_{I,J}(t) = \delta_{I,J} \qquad \text{Eq. (3.6-26)}$$

$$\lim_{t\to \infty} f_{I,J}(t) = P_J \qquad \text{Eq. (3.6-27)}$$

The conditional entropy is given by,

$$S_J(t) = -k_B \sum_{J} f_{I,J}(t) \ln f_{I,J}(t) \qquad \text{Eq.(3.6-28)}$$

The time evolution of the expected value of the configurational is calculated by,

$$\langle S(t) \rangle = \sum_{I} P_I S_J(t) \qquad \text{Eq. (3.6-29)}$$

The time dependent conditional probabilities $f_{I,J}(t)$ can be obtained by solving hierarchical master equations (Eq.(3.6-30)).

$$\frac{df_{I,J}(t)}{dt} = \sum_{K\neq J} W_{K\to J}\big(T(t)\big) f_{I,K}(t) - \sum_{K\neq J} W_{J\to K}\big(T(t)\big) f_{I,J}(t) \qquad \text{Eq.(3.6-30)}$$

Where, $W_{K\to J}$ and $W_{J\to K}$ are the associated reaction rate constants. After a time evolution t, the probability of the state J is given by,

$$P_J(t) = \sum_I P_I \, f_{I,J}(t) \qquad \text{Eq. (3.6-31)}$$

The relaxation takes place over the entire phase space $\boldsymbol{\Gamma_s}$ subjected to available thermal energy and observational time (τ_{obs}). Here we report structural relaxation in a lithium silicate glass from the perspective of the current model using *NMR* spectroscopy. **Figure 3.6.2** shows *1D-NMR* spectra of a binary lithium silicate glass of composition 28% Li_2O - 72% SiO_2 (in moles). One spectrum was recorded on the glass directly quenched from the melt and the other was recorded on the glass quenched and then annealed at 460 ºC for 75 hours. The two spectra show clear differences indicating the structural relaxation. The details of the experimental procedure can be found in the appendix (Section 3.6.4.4).

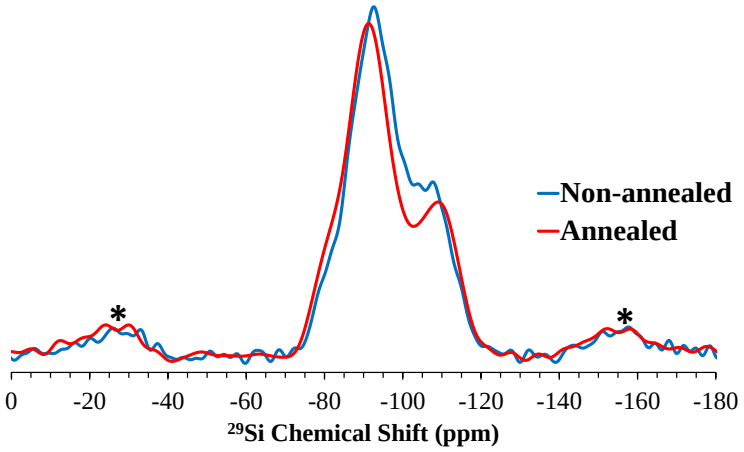

Figure 3.6.2 *NMR* spectra of annealed and non-annealed (as quenched) $28Li_2O$-$72SiO_2$ glass, showing structural relaxation. Asterisks indicate spinning side bands.

3.6.3.4 Test of the model

In this section we show how the proposed model can be used in studying silicate based glasses (or liquids) in conjunction with *NMR* spectroscopy by using an example. The purpose of this section is for the illustration of the usefulness and applicability of the current model.

The chemical shielding on a particular ^{29}Si nucleus depends on the chemical environment around that nucleus. Therefore the ^{29}Si isotropic chemical shift (δ_{iso}) of

nucleus would be function of all the structural parameters n, m, $\boldsymbol{\Phi}$ and $\boldsymbol{\Omega}$: $\delta_{iso}(n, m, \boldsymbol{\Phi}, \boldsymbol{\Omega})$. Since $\boldsymbol{\Phi}$ and $\boldsymbol{\Omega}$ have variance with some expected value, δ_{iso} also would have corresponding variance (σ^2) and an expected value, $\langle\delta_{iso}\rangle$. The variance is given by,[252]

$$\sigma(n,m)^2 = \langle\delta_{iso}(n,m)^2\rangle - \langle\delta_{iso}(n,m)\rangle^2 \qquad \text{Eq. (3.6-32)}$$

We can assume that the variation in δ_{iso} for a given S_n^m unit approximated to a normal distribution (**Figure 3.6.3, Variance in S_n^m**). This would be a component of the spectrum associated to a particular S_n^m unit; and the spectrum of the whole sample, a sum of individual components (Eq. (3.6-33)), is shown in **Figure 3.6.3**. This spectrum corresponds to a hypothetical composition with 28 % R_2O and is generated by calculating the probabilities P_n^m in Eq. (3.6-15) by assuming some realistic values of F_n^m, $\delta_{iso}(n, m)$ and $\sigma(n, m)$ (the procedure is presented in section 3.6.4.5). Then the intensity $I(\delta_{iso})$ of the *NMR* spectrum is given by,

$$I(\delta_{iso}) \propto \sum_{n,m} \frac{P_n^m}{\sigma(n,m)\sqrt{2\pi}} e^{-\frac{(\delta_{iso}-\langle\delta_{iso}(n,m)\rangle)^2}{2\sigma(n,m)^2}} \qquad \text{Eq. (3.6-33)}$$

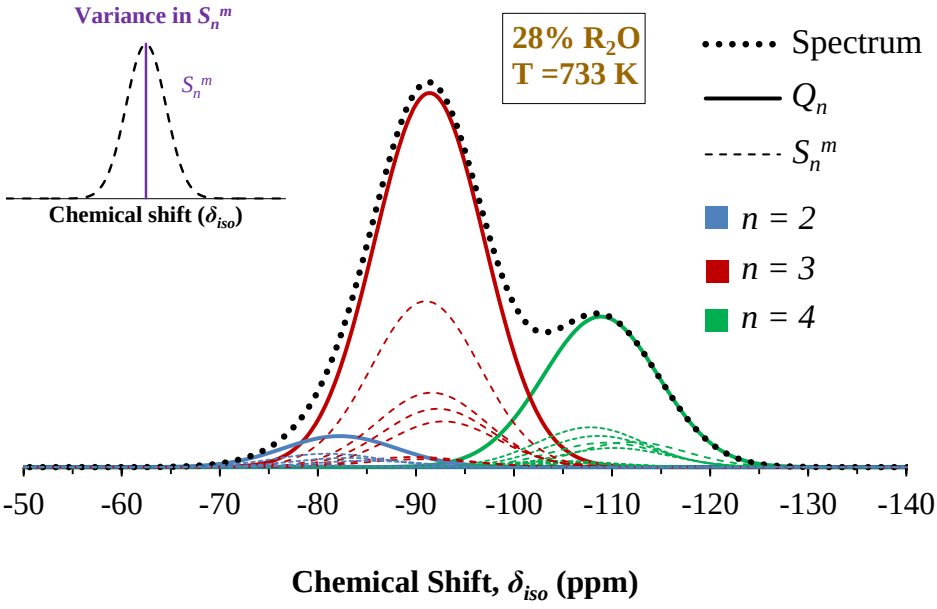

Figure 3.6.3 Simulated *NMR* spectrum of a hypothetical composition using the current model.

This way, using the current model, *NMR* spectrum of a given sample could be theoretically computed. Further, using the probability distribution, properties of the liquids can be computed. The variation of properties with temperature for specific heat, entropy and molar volume are presented in supplementary data (Section 3.6.4.6). In

order to show relaxation behavior of silicate units of this hypothetical composition, we used a relatively simple concept called *broken ergodicity* (*BE*) proposed by Palmer[37] as opposed to *CBE* discussed in the previous section. In *BE*, we divide the phase space $\boldsymbol{\Gamma_s}$ into set of non-ergodic disjoint components where, within each component internal ergodicity still exists. In this present example, we divided the phase space (*nm*–plane, **Figure 3.6.4a**) into three components: (a) $\boldsymbol{\Gamma_1} = \{S_4^1\}$, (b) $\boldsymbol{\Gamma_2} = \{S_4^2, S_3^1\}$ and (c) $\boldsymbol{\Gamma_3} = \boldsymbol{\Gamma_s} \cap \{S_4^1, S_4^2, S_3^1\}$. The reason for selecting these components is because, the structural units belonging to $\boldsymbol{\Gamma_1}$ and $\boldsymbol{\Gamma_2}$ exist in highly polymerized network, and therefore they wouldn't have sufficient time to maintain the ergodicity during the fast quenching of the melt. By enforcing *BE*, probability distribution at some observational time (τ_{obs}) is obtained (**Figure 3.6.4a**). The *NMR* spectra in **Figure 3.6.4b** are generated by,

1. Probability distribution at high temperature (1600 K) was obtained (which corresponds to $t = 0$).

2. Then under the *BE* condition, new probability distribution at 775 K was obtained (which corresponds to $t = \tau_{obs}$).

3. Probability distribution without *BE* condition would yield equilibrium probability at 775 K (corresponds to $t = \infty$).

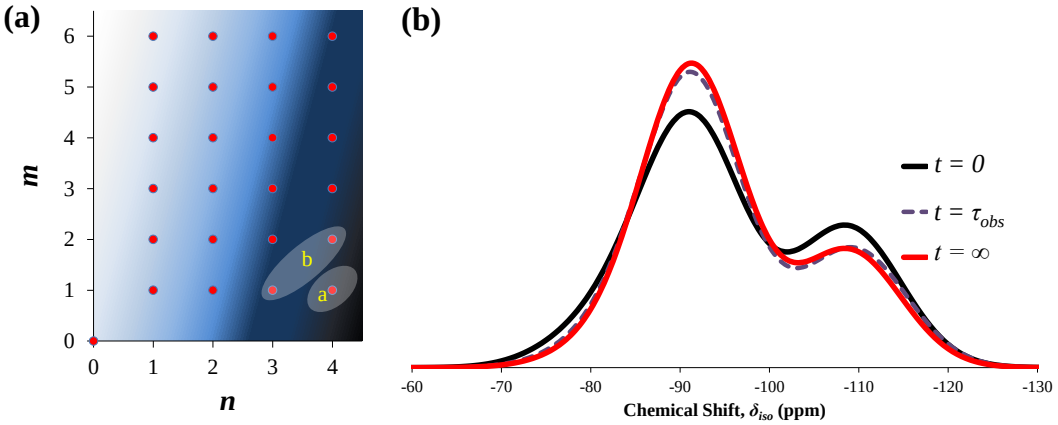

Figure 3.6.4 (a) Phase space in *n* and *m* showing the gradient of polymerization: decreasing from dark to light. (b) Relaxation of silicate structural units with time.

The relaxation behavior simulated in **Figure 3.6.4b** shows characteristics similar to the experimental observations shown in **Figure 3.6.2**. Therefore, the as quenched glass without annealing contains a lot of memory effects which can be probed by *NMR* spectroscopy. This behavior needs to be evaluated for multiple compositions in future

studies. Using the same vibrational frequencies, the variation of probability distribution with composition is plotted in **Figure 3.6.5**.

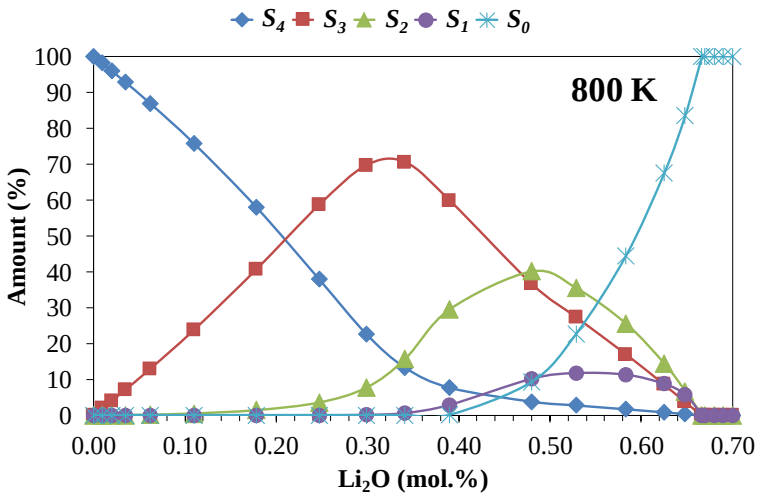

Figure 3.6.5 Variation of probability distribution with composition at 800 K. Dots represent the simulated data points and the lines are just connecting the points to guide the eyes.

3.6.4 Appendix

3.6.4.1 Network connectivity constraints

In a given glass composition, *BO*s characterized by O_{ij} must be conserved. Therefore Eq. (3.6-34) to Eq.(3.6-43) corresponding to 10 different O_{ij} oxygens must hold. Where, p_4^{ijkl}, p_3^{ijk}, p_2^{ij} and p_1^{i}, are the probabilities (notice lower case '*p*' as opposed to upper case '*P*' in *S* notation) associated with Q_4^{ijkl}, Q_3^{ijk}, Q_2^{ij} and Q_1^{i}, units. The *Q* notation is employed here because it is easier to see the connection between right and left hand sides of the equations.

***O*$_{11}$:** $p_1^1 = p_1^1$ Eq. (3.6-34)

***O*$_{12}$:** $p_1^2 = \sum_{j\neq 1} p_2^{1j} + 2p_2^{11}$ Eq. (3.6-35)

***O*$_{13}$:**

$$p_1^3 = \sum_{j,k\neq 1} p_3^{1jk} + 2\sum_{k\neq 1} p_3^{11k} + 3p_3^{111}$$ Eq. (3.6-36)

O₁₄: $$p_1^4 = \sum_{j,k,l\neq 1} p_4^{1jkl} + 2\sum_{k,l\neq 1} p_4^{11kl} + 3\sum_{l\neq 1} p_4^{111l} + 4p_4^{1111}$$ Eq. (3.6-37)

O₂₂: $$\sum_{j\neq 2} p_2^{2j} + 2p_2^{22} = \sum_{j\neq 2} p_2^{2j} + 2p_2^{22}$$ Eq. (3.6-38)

O₂₃: $$\sum_{j\neq 3} p_2^{3j} + 2p_2^{33} = \sum_{j,k\neq 2} p_3^{2jk} + 2\sum_{k\neq 2} p_3^{22k} + 3p_3^{222}$$ Eq. (3.6-39)

O₂₄: $$\sum_{j\neq 4} p_2^{4j} + 2p_2^{44} = \sum_{j,k,l\neq 2} p_4^{2jkl} + 2\sum_{k,l\neq 2} p_4^{22kl} + 3\sum_{l\neq 2} p_4^{222l} + 4p_4^{2222}$$ Eq.(3.6-40)

O₃₃: $$\sum_{j,k\neq 3} p_3^{3jk} + 2\sum_{k\neq 3} p_3^{33k} + 3p_3^{333} = \sum_{j,k\neq 3} p_3^{3jk} + 2\sum_{k\neq 3} p_3^{33k} + 3p_3^{333}$$ Eq.(3.6-41)

O₃₄: $$\sum_{j,k\neq 4} p_3^{4jk} + 2\sum_{k\neq 4} p_3^{44k} + 3p_3^{444} = \sum_{j,k,l\neq 4} p_4^{3jkl} + 2\sum_{k,l\neq 4} p_4^{33kl} + 3\sum_{l\neq 4} p_4^{333l} + 4p_4^{3333}$$ Eq. (3.6-42)

O₄₄: $$\sum_{j,k,l\neq 4} p_4^{4jkl} + 2\sum_{k,l\neq 4} p_4^{44kl} + 3\sum_{l\neq 4} p_4^{444l} + 4p_4^{4444} = \sum_{j,k,l\neq 4} p_4^{4jkl} + 2\sum_{k,l\neq 4} p_4^{44kl} + 3\sum_{l\neq 4} p_4^{444l} + 4p_4^{4444}$$ Eq.(3.6-43)

Eq. (3.6-34) to Eq.(**3.6-43)** can be represented as follows,

$$\sum_{n,m} (i,j)_n^m P_n^m = k_{ij}$$ Eq. (3.6-44)

The coefficients $(i, j)_n^m$ are constants associated to each equation representing a given O_{ij} *BO*. Further, according to Eq. (3.6-34) to Eq.(3.6-43) the values of $(i, j)_n^m = 0$ $\forall\ i = j$; and $k_{ij} = 0\ \forall\ i, j$. The values of the constants are presented in the **Table 3.6.1**.

3.6.4.2 Derivation for the probabilities P_n^m

The solution given by Eq. (3.6-7) is obtained from the Lagrange function $\mathcal{L}(P_n^m)$ with the Lagrange multipliers α, β and γ given by

$$\mathcal{L}(P_n^m) = k_B \sum_{n,m} (P_n^m \ln P_n^m) + \alpha \left[\sum_{n,m} P_n^m - 1\right] + \beta \left[\sum_{n,m} E_n^m P_n^m - \langle E \rangle\right] + \gamma \left[\sum_{n,m} n P_n^m - 2\langle N_{BO} \rangle\right] + \sum_{i,j} \gamma_{ij} \left[\sum_{n,m} (i,j)_n^m P_n^m - k_{ij}\right] \quad \text{Eq. (3.6-45)}$$

Differentiating $\mathcal{L}(P_n{}^m)$ with respect to $P_n{}^m$ would equal zero,

$$\frac{\partial \mathcal{L}(P_n^m)}{\partial P_n^m} = k_B(1 + \ln P_n^m) + \alpha + \beta E_n^m + \gamma n + \sum_{i,j} \gamma_{ij} (i,j)_n^m = 0$$

Rearranging,

$$\ln P_n^m = -\ln Z_{gr} - \frac{\beta E_n^m}{k_B} - \frac{n\gamma}{k_B} - \frac{\sum_{i,j} (i,j)_n^m \gamma_{ij}}{k_B} \quad \text{Eq. (3.6-46)}$$

Where, $\ln Z_{gr} = \frac{(\alpha + k_B)}{k_B}$ and substituting Eq. (3.6-46) in Eq. (3.6-7)

$$S = -k_B \sum_{n,m} \left(- P_n^m \ln Z_{gr} - P_n^m \frac{\beta E_n^m}{k_B} - P_n^m \frac{n\gamma}{k_B} - P_n^m \frac{\sum_{i,j} \gamma_{ij} (i,j)_n^m}{k_B} \right)$$

Solving the above equation using the Eq. (3.6-2) to Eq. **(3.6-5)** gives,

$$S = k_B \ln Z_{gr} + \beta \langle E \rangle + 2\gamma \langle N_{BO} \rangle + \sum_{i,j} \gamma_{ij} k_{ij}$$

Rearranging,

$$\langle E \rangle = \frac{1}{\beta} S - \frac{k_B}{\beta} \ln Z_{gr} - \frac{\gamma}{\beta} (2\langle N_{BO} \rangle) - \sum_{i,j} \frac{\gamma_{ij}}{\beta} k_{ij}$$

Differentiating,

$$d\langle E \rangle = \frac{1}{\beta} dS - \frac{k_B}{\beta} d \ln Z_{gr} - \frac{\gamma}{\beta} d(2\langle N_{BO} \rangle) - \sum_{i,j} \frac{\gamma_{ij}}{\beta} dk_{ij}$$

Comparing the above equation with the *fundamental thermodynamic relation* shown in Eq. (3.6-47),[42]

$$dE = TdS - PdV + \sum \mu_i dn_i \qquad \text{Eq. (3.6-47)}$$

Would yield,

$$\beta = \frac{1}{T} \qquad \text{Eq. (3.6-48)}$$

$$\gamma = -\frac{\mu}{T} \qquad \text{Eq. (3.6-49)}$$

$$\gamma_{ij} = -\frac{\mu_{ij}}{T} \qquad \text{Eq. (3.6-50)}$$

Therefore, substituting Eq. (3.6-47) to Eq. **(3.6-50)** into Eq. (3.6-46) and rearranging gives,

$$P_n^m = \frac{1}{Z_{gr}} e^{\frac{\sum_{i,j}(i,j)_n^m \mu_{ij} + n\,\mu - E_n^m}{k_B T}} \qquad \text{Eq. (3.6-51)}$$

3.6.4.3 Entropy of the liquid

The entropy of the liquid is given by,

$$S = -k_B \sum_{n,m,\boldsymbol{k}} P_n^m(\boldsymbol{k}) \ln P_n^m(\boldsymbol{k}) \qquad \text{Eq. (3.6-52)}$$

$$S = -k_B \sum_{n,m,\boldsymbol{k}} P_n^m(\boldsymbol{k}) \left[-\ln Z_{gr} + \frac{\sum_{i \geq j}(i,j)_n^m \mu_{ij}}{k_B T} + \frac{n\,\mu}{k_B T} - \sum_{\nu=1}^{N_n^m} \left(\frac{1}{2} + k(\nu)\right) \frac{\hbar \omega_n^m(\nu)}{k_B T} \right]$$

$$S = k_B \ln Z_{gr} - \frac{\langle N_{BO} \rangle \mu}{T} + \sum_{n,m,\boldsymbol{k}} P_n^m(\boldsymbol{k}) \sum_{\nu=1}^{N_n^m} \left(\frac{1}{2} + k(\nu)\right) \frac{\hbar \omega_n^m(\nu)}{T}$$

$$S = k_B \ln Z_{gr} - \frac{\langle N_{BO} \rangle \mu}{T} + \sum_{n,m} P_n^m \sum_{\nu=1}^{N_n^m} \frac{\hbar \omega_n^m(\nu)}{T} \left[\frac{1}{2} + \frac{1}{e^{\frac{\hbar \omega_n^m(\nu)}{k_B T}} - 1} \right]$$

$$S = k_B \ln Z_{gr} - \frac{\langle N_{BO} \rangle \mu}{T} + \sum_{n,m} \frac{P_n^m E_n^m}{T}$$

$$S = k_B \ln Z_{gr} - \frac{\langle N_{BO} \rangle \mu}{T} + \frac{\langle E \rangle}{T}$$

Further, the entropy can be split into configurational and vibrational parts,

$$S = k_B \, ln \, Z_{gr} - \frac{\langle N_{BO} \rangle \mu}{T} + \sum_{n,m} \frac{P_n^m E_n^m}{T}$$

$$S = k_B \, ln \, Z_{gr} - \frac{\langle N_{BO} \rangle \mu}{T} + \sum_{n,m} \frac{P_n^m (F_n^m + T S_n^m)}{T}$$

$$S = \sum_{n,m} P_n^m \left[k_B \ln Z_{gr} - \frac{\sum_{i \geq j} (i,j)_n^m \mu_{ij}}{T} - \frac{n \mu}{T} + \frac{F_n^m}{T} + S_n^m \right]$$

$$S = -k_B \sum_{n,m} P_n^m \left[\ln Z_{gr} + \frac{\sum_{i \geq j} (i,j)_n^m \mu_{ij}}{k_B T} + \frac{n \mu}{k_B T} - \frac{F_n^m}{k_B T} \right] + \sum_{n,m} P_n^m S_n^m$$

$$S = -k_B \sum_{n,m} P_n^m \ln P_n^m + \sum_{n,m} P_n^m S_n^m$$

$$S = S_{conf} + S_{vib} \qquad \text{Eq. (3.6-53)}$$

3.6.4.4 Experimental procedure

For the preparation of the glass, SiO_2 and Li_2CO_3 with purity > 99% were weighed in required amounts, and mixed by ball milling then calcined at 800 ºC in alumina crucibles for 1 h in air. The calcined powder was crushed in a mortar and transferred to a Pt crucible for melting at a temperature of 1550 ºC for 1 h in air. Bulk (monolithic) bar shaped glasses were prepared by pouring the melt on a bronze mold. One sample was annealed at 460 ºC for 75 h. X-ray diffraction analysis (not shown) confirmed that the samples were fully amorphous.

^{29}Si *MAS-NMR* spectra were recorded on both annealed and non-annealed glass samples crushed into fine powders. The *NMR* spectrometer (BRUKER Avance III) was operated at a Larmor frequency of 79.5 MHz with a 9.4 T magnetic field, using a 7 mm rotor rotating at 5 kHz. The samples were excited with a 90º flip angle using 900 s delay

time. Both spectra were obtained after Fourier Transformation of 64 scans of Free Induction Decays (FID). Tetramethylsilane was used as chemical shift reference at 0 ppm.

3.6.4.5 Details of simulation

The *NMR* spectrum obtained from the annealed glass was deconvoluted using DMfit software[228] for the units Q_2, Q_3 and Q_4 using mixed Gaussian/Lorentzian line shapes. The amounts of the units obtained were, 6%, 66% and 28% for the units Q_2, Q_3 and Q_4 respectively. Using the current model, the S_n^m distribution was simulated by fitting the appropriate ω_n^m values in order to simulate a realistic probability distribution that is in agreement with the experimentally measured distribution. The fitted ω_n^m values and the probability distributions are presented in **Table 3.6.2 and Table 3.6.3** respectively.

Table 3.6.2 Vibrational frequencies (cm^{-1}) used for the simulation of the model.

S_n^m	$\omega_n^m(1)$	$\omega_n^m(2)$	$\omega_n^m(3)$	$\omega_n^m(4)$	$\omega_n^m(5)$	$\omega_n^m(6)$	$\omega_n^m(7)$	$\omega_n^m(8)$	$\omega_n^m(9)$
S_4^1	1190	1190	1190	990	540	540	540	330	330
S_4^2	1200	1200	1200	1000	550	550	550	340	340
S_4^3	1200	1200	1200	1000	550	550	550	340	340
S_4^4	1200	1200	1200	1000	550	550	550	340	340
S_4^5	1200	1200	1200	1000	550	550	550	340	340
S_4^6	1200	1200	1200	1000	550	550	550	340	340
S_4^7	1200	1200	1200	1000	550	550	550	340	340
S_4^8	1200	1200	1200	1000	550	550	550	340	340
S_4^9	1200	1200	1200	1000	550	550	550	340	340
S_4^{10}	1200	1200	1200	1000	550	550	550	340	340
S_4^{11}	1200	1200	1200	1000	550	550	550	340	340
S_4^{12}	1200	1200	1200	1000	550	550	550	340	340
S_4^{13}	1200	1200	1200	1000	550	550	550	340	340
S_4^{14}	1200	1200	1200	1000	550	550	550	340	340
S_4^{15}	1200	1200	1200	1000	550	550	550	340	340
S_4^{16}	1200	1200	1200	1000	550	550	550	340	340
S_4^{17}	1200	1200	1200	1000	550	550	550	340	340
S_4^{18}	1200	1200	1200	1000	550	550	550	340	340

S_4^{19}	1200	1200	1200	1000	550	550	550	340	340
S_4^{20}	1200	1200	1200	1000	550	550	550	340	340
S_4^{21}	1200	1200	1200	1000	550	550	550	340	340
S_4^{22}	1200	1200	1200	1000	550	550	550	340	340
S_4^{23}	1200	1200	1200	1000	550	550	550	340	340
S_4^{24}	1200	1200	1200	1000	550	550	550	340	340
S_4^{25}	1200	1200	1200	1000	550	550	550	340	340
S_4^{26}	1200	1200	1200	1000	550	550	550	340	340
S_4^{27}	1200	1200	1200	1000	550	550	550	340	340
S_4^{28}	1200	1200	1200	1000	550	550	550	340	340
S_4^{29}	1200	1200	1200	1000	550	550	550	340	340
S_4^{30}	1200	1200	1200	1000	550	550	550	340	340
S_4^{31}	1200	1200	1200	1000	550	550	550	340	340
S_4^{32}	1200	1200	1200	1000	550	550	550	340	340
S_4^{33}	1200	1200	1200	1000	550	550	550	340	340
S_4^{34}	1200	1200	1200	1000	550	550	550	340	340
S_4^{35}	1200	1200	1200	1000	550	550	550	340	340
S_3^{1}	1100	970	970	720	720	530	400	160	160
S_3^{2}	1100	970	970	720	720	530	400	160	160
S_3^{3}	1100	970	970	720	720	530	400	160	160
S_3^{4}	1090	960	960	710	710	520	390	150	150
S_3^{5}	1100	970	970	720	720	530	400	160	160
S_3^{6}	1100	970	970	720	720	530	400	160	160
S_3^{7}	1100	970	970	720	720	530	400	160	160
S_3^{8}	1100	970	970	720	720	530	400	160	160
S_3^{9}	1100	970	970	720	720	530	400	160	160
S_3^{10}	1100	970	970	720	720	530	400	160	160
S_3^{11}	1100	970	970	720	720	530	400	160	160
S_3^{12}	1100	970	970	720	720	530	400	160	160
S_3^{13}	1100	970	970	720	720	530	400	160	160
S_3^{14}	1100	970	970	720	720	530	400	160	160
S_3^{15}	1100	970	970	720	720	530	400	160	160
S_3^{16}	1100	970	970	720	720	530	400	160	160
S_3^{17}	1100	970	970	720	720	530	400	160	160

S_3^{18}	1100	970	970	720	720	530	400	160	160
S_3^{19}	1100	970	970	720	720	530	400	160	160
S_3^{20}	1100	970	970	720	720	530	400	160	160
S_2^{1}	1070	1020	930	800	530	490	420	330	220
S_2^{2}	1070	1020	930	800	530	490	420	330	220
S_2^{3}	1070	1020	930	800	530	490	420	330	220
S_2^{4}	1070	1020	930	800	530	490	420	330	220
S_2^{5}	1070	1020	930	800	530	490	420	330	220
S_2^{6}	1060	1010	920	790	520	480	410	320	210
S_2^{7}	1070	1020	930	800	530	490	420	330	220
S_2^{8}	1070	1020	930	800	530	490	420	330	220
S_2^{9}	1070	1020	930	800	530	490	420	330	220
S_2^{10}	1070	1020	930	800	530	490	420	330	220
S_1^{1}	1050	1050	1000	760	760	490	410	410	300
S_1^{2}	1050	1050	1000	760	760	490	410	410	300
S_1^{3}	1050	1050	1000	760	760	490	410	410	300
S_1^{4}	1050	1050	1000	760	760	490	410	410	300
S_0^{1}	1000	1000	1000	730	730	430	400	400	400

Table 3.6.3 Probability distributions obtained from simulation.

	P_n^m			
	800 K	***1600 K***	***775 K***	***775 K***
	Equilibrium	*Equilibrium*	*Equilibrium*	*Broken Ergodicity*
S_4^{1}	0.043886	0.058121	0.043378	0.089768
S_4^{2}	0.033486	0.047046	0.032849	0.024303
S_4^{3}	0.042741	0.050532	0.042276	0.032541
S_4^{4}	0.054553	0.054277	0.054408	0.044558
S_4^{5}	0.069630	0.058298	0.070021	0.062161
S_4^{6}	0.005182	0.012706	0.004848	0.003959
S_4^{7}	0.006614	0.013648	0.006239	0.005528
S_4^{8}	0.008441	0.014659	0.008029	0.007833
S_4^{9}	0.010774	0.015745	0.010334	0.011227
S_4^{10}	0.001023	0.003686	0.000921	0.001000

S_4^{11}	0.001306	0.003959	0.001185	0.001446
S_4^{12}	0.001667	0.004252	0.001525	0.002105
S_4^{13}	0.000202	0.001069	0.000175	0.000274
S_4^{14}	0.000258	0.001148	0.000225	0.000403
S_4^{15}	0.000000	0.000003	0.000000	0.000000
S_4^{16}	0.000027	0.000395	0.000022	0.000027
S_4^{17}	0.000035	0.000425	0.000029	0.000040
S_4^{18}	0.000044	0.000456	0.000037	0.000058
S_4^{19}	0.000057	0.000490	0.000047	0.000086
S_4^{20}	0.000005	0.000115	0.000004	0.000008
S_4^{21}	0.000007	0.000123	0.000005	0.000011
S_4^{22}	0.000009	0.000132	0.000007	0.000017
S_4^{23}	0.000001	0.000033	0.000001	0.000002
S_4^{24}	0.000001	0.000036	0.000001	0.000003
S_4^{25}	0.000000	0.000010	0.000000	0.000001
S_4^{26}	0.000000	0.000004	0.000000	0.000000
S_4^{27}	0.000000	0.000004	0.000000	0.000000
S_4^{28}	0.000000	0.000004	0.000000	0.000000
S_4^{29}	0.000000	0.000001	0.000000	0.000000
S_4^{30}	0.000000	0.000001	0.000000	0.000000
S_4^{31}	0.000000	0.000000	0.000000	0.000000
S_4^{32}	0.000000	0.000000	0.000000	0.000000
S_4^{33}	0.000000	0.000000	0.000000	0.000000
S_4^{34}	0.000000	0.000000	0.000000	0.000000
S_4^{35}	0.000000	0.000000	0.000000	0.000000
S_3^{1}	0.079954	0.090306	0.079263	0.062813
S_3^{2}	0.102051	0.096998	0.102008	0.086767
S_3^{3}	0.130255	0.104185	0.131281	0.121907
S_3^{4}	0.290382	0.158398	0.299416	0.307641
S_3^{5}	0.013837	0.023876	0.013164	0.013321
S_3^{6}	0.017661	0.025645	0.016941	0.019147
S_3^{7}	0.022542	0.027545	0.021803	0.027745

S_3^8	0.002395	0.006312	0.002186	0.003096
S_3^9	0.003056	0.006780	0.002814	0.004532
S_3^{10}	0.000414	0.001669	0.000363	0.000749
S_3^{11}	0.000068	0.000711	0.000056	0.000091
S_3^{12}	0.000087	0.000764	0.000072	0.000133
S_3^{13}	0.000111	0.000821	0.000093	0.000196
S_3^{14}	0.000012	0.000188	0.000009	0.000022
S_3^{15}	0.000015	0.000202	0.000012	0.000033
S_3^{16}	0.000002	0.000050	0.000002	0.000005
S_3^{17}	0.000000	0.000006	0.000000	0.000000
S_3^{18}	0.000000	0.000006	0.000000	0.000000
S_3^{19}	0.000000	0.000001	0.000000	0.000000
S_3^{20}	0.000000	0.000000	0.000000	0.000000
S_2^1	0.011059	0.025301	0.010359	0.010118
S_2^2	0.016108	0.029817	0.015246	0.016790
S_2^3	0.023463	0.035140	0.022440	0.028198
S_2^4	0.002184	0.007339	0.001967	0.002703
S_2^5	0.003181	0.008650	0.002896	0.004597
S_2^6	0.000729	0.002883	0.000641	0.001302
S_2^7	0.000000	0.000000	0.000000	0.000000
S_2^8	0.000000	0.000000	0.000000	0.000000
S_2^9	0.000000	0.000000	0.000000	0.000000
S_2^{10}	0.000000	0.000000	0.000000	0.000000
S_1^1	0.000188	0.002244	0.000155	0.000254
S_1^2	0.000294	0.002761	0.000245	0.000480
S_1^3	0.000000	0.000000	0.000000	0.000000
S_1^4	0.000000	0.000020	0.000000	0.000001
S_0^1	0.000000	0.000001	0.000000	0.000000

3.6.4.6 Properties of the system

Three properties of the system were generated by taking the glass transition to be at 800 K: heat capacity, entropy and molar volume (**Figure 3.6.6**). The molar volumes are calculated by the equation,

$$V = \sum_{n,m} v_n^m(T) P_n^m(T) \qquad \text{Eq. (3.6-54)}$$

Where,

$$v_n^m(T) = \alpha_n^m + \beta_n^m T \qquad \text{Eq. (3.6-55)}$$

And α_n^m and β_n^m take the following values,

	$\boldsymbol{\alpha_n^m}$	$\boldsymbol{\beta_n^m}$
	cm^3	cm^3K^{-1}
$\boldsymbol{S_0^m}$	8.29×10^{-23}	8.31×10^{-28}
$\boldsymbol{S_1^m}$	6.90×10^{-23}	6.92×10^{-28}
$\boldsymbol{S_2^m}$	5.94×10^{-23}	5.96×10^{-28}
$\boldsymbol{S_3^m}$	5.08×10^{-23}	5.09×10^{-28}
$\boldsymbol{S_4^m}$	4.40×10^{-23}	4.41×10^{-28}

The molar volume is given by,

$$V_M = VN_A x_{Si_2O}$$

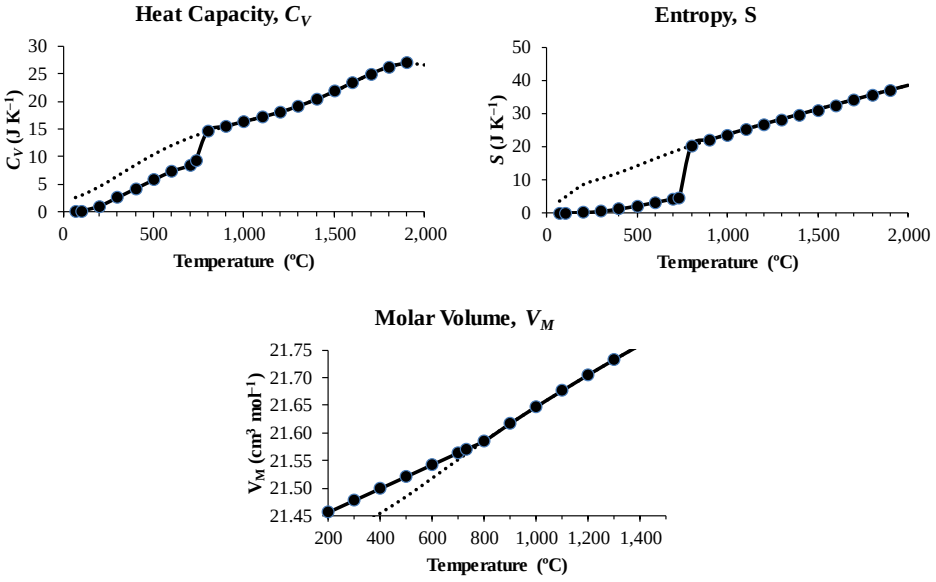

Figure 3.6.6 Variation of some properties with temperature according to the current model.

3.7 Structure and thermal relaxation of network units and crystallization of lithium silicate based glasses doped with oxides of Al and B

Anuraag Gaddam [a, b], Hugo R Fernandes [a], Lionel Montagne [b], Bertrand Doumert [b], José M.F. Ferreira [a]

[a] Department of Materials and Ceramics Engineering, University of Aveiro, CICECO, 3810-193 Aveiro, Portugal.

[b] Univ. Lille, CNRS, Centrale Lille, ENSCL, Univ. Artois, UMR 8181 - UCCS - Unité de Catalyse et Chimie du Solide, F-59000 Lille, France.

Physical Chemistry Chemical Physics (Submitted)

Abstract

The current study reports on the relaxation behaviour of lithium silicate based glasses as probed by NMR spectroscopy. A total of four glass compositions were studied with the parent composition being $28Li_2O–72SiO_2$, and added dopants of Al and B. All the compositions showed significant differences in the NMR spectra of both annealed and non-annealed glasses demonstrating the structural relaxation behaviour. We extended our binary statistical mechanical model to these complex compositions in order to study the relaxation behaviour. By the combined use of the extended statistical mechanical model and broken ergodicity, we shed light on the mechanism of structural relaxation as understood by NMR spectroscopy. We studied the crystallization behaviour of the glasses and reported on the variations of the residual glass composition changes in the crystallization fraction.

3.7.1 Introduction

Glasses are disordered materials due to the lack of periodicity in their long-range structures, which are formed by the cooling of molten inorganic products to a rigid condition without crystallization [31,253]. From the thermodynamic point of view, glasses are non-equilibrium materials because their properties that are pressure, temperature and composition dependent [39,254,255] evolve as the glass continually relaxes toward its corresponding metastable equilibrium liquid state [256,257].

Investigations into the structure−property relationships in silicate glasses are of great importance for understanding a broad range of magmatic processes in earth science and for compositional design and processing optimization of commercial glasses and glass-ceramics [8,258,259]. The binary alkali and alkaline-earth silicate glasses have served as model systems in understanding and developing structure−property relationships in multicomponent silicate glasses. The structures of these binary silicate glasses have therefore been studied extensively in the literature over the last several decades, using a wide variety of spectroscopic and diffraction techniques [258,260,261]. ^{29}Si nuclear magnetic resonance (NMR) spectroscopy has been shown to be a unique and powerful tool for studying the connectivity of SiO_4 tetrahedra in the structural network in these glasses as described by the Q_n-speciation [17,261]. In the Q_n terminology Q represents the tetrahedral unit and n is the number of bridging oxygens (*BO*) atoms, *i.e.* Si−O−Si linkages, per tetrahedron [262–264]. For silicon compounds, n varies between 0 and 4, where Si is a central tetrahedral atom ranging from Q_0, which represents orthosilicates SiO_4^{4-}, Q_4 (tectosilicates), Q_3, Q_2 and Q_1 representing intermediate silicate structures. The Si−O−Si linkages progressively break to form non-bridging oxygen (*NBO*) upon addition of modifier alkali or alkaline-earth oxides to SiO_2 such that Q_n species are converted to Q_{n-1} species and the network connectivity decreases. ^{11}B NMR is a useful technique in identifying the relative amounts of 4– and 3–coordinated boron labelled by the notation B_{IV} and $B_{III,}$ respectively. In glass compositions, both borate and silicate units undergo speciation reaction given by Eq. **(**3.7-1) and Eq**. (**3.7-2).

$$2Q_n \leftrightarrow Q_{n-1} + Q_{n+1} \qquad \text{Eq. (3.7-1)}$$

$$B_{IV} \leftrightarrow B_{IIIs} + NBO$$
$$B_{IIIs} + NBO \leftrightarrow B_{IIIa} \qquad \text{Eq. (3.7-2)}$$

The subscripts correspond to asymmetric (*a*) and symmetric (*s*) *i.e.* boron with and without a *NBO*. Therefore, a given borate unit fluctuates between several structural states [265]. Many researchers have dedicated their efforts on the study of structure of glasses in diverse systems such (*e.g.* silicates [118,266–268], borates [269–271], phosphates [272,273], borosilicates [274,275], etc.), using simple binary or complex multicomponent glass compositions. Our previous studies done by some of the authors also focused on understanding the effects of small amounts of Al and B on lithium silicate compositions [193,239]. However, it is especially important to understand the structure relaxation behaviour on much more simple compositions. Moreover, it would be of great interest to develop a theoretical model which enables predicting the glass structure from its composition and temperature conditions.

Taking into consideration the above mentioned, this paper aims to shed some light on the effect of Al and B on the structure and relaxation of network units and crystallization of lithium silicate based glasses. The glass network structures of the binary and the doped glass compositions were investigated by NMR, and the relaxation of network units was observed experimentally and studied using annealed and non-annealed glasses. This work also aims at demonstrating the feasibility of a theoretical model developed by some of the current authors which allows the simulation of NMR spectrum for the studied glass compositions.

3.7.2 Theoretical background

In our previous paper [242] on statistics of silicate units (S_n^m) in binary glasses with chemical composition $x\mathrm{R_2O}$–$\mathrm{SiO_2}$ ($x \in [0, 2]$), the probability (P_n^m) of occurrence of a particular S_n^m units at given temperature (T) is given by the formula,

$$P_n^m = \frac{1}{Z_{gr}} e^{\frac{\sum_{j>i}(i,j)_n^m \mu_{ij} + n\,\mu - F_n^m}{k_B T}} \qquad \text{Eq. (3.7-3)}$$

Where, n is the number of bridging oxygens (*BO*s) on a given silicate tetrahedron, m corresponds to a particular combination of neighbouring silicate units, $(i, j)_n^m$ are the parameters associated to the network connectivity, μ and μ_{ij} with chemical potentials associated to exchanges in *BO*s and network connectivity respectively, F_n^m is the

Helmholtz free energy associated to a particular S_n^m unit, k_B is the Boltzmann's constant and Z_{gr} is the grand canonical partition function given by,

$$Z_{gr} = \sum_{n,m} e^{\frac{\sum_{j>i}(i,j)_n^m \mu_{ij} + n\,\mu - F_n^m}{k_B T}} \qquad \text{Eq. (3.7-4)}$$

Under a given initial conditions of temperature and composition of glasses, a probability distribution of various silicate units is obtained. If each S_n^m is assigned an associated expected value of chemical shift with some variance, the NMR spectrum of that composition can be simulated. We also reported on the relaxation behaviour observed experimentally and explained the theoretical basis using the concept of broken ergodicity. In this paper, we expand these ideas to multicomponent glass systems containing Al and B.

3.7.3 Experimental procedure

Table 3.7.1 Batch compositions of the glasses in mol%

	G	**G_{Al}**	**G_B**	**$G_{Al–B}$**
Li_2O	28.0	27.7	27.7	27.4
SiO_2	72.0	71.3	71.3	70.6
Al_2O_3	0.0	1.0	0.0	1.0
B_2O_3	0.0	0.0	1.0	1.0

A binary lithium silicate glass with composition $28Li_2O{\cdot}72SiO_2$ (mol%), labelled as G, and three doped compositions containing Al_2O_3 and/or B_2O_3 were synthesized by melt quenching technique using SiO_2, Li_2CO_3, Al_2O_3 and H_3BO_3 precursors in the form of powders (all with purity > 99%). **Table 3.7.1** presents the detailed compositions of the experimental glasses. The powders were homogenously mixed in a ball mill and calcined at 800 ºC for 1 h. Calcined powders were further mixed for homogeneity using mortar–pestle and transferred to platinum crucibles for melting at the temperature of 1550 ºC for 1 h in air. Bulk (monolithic) bar shaped glasses were prepared by pouring the melt on a bronze mould. One sample of each composition was annealed[‡] at 460 ºC

[‡] The word 'annealing' used in the current Section (3.7) does not exactly correspond to annealing used in traditional glass science where, a glass sample is heated to a temperature where viscosity is ~10^{13} Poise to relieve stresses. Throughout this Section the word 'annealing' corresponds to establishing ergodicity at a specified temperature.

for 75 h. The thermal parameters of the experimental glasses were determined by differential thermal analysis (DTA, Perkin-Elmer DTA-7) by heating 35–40 mg of glass powders (<75 μm) at 10 K min^{-1} in high purity, open alumina crucibles under a nitrogen flow. The onset method was used to determine the glass transition temperature (T_g) and the estimated uncertainty is ±5 ºC. Microstructures of glasses were examined by optical microscopy (Stereo Microscope with LED and HD Camera LEICA EZ4HD, Germany, using LAS V4.0 software) and scanning electron microscopy (SEM; SU-70, Hitachi, Tokyo, Japan). Samples for microscopy were prepared by grinding, polishing, and etching for 60 s using 2 vol.% hydrofluoric acid. Crystalline phases present in the glass-ceramics were examined by X-ray diffraction (XRD; Rigaku Geigerflex D/Mac, C Series, Tokyo, Japan) using Cu Kα radiation with 2θ varying from 10º to 60º steps for 0.02 s^{-1}. The density (ρ) of annealed glass samples was measured by Archimedes' method using ethylene glycol as the immersion liquid. Three samples of each glass were measured and the standard deviation was recorded.

^{29}Si MAS-NMR spectra were recorded on both annealed and non-annealed glasses of compositions G, G_{Al} and G_B crushed into fine powders. The NMR spectrometer (BRUKER Avance III) was operated at a Larmor frequency of 79.5 MHz with a 9.4 T magnetic field, using a 7 mm rotor rotating at 5 kHz. The samples were excited with a 90º flip angle using 900 s delay time. Both spectra were obtained after Fourier Transformation of 64 scans of Free Induction Decays (FID). Tetramethylsilane was used as chemical shift reference at 0 ppm. ^{11}B MAS-NMR spectra were recorded on both annealed and non-annealed glasses of compositions G_B and $G_{Al\text{-}B}$ crushed into fine powders. The NMR spectrometer (BRUKER Avance III) was operated at a Larmor frequency of 256.8 MHz with a 18.8 T magnetic field, using a 3.2 mm rotor rotating at 20 kHz. The samples were excited with an 18º flip angle using 10 s delay time. Boric acid was used as chemical shift reference. ^{27}Al MAS-NMR spectra were recorded on both annealed and non-annealed glasses of compositions G_{Al} and $G_{Al\text{-}B}$ crushed into fine powders. The NMR spectrometer (BRUKER Avance III) was operated at a Larmor frequency of 104.2 MHz with a 9.4 T magnetic field, using a 4 mm rotor rotating at 12.5 kHz in HXY mode double. The samples were excited with an 18º flip angle using 2 s delay time. A 0.1M $Al(NO_3)_3$ solution was used as chemical shift reference. The NMR spectra were deconvoluted using the DMfit software [228].

3.7.4 Results

All glass compositions were suitable for easy casting after 1 h of melting at 1550 ºC, resulting in homogeneous and transparent bubble free glasses. The amorphous nature of the as-cast glasses was confirmed by XRD analysis (not presented). All experimental glasses were transparent to naked eyes suggesting absence of visible liquid-liquid phase segregation (*LLPS*). However, the SEM images of the as-cast non-annealed bulk glasses clearly demonstrated the formation of droplet-like zones embedded in glass matrix similarly to reported elsewhere [142,193].

3.7.4.1 NMR

Figure 3.7.1 shows the ^{29}Si NMR spectra of both annealed and non-annealed experimental glasses. There are clear differences between both annealed and non-annealed samples (**Figure 3.7.1a–c**). In order to identify the relative amounts of each Q_n unit, the spectra were deconvoluted using three Gaussian/Lorentzian line shapes corresponding to three units: Q_2, Q_3 and Q_4; an example is shown in **Figure 3.7.1f**. The spectra were deconvoluted such that the relative quantities of each unit account for the chemical composition of the glass. The parameters of NMR deconvolution and relative amounts of each unit are presented in **Table 3.7.4**. In all the glasses, the presence Q_2 is a result of speciation reaction Eq. (3.7-1); otherwise only Q_3 and Q_4 are expected according to the chemical composition of the experimental glasses. In both annealed and non-annealed samples, the degree of speciation Eq. (3.7-1) decreases in the following way: $G > G_B > G_{Al}$. Further, annealing of the glasses resulted in an increase and a decrease of speciation in G and G_{Al} and $G_{B,}$ respectively.

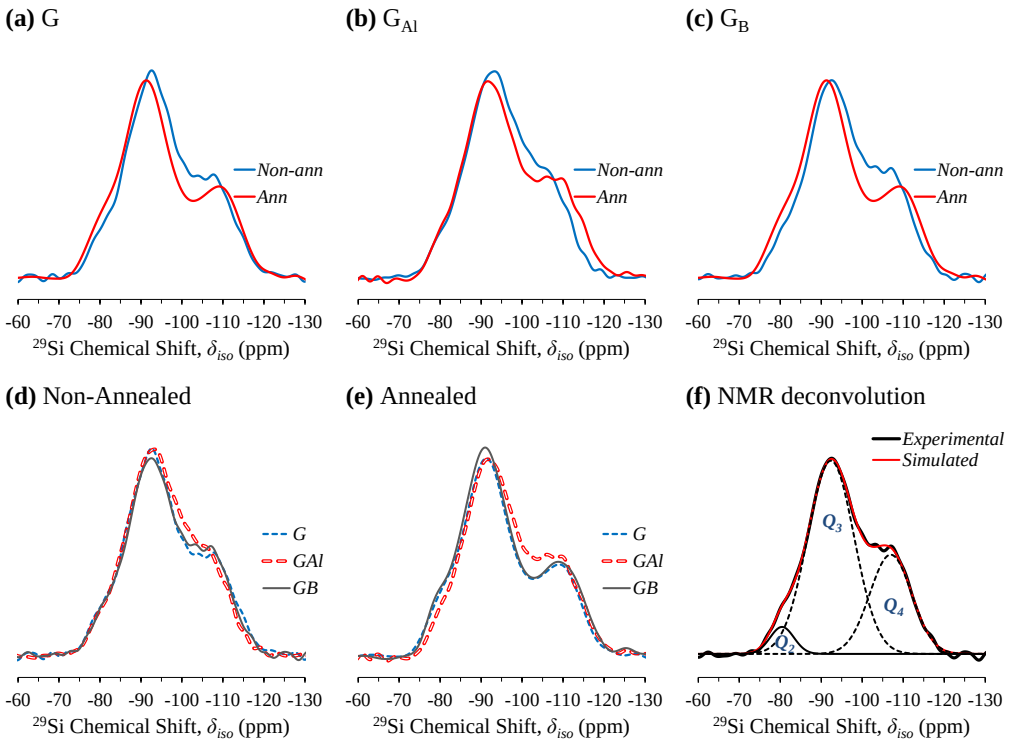

Figure 3.7.1 (a)–(e) ^{29}Si NMR spectra and (f) an example of deconvolution.

Figure 3.7.2 shows the ^{11}B NMR spectra of both annealed and non-annealed experimental glasses. Each spectrum shows two peaks corresponding to two types of B units: B_{III} and B_{IV}. All the spectra were deconvoluted using two line shapes: (1) with second-order quadrupolar effects corresponding to B_{III} and (2) with Gaussian/Lorentzian corresponding to B_{IV}. The parameters of NMR deconvolution and relative amount of each unit are presented in **Table 3.7.5**. According to the values of quadrupolar coupling constant (C_Q) and asymmetry parameter (η), the B_{III} can be assigned to asymmetric three coordinated boron with a *NBO* [276]. In the annealed glasses, changing the composition from G_B to $G_{Al\text{-}B}$ did not cause significant changes in the relative amounts of B species (**Figure 3.7.2c**). However, in both glasses, annealing treatment favoured B_{IV} species (**Figure 3.7.2a and b**). **Figure 3.7.3** shows the ^{27}Al NMR spectra of both annealed and non-annealed experimental glasses. All the spectra have the same line shape and show no differences. To obtain the chemical shift value, one of the spectrum was fitted with Czejeck distribution model according to Neuville *et al.*[156]. The fitting gave a chemical shift value of 59.46 ppm and C_Q of 5.15 MHz. This corresponds to an Al in 4-coordination and charge compensated by a Li^{+1} ion.

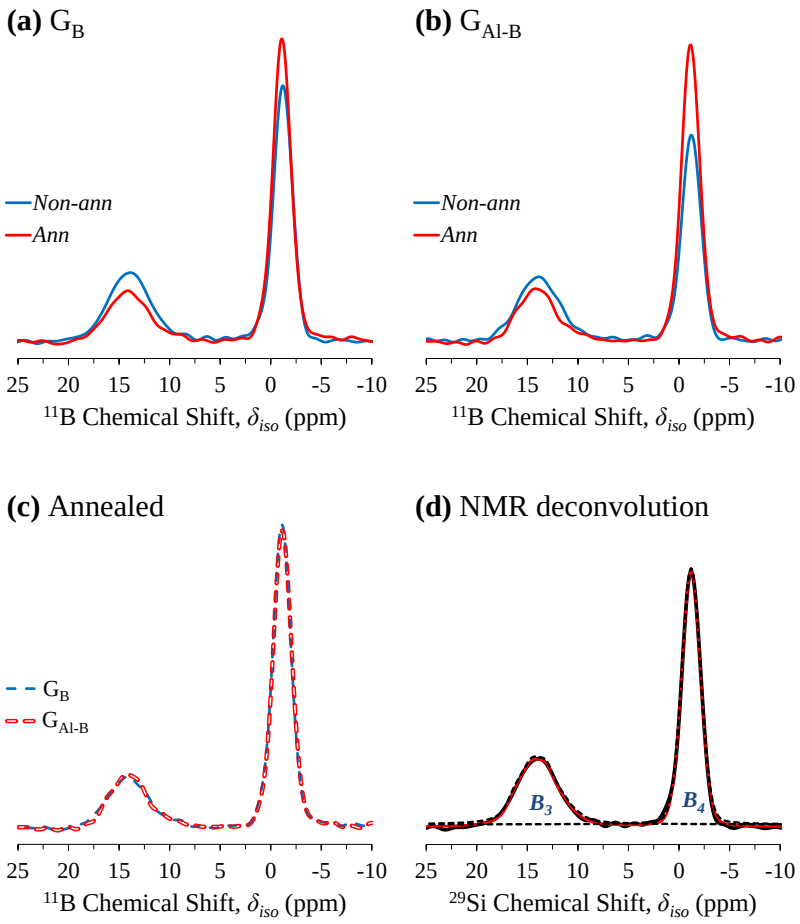

Figure 3.7.2 (a)–(c) ^{11}B NMR spectra and (d) an example of deconvolution.

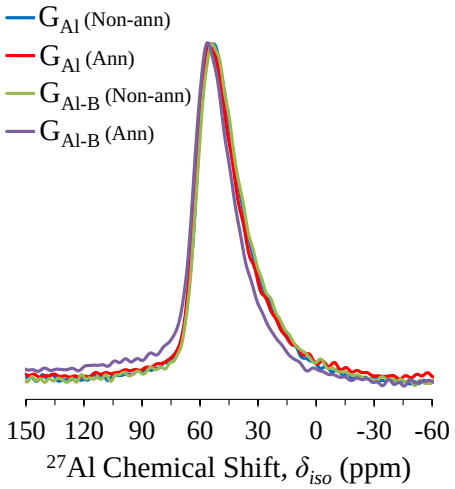

Figure 3.7.3 ^{27}Al NMR spectra of all the glasses.

The glass characteristic temperatures such as glass transition temperature (T_g), onset temperature of crystallization (T_c) and temperature corresponding to maximum crystallization rate (T_p) were obtained from DTA thermographs (**Table 3.7.2**). All glass

compositions featured a single endothermic dip before T_c corresponding to glass transition region, which is approximately at 455 ºC. Accordingly, the annealed samples were heat-treated at 460 ºC. Glasses G and $G_{Al–B}$ present the same value for T_c (559 ºC), which is lower than the values for G_{Al} and G_B (both equal to 576 ºC). The values of T_p follow the same trend as T_c. The values of ΔT (= T_c − T_g) are higher for Al_2O_3-containing compositions suggesting that these glasses are more stable than G and G_B.

The density values of annealed (**Figure 3.7.4**, **Table 3.7.2**) are higher for compositions G_{Al} and $G_{Al–B}$, which is due to the higher molecular weight of Al_2O_3 in comparison to the other oxides present in glasses, and similar trend is observed for the molar volume of experimental glasses. In this paper we defined a new quantity called "network volume" (*NV*), which is the volume occupied by 1 mol of network forming units present in the average composition of the glass. This quantity was estimated according to the following equation:

$$NV = \frac{Li_2O\%\, M_{Li_2O} + SiO_2\%\, M_{SiO_2} + Al_2O_3\%\, M_{Al_2O_3} + B_2O_3\%\, M_{B_2O_3}}{\rho\,(SiO_2\% + 2Al_2O_3\% + 2B_2O_3\%)} \quad \text{Eq. (3.7-5)}$$

Where, *M* is the molar weight. The variation of *NV* with the composition (**Figure 3.7.4**, **Table 3.7.2**) suggests that the addition of Al_2O_3 or B_2O_3 to G have similar effect on the volume of network units and resulted in a contraction of the structure in comparison to the parent composition, while adding both oxides together caused even higher contraction effect.

Table 3.7.2 Thermo-physical properties of the experimental glasses (errors in T_g, T_c and T_p are about ± 2 ºC)

	T_g (ºC)	T_c (ºC)	T_p (ºC)	ΔT (ºC)	ρ (g cm^{-3})	NV (cm^3 mol^{-1})
G	456	559	626	104	2.345 ± 0.003	30.581 ± 0.009
G_{Al}	458	576	649	119	2.352 ± 0.001	30.240 ± 0.002
G_B	455	576	643	107	2.345 ± 0.001	30.147 ± 0.004
$G_{Al–B}$	451	559	627	121	2.358 ± 0.001	29.747 ± 0.003

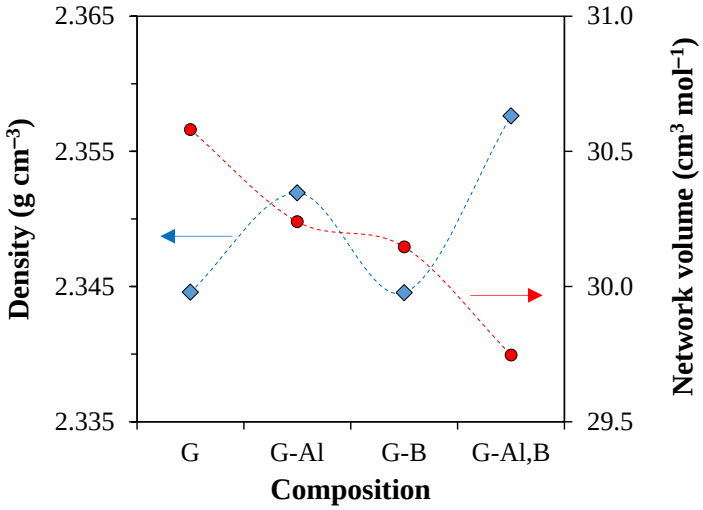

Figure 3.7.4 Density and network volume values for the annealed glasses (the dashed lines are only guides for the eye).

3.7.4.2 Microstructure and phase analysis

Samples nucleated at 460 ºC during different times and heat-treated at optimized growth temperatures for 2 h revealed variations in the *LLPS* appearance. **Figure 3.7.6** shows the evolution of *LLPS* for glass composition G_{Al} after several heat-treatments, demonstrating an increasing of the segregated glass fraction with increasing of nucleating time. Samples nucleated during longer periods of time show some crystallized areas as evidenced by **Figure 3.7.6c**.

Figure 3.7.7 shows the micrographs of glass G_{Al} nucleated at 460 ºC during 8 h revealing the loss of ergodicity (broken ergodicity phenomena) [37]. In **Figure 3.7.7b** two types of microstructure corresponding to distinct glassy phases can be observed (regions A and B) as well as the border between them (indicated by the inserted arrow). Heat-treating the nucleated samples resulted in the crystal growth. **Figure 3.7.8** presents the aspect of glass G_{Al} nucleated at 460 ºC for 10 h and heat-treated at 595 ºC for 2 h. Well dispersed crystals featuring similar shape and size can be observed. In **Figure 3.7.8b** it is possible to see the cloudiness of the sample and crystals growing at the surface (circle A) and at deeper levels (circle B).

The X-ray diffractograms for all samples isothermally treated at 800 ºC for 3 h are presented in **Figure 3.7.9**. Lithium disilicate is the main crystalline phase for all glasses. The presence of small amount of cristobalite is detected in G and Al_2O_3-containing

glasses, while quartz is present in B_2O_3-containing glasses and the intensity of its peaks increased with B_2O_3 content.

3.7.5 Extension of the statistical mechanical model

In this section we present an extension of the statistical mechanical model to take into account the presence of Al and B in the glass network. Let us consider a composition as given in **Table 3.7.3** where, amount of lithium is given by the parameter *x* and the amounts of each network forming unit (P_n^m) are all scaled to unity and becomes the first constraint given by,

$$\sum_{n,m} P_n^m = 1 \qquad \text{Eq. (3.7-6)}$$

Now, the second set of constraints corresponds to each particular network forming units (Si, Al, and B) are given by,

$$\sum_{n,m} f_n^m P_n^m = \langle f \rangle \qquad \text{Eq. (3.7-7)}$$

Where, $f \in \{f_{Si}, f_{Al}, f_B \ldots\}$ is the fraction of each network formers (**Table 3.7.3**) corresponding to different types of atoms (Si, Al, and B). The values f_n^m take either 1 or 0. If the number of network formers is *p*, then the set represented by Eq. (3.7-7) contains *p* number of such equations. By adding all the equations of this set of equation will give Eq. (3.7-8),

$$\sum_f \langle f \rangle = 1 = \sum_{n,m} P_n^m \qquad \text{Eq. (3.7-8)}$$

Therefore, together with Eq. (3.7-6) and Eq. **(3.7-7)** there are only *p* independent constraints. Now, we write constraint for the amount of Li_2O in the chemical composition given by,

$$\sum_{n,m} (CN_n^m - n + cc_n^m) P_n^m = \sum_{n,m} r_n^m P_n^m = \langle 2x \rangle \qquad \text{Eq. (3.7-9)}$$

Where, CN_n^m is the coordination number of a particular network forming unit (Al, B^{IV} Si: 4, and B^{III}: 3), *n* is the number of bridging oxygens and cc_n^m corresponds to charge compensator on a particular network forming unit (it takes values either 0 or 1 depending on whether it is present or not). Further, we also have energy constraint given by,

$$\sum_{n,m} E_n^m P_n^m = \langle E \rangle \qquad \text{Eq. (3.7-10)}$$

Next we write set of constraints related to network connectivity, given by,

$$\sum_{n,m} (i,j)_n^m P_n^m = 0 \qquad \text{Eq. (3.7-11)}$$

Where, $(i,\ j)_n^{\ m}$ is constant associated to different bridging oxygens (O_{ij}). The entropy generated by all the units is given by,

$$S = -k_B \sum_{n,m} P_n^m \ln(P_n^m) \qquad \text{Eq. (3.7-12)}$$

Maximizing the entropy subjected to all the constraints (Eq. (3.7-3) to Eq. (3.7-8)) by method of Lagrange multipliers would give the probability of each kind of unit in the glass network,

$$P_n^m = \frac{1}{Z_{gr}} e^{\frac{\sum_{j>i}(i,j)_n^m \mu_{ij} + \sum_f f_n^m \mu_f + r_n^m \mu_r - E_n^m}{k_B T}} \qquad \text{Eq. (3.7-13)}$$

The full derivation is presented in supplementary information (Section 3.7.7.1). Applying a semi-quantum mechanical approach, $E_n^{\ m}$ can be changed to $F_n^{\ m}$. However, in this paper we will keep using $E_n^{\ m}$. By considering the network connections and *NBO*s in binary silicates, we ended up with 70 different $Q_n^{ij\cdots}$ (or $S_n^{\ m}$) types of units. In order to find out number of types of units when multiple network formers are used, we derive here a generalized formula. Consider a glass composition with n_i different network formers (*e.g.* Si, Al, B_{III}, B_{IV}, P *etc.*) where, $i \in \mathbb{N}$ is the coordination number. For example, in a boroaluminosilicate glass, there would be 3 types of four coordinated units ($n_4 = 3$, corresponding to B_{IV}, Al_{IV} and Si_{IV}) and one type of three coordinated unit ($n_3 = 1$, corresponding to B_{III}); and for the rest of value of i, $n_i = 0$. Each of the network former with coordination number i can take j ($\in [0, i]$) number of *NBO*s; therefore it can stay in $i + 1$ number of states (fully depolymerized to fully polymerized). Therefore, the total number of network forming units having at least one *BO* (by only considering *NBO*s and excluding network connectivity) is given by,

$$\sum_i i n_i \qquad \text{Eq. (3.7-14)}$$

By taking a particular i^{th} coordinated unit with *j – 1 BO*s, the number of units (now considering both *NBO*s and network connectivity) is given by the following multicombination formula,

$$\left(\left(\sum_i in_i \atop j-1\right)\right) = \left(\sum_i in_i + j - 2 \atop j-1\right) \qquad \text{Eq. (3.7-15)}$$

This basically gives the number of ways of choosing *j – 1* items from a total of $\sum in_i$ items with repetition. Thus, the number of units for a given type of network former is,

$$\sum_{j=0}^{i} \left(\sum_i in_i + j - 2 \atop j-1\right) \qquad \text{Eq. (3.7-16)}$$

The total number of units (*NU*) considering all types of network formers is given by,

$$NU = \sum_i n_i \left[\sum_{j=0}^{i} \left(\sum_i in_i + j - 1 \atop j-1\right)\right] \qquad \text{Eq. (3.7-17)}$$

Thus, according to our derived formula, in a pure silicate system: there would be 70 types of Si units; and in aluminosilicate system: 990 (495 types for each Al and Si units); and in borosilicate system: 3,094 (1,365 types for each B_{IV} and Si units and 364 types of B_{III}); in boroaluminosilicate system: 12,444 (3,876 types for each B_{IV}, Al and Si units and 816 types of B_{III}). Hence we see that, as the complexity of the glass increases by adding new formers, the number of types of network forming units increase exponentially. Further, in binary system, by taking network connectivity into account, we have obtained 10 constraint equations corresponding to 10 types of bridging oxygens. We can derive a generalized formula to give number of constraint equations we can get when multiple formers are used. The number of constraint (*NCC*) equations for network connectivity is equal to number of types of *BO*; which is given by the number of ways of choosing 2 network units from the total number of network forming units having at least one *BO* (Eq. (3.7-18)) with repetition; given by,

$$NCC = \left(\binom{\sum_i in_i}{2}\right) = \binom{\sum_i in_i + 1}{2} = \frac{1}{2}\left[\sum_i in_i\right]\left[\sum_i in_i + 1\right] \quad \text{Eq. (3.7-18)}$$

According to this equation, the number of constraint equations for network connectivity in compositions of binary silicates: 10; in aluminosilicates: 36; in borosilicates: 66; and in boroaluminosilicates: 120.

Table 3.7.3 Amounts of units according to the notation of the model.

			460°C			
	Q	**Amount**	**G**	**G_{Al}**	**G_{B}**	**$G_{Al–B}$**
Li_2O	---	x	0.39	0.36	0.38	0.34
$LiAlO_2$	A	f_{Al}	0.00	0.03	0.00	0.03
$LiB^{IV}O_2$	B	f_{B4}	0.00	0.00	0.02	0.02
$B^{III}O_{3/2}$	C	f_{B3}	0.00	0.00	0.01	0.01
SiO_2	S	f_{Si}	1.00	0.97	0.97	0.94

3.7.5.1 Calculations

In this study we simplified the extended model in the previous section by reducing the number of units and network connectivity constraints based on the following assumptions,

1. The compositions contain only Al–O–Si, B–O–Si and Si–O–Si type of bridges but not Al–O–Al or Al–O–B or B–O–B.
2. All the Al units are present in 4-coordination without *NBO*s.
3. All the B_{IV} units are present in 4-coordination without *NBO*s and all the B_{III} units are present in 3-coordination with one *NBO*.
4. All Si exists only as Q_2, Q_3 and Q_4.

The first assumption is justified because of the fact that very small amounts of Al_2O_3 and B_2O_3 are added in to the composition. Further, Loewenstein's Rule prohibits Al–O–Al type linkages in aluminosilicate networks; and in borosilicate networks, B–O–

Si bridges are more stable than B–O–B bridges based on energy consideration [165–167,277]. The second assumption is supported by ^{27}Al NMR spectra (**Figure 3.7.3**) of the current glass compositions, which shows that all Al is in 4-coordination; and the chemical shift of 59 ppm corresponds to Al in highly polymerized site connected to Si tetrahedra by corner sharing [154,157,278]; therefore, no *NBO*s are present on Al tetrahedra. The third assumption is supported by ^{11}B NMR spectra (**Figure 3.7.2**) of the current glass compositions, which shows that B is in two states: B_{IV} and B_{IIIa} (B_{III} with one *NBO*). The ^{11}B chemical shift of B^{IV} unit –1.2 ppm corresponds to reedmergnerite like structural units of boron where, each B^{IV} unit is coordinated with four Si tetrahedrons (this also supports the first assumption) [154,158]. Therefore, a given B unit fluctuates between B_{IV} and, B_{IIIa} according to the reaction Eq. (3.7-2) [265] with some probability taking into account the energy considerations. The fourth assumption is justified by the ^{29}Si NMR spectra (**Figure 3.7.1**) of the current glasses which show only 3 types of units: Q_2, Q_3 and Q_4. Therefore, according to these reasonable assumptions, the number of network units in pure silicate glasses is reduced to 31; in aluminosilicate glasses to 80; in borosilicate glasses to 141. And, the number of constraints for network connectivity reduces for pure silicate to: 3; for aluminosilicate glasses to 6; for borosilicate glasses to 9. The calculations for the reduced number of units and constraints can be found in the (Section 3.7.7.2).

Table 3.7.4 NMR parameters for ^{29}Si deconvolution (errors in δ_{iso} are ± 0.5 ppm)

		δ_{iso} (ppm)			*FWHM* (ppm)			Amount (%)		
		Q^2	Q^3	Q^4	Q^2	Q^3	Q^4	Q^2	Q^3	Q^4
Non-ann.	**G**	–79.8	–92.3	–107.8	6.3	13.9	12.2	3.9	68.4	27.7
	G_{Al}	–80.1	–92.6	–106.7	6.6	14.6	11.8	3.0	71.7	25.2
	G_B	–80.5	–92.4	–107.0	6.8	13.4	12.0	4.7	65.2	30.1
Ann.	**G**	–79.6	–91.2	–108.7	6.9	13.5	12.4	6.0	66.0	28.0
	G_{Al}	–80.0	–91.9	–108.5	5.3	14.4	13.2	2.3	67.4	30.3
	G_B	–79.2	–91.0	–109.2	5.5	13.8	13.0	4.4	67.0	28.6

Therefore, based on these assumptions, the values of P_n^m (Eq. (3.7-10)) were fitted to the NMR data (**Table 3.7.4 and Table** 3.7.5) by adjusting E_n^m values at T = 460 ºC (the annealing temperature). The final results for the distribution are shown in **Table 3.7.6**. In the **Table 3.7.6**, S_n^m corresponds to Si tetrahedron for G, G_{Al} and G_B; A_n^m

corresponds to Al and B^{IV} tetrahedra G_{Al} and G_B respectively; and B_n^m corresponds to B^{III} trigonal unit.

Table 3.7.5 NMR parameters for ^{11}B deconvolution

	Non-Annealed				Annealed			
Boron Site	δ_{iso} **(ppm)**	C_Q **(MHz)**	η	**Amount (%)**	δ_{iso} **(ppm)**	C_Q **(MHz)**	η	**Amount (%)**
G_B								
B_{IV}	–1.21	---	---	62.3	–1.10	---	---	74.0
B_{III}	17.05	2.75	0.56	37.7	17.23	2.77	0.56	26.0
$G_{Al\text{-}B}$								
B_{IV}	–1.22	---	---	59.0	–1.15	---	---	74.25
B_{III}	16.79	2.68	0.52	41.0	17.12	2.68	0.58	25.75

3.7.6 Discussion

3.7.6.1 Glass Structure

In this section, we discuss the equilibrium structure of the glass at a temperature of 460 ºC; this is the temperature at which all the glasses were annealed for 75 h. The deconvolution of NMR spectra to individual components of Q_2, Q_3, Q_4, B^{III} and B^{IV} (**Table 3.7.4 and Table** 3.7.5) gives a rough quantification for the distribution of these units. In all the compositions, the Q_2 peak shows a ^{29}Si chemical shift value of approximately –80 ppm (**Table 3.7.4**). However, the value of the ^{29}Si chemical shift [115,279] associated with crystalline and glass of *LS* composition are –75 and –73 ppm respectively. Therefore, from this extra shielding we can conclude that, the Q_2 units are connected to Q_3 or Q_4 units rather than to Q_2 units (*i.e.* S_2^{22} units). The simulation using the extended statistical mechanical model is in agreement with the experimental result which shows negligible amounts of S_2^{22} units (**Table 3.7.6**). Moreover, a small FWHM varying between 5 to 7 ppm for the Q_2 peak shows from NMR deconvolution (**Table 3.7.4**) suggests that only few Q_2^{ij} units are present in the glass. Again the simulation is in agreement with this result, showing only 4 to 5 Q_2^{ij} units (**Table 3.7.6**). In contrast, the Q_3 and Q_4 species have a range of units ranging from 10 to 12 showing a large *FWHM*. Further, according to the simulation, significant amount of Q_3 units are

connected to Q_4 units (S_3^{444}, S_3^{344} and S_3^{334}); and majority of Q_4 units are connected to Q_3 units (S_4^{3333}, S_4^{3334} and S_4^{3344}).

The Al tetrahedra connected to Q_4 and Q_3 units have ^{27}Al NMR chemical shifts in the range of 52 to 64 ppm and 65 to 74 ppm respectively [157]. The ^{27}Al NMR spectra of current glasses (**Figure 3.7.3**) shows a broad peak positioned at 59.5 ppm suggests that Al units are connected to a range to Q_3 to Q_4 units on each corners. Again, this experimental observation is confirmed by the statistical mechanical simulation which shows that presence of A_4^{4444}, A_4^{3444}, A_4^{3344}, A_4^{3334} and A_4^{3333} (**Table 3.7.6**) for the sample G_{Al}. The ^{11}B chemical shift for reedmergnerite mineral is –1.9 ppm [280]; in this crystal B^{IV} units are coordinated with Q_4 Si units [160]. In current compositions, ^{11}B chemical shifts values for B^{IV} units were found to be ~ –1.2 ppm. The extra deshielding effect must be caused due to B^{IV} units coordinated to Q_3 Si units. This is confirmed by the statistical mechanical simulation, which shows the presence of only A_4^{3444}, A_4^{3344}, A_4^{3334} and A_4^{3333} (**Table 3.7.6**) for the sample G_B. Finally, the simulation shows that the B^{III} units are coordinated mainly to Q_3 and Q_4 Si units (B_2^{34} and B_2^{33} for the sample G_B). In this paper, even with approximate fitting of the E_n^m values, there is a good agreement of statistical mechanical model and the experiments.

The new quantity introduced in this paper called *NV* decreases with from G to G_{Al}, G to G_B and G to $G_{Al\text{-}B}$ (**Figure 3.7.4** and **Table 3.7.2**). In binary Li_2O–SiO_2 glasses, the density of the system monotonically increases with Li_2O % [8]. Likewise, *NV* also increases monotonically with Li_2O % (Section 3.7.7.3). This can be understood by a simple analogy: substituting Li_2O can be considered as replacing Q_4 with Q_3; since Q_3 has extra one atom (Li), it would occupy larger volume. Now, if tetrahedra of Si are replaced by Al, the value of *NV* is expected to increase because, Al has larger atomic radii than Si; additionally it is also accompanied by a charge compensating ion. This may not be the case for B tetrahedra because of their smaller atomic radii; same is the case for trigonal B units. **Table 3.7.3** shows the compositions of all the glasses with network forming units scaled to unity. When going from composition G to G_{Al}, some tetrahedra of Si are replaced by Al and the amount of Li_2O decreased: the two effects would result in increase and decrease in *NV*. When going from composition G to G_B however, both decrement in Li_2O and replacement of Si units show a further accentuated decrease in *NV* as expected. Finally, going from composition G to $G_{Al\text{-}B}$ shows a combined effect of G_{Al} and G_B.

Table 3.7.6 P_n^m distribution calculated (to 100%) from the statistical model at T = 460 ºC

Q_n^m	G	G_{Al}	G_B	Q_n^m	G	G_{Al}	G_B	Q_n^m	G	G_{Al}	G_B	Q_n^m	G	G_{Al}	G_B
S_4^{4444}	2.3	2.4	2.4	$S_4^{344\beta}$	0.0	0.0	0.1	S_3^{334}	16.5	14.5	14.8	S_2^{24}	0.2	0.1	0.1
S_4^{3444}	3.1	3.2	3.2	$S_4^{334\beta}$	0.0	0.0	0.1	S_3^{333}	23.0	19.7	20.0	S_2^{23}	0.3	0.1	0.1
S_4^{3344}	4.4	4.3	4.4	$S_4^{333\beta}$	0.0	0.0	0.1	S_3^{244}	1.4	0.9	0.9	S_2^{22}	0.0	0.0	0.0
S_4^{3334}	6.1	5.9	5.9	$S_4^{244\beta}$	0.0	0.0	0.0	S_3^{234}	1.9	1.2	1.2	$S_2^{4\alpha}$	0.0	0.0	0.0
S_4^{3333}	8.5	8.0	8.0	$S_4^{234\beta}$	0.0	0.0	0.0	S_3^{233}	2.7	1.6	1.7	$S_2^{3\alpha}$	0.0	0.0	0.0
S_4^{2444}	0.4	0.3	0.3	$S_4^{233\beta}$	0.0	0.0	0.0	S_3^{224}	0.2	0.1	0.1	$S_2^{2\alpha}$	0.0	0.0	0.0
S_4^{2344}	0.6	0.4	0.4	$S_4^{224\beta}$	0.0	0.0	0.0	S_3^{223}	0.3	0.1	0.1	$S_2^{\alpha\alpha}$	0.0	0.0	0.0
S_4^{2334}	0.8	0.6	0.6	$S_4^{223\beta}$	0.0	0.0	0.0	S_3^{222}	0.0	0.0	0.0	$S_2^{4\beta}$	0.0	0.0	0.0
S_4^{2333}	1.2	0.8	0.8	$S_4^{222\beta}$	0.0	0.0	0.0	$S_3^{44\alpha}$	0.0	1.9	1.4	$S_2^{3\beta}$	0.0	0.0	0.0
S_4^{2244}	0.1	0.0	0.0	$S_4^{44\alpha\beta}$	0.0	0.0	0.0	$S_3^{34\alpha}$	0.0	2.5	1.9	$S_2^{2\beta}$	0.0	0.0	0.0
S_4^{2234}	0.1	0.1	0.1	$S_4^{34\alpha\beta}$	0.0	0.0	0.0	$S_3^{33\alpha}$	0.0	3.4	2.5	$S_2^{\alpha\beta}$	0.0	0.0	0.0
S_4^{2233}	0.2	0.1	0.1	$S_4^{33\alpha\beta}$	0.0	0.0	0.0	$S_3^{24\alpha}$	0.0	0.2	0.2	$S_2^{\beta\beta}$	0.0	0.0	0.0
S_4^{2224}	0.0	0.0	0.0	$S_4^{24\alpha\beta}$	0.0	0.0	0.0	$S_3^{23\alpha}$	0.0	0.3	0.2	A_4^{4444}	0.0	0.1	0.1
S_4^{2223}	0.0	0.0	0.0	$S_4^{23\alpha\beta}$	0.0	0.0	0.0	$S_3^{22\alpha}$	0.0	0.0	0.0	A_4^{3444}	0.0	0.2	0.1
S_4^{2222}	0.0	0.0	0.0	$S_4^{22\alpha\beta}$	0.0	0.0	0.0	$S_3^{4\alpha\alpha}$	0.0	0.1	0.0	A_4^{3344}	0.0	0.4	0.3
$S_4^{444\alpha}$	0.0	0.3	0.2	$S_4^{44\beta\beta}$	0.0	0.0	0.0	$S_3^{3\alpha\alpha}$	0.0	0.1	0.0	A_4^{3334}	0.0	0.7	0.5
$S_4^{344\alpha}$	0.0	0.4	0.3	$S_4^{34\beta\beta}$	0.0	0.0	0.0	$S_3^{2\alpha\alpha}$	0.0	0.0	0.0	A_4^{3333}	0.0	1.4	1.0
$S_4^{334\alpha}$	0.0	0.5	0.4	$S_4^{33\beta\beta}$	0.0	0.0	0.0	$S_3^{\alpha\alpha\alpha}$	0.0	0.0	0.0	A_4^{2444}	0.0	0.0	0.0
$S_4^{333\alpha}$	0.0	0.7	0.6	$S_4^{24\beta\beta}$	0.0	0.0	0.0	$S_3^{44\beta}$	0.0	0.0	0.2	A_4^{2344}	0.0	0.0	0.0
$S_4^{244\alpha}$	0.0	0.0	0.0	$S_4^{23\beta\beta}$	0.0	0.0	0.0	$S_3^{34\beta}$	0.0	0.0	0.3	A_4^{2334}	0.0	0.0	0.0
$S_4^{234\alpha}$	0.0	0.1	0.0	$S_4^{22\beta\beta}$	0.0	0.0	0.0	$S_3^{33\beta}$	0.0	0.0	0.4	A_4^{2333}	0.0	0.0	0.0
$S_4^{233\alpha}$	0.0	0.1	0.1	$S_4^{4\alpha\alpha\beta}$	0.0	0.0	0.0	$S_3^{24\beta}$	0.0	0.0	0.0	A_4^{2244}	0.0	0.0	0.0
$S_4^{224\alpha}$	0.0	0.0	0.0	$S_4^{3\alpha\alpha\beta}$	0.0	0.0	0.0	$S_3^{23\beta}$	0.0	0.0	0.0	A_4^{2234}	0.0	0.0	0.0
$S_4^{223\alpha}$	0.0	0.0	0.0	$S_4^{2\alpha\alpha\beta}$	0.0	0.0	0.0	$S_3^{22\beta}$	0.0	0.0	0.0	A_4^{2233}	0.0	0.0	0.0
$S_4^{222\alpha}$	0.0	0.0	0.0	$S_4^{4\alpha\beta\beta}$	0.0	0.0	0.0	$S_3^{4\alpha\beta}$	0.0	0.0	0.0	A_4^{2224}	0.0	0.0	0.0
$S_4^{44\alpha\alpha}$	0.0	0.0	0.0	$S_4^{3\alpha\beta\beta}$	0.0	0.0	0.0	$S_3^{3\alpha\beta}$	0.0	0.0	0.0	A_4^{2223}	0.0	0.0	0.0
$S_4^{34\alpha\alpha}$	0.0	0.0	0.0	$S_4^{2\alpha\beta\beta}$	0.0	0.0	0.0	$S_3^{2\alpha\beta}$	0.0	0.0	0.0	A_4^{2222}	0.0	0.0	0.0
$S_4^{33\alpha\alpha}$	0.0	0.0	0.0	$S_4^{4\beta\beta\beta}$	0.0	0.0	0.0	$S_3^{4\beta\beta}$	0.0	0.0	0.0	B_2^{44}	0.0	0.0	0.1
$S_4^{24\alpha\alpha}$	0.0	0.0	0.0	$S_4^{3\beta\beta\beta}$	0.0	0.0	0.0	$S_3^{3\beta\beta}$	0.0	0.0	0.0	B_2^{34}	0.0	0.0	0.2
$S_4^{23\alpha\alpha}$	0.0	0.0	0.0	$S_4^{2\beta\beta\beta}$	0.0	0.0	0.0	$S_3^{2\beta\beta}$	0.0	0.0	0.0	B_2^{33}	0.0	0.0	0.4
$S_4^{22\alpha\alpha}$	0.0	0.0	0.0	$S_4^{\alpha\alpha\alpha\beta}$	0.0	0.0	0.0	$S_3^{\alpha\alpha\beta}$	0.0	0.0	0.0	B_2^{24}	0.0	0.0	0.0
$S_4^{4\alpha\alpha\alpha}$	0.0	0.0	0.0	$S_4^{\alpha\alpha\beta\beta}$	0.0	0.0	0.0	$S_3^{\alpha\beta\beta}$	0.0	0.0	0.0	B_2^{23}	0.0	0.0	0.0
$S_4^{3\alpha\alpha\alpha}$	0.0	0.0	0.0	$S_4^{\alpha\beta\beta\beta}$	0.0	0.0	0.0	$S_3^{\beta\beta\beta}$	0.0	0.0	0.0	B_2^{22}	0.0	0.0	0.0
$S_4^{2\alpha\alpha\alpha}$	0.0	0.0	0.0	$S_4^{\beta\beta\beta\beta}$	0.0	0.0	0.0	S_2^{44}	1.0	0.7	0.7				
$S_4^{\alpha\alpha\alpha\alpha}$	0.0	0.0	0.0	S_3^{444}	8.5	7.9	8.1	S_2^{34}	1.6	1.1	1.1				
$S_4^{444\beta}$	0.0	0.0	0.0	S_3^{344}	11.8	10.7	10.9	S_2^{33}	2.6	1.7	1.8				

3.7.6.2 Structural relaxation

Now, we turn our attention to the relaxation behaviour of the glass structure. **Figure 3.7.1a–c** shows the differences in the ^{29}Si NMR spectra before and after annealing the glass at 460 ºC for the samples G, G_{Al} and G_B respectively. The spectra for all the samples show significant differences before and after annealing. The results of simple deconvolution of the spectra for the quantification of Q_2, Q_3 and Q_4 units before and after annealing is presented in **Table 3.7.4**. The peaks not only show differences in the relative amounts but also, the differences are seen in the values of δ_{iso} and *FWHM*. Also, the ^{11}B NMR spectra (**Figure 3.7.2a and b**) show significant differences before and after annealing. The quantification of the ^{11}B NMR spectra (**Table 3.7.5**) shows that after annealing treatment the relative amounts of B^{IV} units increase.

The structure of the annealed glasses can be thought of as the equilibrium structure of those glasses at annealing temperature of 460 ºC. Whereas, non-annealed glasses would not have sufficient time to relax in order to achieve equilibrium structure and thus have a non-equilibrium structure. This behaviour can be explained by the concept of broken ergodicity as proposed by Palmer [37]. In this model, initially the system is brought to equilibrium at temperature T_1; and the system being probabilistically distributed over the entire phase space. Now, the phase space is broken into several individual components having internal ergodicity but among the components, there is confinement. With this condition of broken ergodicity, the state of the system any other temperature T_2 can be obtained. This new state represents the non-equilibrium state of the system. In **Figure 3.7.5**, we simulated the ^{29}Si NMR spectrum assuming some expected chemical shift with variance for each silicate unit for both annealed and non-annealed glasses of composition G_B. In the case annealed glass, the probabilities were calculated at 460 ºC. For non-annealed glass however, broken ergodicity was used where, the glass was initially equilibrated at 1200 ºC and broken into four components: S_4^{4444}, S_4^{4444}, S_3^{4444} and rest of the states. Now, probability distribution was calculated for each component at 460 ºC. The simulation of ^{29}Si NMR spectra for the probability distributions for both effects are presented in **Figure 3.7.5**; resembles the experimental result **Figure 3.7.1c**. This simple simulation of relaxation using the concept of broken ergodicity illustrated the mechanism. In reality the behaviours of relaxation is much more complicated and must be studied using the

concept of continuously broken ergodicity [38,39]. The relaxation would not only happen by redistribution network units but variations in bond lengths and bond angles are also involved.

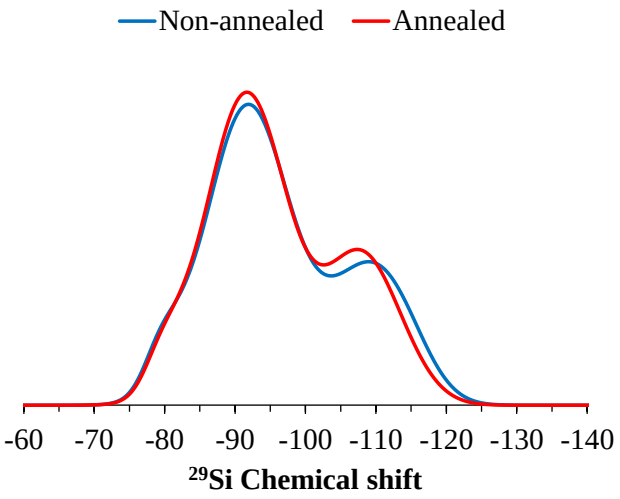

Figure 3.7.5 Simulated ^{29}Si NMR spectrum of annealed and non-annealed glasses of G_B composition.

3.7.6.3 Crystallization

Treatments at convenient temperature and time enable LS_2 crystals grow to sizes visible by naked eye (**Figure 3.7.8a**). As crystals grow, glass samples became less transparent and turn cloudiness as revealed by **Figure 3.7.8b**, where crystals in deeper positions in glass volume appear blurred. This increasing in cloudiness is due to the increasing of *LLPS*. This might be explained by the compositional change which takes place in the glassy phase reservoir as crystal fraction increases as evidenced by **Figure 3.7.6** from (a) to (d). Although crystals had same size, the crystal fraction increased due to increasing number of nuclei with increasing nucleation time. The precipitation and growth of LS_2 crystals causes the depletion of LiO_2 from the glassy phase which in turn shifts the composition of the remaining glass to an innermost location in the immiscibility dome of the LiO_2–SiO_2 phase diagram [47,183], resulting in the increasing of the *LLPS*. Therefore, higher nucleation promotes the formation of more LS_2 crystals and consequent increasing of crystal fraction resulting in enhanced *LLPS*.

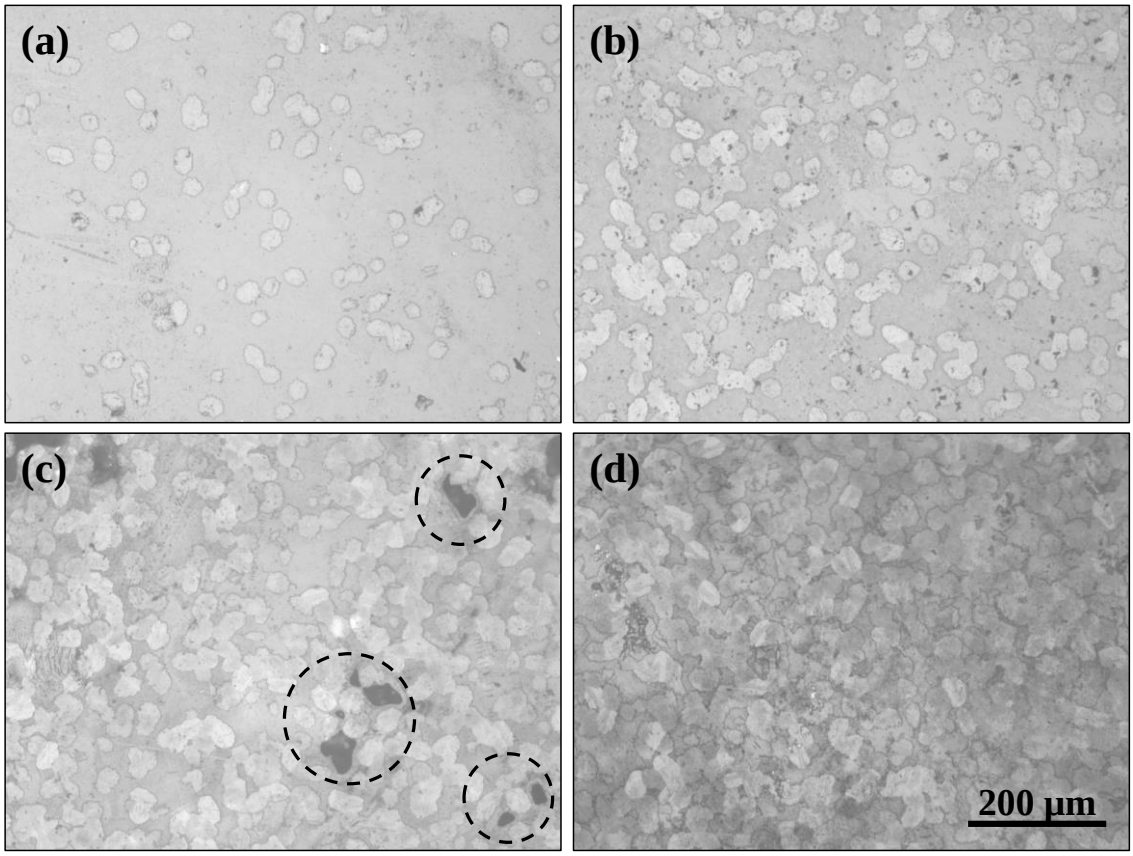

Figure 3.7.6 *LLPS* of glass G_{Al} nucleated at 460 ºC during different times: (a) 5 h, (b) 8 h, (c) 12 h, and (d) 15 h. All glasses were further heat-treated at 595 ºC for 2 h. The dashed circles in (c) show some crystallized areas.

Each separated region presented in **Figure 3.7.6** is composed by even smaller droplets as shown at higher magnification (**Figure 3.7.7**). The different morphologies of the two separated areas are evidenced in **Figure 3.7.7b** by the zones denoted by A and B, as well as the well delimited border between them (indicated by the arrow in **Figure 3.7.7b**). The larger separated regions shown in **Figure 3.7.6** remain unmixed because there is insufficient time for the system to equilibrate during the time of measurement (*i.e.* to reach the equilibrium conditions). If sufficient time was given to the system, the equilibrium status would be reached and eventually the separated phases would mix together. The finer droplets within these big regions appear when the glass cools down due to new reached equilibrium.

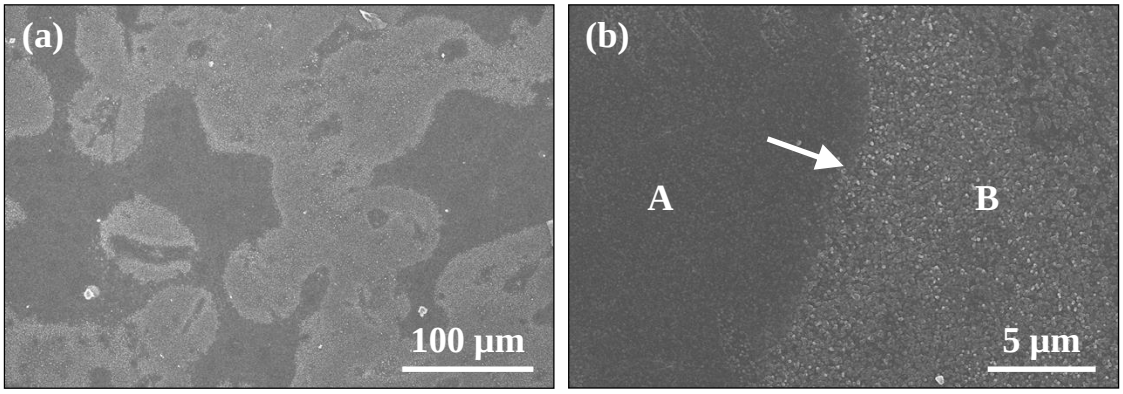

Figure 3.7.7 Micrographs of glass G_{Al} nucleated at 460 ºC during 8 h. In (b) two distinct areas are represented by A and B, while the arrow indicates the border between them.

We observe glass on a time scale that is much shorter than the structural relaxation times. Hence, glass is non-ergodic and with the elapse of time, the ergodicity is restored and the glass properties reach an equilibrium value [281]. The broken ergodicity that is mentioned in the previous section is also visible at a larger scale. **Figure 3.7.10** shows a schematic representation of dynamics of *LLPS* for different observation times. For an insufficient time, *i.e.* for $t = \tau_{obs}$, two distinct phases are visible (**Figure 3.7.7a**) and each one also presents immiscibility (**Figure 3.7.7b**). The separated phases within the larger separated ones would eventually mix for longer observation times, *i.e.* $t = \infty$.

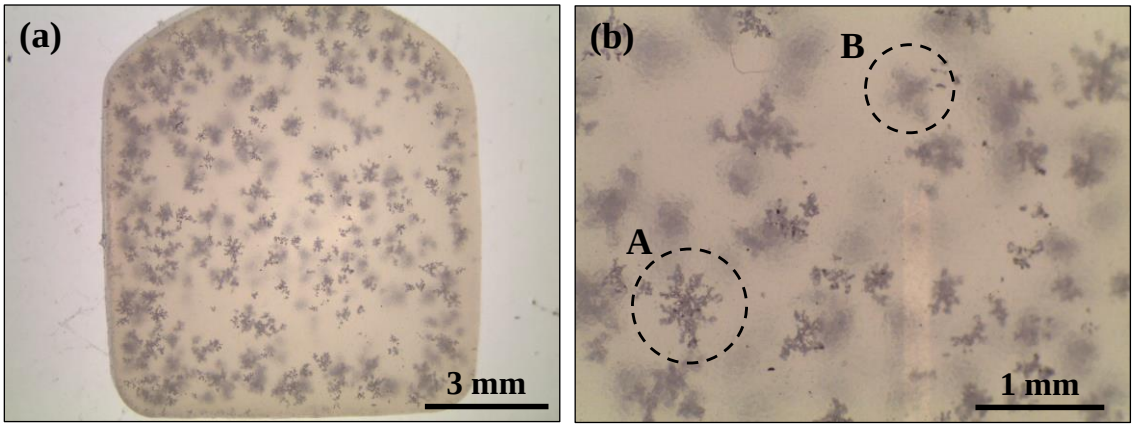

Figure 3.7.8 Appearance of glass G_{Al} nucleated at 460 ºC for 10 h and heat-treated at 595 ºC for 2 h and (b) represents the same sample at higher magnification and the dashed circles show crystals growing at different depth levels.

Al_2O_3 reduces the overall tendency of the glass to devitrify enhancing the glass stability [193], as estimated from the simple glass stability parameter ΔT (**Table 3.7.2**), which is in accordance with the crystalline phase assemblage shown in **Figure 3.7.9**. In

G_{Al} only a very small peak of SiO_2 crystalline phase (cristobalite) is visible, while B-containing glasses exhibited the presence of two SiO_2 polymorphs (quartz and cristobalite), showing relatively strong peaks of quartz. The precipitation of these phases in G_B and $G_{Al–B}$ is probably due to a less stable glassy phase and to a lowering viscosity promoted by the presence of B_2O_3 [193].

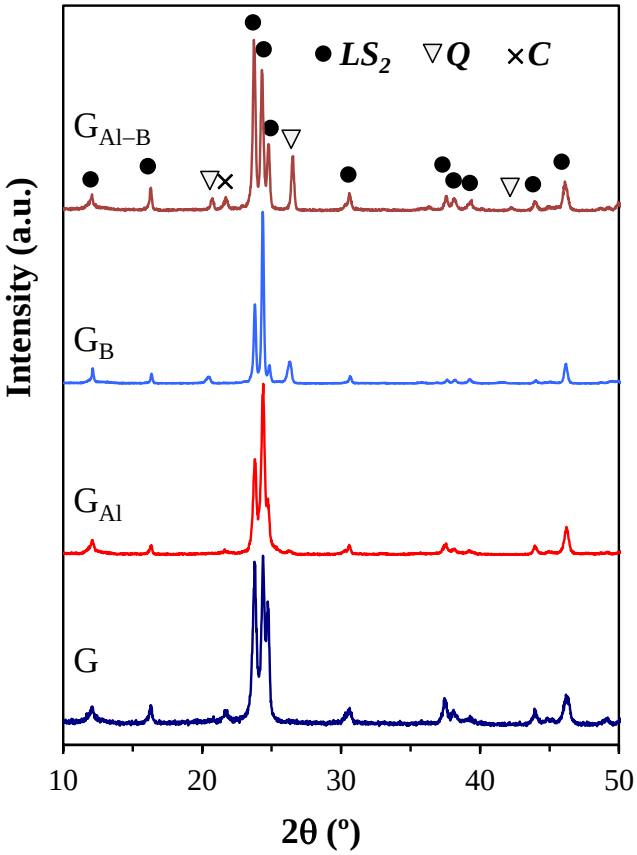

Figure 3.7.9 X-ray diffraction patterns of crystallized glasses at 800 ºC for 3 h normalized to the maximum peak. [*LS_2*: lithium disilicate ($Li_2Si_2O_5$, ICDD 04-009-4359); *C*: cristobalite (SiO_2, ICDD 01-082-0512); *Q*: quartz (SiO_2, ICDD 01-082-0512].

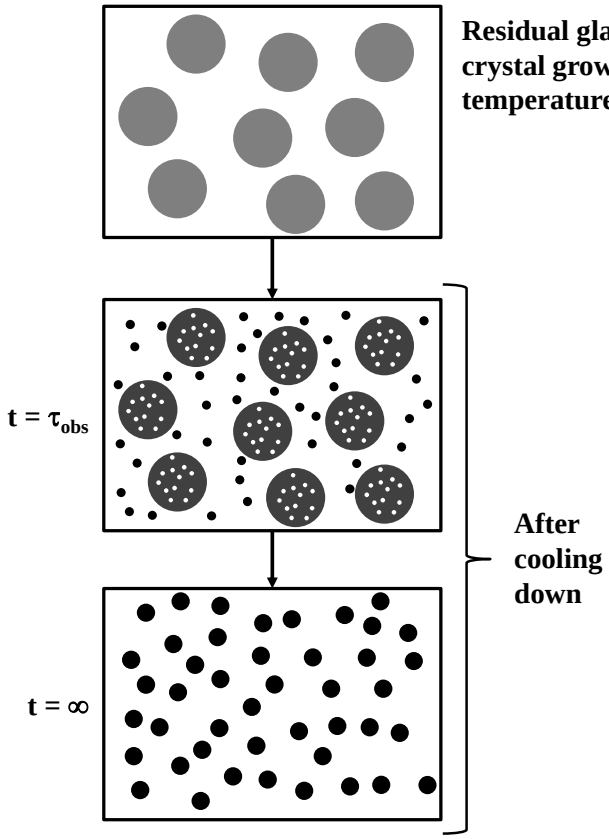

Figure 3.7.10 Schematic representation of dynamics of *LLPS* at different observation times.

3.7.7 Supplementary Information

3.7.7.1 Derivation of the model

The solution given by Eq. (3.7-13) is obtained from the Lagrange function $\mathcal{L}(P_n{}^m)$ with the Lagrange multipliers α, β, γ, $\{\gamma_f\}$ and $\{\gamma_{ij}\}$ corresponding to the following constraints,

$$\sum_{n,m} P_n^m = 1$$

$$\sum_{n,m} E_n^m P_n^m = \langle E \rangle$$

$$\sum_{n,m} r_n^m P_n^m = \langle 2x \rangle$$

$$\sum_{n,m} f_n^m P_n^m = \langle f \rangle$$

Where, $f \in \{f_{Si}, f_{Al}, f_B \ldots\}$

$$\sum_{n,m} (i,j)_n^m P_n^m = k_{ij}$$

$$\mathcal{L}(P_n^m) = k_B \sum_{n,m} (P_n^m \ln P_n^m) + \alpha \left[\sum_{n,m} P_n^m - 1\right] + \beta \left[\sum_{n,m} E_n^m P_n^m - \langle E \rangle\right] + \gamma \left[\sum_{n,m} r_n^m P_n^m - \langle 2x \rangle\right] + \sum_f \gamma_f \left[\sum_{n,m} f_n^m P_n^m - \langle f \rangle\right] + \sum_{i,j} \gamma_{ij} \left[\sum_{n,m} (i,j)_n^m P_n^m - k_{ij}\right] \quad \text{Eq. (3.7-19)}$$

Differentiating $\mathcal{L}(P_n^m)$ with respect to P_n^m would equal zero,

$$\frac{\partial \mathcal{L}(P_n^m)}{\partial P_n^m} = k_B(1 + \ln P_n^m) + \alpha + \beta E_n^m + \gamma r_n^m + \sum_f \gamma_f f_n^m + \sum_{j>i} \gamma_{ij} (i,j)_n^m = 0$$

Rearranging,

$$\ln P_n^m = -\ln Z_{gr} - \frac{\beta E_n^m}{k_B} - \frac{r_n^m \gamma}{k_B} - \frac{\sum_{i,j} f_n^m \gamma_f}{k_B} - \frac{\sum_{i,j} (i,j)_n^m \gamma_{ij}}{k_B} \quad \text{Eq. (3.7-20)}$$

Where, $\ln Z_{gr} = \frac{(\alpha + k_B)}{k_B}$ and substituting Eq. (3.7-20) in Eq. (3.7-12)

$$S = -k_B \sum_{n,m} \left(- P_n^m \ln Z_{gr} - P_n^m \frac{\beta E_n^m}{k_B} - P_n^m \frac{r_n^m \gamma}{k_B} - P_n^m \frac{\sum_f f_n^m \gamma_f}{k_B} - P_n^m \frac{\sum_{j>i} (i,j)_n^m \gamma_{ij}}{k_B} \right)$$

Solving using the constraint equations,

$$S = k_B \ln Z_{gr} + \beta \langle E \rangle + \gamma \langle 2x \rangle + \sum_f \gamma_f \langle f \rangle + \sum_{j>i} \gamma_{ij} k_{ij}$$

Rearranging,

$$\langle E \rangle = \frac{1}{\beta} S - \frac{k_B}{\beta} \ln Z_{gr} - \frac{\gamma}{\beta} \langle 2x \rangle - \sum_f \frac{\gamma_f}{\beta} \langle f \rangle - \sum_{j>i} \frac{\gamma_{ij}}{\beta} k_{ij}$$

Differentiating,

$$d\langle E\rangle = \frac{1}{\beta}dS - \frac{k_B}{\beta}d\ln Z_{gr} - \frac{\gamma}{\beta}d\langle 2x\rangle - \sum_f \frac{\gamma_f}{\beta}d\langle f\rangle - \sum_{j>i}\frac{\gamma_{ij}}{\beta}dk_{ij}$$

Comparing the above equation with the *fundamental thermodynamic relation* (A3),[S1]

$$dE = TdS - PdV + \sum \mu_i dn_i \qquad \text{Eq. (3.7-21)}$$

Would yield,

$$\beta = \frac{1}{T} \qquad \text{Eq. (3.7-22)}$$

$$\begin{aligned} \gamma &= -\frac{\mu}{T} \\ \gamma_f &= -\frac{\mu_f}{T} \\ \gamma_{ij} &= -\frac{\mu_{ij}}{T} \end{aligned} \qquad \text{Eq. (3.7-23)}$$

Therefore, substituting Eq. (3.7-22) and Eq. (3.7-23) into Eq. (3.7-20) and rearranging gives,

$$P_n^m = \frac{1}{Z_{gr}} e^{\frac{\sum_{j>i}(i,j)_n^m \mu_{ij} + \sum_f f_n^m \mu_f + r_n^m \mu_r - E_n^m}{k_B T}} \qquad \text{Eq. (3.7-24)}$$

3.7.7.2 Reduced number of units

a. Composition G

For composition G, the only units are Q_2, Q_3 and Q_4. The number of combinations of neighbouring units for each is calculated by,

$$\boldsymbol{Q_2}: \left(\binom{3}{2}\right) = \binom{3+2-1}{2} = \binom{4}{2} = 6$$

$$\boldsymbol{Q_3}: \left(\binom{3}{3}\right) = \binom{3+3-1}{3} = \binom{5}{3} = 10$$

$$\boldsymbol{Q_4}: \left(\binom{3}{4}\right) = \binom{3+4-1}{4} = \binom{6}{4} = 15$$

Total number of units is 31. Number of constraint equations is equal to number types of *BO*s O_{ij}. Calculated by,

$$\boldsymbol{O_{ij}}: \left(\binom{3}{2}\right) - 3 = \binom{3+2-1}{2} - 3 = \binom{4}{2} - 3 = 6 - 3 = 3$$

Total number of network connectivity constraint equations is 3.

b. Composition G_{Al}

For composition G_{Al}, the only units are Q_2, Q_3, Q_4 and Al^{IV}. The number of combinations of neighbouring units for each is calculated by,

$$\boldsymbol{Q_2}: \left(\binom{4}{2}\right) = \binom{4+2-1}{2} = \binom{5}{2} = 10$$

$$\boldsymbol{Q_3}: \left(\binom{4}{3}\right) = \binom{4+3-1}{3} = \binom{6}{3} = 20$$

$$\boldsymbol{Q_4}: \left(\binom{4}{4}\right) = \binom{4+4-1}{4} = \binom{7}{4} = 35$$

$$\boldsymbol{Al^{IV}}: \left(\binom{3}{4}\right) = \binom{3+4-1}{4} = \binom{6}{4} = 15$$

Total number of units is 80. Number of constraint equations is equal to number types of *BO*s O_{ij}. Calculated by,

$$\boldsymbol{O_{ij}}: \left(\binom{3}{2}\right) - 3 + 3 = \binom{3+2-1}{2} = \binom{4}{2} = 6$$

Total number of network connectivity constraint equations is 6.

c. Composition G_B

For composition G_B, the only units are Q_2, Q_3, Q_4, B^{IV} and B^{III}. The number of combinations of neighbouring units for each is calculated by,

$$\boldsymbol{Q_2}: \left(\binom{5}{2}\right) = \binom{5+2-1}{2} = \binom{6}{2} = 15$$

$$\boldsymbol{Q_3}: \left(\binom{5}{3}\right) = \binom{5+3-1}{3} = \binom{7}{3} = 35$$

$$\boldsymbol{Q_4}: \left(\binom{5}{4}\right) = \binom{5+4-1}{4} = \binom{8}{4} = 70$$

$$\boldsymbol{B^{IV}}: \left(\binom{3}{4}\right) = \binom{3+4-1}{4} = \binom{6}{4} = 15$$

$$\boldsymbol{B^{III}}: \left(\binom{3}{2}\right) = \binom{3+2-1}{2} = \binom{4}{2} = 6$$

Total number of units is 141. Number of constraint equations is equal to number types of *BO*s O_{ij}. Calculated by,

$$\boldsymbol{O_{ij}}: \left(\binom{3}{2}\right) - 3 + 3 + 3 = \binom{3+2-1}{2} + 3 = \binom{4}{2} + 3 = 6 + 3 = 9$$

Total number of network connectivity constraint equations is 9.

3.7.7.3 Network volume for binary lithium silicate

The variation of NV for binary lithium silicate glass; the density data was taken from Shelby.[8]

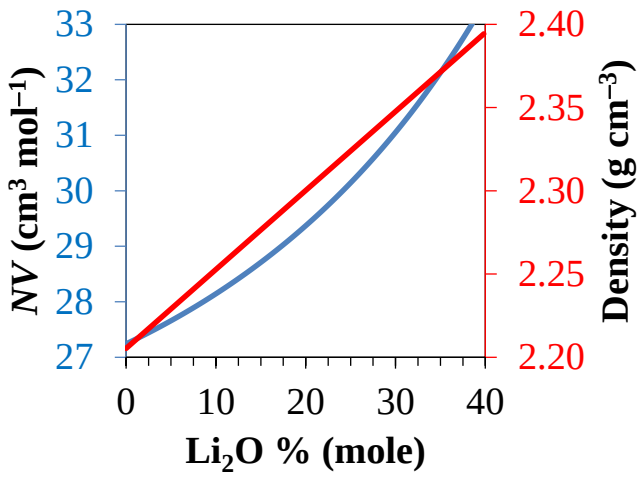

Figure 3.7.11 Variation of density and network volume with composition.

3.7.7.4 Differential thermal analysis

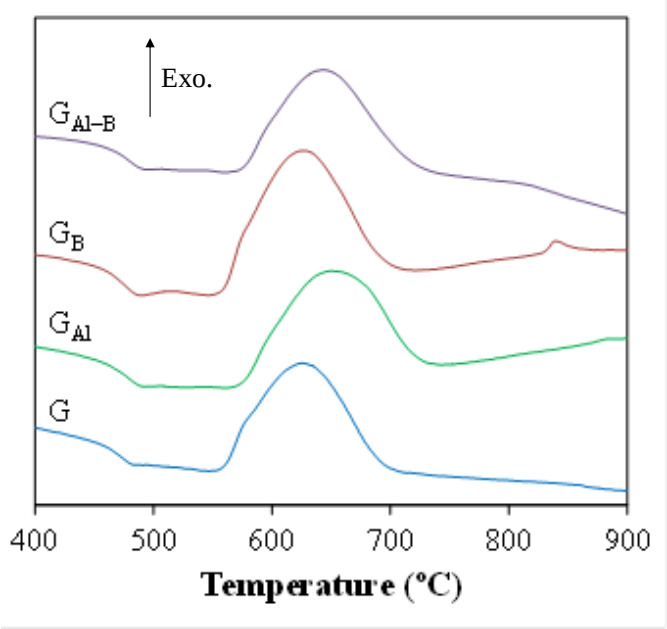

Figure 3.7.12 DTA of experimental glasses

Chapter 4

Conclusions

Then I beheld all the work of God, that a man cannot find out the work that is done under the sun: because though a man labour to seek it out, yet he shall not find it; yea further; though a wise man think to know it, yet shall he not be able to find it.

(Ecclesiastes 8:17)

4.1 Summary

4.1.1 Role of manganese on the structure, crystallization and sintering of non-stoichiometric lithium disilicate glasses

Small additions of MnO_2 to the experimental glass imparted huge changes on crystallization of bulk/particulate glasses and on sintering behaviour of glass powder compacts. The following conclusions could be drawn from the study presented in Section 3.2:

1. Well-known redox equilibrium of Mn^{2+}/Mn^{3+} with predominance of Mn^{3+} was established in Mn-doped glasses giving rise to purple colour.

2. MAS-NMR and FTIR spectroscopy suggest a network modifier role for Mn; whereas relatively constant T_g values (458–467 ºC), increasing V_m and decreasing phase separation suggest network former role.

3. The involvement of Mn in the formation of individual molecular units in the interstitials of the depolymerized glass network explanation is the proposed conciliating view about the role of Mn in glasses. Large crystal field parameters (Δ_o, B) and the lowering trend for glass-in-glass phase separation both agree with this hypothesis.

4. The lowering trend for glass-in-glass phase separation in turn lead to reduced bulk nucleation. Therefore Mn increased the kinetic barrier for nucleation near T_g.

5. Oppositely, the peak crystallization temperature (T_P) from DTA showed a decreasing trend pointing out to lower activation energy for crystallization from a less polymerized glass network.

6. Sintering and crystallization occurred at lower temperatures in Mn-doped glass powder compacts conferring higher strength at low sintering temperatures. But the occurrence of foaming in Mn-doped samples at higher temperatures drastically reduced density and mechanical strength.

4.1.2 Glass structure and crystallization of Al and B containing glasses belonging to the $Li_2O–SiO_2$ system

The current study investigated the role of both Al and B on glass structure, phase segregation, nucleation and crystallization when added at a small concentration. The following are the broad conclusions that are drawn from the study presented in Section 3.3.

1. Al goes in to glass network in 4-fold coordination whereas B goes in as both 4- and 3-fold coordination. This B speciation resulted in the depolymerisation of glass network, increasing the percentage of *NBO*s.

2. Therefore, with B substitution glasses showed decreasing viscosity, molar volumes, oxygen densities and glass transition temperatures.

3. The simultaneous mixture of Al and B into the glass composition resulted in the increased configurational entropy. Therefore, in mixed Al and B glasses the increased entropy resulted in decreased driving force for *LLPS*.

4. Glass GB_{100} exhibited highest crystal nucleation rate compared to all the other glasses due to fastest kinetics of *LLPS*, while glasses containing simultaneous mixture of Al and B featured the lowest crystal nucleation rate, which is correlated with the previous conclusion.

5. In Al rich glasses lithium metasilicate crystallizes at initial stages and then transforms into LS_2 at higher temperatures. However with B addition glasses crystallize directly into LS_2.

4.1.3 Influence of Al_2O_3 and B_2O_3 on sintering and crystallization of lithium silicate glass system

The work presented in Section 3.4 is a continuation of the work reported in Section 3.3, which dealt with liquid-liquid phase segregation and crystal nucleation phenomena occurring in bulk glasses of the same compositions. The work presented in Section 3.4 deals with the influence of Al and B oxides on the sintering behaviour and crystallization of glass powders from lithium silicate glass system. The following conclusions can be drawn from this study:

1. B_2O_3 and Al_2O_3 added as dopants modify the thermodynamic equilibrium of the system and this change is mainly entropy driven. Increased entropy leads to a more stable liquid phase.

2. B_2O_3 and Al_2O_3 also slowdown the kinetics of crystallization which is mainly dependent on the thermodynamic driving force and the polymerization level of the glass network.

3. After initial crystallization events, the compositions become richer in dopants and enthalpic contributions from the dopants also have influence on the state of the system.

4. Although LS_2 and polymorphs of SiO_2 feature greater driving force for the crystallization, there will be kinetic restriction for the crystallization of these phases and LS with small driving force crystallizes with the available Q^2 units resulting in a sequence of crystallization in the order: LS, LS_2 and SiO_2.

5. The sintering initiates in all the glasses at temperatures slightly above T_g and well sintered and dense glass-ceramics were obtained after sintering of glass powders at 850–900 ºC for 1 h with crystalline phase assemblage dominated by LS_2.

4.1.4 The roles of P_2O_5 and SiO_2/Li_2O ratio on the network structure and crystallization kinetics of non-stoichiometric lithium disilicate based glasses

The work presented in Section 3.5 revealed that in non-stoichiometric multicomponent $Li_2O–K_2O–Al_2O_3–SiO_2$ systems, both the SiO_2/Li_2O molar ratio and the addition of P_2O_5 play important roles in determining the crystallization behaviour upon heat treatment, and the crystalline phase assemblage and structure of the resulting glasses. From the results presented and discussed in this section, the following specific conclusions can be drawn:

1. Adding P_2O_5 to glasses led to an overall increase in polymerization of the glass network.

2. The activation energy for crystallization, E_c, decreased with increasing Li content further, it showed a more accentuated decrease when P_2O_5 is added.

3. The values of Avrami parameters being less than 2 for *G24* and *G26*, are consistent with microstructures and evidenced the surface crystallization.

4. The presence of P_2O_5 enhanced the crystallization of *LS* at lower temperatures (when compared with P_2O_5-free compositions) and promoted the formation of LS_2 at temperatures above 800 ºC.

5. The enhanced formation of the crystalline phases in compositions containing P_2O_5 can be explained as a result of heterogeneous nucleation at the interface of an amorphous *LP* phase and the glass matrix.

4.1.5 Statistics of silicate units in binary glasses

In the Section 3.6 a new model based on statistical mechanics to describe the distribution of various silicate units in glasses was presented. The system was considered to be grand canonical ensemble of silicate units which exchange energy and network modifiers with the reservoir. The current model could find its usefulness in several applications. These include, *LLPS*, crystal nucleation and glass relaxation. Since statistical mechanics uses microscopic properties to obtain macroscopic properties, several bulk properties of the glass can be easily calculated using the current model.

4.1.6 Structure and thermal relaxation of network units and crystallization of lithium silicate based glasses doped with oxides of Al and B

The investigation presented in Section 3.7 reports the relaxation behaviour of the glasses belonging to lithium silicate system by NMR spectroscopy. A statistical mechanical model based on the previous model presented in Section 3.6 was developed in order to address this issue. The structural relaxation behaviour employing the concept of broken ergodicity and the statistical mechanical model was simulated to shed light on the mechanism. The crystallization behaviour of the glasses was studied using microscopy and XRD. The changes in the residual glass composition with crystallization are reported.

Chapter 5

Future Work

And further, by these, my son, be admonished: of making many books there is no end; and much study is a weariness of the flesh.

(Ecclesiastes 12:12)

5.1 Future prospects

The following are the potentially important future works based on the current thesis:

1. In order to fully validate the Q_n statistics models shown in Eq. (3.6-15) and Eq. **(3.7-13)**, the vibrational frequencies of each S_n^m microstate must be calculated using quantum mechanical calculations. And the theory should be rigorously tested with experiments.

2. Currently the NMR spectra is deconvoluted empirically using softwares such as DMfit.[228] However, new softwares could be developed based on Q_n statistics model presented in Eq. (3.7-13).

3. Development of completely new nucleation theory established on the ideas discussed in section 3.1.3. The development of this new theory would require understanding nucleation based on combinatorics and topology. Further, the theory should be supported by large amount of experimental data. The experiments should involve obtaining temperature dependence of Q_n distribution of binary glasses therefore; *in-situ* high temperature NMR spectroscopes would be required.

4. The models developed for Q_n speciation (Eq. (3.6-15) and Eq. (3.7-13)) do not address *LLPS* directly. Therefore the models have to be extended to address also *LLPS*. Since Eq. (3.6-15) and Eq. (3.7-13) model a glass system to be like a gas consisting of Q_n units, the problem of *LLPS* should solved by understand phase separations in gas-like systems. There are some granular systems which are considered to be as gas-like systems and exhibit phase separation.[282,283] These systems might inspire developing models for *LLPS* in glass systems based on Eq. (3.6-15) and Eq. (3.7-13).

References

(1) Höland, W.; Beall, G. *Glass-Ceramic Technology*; The American Ceramic Society: Westerville, Ohio, 2002.

(2) Fokin, V. M.; Zanotto, E. D.; Yuritsyn, N. S.; Schmelzer, J. W. P. P. Homogeneous Crystal Nucleation in Silicate Glasses: A 40 Years Perspective. *J. Non. Cryst. Solids* **2006**, *352*, 2681–2714.

(3) Zanotto, E. D. Glass Crystallization Research - A 36-Year Retrospective. Part I, Fundamental Studies. *Int. J. Appl. Glas. Sci.* **2013**, *4*, 105–116.

(4) Zanotto, E. D. Glass Crystallization Research - A 36-Year Retrospective. Part II, Methods of Study and Glass-Ceramics. *Int. J. Appl. Glas. Sci.* **2013**, *4*, 117–124.

(5) Anderson, P. W. Through the Glass Lightly. *Science (80-.).* **1995**, *267*, 1615–1616.

(6) Montazerian, M.; Singh, S. P.; Zanotto, E. D. An Analysis of the Glass-Ceramic Research and Commercialization. *Am. Ceram. Soc. Bull.* **2015**, *94*, 30–35.

(7) Mauro, J. C. Realizing the Potential of Glass-Ceramics in Industry. *Am. Ceram. Soc. Bull.* **2015**, *94*, 35.

(8) Shelby, J. *Introduction to Glass Science and Technology*; 2nd ed.; The Royal Society of Chemistry: Thomas Graham House, Science Park, Milton Road, Cambridge CB4 OWF, UK, 2005.

(9) Zachariasen, W. H. The Atomic Arrangement in Glass. *J. Am. Chem. Soc.* **1932**, *54*, 3841–3851.

(10) Stebbins, J. F.; Oglesby, J. V; Kroeker, S. Oxygen Triclusters in Crystalline CaAl4O7 (Grossite) and in Calcium Aluminosilicate Glasses: 17O NMR. *Am. Mineral.* **2001**, *86*, 1307–1311.

(11) Dupree, R.; Ford, N.; Holland, D. An Examination of the 29Si Environment in the PbO-SiO2 System by Magic Angle Spinning Nuclear Magnetic Resonance Part 1. Glasses. *Phys. Chem. Glas.* **1987**, *28*, 78–84.

(12) Gurman, S. J. Bond Ordering in Silicate Glasses: A Critique and a Re-Solution. *J. Non. Cryst. Solids* **1990**, *125*, 151–160.

(13) Shakhmatkin, B. A.; Vedishcheva, N. M.; Shultz, M. M.; Wright, A. C. The Thermodynamic Properties of Oxide Glasses and Glass-Forming Liquids and Their Chemical Structure. *J. Non. Cryst. Solids* **1994**, *177*, 249–256.

(14) Shakhmatkin, B. A.; Vedishcheva, N. M. Thermodynamic Studies of Oxide Glass-Forming Liquids by the Electromotive Force Method. *J. Non. Cryst. Solids* **1994**, *171*, 1–30.

(15) Schneider, J.; Mastelaro, V. R.; Zanotto, E. D.; Shakhmatkin, B. a.; Vedishcheva, N. M.; Wright, A. C.; Panepucci, H. Q_n Distribution in Stoichiometric Silicate Glasses: Thermodynamic Calculations and ^{29}Si High Resolution NMR Measurements. *J. Non. Cryst. Solids* **2003**, *325*, 164–178.

(16) Edén, M. NMR Studies of Oxide-Based Glasses. *Annu. Reports Sect. "C" (Physical Chem.* **2012**, *108*, 177.

(17) Eckert, H. Structural Characterization of Noncrystalline Solids and Glasses Using Solid State NMR. *Prog. Nucl. Magn. Reson. Spectrosc.* **1992**, *24*, 159–293.

(18) Brandriss, M. E.; Stebbins, J. F. Effects of Temperature on the Structures of Silicate Liquids: 29Si NMR Results. *Geochim. Cosmochim. Acta* **1988**, *52*, 2659–2669.

(19) Sen, S.; Maekawa, H.; Papatheodorou, G. N. Short-Range Structure of Invert Glasses along the Pseudo-Binary Join $MgSiO_3$-Mg_2SiO_4: Results from ^{29}Si and ^{25}Mg MAS NMR Spectroscopy. *J. Phys. Chem. B* **2009**, *113*, 15243–15248.

(20) Kaseman, D. C.; Retsinas, A.; Kalampounias, A. G.; Papatheodorou, G. N.; Sen, S. Q-Speciation and Network Structure Evolution in Invert Calcium Silicate Glasses. *J. Phys. Chem. B* **2015**, *119*, 8440–8445.

(21) Kroeker, S.; Stebbins, J. F. Three-Coordinated Boron-11 Chemical Shifts in Borates. **2001**.

(22) Dell, W. J.; Bray, P. J. ^{11}B NMR Studies and Structural Modeling of Na_2O - B_2O_3 - SiO_2 Glasses of High Soda Content. *J. Non- Cryst. Solids* **1983**, *58*, 1–16.

(23) Zhong, J.; Wu, X.; Liu, M. L.; Bray, P. J. Structural Modeling of Lithium Borosilicate Glasses via NMR Studies. *J. Non. Cryst. Solids* **1988**, *107*, 81–87.

(24) MacKenzie, J. W.; Bhatnagar, A.; Bain, D.; Bhowmik, S.; Parameswar, C.; Budhwani, K.; Feller, S. A.; Royle, M. L.; Martin, S. W. ^{29}Si MAS-NMR Study of the Short Range Order in Alkali Borosilicate Glasses. *J. Non. Cryst. Solids* **1994**, *177*, 269–276.

(25) Miura, Y.; Kusano, H.; Nanba, T.; Matsumoto, S. X-Ray Photoelectron Spectroscopy of Sodium Borosilicate Glasses. *J. Non. Cryst. Solids* **2001**, *290*, 1–14.

(26) Reiner, M. The Deborah Number. *Phys. Today* **1964**, *17*, 62.

(27) Varshneya, A. K. *Fundamentals of Inorganic Glasses*; Academic Press: London, 1994.

(28) Mazurin, O. V. Problems of Compatibility of the Values of Glass Transition Temperatures Published in the World Literature. *Glas. Phys. Chem.* **2007**, *33*, 22–36.

(29) Tool, A. Q. Relation between Inelastic Deformability and Thermal Expansion of Glass in Its Annealing Range. *J. Am. Ceram. Soc.* **1946**, *29*, 240–253.

(30) Ritland, H. N. Limitatios of the Fictive Temperature Concept. *J. Am. Ceram. Soc.* **1956**, *39*, 1954–1957.

(31) Debenedetti, P. G.; Stillinger, F. H. Supercooled Liquids and the Glass Transition. *Nature* **2001**, *410*, 259–267.

(32) Stillinger, F. H.; Weber, T. A. Hidden Structure in Liquids. *Phys. Rev. A* **1982**, *25*, 978–989.

(33) Middleton, T. F.; Wales, D. J. Energy Landscapes of Model Glasses. II. Results for Constant Pressure. *J. Chem. Phys.* **2003**, *118*, 4583.

(34) Stillinger, F. H. A Topographic View of Supercooled Liquids and Glass Formation. *Science* **1995**, *267*, 1935–1939.

(35) Mauro, J. C.; Varshneya, A. K. A Nonequilibrium Statistical Mechanical Model

of Structural Relaxation in Glass. *J. Am. Ceram. Soc.* **2006**, *89*, 1091–1094.

(36) Mauro, J. C.; Loucks, R. J.; Gupta, P. K. Metabasin Approach for Computing the Master Equation Dynamics of Systems with Broken Ergodicity. *J. Phys. Chem. A* **2007**, *111*, 7957–7965.

(37) Palmer, R. G. Broken Ergodicity. *Adv. Phys.* **1982**, *31*, 669–735.

(38) Mauro, J. C.; Gupta, P. K.; Loucks, R. J. Continuously Broken Ergodicity. *J. Chem. Phys.* **2007**, *126*, 184511.

(39) Mauro, J. C.; Smedskjaer, M. M. Statistical Mechanics of Glass. *J. Non. Cryst. Solids* **2014**, *396–397*, 41–53.

(40) Vogel, W. Phase Separation in Glass. *J. Non. Cryst. Solids* **1977**, *25*, 170–214.

(41) James, P. F. Liquid-Phase Separation in Glass-Forming Systems. *J. Mater. Sci.* **1975**, *10*, 1802–1825.

(42) Gaskell, D. R. *Introduction to the Thermodynamics of Materials*; 4th ed.; Taylor & Francis Group: New York, 2003.

(43) Cahn, J. W.; Hilliard, J. E. Free Energy of a Nonuniform System. I. Interfacial Free Energy. *J. Chem. Phys.* **1958**, *28*, 258.

(44) Cahn, J. W. Free Energy of a Nonuniform System. II. Thermodynamic Basis. *J. Chem. Phys.* **1959**, *30*, 1121.

(45) Cahn, J. W.; Hilliard, J. E. Free Energy of a Nonuniform System. III. Nucleation in a Two-Component Incompressible Fluid. *J. Chem. Phys.* **1959**, *31*, 688.

(46) Charles, R. J. Immiscibility and Its Role in Glass Processing. *Ceram. Bull.* **1973**, *52*, 673–680.

(47) Charles, R. J. Activities in Li_2O , Na_2O-, and K_2O-SiO_2 Solutions. *J. Am. Ceram. Soc.* **1967**, *50*, 631–641.

(48) Charles, R. J. Metastable Liquid Immiscibility in Alkali Metal Oxide-Silica Systems. *J. Am. Ceram. Soc.* **1966**, *49*, 55–62.

(49) Ohlberg, S. M.; Golob, H. R.; Hammel, J. J.; Lewchuk, R. R. Noncrystalline

Microphase Separation in Soda-Lime-Silica Glass. *J. Am. Ceram. Soc.* **1965**, *48*, 331–332.

(50) West, A. R. *Solid State Chemistry and Its Applications*; 2nd ed.; John Wiley and Sons: New Delhi, India, 2014.

(51) Kracek, F. C. The Cristobalite Liquidus in the Alkali Oxide-Silica System and the Heat of Fusion of Cristobalite. *J. Am. Chem. Soc.* **1930**, *52*, 1436–1442.

(52) Levin, E. M. Liquid Immiscibility in Oxide Systems. In *Phase Diagrams - Materials Science and Technology, Vol 3*; Alper, A. M., Ed.; Academic Press: New York, 1970.

(53) Vogel, W. *Structure and Crystallization of Glasses*; Leipzig.; Pergamon Press: Vieweg & Sohn GmbH, Burgplatz 1, Braunschweig, 1971.

(54) Warren, B. E.; Pincus, A. G. Atomic Consideration of Immiscibility in Glass Systems. *J. Am. Ceram. Soc.* **1940**, *23*, 301–304.

(55) Levin, E. M.; Block, S. Structural Interpretation of Immiscibility in Oxide Systems: I, Analysis and Calculation of Immiscibility. *J. Am. Ceram. Soc.* **1957**, *40*, 95–106.

(56) Block, S.; Levin, E. M. Structural Interpretation of Immiscibility in Oxide Systems: II, Coordination Principles Applied to Immiscibility. *J. Am. Ceram. Soc.* **1957**, *40*, 113–118.

(57) Levin, E. M.; Block, S. Structural Interpretation of Immiscibility in Oxide Systems: III, Effect of Alkalis and Alumina in Ternary Systems. *J. Am. Ceram. Soc.* **1958**, *41*, 49–54.

(58) Levin, E. M. Structural Interpretation of Immiscibility in Oxide Systems: IV, Occurrence, Extent, and Temperature of the Monotectic. *J. Am. Ceram. Soc.* **1967**, *50*, 29–38.

(59) Hudon, P.; Baker, D. R. The Nature of Phase Separation in Binary Oxide Melts and Glasses. I. Silicate Systems. *J. Non. Cryst. Solids* **2002**, *303*, 299–345.

(60) Fokin, V. M.; Reis, R. M. C. V.; Abyzov, A. S.; Chinaglia, C. R.; Zanotto, E. D.

Nonstoichiometric Crystallization of Lithium Metasilicate–calcium Metasilicate Glasses. Part 1 — Crystal Nucleation and Growth Rates. *J. Non. Cryst. Solids* **2013**, *362*, 56–64.

(61) Gutzow, I.; Schmelzer, J. *The Vitreous State: Thermodynamics, Structure, Rheology, and Crystallization*; 2nd ed.; Springer-Verlag: Berlin, 1995.

(62) Glasstone, S.; Laidler, K. J.; Eyring, H. *The Theory of Rate Processes: The Kinetics of Chemical Reactions, Viscosity, Diffusion and Electrochemical Phenomena*; McGraw-Hill Book Company, 1941.

(63) Gilmer, G. H. Computer Simulation of Crystal Growth. *J. Cryst. Growth* **1977**, *42*, 3–10.

(64) Kolmogorov, A. N. No Title. *Izv. Akad. Nank* **1937**, *3*, 355.

(65) Johnson, W. A.; Mehl, K. F. Reaction Kinetics in Processes of Nucleation and Growth. *Trans. Am. Inst. Min. Eng.* **1939**, *135*, 416–472.

(66) Avrami, M. Kinetics of Phase Change. I — General Theory. *J. Chem. Phys.* **1939**, *7*, 1103–1112.

(67) Avrami, M. Kinetics of Phase Change. II Transformation-Time Relations for Random Distribution of Nuclei. *J. Chem. Phys.* **1940**, *8*, 212.

(68) Avrami, M. Avrami M. Kinetics of Phase Change. III — Granulation, Phase Change, and Microstructure. *J. Chem. Phys.* **1941**, *9*, 177–184.

(69) Weinberg, M. C.; Iii, D. P. B.; Shneidman, V. A. Crystallization Kinetics and the JMAK Equation. **1997**, *219*, 89–99.

(70) Kaischew, R.; Stranski, I. N. No Title. *Z. Phys. Chem.* **1934**, *26*, 317.

(71) Volmer, M.; Weber, A. No Title. *Z. Phys. Chem.* **1926**, *119*, 227.

(72) Becker, R.; Döring, W. Kinetische Behandlung Der Keimbildung in Übersättigten Dämpfen. *Ann. Phys.* **1935**, *416*, 719–752.

(73) Neilson, G. F.; Weinberg, M. C. A Test of Classical Nucleation Theory: Crystal Nucleation of Lithium Disilicate Glass. *J. Non. Cryst. Solids* **1979**, *34*, 137–147.

(74) Gonzalez-Oliver, C. J. R.; James, P. F. Crystal Nucleation and Growth in a Na2O.2CaO.3SiO2 Glass. *J. Non. Cryst. Solids* **1980**, *38*, 699–704.

(75) Zanotto, E. D.; James, P. F. Experimental Test of the General Theory of Transformation Kinetics: Homogeneous Nucleation in a BaO · 2SiO2 Glass. *J. Non. Cryst. Solids* **1988**, *104*, 70–72.

(76) Zanotto, E. D.; Galhardi, A. Experimental Test of the General Theory of Transformation Kinetics: Homogeneous Nucleation in a Na2O·2CaO·3SiO2 Glass. *J. Non. Cryst. Solids* **1988**, *104*, 73–80.

(77) Reidies, A. H. H. *Manganese Compounds*; Wiley-VCH, 2002; pp. 495–542.

(78) Bach, H.; Krause, D. *Low Thermal Expansion Glass Ceramics*; Springer: Berlin, 1995.

(79) Van Noort, R. *Introduction to Dental Materials*; Mosby: Sheffield, 2002.

(80) White, W. B.; Knight, D. S. S. Defects in Glasses. *Mater. Res. Soc. Symp. Proc.* **1986**, *61*, 283–293.

(81) Turner, W. H.; Turner, J. E. Absorption Spectra and Concentration-Dependent Luminescence of Mn^{2+} in Silicate Glasses. *J. Am. Ceram. Soc.* **1970**, *53*, 329–335.

(82) Schreiber, H. Redox Processes in Glass-Forming Melts. *J. Non. Cryst. Solids* **1986**, *84*, 129–141.

(83) Schreiber, H. D.; Kochanowski, B. K.; Schreiber, C. W.; Morgan, A. B.; Coolbaugh, M. T.; Dunlap, T. G. Compositional Dependence of Redox Equilibria in Sodium Silicate Glasses. *J. Non. Cryst. Solids* **1994**, *177*, 340–346.

(84) Sarukhanishvili, A. V; Shashek, Y.; Shapanidze, E. V; Sarukhanishvili, I. A. Waste Materials from the Production of Electrolytic Manganese Dioxide in the Glass Vessel Industry. *Steklo i Keramika* **1992**, *4*, 4–5.

(85) Rode, E. A. *Oxygen Compounds of Manganese [in Russian]*; Izvestiya Akademii Nauk SSSR: Moscow, 1952.

(86) Bufala, R. La Coloración de Los Vidrios de Silicato Por Los Elementos de

Transición. Parte lIl: Cobalto. *Bol. da la Soc. Esp. Cerámica e Vidr.* **1971**, *10*, 247–260.

(87) Bratu, I.; Ardelean, I.; Barbu, A.; Mih, V.; Maniu, D.; Botezan, G. Spectroscopic Investigation of Some Lead Phosphate Oxide Glasses Containing Manganese Ions. *J. Mol. Struct.* **1999**, *482–483*, 689–692.

(88) Orgel, L. E. Band Widths in the Spectra of Manganous and Other Transition-Metal Complexes. *J. Chem. Phys.* **1955**, *23*, 1824–1826.

(89) Parke, S.; Webb, R. S. Fluorescence of Copper in Glass. *Phys. Chem. Glas.* **1972**, *13*, 157–160.

(90) Simkin, D.; Oyama-Gannon, K.; Menassa, P.; Taylor, P. Luminescent Activators as Probes for the Study of the Thermal Phase Separation of Glasses. *J. Lumin.* **1981**, *24–25*, 107–110.

(91) Mohan, N. K.; Reddy, M. R.; Jayasankar, C. K.; Veeraiah, N. Spectroscopic and Dielectric Studies on MnO Doped PbO–Nb_2O_5–P_2O_5 Glass System. *J. Alloys Compd.* **2008**, *458*, 66–76.

(92) Reddy, M. S.; Murali Krishna, G.; Veeraiah, N. Spectroscopic and Magnetic Studies of Manganese Ions in ZnO–Sb_2O_3–B_2O_3 Glass System. *J. Phys. Chem. Solids* **2006**, *67*, 789–795.

(93) Pradell, T.; Molina, G.; Molera, J.; Pla, J.; Labrador, a. The Use of Micro-XRD for the Study of Glaze Color Decorations. *Appl. Phys. A* **2012**, *111*, 121–127.

(94) Caggiani, M. C.; Colomban, P. Raman Identification of Strongly Absorbing Phases: The Ceramic Black Pigments. *J. Raman Spectrosc.* **2011**, *42*, 839–843.

(95) Karasu, B.; Turan, S. Effects of Cobalt, Copper, Manganese and Titanium Oxide Additions on the Microstructures of Zinc Containing Soft Porcelain Glazes. *J. Eur. Ceram. Soc.* **2002**, *22*, 1447–1455.

(96) Srisittipokakun, N.; Kirdsiri, K.; Kaewkhaoi, J.; Kedkaewdan, C.; Limsuwan, P. Absorption and Coloration of MnO_2 Doped in Soda-Lime-Silicate and Soda-Lime-Borate Glasses. *Procedia Eng.* **2011**, *8*, 261–265.

(97) Cheng, T. W.; Huang, M. Z.; Tzeng, C. C.; Cheng, K. B.; Ueng, T. H. Production of Coloured Glass-Ceramics from Incinerator Ash Using Thermal Plasma Technology. *Chemosphere* **2007**, *68*, 1937–1945.

(98) Sun, Y.; Wang, Z.; Tian, J.; Cao, X. Coloration of Mica Glass Ceramic for Use in Dental CAD/CAM System. *Zhonghua Kou Qiang Yi Xue Za Zhi* **2003**, *38*, 137–139.

(99) Bogomolova, L. D.; E.G., G.; Krasil'nikova, N. A.; Sakharov, V. V. EPR of Mn^{2+} Ions in Heavy Metal Fluoride Glasses. *J. Non. Cryst. Solids* **1985**, *69*, 299–307.

(100) Van Die, A.; Leenaers, A. C. H. I.; Blasse, G.; Van Der Weg, W. F. Germanate Glasses as Hosts for Luminescence of Mn^{2+} and Cr^{3+}. *J. Non. Cryst. Solids* **1988**, *99*, 32–44.

(101) Rao, A. S.; Sreedhar, B.; Rao, J. L.; Lakshman, S. J. V. Electron Paramagnetic Resonance and Optical Absorption Spectra of Mn^{2+} Ions in Alkali Zinc Borosulphate Glasses. *J. Non. Cryst. Solids* **1992**, *144*, 169–174.

(102) Srinivasarao, G.; Veeraiah, N. Study on Various Physical Properties of PbO–As_2O_3 Glasses Containing Manganese Ions. *J. Alloys Compd.* **2001**, *327*, 52–65.

(103) Ardelean, I.; Ilonca, G.; Simin, V.; Cozar, O.; Ioncu, V. Magnetic Properties of x(MnO).(1-x)[Bi_2O_3.PbO] Glasses. *Solid State Commun.* **1996**, *98*, 651–653.

(104) Wang, X.-R.; Zhang, Y.; Ma, T.; Deng, C.-S.; Dai, X.-M. Effects of MnO_2 Concentration on Dielectric Properties of Barium Strontium Titanate Glass Ceramics. *Ceram. Int.* **2012**, *38*, S57--S60.

(105) Vaidhyanathan, B.; Kumar, C. P.; Rao, J. L.; Rao, K. J. Spectroscopic Investigations of Manganese Ions in Microwave-Prepared $NaPO_3$-PbO Glasses. *Phys. Chem. Glas.* **1998**, *59*, 121–128.

(106) Sreekanth Chakradhar, R. P.; Ramesh, K. P.; Rao, J. L.; Ramakrishna, J. Mixed Alkali Effect in Borate glasses—EPR and Optical Absorption Studies in xNa_2O–(30-x)K_2O–70B_2O_3 Glasses Doped with Mn^{2+}. *J. Phys. Chem. Solids* **2003**, *64*, 641–650.

(107) Durga, D. K.; Veeraiah, N. Role of Manganese Ions on the Stability of ZnF_2–P_2O_5–TeO_2 Glass System by the Study of Dielectric Dispersion and Some Other Physical Properties. *J. Phys. Chem. Solids* **2003**, *64*, 133–146.

(108) Giehl, J. M.; Miranda, a. R.; Pontuschka, W. M.; Navarro, M.; Costa, Z. M. EPR Study of MnO and MnO_2 Doped Barium Aluminoborate Glasses. *J. Supercond. Nov. Magn.* **2012**, *26*, 2295–2298.

(109) Winterstein, A.; Akamatsu, H. Magnetic and Magneto-Optical Quenching in (Mn^{2+}, Sr^{2+}) Metaphosphate Glasses. *Opt. Mater. Express* **2013**, *3*, 184–193.

(110) Terczyńska-Madej, A.; Cholewa-Kowalska, K.; Łączka, M. Coordination and Valence State of Transition Metal Ions in Alkali-Borate Glasses. *Opt. Mater. (Amst).* **2011**, *33*, 1984–1988.

(111) Konidakis, I.; Varsamis, C. Structure and Properties of Mixed Strontium−Manganese Metaphosphate Glasses. *J. Phys. Chem. C* **2010**, *114*, 9125–9138.

(112) Nelson, C.; White, W. B. Transition Metal Ions in Silicate melts—I. Manganese in Sodium Silicate Melts. *Geochim. Cosmochim. Acta* **1980**, *44*, 887–893.

(113) Paul, A. *Chemistry of Glasses*; 2nd ed.; Chapman and Hall, 1990.

(114) Innocenzi, P. Infrared Spectroscopy of Sol–gel Derived Silica-Based Films: A Spectra-Microstructure Overview. *J. Non. Cryst. Solids* **2003**, *316*, 309–319.

(115) Schramm, C. M.; De Jong, B. H. W. S.; Parziale, V. E. ^{29}Si Magic Angle Spinning NMR Study on Local Silicon Environments in Amorphous and Crystalline Lithium Silicates. *J. Am. Chem. Soc.* **1984**, *106*, 4396–4402.

(116) Fernandes, H. R.; Tulyaganov, D. U.; Goel, A.; Ferreira, J. M. F. Structural Characterisation and Thermo-Physical Properties of Glasses in the Li_2O-SiO_2-Al_2O_3-K_2O System. *J. Therm. Anal. Calorim.* **2011**, *103*, 827–834.

(117) Abo-Mosallam, H. A.; Hill, R. G.; Karpukhina, N.; Law, R. V. MAS-NMR Studies of Glasses and Glass-Ceramics Based on a Clinopyroxene–fluorapatite System. *J. Mater. Chem.* **2010**, *20*, 790–797.

(118) Stebbins, J. F.; Kroeker, S.; Lee, S. K.; Kiczenski, T. J. Quantification of Five-

and Six-Coordinated Aluminium Ions in Aluminosilicate and Fluoride-Containing Glasses by High-Field, High-Resolution ^{27}Al NMR. *J. Non. Cryst. Solids* **2000**, *275*, 1–6.

(119) Cabral Jr, A.; Fredericci, C.; Zanotto, E. A Test of the Hrubÿ Parameter to Estimate Glass-Forming Ability. *J. Non. Cryst. Solids* **1997**, *219*, 182–186.

(120) Duffy, J. a. Optical Basicity: A Practical Acid-Base Theory for Oxides and Oxyanions. *J. Chem. Educ.* **1996**, *73*, 1138–1142.

(121) Terczynska-Madej, A.; Cholewa-Kowalska, K.; Laczka, M. The Effect of Silicate Network Modifiers on Colour and Electron Spectra of Transition Metal Ions. *Opt. Mater. (Amst).* **2010**, *32*, 1456–1462.

(122) Claes, P.; Decelle, E. Redox Chemistry in Glass Melts out of Equilibrium with Their Gaseous Atmosphere. *J. Non. Cryst. Solids* **2001**, *288*, 37–45.

(123) Thiemsorn, W.; Keowkamnerd, K.; Phanichphant, S.; Suwannathada, P.; Hessenkemper, H. Influence of Glass Basicity on Redox Interactions of Iron-Manganese-Copper Ion Pairs in Soda-Lime-Silica Glass. *Glas. Phys. Chem.* **2011**, *34*, 19–29.

(124) Duffy, J. A.; Ingram, M. D.; Fong, S.; Du, J. A.; Ingram, M. D.; Fong, S. Effect of Basicity on Chemical Bonding of Metal Ions in Glass and Its Relevance to Their Stability. *Phys. Chem. Chem. Phys.* **2000**, *2*, 1829–1833.

(125) Nelson, C. Transition Metal Ions in Glasses: Network Modifiers or Quasi-Molecular Complexes? *Mater. Res. Bull.* **1983**, *18*, 959–966.

(126) Mortuza, M. G.; Dupree, R.; Holland, D. Studies of the Effect of Paramagnetic Impurity in the Structure of Sodium Disilicate Glass. *J. Mater. Sci.* **2000**, *35*, 2829–2832.

(127) Higazy, A. A.; Hussein, A.; Awaida, M. A. A Study of the Optical Absorption Edge in Silicate Glasses Containing TiO_2 Oxide. *J. Mater. Sci. Lett.* **1989**, *24*, 2203–2208.

(128) Vogel, W. *Glass Chemistry*; Springer: Berlin, 1994.

(129) Shannon, R. Revised Effective Ionic Radii and Systematic Studies of Interatomic Distances in Halides and Chalcogenides. *Acta Crystallogr. Sect. A* **1976**, *32*, 751–767.

(130) Carter, C. B.; Norton, M. G. *Ceramic Materials - Science and Engineering*; First.; Springer: New York, 2007.

(131) Zanotto, E. D. Isothermal and Adiabatic Nucleation in Glass. *J. Non. Cryst. Solids* **1987**, *89*, 361–370.

(132) Zanotto, E. D.; James, P. F.; Craievich, A. F. The Effects of Amorphous Phase Separation on Crystal Nucleation Kinetics in BaO-SiO_2 Glasses - Part 3 Isothermal Treatments at 718 to 760 °C; Small-Angle X-Ray Scattering Results. *J. Mater. Sci.* **1986**, *21*, 3050–3064.

(133) Ramsden, A.; James, P. The Effects of Amorphous Phase Separation on Crystal Nucleation Kinetics in BaO-SiO_2 Glasses. *J. Mater. Sci.* **1984**, *19*, 1406–1419.

(134) Fernandes, H. R.; Tulyaganov, D. U.; Pascual, M. J.; Kharton, V. V.; Yaremchenko, A. a.; Ferreira, J. M. F. The Role of K_2O on Sintering and Crystallization of Glass Powder Compacts in the Li_2O–K_2O–Al_2O_3–SiO_2 System. *J. Eur. Ceram. Soc.* **2012**, *32*, 2283–2292.

(135) Saint-Jean, S. J. Advanced Ceramics for Dentistry. In *Advanced Ceramics for Dentistry*; Shen, J. Z.; Kosmac, T., Eds.; Butterworth-Heinemann: 225 Wyman Street, Waltham, MA 02451, USA, 2014; pp. 255–277.

(136) Zanotto, E. D. A Bright Future for Glass-Ceramics. *Am. Ceram. Soc. Bull.* **2010**, *89*, 19–27.

(137) Rukmani, S. J.; Brow, R. K.; Reis, S. T.; Apel, E.; Rheinberger, V.; Höland, W. Effects of V and Mn Colorants on the Crystallization Behavior and Optical Properties of Ce-Doped Li-Disilicate Glass?Ceramics. *J. Am. Ceram. Soc.* **2007**, *90*, 706–711.

(138) Von Clausbruch, C. S.; Schweiger, M.; Höland, W.; Rheinberger, V.; Holand, W.; Rheinberger, V. The Effect of P_2O_5 on the Crystallization and Microstructure of Glass-Ceramics in the SiO_2-Li_2O-K_2O-ZnO-P_2O_5 System. *J. Non. Cryst.*

Solids **2000**, *263*, 223–229.

(139) Krüger, S.; Deubener, J.; Ritzberger, C.; Höland, W. Nucleation Kinetics of Lithium Metasilicate in ZrO_2 -Bearing Lithium Disilicate Glasses for Dental Application. *Int. J. Appl. Glas. Sci.* **2013**, *4*, 9–19.

(140) Huang, S.; Huang, Z.; Gao, W.; Cao, P. Structural Response of Lithium Disilicate in Glass Crystallization. *Cryst. Growth Des.* **2014**, *14*, 5144–5151.

(141) Fernandes, H. R.; Tulyaganov, D. U.; Ferreira, J. M. F. The Role of P_2O_5, TiO_2 and ZrO_2 as Nucleating Agents on Microstructure and Crystallization Behaviour of Lithium Disilicate-Based Glass. *J. Mater. Sci.* **2012**, *48*, 765–773.

(142) Fernandes, H. R.; Tulyaganov, D. U.; Goel, A.; Ribeiro, M. J.; Pascual, M. J.; Ferreira, J. M. F. Effect of Al_2O_3 and K_2O Content on Structure, Properties and Devitrification of Glasses in the Li_2O-SiO_2 System. *J. Eur. Ceram. Soc.* **2010**, *30*, 2017–2030.

(143) Fernandes, H. R.; Tulyaganov, D. U.; Goel, A.; Ferreira, J. M. F. Effect of K_2O on Structure–property Relationships and Phase Transformations in Li_2O–SiO_2 Glasses. *J. Eur. Ceram. Soc.* **2012**, *32*, 291–298.

(144) Gaddam, A.; Fernandes, H. R.; Tulyaganov, D. U.; Pascual, M. J.; Ferreira, J. M. F. Role of Manganese on the Structure, Crystallization and Sintering of Non-Stoichiometric Lithium Disilicate Glasses. *RSC Adv.* **2014**, *4*, 13581–13592.

(145) Fernandes, H. R.; Tulyaganov, D. U.; Goel, I. K.; Ferreira, J. M. F. Crystallization Process and Some Properties of Li_2O-SiO_2 Glass-Ceramics Doped with Al_2O_3 and K_2O. *J. Am. Ceram. Soc.* **2008**, *91*, 3698–3703.

(146) Müller, E.; Heide, K.; Zanotto, E. D. Influence of Cation Coordination on Nucleation in Silicate Glasses. *Zeitschrift für Krist.* **1992**, *200*, 287–294.

(147) Nanba, T.; Nishimura, M.; Miura, Y. A Theoretical Interpretation of the Chemical Shift of ^{29}Si NMR Peaks in Alkali Borosilicate Glasses. *Geochim. Cosmochim. Acta* **2004**, *68*, 5103–5111.

(148) Fernandes, H. R.; Tulyaganov, D. U.; Goel, A.; Ferreira, J. M. F. Structural Characterisation and Thermo-Physical Properties of Glasses in the Li_2O–SiO_2–

Al_2O_3–K_2O System. *J. Therm. Anal. Calorim.* **2011**, *103*, 827–834.

(149) Fernandes, H. R. Development of Lithium Disilicate Based Glass-Ceramics - PhD Thesis, University of Aveiro, 2012.

(150) Fernandes, H. R.; Tulyaganov, D. U.; Ferreira, J. M. F. Al_2O_3/K_2O-Containing Non-Stoichiometric Lithium Disilicate-Based Glasses: A Study of Crystallization Kinetics. *J. Therm. Anal. Calorim.* **2013**, *112*, 1359–1368.

(151) Fernandes, H. R.; Tulyaganov, D. U.; Pascual, M. J.; Ferreira, J. M. F. Structure–property Relationships and Densification-Crystallization Behaviours of Simplified Lithium Disilicate Glass Compositions. *Ceram. Int.* **2014**, *40*, 129–140.

(152) Zanotto, E. D.; Craievich, A. F. The Role of Amorphous Phase Separation in Crystal Nucleation in Splat Cooled Li_2O-SiO_2 Glasses. *J. Mater. Sci.* **1981**, *16*, 973–982.

(153) Limpt, J. A. C. van. Modeling of Evaporation Processes in Glass Melting Furnaces, Eindhoven University of Technology, 2007.

(154) MacKenzie, K. J. D.; Smith, M. E. *Multinuclear Solid-State NMR of Inorganic Materials*; 1st ed.; Pergamon: Amsterdam, 2002.

(155) Bunker B.C.; Tallant, D. R.; Kirkpatrick, R. J.; Turner, G. l. Multinuclear Nuclear Magnetic Resonance and Raman Investigation of Sodium Borosilicate Glass Structures. *Phys. Chem. Glas.* **1990**, *31*, 30–41.

(156) Neuville, D. R.; Cormier, L.; Massiot, D. Al Environment in Tectosilicate and Peraluminous Glasses: A ^{27}Al MQ-MAS NMR, Raman, and XANES Investigation. *Geochim. Cosmochim. Acta* **2004**, *68*, 5071–5079.

(157) Kirkpatrick, R. J.; Oestrike, R.; Weiss, C. A. J.; Smith, K. A.; Oldfield, E. High-Resolution ^{27}Al and ^{29}Si NMR Spectroscopy of Glasses and Crystals along the Join $CaMgSi_2O_6$-$CaAl_2SiO_6$. *Am. Mineral.* **1986**, *71*, 705–711.

(158) Parkinson, B. G.; Holland, D.; Smith, M. E.; Howes, a P.; Scales, C. R. The Effect of Oxide Additions on Medium-Range Order Structures in Borosilicate Glasses. *J. Phys. Condens. Matter* **2007**, *19*, 415114.

(159) Emerson, J. F.; Bray, P. J. NMR Analysis of Glass Structure. In *Experimental Techniques of Glass Science*; Simmons, C. J.; El-Bayoumi, O. H., Eds.; The American Ceramic Society: Westerville, Ohio, 1993; pp. 77–99.

(160) Manara, D.; Grandjean, A.; Neuville, D. R. Advances in Understanding the Structure of Borosilicate Glasses: A Raman Spectroscopy Study. *Am. Mineral.* **2009**, *94*, 777–784.

(161) Matson, D. W.; Sharma, S. K.; Philpotts, J. A. Raman Spectra of Some Tectosilicates and of Glasses along the Orthoclase-Anorthite and Nepheline-Anorthite Joins. *Am. Mineral.* **1986**, *71*, 694–704.

(162) Hrubý, A. Evaluation of Glass-Forming Tendency by Means of DTA. *Czechoslov. J. Phys.* **1972**, *22*, 1187–1193.

(163) Fokin, V. V. M.; Zanotto, E. D.; Schmelzer, J. W. P. J. Homogeneous Nucleation versus Glass Transition Temperature of Silicate Glasses. *J. Non. Cryst. Solids* **2003**, *321*, 52–65.

(164) Lippmaa, E.; Magi, M.; Samoson, A.; Tarmak, M.; Engelbardtlb, G. Investigation of the Structure of Zeolites by Solid-State High-Resolution ^{29}Si NMR Spectroscopy. *J. Am. Chem. Soc.* **1981**, *103*, 4992–4996.

(165) Loewenstein, W. The Distribution of Aluminum in the Tetrahedra of Silicates and Aluminates. *Am. J. Sci.* **1954**, *39*, 92–96.

(166) Tossell, J. A. A Theoretical Study of the Molecular Basis of the Al Avoidance Rule and of the Spectral Characteristics of Al–O–Al Linkages. *Am. Mineral.* **1993**, *78*, 911–920.

(167) Larin, A. V. The Loewenstein Rule: The Increase in Electron Kinetic Energy as the Reason for Instability of Al–O–Al Linkage in Aluminosilicate Zeolites. *Phys. Chem. Miner.* **2013**, *40*, 771–780.

(168) Martel, L.; Massiot, D.; Deschamps, M. Phase Separation in Sodium Silicates Observed by Solid-State MAS-NMR. *J. Non. Cryst. Solids* **2014**, *390*, 37–44.

(169) Martens, R.; Müller-Warmuth, W. Structural Groups and Their Mixing in Borosilicate Glasses of Various Compositions – an NMR Study. *J. Non. Cryst.*

Solids **2000**, *265*, 167–175.

(170) Du, L.; Stebbins, J. F. Nature of Silicon-Boron Mixing in Sodium Borosilicate Glasses: A High-Resolution ^{11}B and ^{17}O NMR Study. *J. Phys. Chem. B* **2003**, *3*, 10063–10076.

(171) Duffy, J. A.; Ingram, M. D. An Interpretation of Glass Chemistry in Terms of the Optical Basicity Concept. *J. Non. Cryst. Solids* **1976**, *21*, 373–410.

(172) Geisinger, K. L.; Oestrike, R.; Navrotsky, A.; Turner, G. L.; Kirkpatrick, R. J. Thermochemistry and Structure of Glasses along the Join $NaAlSi_3O_8$-$NaBSi_3O_8$. *Geochim. Cosmochim. Acta* **1988**, *52*, 2405–2414.

(173) Brown, I. D.; Shannon, R. D. Empirical Bond-Strength–bond-Length Curves for Oxides. *Acta Crystallogr. Sect. A* **1973**, *29*, 266–282.

(174) Wong, J.; Angell, C. A. *Glass Structure by Spectroscopy*; Marcel Dekker: 270 Madison Avenue, New York, 1976.

(175) Zanotto, E. D.; Craievich, A. F.; James, P. F. SAXS and TEM Studies of Phase Separation in BaO–SiO_2 Glasses. *J. Phys.* **1982**, *43*, 107–110.

(176) Craievich, A. F.; Zanotto, E. D.; James, P. F. Kinetics of Sub-Liquidus Phase Separation in Silicate and Borate Glasses. A Review. *Bull. Soc. Fr. Min. Cris.* **1983**, *106*, 169–184.

(177) Haller, W.; Blackburn, D. H.; Wagstaff, F. E.; Charles, R. J. Metastable Immiscibility Surface in the System Na_2O-B_2O_3-SiO_2. *J. Am. Ceram. Soc.* **1970**, *53*, 34–39.

(178) Charles, R. J. The Origin of Immiscibility in Silicate Solution. *Phys. Chem. Glas.* **1969**, *10*, 169–178.

(179) Topping, J.; Murthy, M. Effect of Small Additions of Al_2O_3 and Ga_2O_3 on the Immiscibility Temperature of Na_2O-SiO_2 Glasses. *J. Am. Ceram. Soc.* **1973**, *56*, 270–275.

(180) Glasser, F. P. Crystallization of Lithium Disilicate from Li_2O-SiO_2 Glasses. *Phys. Chem. Glas.* **1967**, *8*, 224–232.

(181) West, A. R.; Glasser, F. P. Crystallization of Li_2O-SiO_2 Glasses. In *Advances in nucleation and crystallization in glasses*; Hench, L. L.; Freiman, S. W., Eds.; The American Ceramic Society: Columbus, Ohio, United States, 1971; pp. 151–165.

(182) Zanotto, E. D.; James, P. The Compositional Dependence of Crystal Nucleation in Li2O–SiO2 Glasses. *Glas. Ber* **1983**, *56k*, 794–799.

(183) Kracek, F. C. The Binary System Li_2O-SiO_2. *J. Phys. Chem.* **1930**, *34*, 2641–2650.

(184) Strnad, Z. *Glass Science and Technology*; Elsevier: New York, 1986; Vol. 8.

(185) Rabinovich, E. M. Preparation of Glass by Sintering. *J. Mater. Sci.* **1985**, *20*, 4259–4297.

(186) Strnad, Z. *Glass-Ceramic Materials*; Elsevier: Amsterdam, 1986.

(187) Sarkisov, P. D.; Orlova, L. A.; Popovich, N. V.; Bruntsch, R.; Chainikova, A. S.; Klinkmueller, K.; Shchegoleva, N. E. Sintering and Crystallization during the Production of Strontium-Anortite Glass Ceramic. *Glas. Ceram.* **2013**, *69*, 306–312.

(188) Zhang, Y.; Huang, J.; Ma, T.; Wang, X.; Deng, C.; Dai, X. Sintering Temperature Dependence of Energy-Storage Properties in (Ba,Sr)TiO_3 Glass-Ceramics. *J. Am. Ceram. Soc.* **2011**, *94*, 1805–1810.

(189) Lo, C. L.; Duh, J. G.; Chiou, B. S. Low Temperature Sintering and Crystallisation Behaviour of Low Loss Anorthite-Based Glass-Ceramics. *J. Mater. Sci.* **2003**, *38*, 693–698.

(190) Monmaturapoj, N.; Lawita, P.; Thepsuwan, W. Characterisation and Properties of Lithium Disilicate Glass Ceramics in the SiO_2-Li_2O-K_2O-Al_2O_3 System for Dental Applications. *Adv. Mater. Sci. Eng.* **2013**, *2013*, 1–11.

(191) Barrett, J. M.; Clark, D. E.; Hench, L. L. Glass-Ceramic Dental Restorations, 1980.

(192) Wu TW), Cannon, Warren R. (East Brunswick, NJ), Panzera, Carlino (Belle Mead, NJ), J. (Tainan. Castable Glass-Ceramic Composition Useful as Dental

Restorative, 1985.

(193) Gaddam, A.; Fernandes, H. R.; Ferreira, J. M. F. Glass Structure and Crystallization of Al and B Containing Glasses Belonging to the $Li_2O–SiO_2$ System. *RSC Adv.* **2015**, *5*, 41066–41078.

(194) Kissinger, H. E. Reaction Kinetics in Differential Thermal Analysis. *Anal. Chem.* **1957**, *29*, 1702–1706.

(195) Ferreira, E. B.; Lima, M. L.; Zanotto, E. D. DSC Method for Determining the Liquidus Temperature of Glass-Forming Systems. *J. Am. Ceram. Soc.* **2010**, *93*, 3757–3763.

(196) Chase, M. W. J. *NIST-JANAF Thermochemical Tables*; 4th ed.; American Chemical Society, 1998.

(197) Culp, L.; McLaren, E. A. Lithium Disilicate: The Restorative Material of Multiple Options. *Compend. Contin. Educ. Dent.* **2010**, *31*, 716–720, 722, 724–725.

(198) Hervig, R. L.; Navrotsky, A. Thermochemistry of Sodium Borosilicate Glasses. *J. Am. Ceram. Soc.* **1985**, *68*, 314–319.

(199) Charles, R. J.; Wagstaff, F. E. Metastable Immiscibility in the B_2O_3-SiO_2 System. *J. Am. Ceram. Soc.* **1968**, *51*, 16–20.

(200) Bischoff, C.; Eckert, H.; Apel, E.; Rheinberger, V. M.; Höland, W. Phase Evolution in Lithium Disilicate Glass-Ceramics Based on Non-Stoichiometric Compositions of a Multi-Component System: Structural Studies by ^{29}Si Single and Double Resonance Solid State NMR. *Phys. Chem. Chem. Phys.* **2011**, *13*, 4540–4551.

(201) Huang, S.; Huang, Z.; Gao, W.; Cao, P. Trace Phase Formation, Crystallization Kinetics and Crystallographic Evolution of a Lithium Disilicate Glass Probed by Synchrotron XRD Technique. *Sci. Rep.* **2015**, *5*, 9159 1-5.

(202) Gaddam, A.; Goyal, M.; Jain, S.; Bhargava, P. Lithium Disilicate Based Glass-Ceramics for Dental Applications. *Trans. Indian Ceram. Soc.* **2013**, *72*, 56–60.

(203) Fernandes, H. R.; Gaddam, A.; Tulyaganov, D. U.; Ferreira, J. M. F. Structure, Properties and Crystallization of Non-Stoichiometric Lithium Disilicate Glasses Containing CaF2. *J. Non. Cryst. Solids* **2014**, *406*, 54–61.

(204) Vijh, A. K. Correlation between the Thermodynamic Driving Force and the Kinetic Activation Energy for the Thermal Oxidation of Metals. *J. Mater. Sci. Lett.* **1988**, *7*, 139–140.

(205) Stebbins, J. F.; Ellsworth, S. E. Temperature Effects on Structure and Dynamics in Borate and Borosilicate Liquids: High-Resolution and High-Temperature NMR Results. *J. Am. Ceram. Soc.* **1996**, *79*, 2247–2256.

(206) Smedskjaer, M. M.; Mauro, J. C.; Youngman, R. E.; Hogue, C. L.; Potuzak, M.; Yue, Y. Topological Principles of Borosilicate Glass Chemistry. *J. Phys. Chem. B* **2011**, *115*, 12930–12946.

(207) Chase, M. W.; Curnutt, J. L.; Downey, J. R.; McDonald, R. A.; Syverud, A. N.; Valenzuela, E. A. JANAF Thermochemical Tables, 1982 Supplement. *J. Phys. Chem. Ref. Data* **1982**, *11*, 695.

(208) McMillan, P. W. *Glass–Ceramics*; Academic Press: London, 1979.

(209) Stookey, S. D. Catalyzed Crystallization of Glass in Theory and Practice. *Ind. Eng. Chem.* **1959**, *51*, 805–808.

(210) Iqbal, Y.; Lee, W. . E.; Holland, D.; James, P. . F. Metastable Phase Formation in the Early Stage Crystallisation of Lithium Disilicate Glass. *J. Non. Cryst. Solids* **1998**, *224*, 1–16.

(211) James, P. F. Kinetics of Crystal Nucleation in Silicate Glasses. *J. Non. Cryst. Solids* **1985**, *73*, 517–540.

(212) Zanotto, E. D. Metastable Phases in Lithium Disilicate Glasses. *J. Non. Cryst. Solids* **1997**, *219*, 42–48.

(213) Ray, C. S.; Day, D. E.; Huang, W.; Narayan, K. L.; Cull, T. S.; Kelton, K. F. Non-Isothermal Calorimetric Studies of the Crystallization of Lithium Disilicate Glass. *J. Non. Cryst. Solids* **1996**, *204*, 1–12.

(214) Tulyaganov, D. U.; Agathopoulos, S.; Kansal, I.; Valério, P.; Ribeiro, M. J.; Ferreira, J. M. F. Synthesis and Properties of Lithium Disilicate Glass-Ceramics in the System SiO_2–Al_2O_3–K_2O–Li_2O. *Ceram. Int.* **2009**, *35*, 3013–3019.

(215) Holland, D.; Iqbal, Y.; James, P.; Lee, B. Early Stages of Crystallisation of Lithium Disilicate Glasses Containing P_2O_5 - An NMR Study. *J. Non. Cryst. Solids* **1998**, *232–234*, 140–146.

(216) Zheng, X.; Wen, G.; Song, L.; Huang, X. X. Effects of P_2O_5 and Heat Treatment on Crystallization and Microstructure in Lithium Disilicate Glass Ceramics. *Acta Mater.* **2008**, *56*, 549–558.

(217) Iqbal, Y.; Lee, W. E.; Holland, D.; James, P. F. Crystal Nucleation in P_2O_5-Doped Lithium Disilicate Glasses. *J. Mater. Sci.* **1999**, *34*, 4399–4411.

(218) Echevería, L. M. New Lithium Disilicate Glass-Ceramics. *Bol. da la Soc. Esp. Cerámica e Vidr.* **1992**, *5*, 183–188.

(219) Beall, G. H. Glass-Ceramics: Recent Developments and Application. *Ceram. Trans.* **1993**, *30*, 241–266.

(220) Höland, W.; Apel, E.; van Hoen, C.; Rheinberger, V. Studies of Crystal Phase Formations in High-Strength Lithium Disilicate Glass-Ceramics. *J. Non. Cryst. Solids* **2006**, *352*, 4041–4050.

(221) Fernandes, H. R.; Tulyaganov, D. U.; Goel, A.; Ferreira, J. M. F. Effect of K_2O on Structure-Property Relationships and Phase Transformations in Li_2O-SiO_2 Glasses. *J. Eur. Ceram. Soc.* **2012**, *32*, 291–298.

(222) Goswami, M.; Kothiyal, G. P.; Montagne, L.; Delevoye, L. MAS-NMR Study of Lithium Zinc Silicate Glasses and Glass-Ceramics with Various ZnO Content . *J. Solid State Chem.* **2008**, *181*, 269–275.

(223) Bengisu, M.; Brow, R. K.; White, J. E. Interfacial Reactions between Lithium Silicate Glass-Ceramics and Ni-Based Superalloys and the Effect of Heat Treatment at Elevated Temperatures. *J. Mater. Sci.* **2004**, *39*, 605–618.

(224) Zhang, P.; Li, X.; Yang, J.; Xu, S. The Crystallization and Microstructure Evolution of Lithium Disilicate-Based Glass-Ceramic. *J. Non. Cryst. Solids*

2014, *392–393*, 26–30.

(225) Gaddam, A.; Fernandes, H. R.; Pascual, M. J.; Ferreira, J. M. F. Influence of Al_2O_3 and B_2O_3 on Sintering and Crystallization of Lithium Silicate Glass System. *J. Am. Ceram. Soc.* **2016**, *99*, 833–840.

(226) Goharian, P.; A. Nemati, A.; M. Shabanian, M.; Afshar, a.; Nemati, a.; Shabanian, M.; Afshar, a. Properties, Crystallization Mechanism and Microstructure of Lithium Disilicate Glass–ceramic. *J. Non. Cryst. Solids* **2010**, *356*, 208–214.

(227) Pernice, P.; Aronne, A.; Marotta, A. Non-Isothermal Devitrification and Electrical Conductivity of Glasses near the Li_2O_3 Composition. *Thermochim. Acta* **1990**, *157*, 77–82.

(228) Massiot, D.; Fayon, F.; Capron, M.; King, I.; Le Calvé, S.; Alonso, B.; Durand, J.-O.; Bujoli, B.; Gan, Z.; Hoatson, G. Modelling One- and Two-Dimensional Solid-State NMR Spectra. *Magn. Reson. Chem.* **2002**, *40*, 70–76.

(229) Kissinger, H. E. Variation of Peak Temperature with Heating Rate in Differential Thermal Analysis. *J. Res. Natl. Bur. Stand. (1934).* **1956**, *57*, 217.

(230) Matusita, K.; Komatsu, T.; Yokota, R. Kinetics of Non-Isothermal Crystallization Process and Activation Energy for Crystal Growth in Amorphous Materials. *J. Mater. Sci.* **1984**, *19*, 291–296.

(231) Augis, J. A.; Bennett, J. E. Calculation of the Avrami Parameters for Heterogeneous Solid State Reactions Using a Modification of the Kissinger Method. *J. Therm. Anal. Calorim.* **1978**, *13*, 283–292.

(232) Ligero, R. A.; Vázques, J.; Casas-Ruiz, M.; Jimenez-Garay, R. A Comparative Study of Different Methods for Calculating the Set of Kinetic Parameters Which Describe the Crystallization Reaction of a Glassy Alloy. *Thermochim. Acta* **1992**, *197*, 319–327.

(233) Wagner, C.; Villares, P.; Vázquez, J.; Jiménez-Garay, R. Some Methods for Kinetic Studies of Non-Isothermal Crystallization in $Sn_{0.08}As_{0.26}Se_{0.66}$ Alloy. *Mater. Lett.* **1993**, *15*, 370–375.

(234) Vazquez, J.; Wagner, C.; Villares, P.; Jimenez-Garay, R. A Theoretical Method for Determining the Crystallized Fraction and Kinetic Parameters by DSC, Using Non-Isothermal Techniques. *Acta Mater.* **1996**, *44*, 4807–4813.

(235) Pratap, A.; Lad, K. N.; Rao, T. L. S.; Majmudar, P.; Saxena, N. S. Kinetics of Crystallization of Amorphous $Cu_{50}Ti_{50}$ Alloy. *J. Non. Cryst. Solids* **2004**, *345&346*, 178–181.

(236) Kundu, R. S.; Dult, M.; Punia, R.; Parmar, R.; Kishore, N. Titanium Induced Structural Modifications in Bismuth Silicate Glasses. *J. Mol. Struct.* **2014**, *1063*, 77–82.

(237) Brandriss, M. E.; Stebbins, J. F. Effects of Temperature on the Structures of Silicate Liquids: ^{29}Si NMR Results. *Geochim. Cosmochim. Acta* **1988**, *52*, 2659–2669.

(238) Mauro, J. C. Statistics of Modifier Distributions in Mixed Network Glasses. *J. Chem. Phys.* **2013**, *138*, 12A522.

(239) Gaddam, A.; Fernandes, H. R.; Pascual, M. J.; Ferreira, J. M. F. Influence of Al2O3 and B2O3 on Sintering and Crystallization of Lithium Silicate Glass System. *J. Am. Ceram. Soc.* **2016**, *99*, 833–840.

(240) Dirken, P. J.; Nachtegaal, G. H.; Kentgens, A. P. M. Off-Resonance Nutation Nuclear Magnetic Resonance Study of Framework Aluminosilicate Glasses with Li, Na, K, Rb or Cs as Charge-Balancing Cation. *Solid State Nucl. Magn. Reson.* **1995**, *5*, 189–200.

(241) Headley, T. G. J.; Loehman, R. E. Crystallization of Glass–Ceramics by Epitaxial Growth. *J. Am. Ceram. Soc.* **1984**, *67*, 620–625.

(242) Gaddam, A.; Montagne, L.; Ferreira, J. M. F. Statistics of Silicate Units in Binary Glasses. *J. Chem. Phys.* **2016**, *145*, 124505.

(243) Stebbins, J. F.; Sen, S. Oxide Ion Speciation in Potassium Silicate Glasses: New Limits from 17O NMR. *J. Non. Cryst. Solids* **2013**, *368*, 17–22.

(244) Nesbitt, H. W.; Bancroft, G. M.; Henderson, G. S.; Ho, R.; Dalby, K. N.; Huang, Y.; Yan, Z. Bridging, Non-Bridging and Free (O2–) Oxygen in Na2O-SiO2

Glasses: An X-Ray Photoelectron Spectroscopic (XPS) and Nuclear Magnetic Resonance (NMR) Study. *J. Non. Cryst. Solids* **2011**, *357*, 170–180.

(245) Vedishcheva, N. M.; Shakhmatkin, B. A.; Shultz, M. M.; Wright, A. C. The Thermodynamic Modelling of Glass Properties: A Practical Proposition? *J. Non. Cryst. Solids* **1996**, *196*, 239–243.

(246) Olivier, L.; Yuan, X.; Cormack, A. N.; Jäger, C. Combined Double Quantum NMR and MD Simulation Studies of Network Connectivities of Binary $Na_2O{\cdot}SiO_2$ Glasses: New Prospects and Problems. *J. Non. Cryst. Solids* **2001**, *293–295*, 53–66.

(247) Machacek, J.; Gedeon, O.; Liska, M. Group Connectivity in Binary Silicate Glasses. *J. Non. Cryst. Solids* **2006**, *352*, 2173–2179.

(248) Brawer, S. Theory of the Vibrational Spectra of Some Network and Molecular Glasses. *Phys. Rev. B* **1975**, *11*, 3173–3194.

(249) *Problems in Thermodynamics and Statistical Physics*; Landsberg, P. T., Ed.; Pion Limited: Bristol, 1989.

(250) Sciortino, F. Potential Energy Landscape Description of Supercooled Liquids and Glasses. *J. Stat. Mech. Theory Exp.* **2005**, *2005*, P05015.

(251) Gupta, P. K. Perspective: Thermodynamics of Structural Glasses. *J. Non. Cryst. Solids* **2015**, *407*, 154–160.

(252) Drake, A. W. *Fundamentals of Applied Probability Theory*; McGraw-Hill: New York, 1988.

(253) Yamane, M.; Asahara, Y. *Glasses for Photonics*; Cambridge University Press: Cambridge, 2004.

(254) Varshneya, A. K.; Mauro, J. C. Comment on Misconceived ASTM Definition of Glass by A. C. Wright. *Glas. Technol. Eur. J. Glas. Sci. Technol. Part A* **2010**, *51*, 28–30.

(255) Mauro, J. C.; Allan, D. C.; Potuzak, M. Nonequilibrium Viscosity of Glass. *Phys. Rev. B* **2009**, *80*, 094204–094222.

(256) Yue, Y. Z.; Angell., C. A. Clarifying the Glass-Transition Behaviour of Water by Comparison with Hyperquenched Inorganic Glasses. *Nature* **2004**, *427*, 717–720.

(257) Angell, C. a.; Ngai, K. L.; McKenna, G. B.; McMillan, P. F.; Martin, S. W. Relaxation in Glassforming Liquids and Amorphous Solids. *J. Appl. Phys.* **2000**, *88*, 3113.

(258) Mysen, B. O.; Richet, P. *Silicate Glasses and Melts: Properties and Structure*; Elsevier: Amsterdam, 2005.

(259) Rawson, H. *Glasses and Their Applications*; Institute of Metals: London, 1991.

(260) *Dynamics, and Properties of Silicate Melts*; Stebbins, J. F.; McMillan, P. F.; Dingwell, D. B., Eds.; Mineralogical Society of America: Washington, DC, 1995.

(261) Greaves, G. N.; Sen, S. Inorganic Glasses, Glass-Forming Liquids and Amorphizing Solids. *Adv. Phys.* **2007**, *56*, 1–166.

(262) Cormier, L.; Calas, G.; Beuneu, B. Structural Changes between Soda-Lime Silicate Glass and Melt. *J. Non. Cryst. Solids* **2011**, *357*, 926–931.

(263) Efimov, A. M. Vibrational Spectra, Related Properties, and Structure of Inorganic Glasses. *J. Non. Cryst. Solids* **1999**, *253*, 95–118.

(264) Rabinovich, E. M. Lead in Glasses. *J. Mater. Sci.* **1976**, *11*, 925–948.

(265) Sen, S.; Xu, Z.; Stebbins, J. . Temperature Dependent Structural Changes in Borate, Borosilicate and Boroaluminate Liquids: High-Resolution 11B, ^{29}Si and ^{27}Al NMR Studies. *J. Non. Cryst. Solids* **1998**, *226*, 29–40.

(266) Bechgaard, T. K.; Goel, A.; Youngman, R. E.; Mauro, J. C.; Rzoska, S. J.; Bockowski, M.; Jensen, L. R.; Smedskjaer, M. M. Structure and Mechanical Properties of Compressed Sodium Aluminosilicate Glasses: Role of Non-Bridging Oxygens. *J. Non. Cryst. Solids* **2016**, *441*, 49–57.

(267) Pedone, A. Recent Advances in Solid-State NMR Computational Spectroscopy: The Case of Alumino-Silicate Glasses. *Int. J. Quantum Chem.* **2016**, n/a-n/a.

(268) Nesbitt, H. W.; Henderson, G. S.; Bancroft, G. M.; Ho, R. Experimental

Evidence for Na Coordination to Bridging Oxygen in Na-Silicate Glasses: Implications for Spectroscopic Studies and for the Modified Random Network Model. *J. Non. Cryst. Solids* **2015**, *409*, 139–148.

(269) Jiao, Q.; Li, G.; Zhou, D.; Qiu, J. Effect of the Glass Structure on Emission of Rare-Earth-Doped Borate Glasses. *J. Am. Ceram. Soc.* **2015**, *98*, 4102–4106.

(270) Hasan, M. S.; Werner-Zwanziger, U.; Boyd, D. Composition-Structure-Properties Relationship of Strontium Borate Glasses for Medical Applications. *J. Biomed. Mater. Res. A* **2015**, *103*, 2344–2354.

(271) Smedskjaer, M. M.; Youngman, R. E.; Striepe, S.; Potuzak, M.; Bauer, U.; Deubener, J.; Behrens, H.; Mauro, J. C.; Yue, Y. Irreversibility of Pressure Induced Boron Speciation Change in Glass. *Sci. Rep.* **2014**, *4*, 3770.

(272) Szumera, M. Molybdenum Modified Phosphate Glasses Studied by ^{31}P MAS NMR and Raman Spectroscopy. *Spectrochim. Acta. A. Mol. Biomol. Spectrosc.* **2015**, *137*, 111–115.

(273) Muñoz-Senovilla, L.; Venkatachalam, S.; Muñoz, F.; Van Wüllen, L. Relationships between Fragility and Structure through Viscosity and High Temperature NMR Measurements in Li_2O–ZnO–P_2O_5 Phosphate Glasses. *J. Non. Cryst. Solids* **2015**, *428*, 54–61.

(274) Bourhis, K.; Massera, J.; Petit, L.; Ihalainen, H.; Fargues, A.; Cardinal, T.; Hupa, L.; Hupa, M.; Dussauze, M.; Rodriguez, V.; et al. Influence of P_2O_5 and Al_2O_3 Content on the Structure of Erbium-Doped Borosilicate Glasses and on Their Physical, Thermal, Optical and Luminescence Properties. *Mater. Res. Bull.* **2015**, *63*, 41–50.

(275) Nicoleau, E.; Angeli, F.; Schuller, S.; Charpentier, T.; Jollivet, P.; Moskura, M. Rare-Earth Silicate Crystallization in Borosilicate Glasses: Effect on Structural and Chemical Durability Properties. *J. Non. Cryst. Solids* **2016**, *438*, 37–48.

(276) Zhong, J.; Bray, P. J. Change in Boron Coordination in Alkali Borate Glasses, and Mixed Alkali Effects, as Elucidated by NMR. *J. Non. Cryst. Solids* **1989**, *111*, 67–76.

(277) Lee, S. K.; Musgrave, C. B.; Zhao, P.; Stebbins, J. F. Topological Disorder and Reactivity of Borosilicate Glasses: Quantum Chemical Calculations and ^{17}O and ^{11}B NMR Study. *J. Phys. Chem. B* **2001**, *105*, 12583–12595.

(278) Phillips, B.; Kirkpatrick, R. J.; Hovis, G. ^{27}Al, ^{29}Si, and ^{23}Na MAS NMR Study of an Al, Si Ordered Alkali Feldspar Solid Solution Series. *Phys. Chem. Miner.* **1988**, *16*, 262–275.

(279) Emerson, J. F.; Stallworth, P. E.; Bray, P. J. High-Field 29Si NMR Studies of Alkali Silicate Glasses. *J. Non. Cryst. Solids* **1989**, *113*, 253–259.

(280) Turner, G. L.; Smith, K. A.; Kirkpatrick, R. J.; Oldfield, E. Boron-11 Nuclear Magnetic Resonance Spectroscopic Study of Borate and Borosilicate Minerals and a Borosilicate Glass. *J. Magn. Reson.* **1986**, *67*, 544–550.

(281) Kaur, G. *Solid Oxide Fuel Cell Components - Interfacial Compatibility of SOFC Glass Seals*; Springer: New York, 2016.

(282) Clewett, J. P. D.; Roeller, K.; Bowley, R. M.; Herminghaus, S.; Swift, M. R. Emergent Surface Tension in Vibrated, Noncohesive Granular Media. *Phys. Rev. Lett.* **2012**, *109*, 228002.

(283) Roeller, K.; Clewett, J. P. D.; Bowley, R. M.; Herminghaus, S.; Swift, M. R. Liquid-Gas Phase Separation in Confined Vibrated Dry Granular Matter. *Phys. Rev. Lett.* **2011**, *107*, 48002.